

High-Throughput Methods in Quantum Chemistry Directed Catalyst Search

DISSERTATION

zur Erlangung des akademischen Grades
Doktor der Naturwissenschaften
(Dr. rer. nat.)

an der
Fakultät für Mathematik, Informatik und Naturwissenschaften
im Fachbereich Chemie
der
Universität Hamburg

vorgelegt von
Jan-Philipp Werner

Hamburg, 2011

Die hier vorliegende Arbeit wurde im Zeitraum zwischen November 2007 und Oktober 2011 am Institut für Anorganische und Angewandte Chemie der Universität Hamburg im Arbeitskreis von Prof. Dr. P. Burger angefertigt.

Gutachter:

Prof. Dr. P. Burger

Prof. Dr. T. Schwabe

Tag der Disputation: 09. Dezember 2011

Danksagung

An erster Stelle danke ich Herrn Prof. Dr. Peter Burger für die Überlassung des spannenden und herausfordernden Themas, die Hilfsbereitschaft und die vielen anregenden Diskussionen.

Bei Herrn JProf. Dr. Tobias Schwabe, den ich schon bei einem Forschungsaufenthalt in Münster kennenlernen konnte, bedanke ich mich für die Übernahme des Korreferats.

Allen Mitgliedern unseres Arbeitskreises danke ich für die Hilfsbereitschaft, die ruhige Arbeitsatmosphäre und die vielen Kuchenrunden. Mein Dank gilt Dr. Andrey Rogachev für die Einführung in die CASSCF-Methoden. Bei Thorsten Werner bedanke ich mich für die große und stete Hilfe beim Aufbau und Betrieb der Computer-Cluster.

Herrn Prof. Klaus Theopold und seiner gesamten Arbeitsgruppe danke ich für die schöne Zeit in Delaware und die Heranführung an die Chemie des Chroms.

Bei meinen drei Praktikanten, Carmen, Lukas und Mazlum, bedanke ich mich für ihre Mitarbeit.

Danke auch an die Freunde, die mich beim Korrekturlesen sehr unterstützt haben.

Für die liebevolle Unterstützung über die lange Zeit danke ich ganz besonders meiner Familie und insbesondere meiner Frau Julia.

Contents

List of Abbreviations	v
I. Introduction	1
II. Theory	9
1. Electronic Structure Methods	11
1.1. Multiconfigurational Self-Consistent Field (MCSCF)	12
1.2. Complete Active Space Perturbation Theory of the 2nd Order (CASPT2)	13
1.3. Density Functional Theory	14
1.3.1. First Rung: LSDA	16
1.3.2. Second Rung: GGA	17
1.3.3. Third Rung: meta-GGA	17
1.3.4. Fourth Rung: hyper-GGA	17
1.3.5. Fifth Rung	18
1.3.6. Remarks	19
2. Probabilistic Optimization Algorithms	21
2.1. Introduction	21
2.2. Genetic Algorithms	21
2.2.1. Terminology	22
2.2.2. Selection	26
2.2.3. Representation Scheme	30
3. Neural Networks	31
3.1. Feed Forward Networks	31
3.2. Applications	34
III. Method and Model Evaluation	35
4. Introduction	37
5. Imido Chromium Complexes as Fluoroolefin Polymerization Catalysts	39
5.1. Introduction	40
5.2. Results and Discussion	42
5.2.1. The Model Complex $[\text{Cr}(\text{NH})_2(\text{Me})_2]$	42

5.2.2.	Model Mechanism	44
5.2.3.	Reference Calculations	47
5.2.4.	Dependence on the Density Functional	52
5.2.5.	Alternative Mechanisms	56
5.2.5.1.	β -F elimination <i>via</i> σ -bond metathesis	56
5.2.5.2.	Cycloaddition of the olefin	57
5.3.	Summary	59
6.	Imido Chromium Complexes as Ethene Polymerization Catalysts	61
6.1.	Introduction	62
6.2.	Results and Discussion	64
6.2.1.	Method Dependence	64
6.2.2.	Insertion Mechanism	71
6.3.	Summary	74
IV.	Optimizations	75
7.	Introduction	77
8.	Target Based Random	81
8.1.	Introduction	82
8.2.	Exploring a QSAR: Angle Scanning	82
8.3.	Candidate Construction and Evaluation	87
8.4.	Exemplary Catalyst Candidates	91
8.5.	Conclusions	94
9.	Evolutionary Methods	97
9.1.	Introduction	98
9.2.	Optimization	99
9.2.1.	Optimization Space	99
9.2.2.	Fitness function	100
9.2.3.	Evaluation procedure	102
9.2.4.	Optimization Runs	105
9.2.5.	Data Evaluation	109
9.2.6.	Selected Candidates	116
9.3.	Conclusions	120
V.	Approaches <i>in vitro</i>	123
10.	Lead Syntheses	125
10.1.	Goal and Approach	125
10.2.	Syntheses of Ligands	129
10.2.1.	1,1'-(1,4-phenylene)bis(2-methylpropan-2-amine) (1)	129
10.2.2.	2,4-Dimethyl-6-(methylsulfonyl)aniline (2)	133

10.3. Attempted preparations of chelate diimido chromium(VI) complexes (3 and analogs)	134
10.3.1. Transaminations	135
10.3.2. Synthesis from the trimethylsilylamine 4	137
10.3.3. Synthesis from sulfinylamine	138
10.4. Attempted preparations of the phenylimido complex 5	138
10.5. Conclusions	139
VI. Experimental Part	141
11. Computational Details	143
12. Random Construction	147
12.1. Angle Scanning	148
12.2. Candidate Construction	148
13. Genetic Algorithm: ChemScreen-GA	151
13.1. Selection Method	152
13.2. Logic and Data Handling	154
13.2.1. The Fitness Function	157
13.2.2. Reproduction Operators	157
13.3. Aniline Derivatives – Parameter Evaluation	157
13.3.1. Mutation Probability	160
13.3.2. Number of Elitists	161
14. Syntheses of Candidate Catalysts	163
14.1. Experimental Details	164
Summary	171
Zusammenfassung	177
Appendix	i
A. Computational Considerations	iii
A.1. Cluster Setup	iii
A.1.1. Introduction	iv
A.1.2. Implementation	v
A.1.2.1. Software and Configuration	vii
A.2. Scaling	x
List of Figures	xiii

List of Tables	xvii
Bibliography	xix
Hazardous materials	xxxii

List of Abbreviations

B88	Becke 1988 (exchange functional)	LSDA	local spin density approximation
BP	backpropagation	LYP	Lee-Yang-Parr (correlation functional)
BSSE	basis set superposition error	M06-L	Truhlar and Zhao's Minnesota 2006 local (exchange-correlation functional)
CI	configuration interaction	MAE	mean absolute error
CCSD(T)	coupled cluster singles and doubles with perturbative triples correction	MCSCF	multi-configuration self-consistent field
ccNUMA	cache-coherent non-uniform memory access	MSE	mean squared error
CAS	complete active space	MO	molecular orbital
CP	Cole-Perdew (correlation functional)	MP	Møller-Plesset
DFT	density functional theory	PBE	Perdew-Becke-Ernzerhof (exchange-correlation functional)
D-RMS	distributed-resource management system	POA	probabilistic optimization algorithm
FFN	feed-forward network	PDD	2,2-bistrifluoromethyl-4,5-dichloro-4,5-difluoro-1,3-dioxolane
GA	genetic algorithm	PTFE	polytetrafluoroethene
GGA	generalized gradient approximation	PVDF	poly- <i>gem</i> -difluoroethene
GbE	gigabit ethernet	P86	Perdew 1986 (correlation functional)
HF	Hartree-Fock	PW91	Perdew-Wang 1991 (exchange-correlation functional)
HK	Hohenberg-Kohn	PW92	Perdew-Wang 1992 (correlation functional)
ICCC	Inorganic Chemistry Computational Cluster	PZ81	Perdew-Zunger 1981 (correlation functional)
IPC	interprocess communication	QP	quickpropagation
KS	Kohn-Sham		
LAN	local area network		
LDA	local density approximation		

QSAR	quantitative structure activity relationship	SMP	symmetric multi processing
QSPR	quantitative structure property relationship	SUS	statistic universal sampling
RASSCF	restricted active space self-consistent field	TMSCI	trimethylsilyl chloride
RPA	random phase approximation	TPSS	Tao-Perdew-Staroverov-Scuseria (exchange-correlation functional)
SGE	Sun Grid Engine	vdW	van-der-Waals
SMILES	<u>s</u> implified <u>m</u> olecular <u>i</u> nput <u>l</u> ine <u>e</u> ntry <u>s</u> ystem	VWN	Vosko-Wilk-Nusair (correlation functional)

Part I.

Introduction

The discovery of new chemical compounds with yet unprecedented properties has long been ruled by serendipity [1]. Even if related compounds with similar properties are known or promising compound classes are identified, uncertainty remains, whether a targeted compound exhibits the desired property and if it can be prepared.

Computational chemistry can help to remove some of the uncertainty in the discovery process in different ways [2]. First, by applying theoretical chemistry methods it can help to better understand a problem, e.g. how a specific property is connected to the molecular structure [3]. Second, by determination of the thermodynamics it can verify whether the compounds are potentially stable at all [4]. And eventually third, by investigating also kinetics leading to or from the compounds it can evaluate formation and decomposition pathways. Ideally, the highest level of theory is applied to catch as much of the underlying physics as possible. This approach is limited to small molecules or models thereof, as these computations demand considerable user intervention and computing time. Alternatively, strongly parameterized semi-empirical and force-field methods can be used. They trade accuracy for speed, when effects have to be modeled which were not included during parameter determination.

A development which helps to make larger chemical systems treatable by higher-level methods is known as "Moore's Law" [5]. Following this law, the transistor count doubles approximately every two years and with it does processing power at nearly constant prices per chip. A second empirical relationship is known as "Kooimey's Law": The number of computations per consumed kWh doubles approximately every 1.6 years [6]. From these relationships it is evident that in foreseeable future, researchers will have the processing resources to treat extremely large numbers of realistic chemical systems using sufficiently accurate methods. Yet, the creation of computing tasks, i.e. the construction of molecular structures to be evaluated, has to become automated in order to allow the efficient use of resources.

In drug discovery the application of computational chemistry is advanced. During the last century research in this field has evolved from intuition and empirical observation with merely accidental findings to a more rational and planned process, where the outcome is almost statistically determined [7]. Several technological and scientific inventions boosted the discovery process to its current state. These include, but are not limited to, the better understanding of biology, instrumentation, laboratory automation and combinatorial chemistry. With the elucidation of

3D protein structures beginning in the 1970s the structure-based rational drug design arose which led to many successful drug discoveries [8–10]. In the 1980s the computer started to aid in the design by ligand fitting [11]. Combinatorial chemistry to construct huge libraries of new compounds evolved in the 1980s and 1990s. Contrasting the rational concept, the use of these libraries combined with automated high-throughput screening of the compounds' activities presents a systematic approach to benefit from mere chance. This approach evolved into the design of focused libraries [12] and thus became rational again. In the 1990s the computer based screening of virtual libraries began to accompany the experimental screening. It has since become an integral part of modern drug discovery [13].

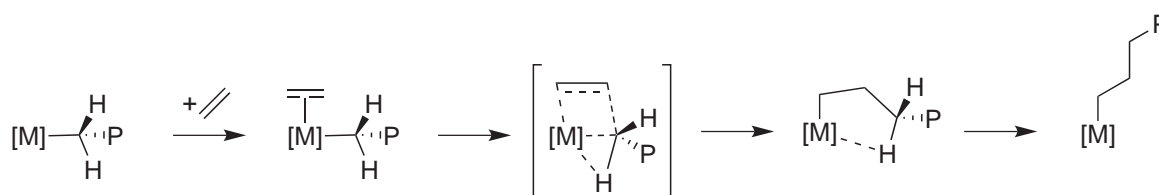
Contrary to the drug development, olefin polymerization catalysts have much longer remained the domain of intuition guided research. From the Ziegler-Natta catalysts discovered in the mid 1950s, which allowed the α -olefin polymerization at low pressure [14, 15], it took until 1982 when the first well defined and structurally characterized olefin polymerization catalysts were reported [16, 17]. Kaminsky's and Sinn's serendipitous finding that methylaluminoxane combined with Group 4 metallocenes produces highly active and long-lived polymerization catalysts [18] led to massive research in the field of metallocenes and to the introduction of these catalysts into industrial production [19].

In 1997 the Symyx company developed a screening workflow for the synthesis and screening of ligand-metal combinations for the discovery of new non-metallocene catalysts. Within less than three years it allowed the testing of more than 1500 ligands in nearly 100000 experiments leading to the discovery of many new classes of catalysts. Thus, high-throughput experimentation was introduced with success into the field of homogeneous catalysis [20].

The computational investigation of olefin polymerization by heterogeneous Ziegler-Natta systems and later homogeneous metallocenes reaches back into the 1970s [21]. Metallocenes are today probably the most extensively investigated organometallic systems [22]. The generally accepted mechanism for olefin polymerization by Group 3 and 4 alkyl metallocenes is the Cossee-Arlman mechanism [23–26]. Starting from a d^0 configured 14 electron complex, which is singly positively charged for Group 4 and neutral for Group 3 metallocenes, the formation of a side-on complex by π -complexation of the olefin, e.g. ethene, is the first step (Scheme 0.1).

In the second step the σ -bonded polymer chain migrates to the π -coordinated olefin and the olefin inserts (migratory insertion). An α -H-agostic interaction in the transi-

tion state of this step was proposed as an addition by Green, Rooney and Brookhart [27, 28].



Scheme 0.1. Modified Cossee-Arlman mechanism for olefin polymerization by early transition metals. The α -H-agostic interaction in the transition state is an addition by Green, Rooney and Brookhart. The growing polymer chain is abbreviated as “P”, the metal center as “M”.

Much effort was spent in recent years in modeling of catalysts to better understand the selectivities of chiral metallocenes [29], which were introduced by Brintzinger, who synthesized chiral *ansa*-metallocenes [30]. Not only the investigation but also the design of novel catalysts including the screening of numerous catalysts was performed *in silico* [31]. Yet, computational high-throughput screening is lacking in homogeneous transition metal catalysis and especially in olefin polymerization research.

Transition metal complexes can not easily be treated by low-level techniques, e.g. force-field or semi-empirical methods [32, 33]. Although both methodologies could be parametrized to approach a very specific problem¹, the transfer to sometimes even apparently similar systems might fail. Their often complicated electronic structures with close to degenerate states give rise to significant electron correlation and make transition metal complexes hard to treat computationally [33]. While high level wave function theory methods are sophisticated enough to describe the systems, their demand in computational resources is so high that only small models can be treated. The progress in the development of density functional methods established them as valuable alternative to wave function theory. Many studies for the design of metallocene based olefin polymerization catalysts rely on density functional methods or methods combining these with molecular mechanics [35]. With the development of acceleration techniques such as the resolution of identity [36, 37] and powerful computers available to the researcher, even realistically sized molecules have become treatable with excellent accuracy/precision-computation time profiles. The study of transition metal catalyzed reactions was put into the

¹ Both semi-empirical and force-field methods have indeed been used with success for example in the prediction of selectivities for differently sterically crowded metallocenes [34].

reach of high-throughput computations [38] and a first approach for the cleavage of dinitrogen – employing very small models though – has recently been published [39].

Object of the high-throughput investigations in this work is the coordinative polymerization of α -olefins. The scale of poly- α -olefin production, with polyethene alone having a 65 Mt/a output in 2008 [40], highlights its importance. In recent years much interest has evolved in the field of non-metallocene catalysts to supersede traditional metallocene catalyst by higher activities, different tuning possibilities to influence for example the tacticity, or compatibility with a wider range of co-monomers [41, 42]. Though, general availability is still lacking for catalysts for the coordinative polymerization of polar monomers [41, 43]. Especially fluoroolefins, which are used to produce highly resistant polymers, e.g. polyvinylfluoride or polytetrafluoroethene (PTFE), impose serious problems to classical Group 4 based catalysts.

Since the serendipitous discovery of Teflon at DuPont de Nemours and Co. in 1938 [44, 45], fluoropolymers have gained a substantial importance in technological application. Teflon is the polymer with the most pronounced “fluoropolymeric” properties. The high bond energy of the C–F bond (116 kcal/mol) and the shielding of the carbon backbone by the fluorine atoms are the key factors of fluoropolymers leading to their outstanding chemical, thermal and UV-light resistances [46]. Increasing the fluorine content of a polymer increases its chemical and solvent resistance, flame resistance and photostability. Compared to most engineering thermoplastics, the mechanical properties are typically poorer [47]. The major commercial fluoropolymers are PTFE and poly-*gem*-difluoroethene (PVDF) (Figure 0.1).

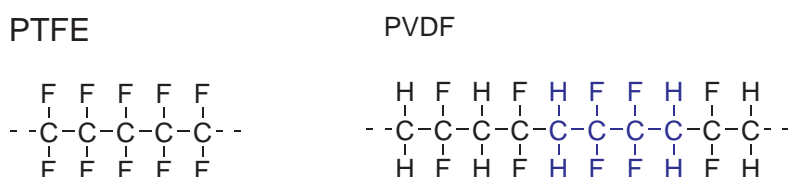


Figure 0.1.. Structures of polytetrafluoroethene (PTFE) and poly-*gem*-difluoroethene (PVDF). For PVDF the regular head-tail arrangement of monomer units is printed in black while a head-head arrangement is marked in blue.

Both polymers are produced under radical reaction conditions. Possessing a close to perfectly linear non-branched structure, PTFE exhibits a crystallinity of 92–98% [47]. It is insoluble in most solvents and can not be melt-processed by standard

methods due to its high melt viscosity of 1–10 GPa·s [48]. To obtain an amorphous polymer, which is soluble and melt-processable, free radical copolymerization is performed employing tetrafluoroethene and for example 2,2-bistrifluoromethyl-4,5-dichloro-4,5-difluoro-1,3-dioxolane (PDD) as monomers [46]. These copolymers are expensive and alternative processes to less crystalline perfluorinated polymers are needed. In PVDF the crystallinity is much lower (35–70%), which is caused by head-to-tail or tail-to-head defects (see Figure 0.1) [47]. Both, making PTFE less crystalline by controlled random copolymerization and making PVDF more crystalline by enforcing a higher tacticity, could be achieved by coordinative polymerization. This would be in analogy to the production of linear-low density polyethene – a copolymer of ethene and higher α -olefins – and of isotactic polypropylene. The first can be produced using Ziegler-Natta or Philips type catalysts, the latter with metallocene catalysts. These two alterations are just examples for potential improvements by coordinative polymerization, the incorporation of small amounts of fluoroolefins into a polyhydrocarbon by direct copolymerization is yet another. Radical copolymerization of α -olefins with fluoroolefins yields branched low-density polymers [49] and other methods either give non-uniform fluorine distributions and lead to crosslinking (direct fluorination of polyolefins) [50] or involve the use of expensive monomers, e.g. ring opening metathesis of fluorinated norbornenes [51]. To conclude, the discovery of coordination catalyst for highly polar olefins is anticipated to lead to a similar boost in the design of novel polymer-structures as observed for polyethene with the advent of Ziegler-Natta catalysts, which were inaccessible with the prior radical based processes, e.g. highly stereoregular polymers.

Central among the problems imposed to Group 4 polymerization catalysts is that metal fluorides are stable deactivation products [52–54]. The binding of fluorine to the metal center can be understood in the frame of Pearson's hard-soft acid-base concept [55] as a favorable hard-hard interaction. The coordination of polar functional groups to the chemically hard metal center leads to low insertion reactivities or complete deactivation [56]. Therefore, the elimination of a fluorine atom from the growing polymer chain and its transfer to the metal center is a catalyst deactivation process. Many efforts have been made to employ softer late transition metals as (co)polymerization catalysts for polar olefins [42]. Interestingly, although still considered chemically hard, diimido chromium(VI) complexes (see Figure 0.2) were found to be remarkably tolerant toward polar substrates [57] and active in ethylene polymerization [58].



Figure 0.2.. General structure of neutral (left) and cationic (right) diimido chromium complexes.

These catalysts are closely related to the Group 4 metallocenes by an isolobal relationship. When the two cyclopentadienyl ligands of a metallocene are replaced by imido ligands and the Group of the metal is changed from 4 to 6, electron counting and the approximate orbital shapes are constant. The neutral complexes are active in the insertion (co)polymerization of methyl methacrylate, acrylonitrile and vinyl acetate [57, 59] and the cationic complexes for ethene [58]. Because of these remarkable reactivities and the potential tuning possibilities by substitution of the imido ligands, they are selected as the objects of study. Two questions are central: i) can diimido chromium(VI) complexes be computationally optimized to polymerize fluoroolefins? ii) How can their activity in olefin polymerization be enhanced?

It is the objective of this dissertation to find approaches to systematic and automatic computational investigations of catalytic systems by density functional methods, which are suited to run on standard computer cluster hardware. Thereby, a contribution is made to more time and cost efficient catalyst discovery processes.

Before any automated optimization or screening can be addressed, insight into the system under consideration is important. Therefore, mechanistic details of the targeted reactions have to be investigated in a first step to derive working models for the reactions. It deserves a special mention that experimental evidence for the fluoroolefin polymerization catalyzed by chromium systems is non-existent and the mechanisms are approached computationally. It is known that especially for transition metal systems different density functionals often give varying energies [60]. The application of density functional theory to transition metals is therefore involved and a thorough calibration of the applied methods to high level wave function approaches is performed. Guided by mechanistic insight, fully automatic optimizations of the catalysts are strived for.

Part II.
Theory

1. Electronic Structure Methods

Starting from the single determinantal Hartree-Fock (HF) method¹, a series of improvements has been made in wave function theory. When performing an HF calculation, the resulting energy is only about 99% correct. The remaining 1%, the difference between the exact energy E^{exact} and the HF energy E^{HF} which HF cannot account for, is within a given basis set the electron correlation energy E_C (Eq. 1.1):

$$E_C = E^{\text{exact}} - E^{\text{HF}} \quad (1.1)$$

Although this energy portion is small, it is essential to describe chemical phenomena for which accuracies close to the 1 kcal/mol range are required. Since the trial wave function obtained by HF is the best one-determinantal, it is natural to expand the wave function Ψ by adding more Slater determinants Φ_i (Eq. 1.2):

$$\Psi = a_0\Phi_{\text{HF}} + \sum_{i=1} a_i\Phi_i \quad (1.2)$$

where Φ_{HF} denotes the HF-determinant and Φ_i the additional determinants. Starting from an HF wave function one can construct a trial wave function as a linear combination of determinants and optimize the expansion coefficients a_i to minimize the energy. This method is called configuration interaction (CI). If only single and double excitations from the reference (HF) determinant are allowed to generate excited determinants, the abbreviation is CISD for CI singles and doubles. CISD is a non-size extensive method, that means the larger the system the less correlation energy is recovered. Typically, 80%–90% are found for small systems. It scales with the basis set size as M^6 , where M is the number of basis functions. For comparison, the coupled cluster singles and doubles with perturbative triples correction method (CCSD(T)) scales as M^7 . With the latter method chemical accuracy in the 1 kcal/mol range is often achieved [62].

CI is a very seldom used method because of the shortcomings of size-inextensivity and low percentage of recovered correlation energy in relation to its computational

¹ For an introduction, the reader is referred to quantum mechanics textbooks, e.g. [61].

demand, and alternatives have been invented. The ones mostly used within this work will be discussed briefly in the following.

1.1. Multiconfigurational Self-Consistent Field (MCSCF)

A direct extension of HF with more flexibility are the multi-configuration self-consistent field (MCSCF) methods. They can be regarded to as a full CI (all excitations allowed) where besides the expansion coefficients also the molecular orbitals (MOs) used to construct the determinants are optimized. Since a full CI can not be handled but for the smallest systems, a commonly used variant is complete active space (CAS), as illustrated in Figure 1.1. The orbital space is divided into three regimes: As in HF, there is an inactive space where all orbitals are doubly occupied and there is a virtual space which is unoccupied. The third space is the so called "active space" within which all possible excitations are allowed.

This active space can not be chosen to be very large due to the high computational demand. The number of configurations generated by excitations is growing factorially with the number of electrons/orbitals. Today, active spaces of up to 16 electrons in 16 orbitals, denoted as [16,16]-CASSCF, can be treated.

To include more orbitals, the restricted active space self-consistent field (RASSCF) method has been invented [63]. The active space from a CAS calculation is further subdivided into the RAS1, RAS2 and RAS3 spaces. Within RAS2 again a full CI is performed, whereas from RAS1 excitations are treated only to an extent which is defined by the user by explicitly allowing the highest possible level of excitation. Excitations to the RAS3 space are treated with the same manner.

The MCSCF methods are again not size-extensive. They usually give a very unbalanced description of the electronic system, since within the active space (or RAS2) all correlation is recovered while none is recovered in the inactive space and from or to the inactive space. From RAS1 and RAS3 (see above) only some correlation is included. It is therefore essential to choose an active space well adapted to the problem under investigation. This means that for example orbitals exhibiting the largest changes in the course of a reaction should be included as should be ones needed to describe strong static correlation.

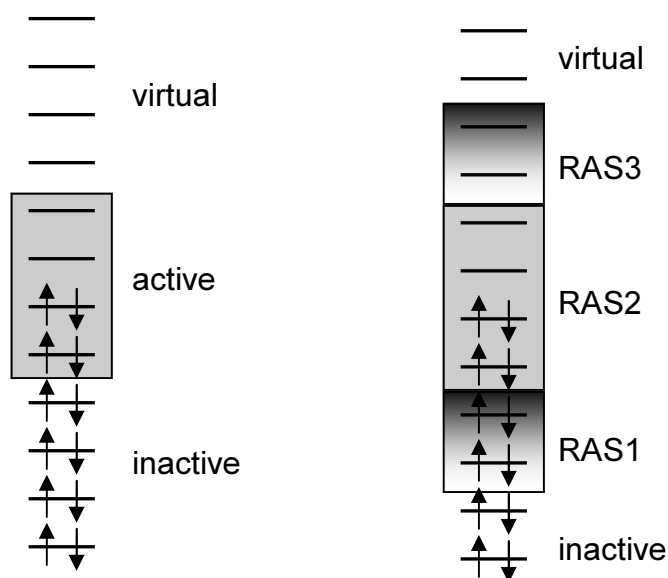


Figure 1.1.. Illustration of a [4,4]-CAS (left) and a RAS (right).

1.2. Complete Active Space Perturbation Theory of the 2nd Order (CASPT2)

Different schemes were developed to account for the electron correlation outside the active space and between active and inactive space and thus to improve the qualitatively correct CASSCF wave function to be quantitatively correct. These include the multi-reference CI and multi-reference coupled cluster [64–66] or coupled pair methods [67]. Less computationally demanding are (Rayleigh-Schrödinger) perturbative treatments [68]. In perturbative methods the general assumption is that a sought solution differs only slightly from an actually known solution. In case the Schrödinger equation is solved using a known Hamilton operator \mathbf{H}_0 , this operator may be perturbed by a perturbation operator \mathbf{H}' (Eq. 1.3):

$$\mathbf{H} = \mathbf{H}_0 + \lambda\mathbf{H}' \quad (1.3)$$

with λ being a parameter adjusting the strength of the perturbation. Performing a Taylor expansion for the energy and wave function as powerseries of the perturbation parameter, one obtains an expression in which the zeroth-order term represents the unperturbed wave function or energy. All higher terms are corrections. If the series are truncated after the quadratic term, the result is a perturbative approach of second order.

For the actual calculation of energies, a Hamilton operator has to be chosen. For single reference cases, i.e. perturbations to a HF wave function, usually the sum over Fock operators is chosen in order to calculate the energy, leading to the Møller-Plesset (MP) perturbation theory [69]. First order MP theory yields just HF energies, while second order MP includes electron correlation.

The choice of a Hamiltonian for multi-reference wave functions is not straightforward, but some theories have evolved and are best tested on the second order level, including CASPT2 [70], NEVPT2 [71] and MCQDPT2 [72].

1.3. Density Functional Theory

The foundation of density functional theory (DFT) was laid by Hohenberg and Kohn in 1964, showing that the Hamiltonian of an N -electron system is in principle determined by the ground-state electron density ρ (Hohenberg-Kohn (HK)-theorem); its ground-state wave function and energy are thereby determined too [73].

This has to be compared to the classical wave function approach. In the latter case the energy of a system is unknown, we usually have to solve the time independent Schrödinger equation. The Hamilton operator \mathbf{H} acts on the wave function Ψ , and Ψ has to be determined. The problem is that for an N -electron system Ψ depends on $3N$ ($4N$ if spin is included) coordinates, 3 (4) for each electron. A wave function therefore becomes very complex for large numbers of electrons. In contrast, the electron density always depends on only 3 coordinates, independently of the number of electrons. The problem is that the functional connecting ρ with E is not known.

The design of such functionals is the heart of DFT method development. The energy's density dependence $E[\rho]$ is decomposed into the following terms (Eq. 1.4):

$$E[\rho] = T[\rho] + E_{\text{ne}}[\rho] + E_{\text{ee}}[\rho] \quad (1.4)$$

Here $T[\rho]$ is the kinetic energy, $E_{\text{ne}}[\rho]$ the electron-nuclei interaction and $E_{\text{ee}}[\rho]$ the electron-electron interaction. The core-core interaction is skipped, since it is constant within the Born-Oppenheimer approximation. With $E_{\text{ne}} = \int \rho(\mathbf{r}) \mathbf{V}_{\text{ne}} \mathbf{d}\mathbf{r}$ only $T[\rho]$ and $E_{\text{ee}}[\rho]$ remain unknown. Usually E_{ee} is split into the Coulomb part $J[\rho]$, which is again solved with its classical expression, and the exchange part $K[\rho]$.

For a non-interacting uniform electron gas, equations for $T[\rho]$ and $K[\rho]$ can be derived exactly, which lead to the development of the *Thomas-Fermi* theory and *Thomas-Fermi-Dirac* model [74]. As a uniform electron gas assumption does not hold very well for atoms and molecules, bonding could not be predicted with these models. The main source of error was that the kinetic energy was represented poorly.

The use of DFT in computational chemistry was finally initiated by the Kohn-Sham (KS)-theorem in 1965, asserting that the ground-state density can be found by solving exact self-consistent one-electron Schrödinger equations for Kohn-Sham orbitals with occupation number 1 or 0, from which the electron density may be calculated by summing the squares of the occupied orbitals [75]. It is assumed that electrons are non-interacting and the kinetic energy can be calculated exactly (Eq. 1.5):

$$T_S = \sum_{i=1}^N \langle \phi_i | -\frac{1}{2} \nabla^2 | \phi_i \rangle \quad (1.5)$$

The subscript S denotes that the kinetic energy is calculated from only one Slater determinant, composed of molecular orbitals ϕ (KS-orbitals). Since in reality electrons are interacting, Equation 1.5 cannot provide the total kinetic energy, but the deviation from the exact result is small. This small amount of electron-electron interaction energy is expressed in an exchange-correlation term $E_{XC}[\rho]$. The general DFT expression for a system's energy E_{DFT} is thus formulated as (Eq. 1.6):

$$E_{DFT}[\rho] = T_S[\rho] + E_{ne}[\rho] + J[\rho] + E_{XC}[\rho] \quad (1.6)$$

In practice, the DFT developer has to find a suitable exchange-correlation functional to calculate E_{XC} . Then the total energy can be determined using the variational principle by using trial solutions for the KS-orbitals, which can be expanded by basis functions in analogy to the HF method.

Often the exchange-correlation functional is split into two parts: the exchange expression $E_X[\rho]$ and the correlation expression $E_C[\rho]$. It is, however, not clear that such an assumption can be made. Exchange-correlation functionals can be grouped following Perdew's famous "Jacob's Ladder" [76] (see Figure 1.2), on which each step represents an increase in sophistication, with which an approximation to the true expressions is sought.

The ladder connects the "Hartree world", in which electron correlation is not accounted for, with the "heaven of chemical accuracy" where calculations can be

carried out with errors in relative energies below 1 kcal/mol. The different classes of functionals will be briefly explained in the following.

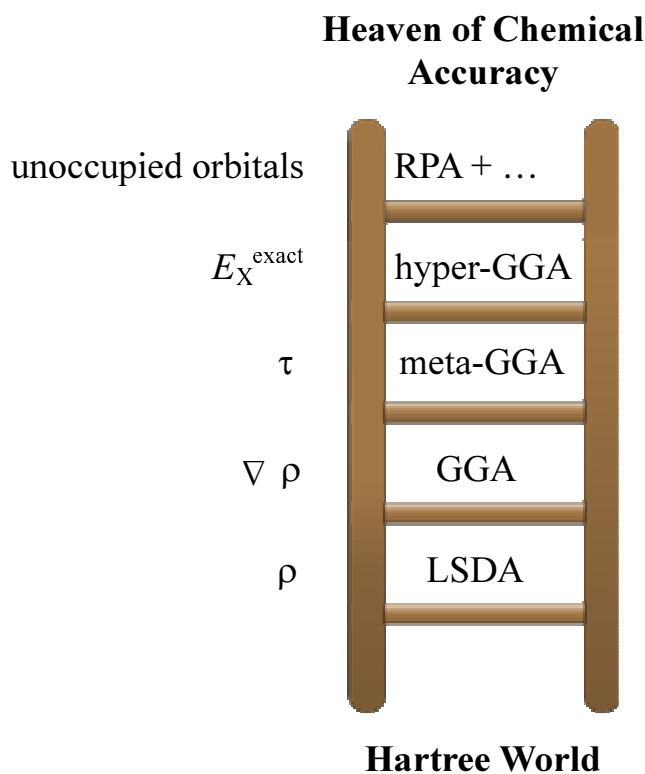


Figure 1.2.. The Jacob's ladder of density functional approximations. Additions are made successively to lead from a "Hartree World" with $E_{XC} = 0$ to the heaven of chemical with sub-1 kcal/mol errors in relative energies. Graphic adapted from [77].

1.3.1. First Rung: LSDA

The first rung on the ladder represents semilocal approximations. An approximation is regarded as semilocal, if its energy density depends only on the electron density and orbitals in an infinitesimal neighborhood of a given position. Otherwise, it is said to be fully nonlocal. The local spin density approximation (LSDA) is based on the model of a uniform electron gas. The exchange part can be derived analytically to yield the local density approximation (LDA) or LSDA, from which the latter is more appropriate if spin-densities for α and β electrons differ. For the correlation part, which is simply neglected in the case of Slater's X_α method [78], functionals are usually constructed to fit numerically derived densities of the uniform electron gas. The most famous include the Vosko-Wilk-Nusair (VWN) [79],

Perdew-Wang 1992 (PW92) [80], Perdew-Zunger 1981 (PZ81) [81] and Cole-Perdew (CP) [82] functionals.

1.3.2. Second Rung: GGA

The generalized gradient approximation (GGA) functionals present the second rung on the ladder. They try to treat the non-uniformity of real systems by the inclusion of the derivatives of the density. They can be either constructed to modify the LSDA energies in terms of a correction or as completely unique functionals.

The LSDA approaches can be regarded as being *ab initio* and non-empirical, since they take no parameters for the exchange, and parameters are used only to interpolate the numerically known correlation functional. For GGA functionals this changes and they can be either designed to reproduce experimental or high-level theoretical data, including the fitting of a parameter set to these, or to satisfy physical constraints. The latter can even be parameter-free and stay non-empirical, while the first have to be regarded to as empirical functionals. In principle, the ladder could be split into a non-empirical and an empirical from this point onwards.

One of the most widely used non-empirical functionals is the Perdew-Becke-Ernzerhof (PBE) functional [83, 84], while Becke 1988 (B88) [85] is certainly the most commonly used empirical exchange functional.² Other well known functionals include Perdew 1986 (P86) [87] and Lee-Yang-Parr (LYP) correlation [88] and Perdew-Wang 1991 (PW91) exchange-correlation [89].

1.3.3. Third Rung: meta-GGA

The next and highest semilocal rung includes the orbital kinetic energy density τ . A non-empirical example is the Tao-Perdew-Staroverov-Scuseria (TPSS) functional [90], an empirical one is Truhlar and Zhao's Minnesota 2006-local (M06-L) [91].

1.3.4. Fourth Rung: hyper-GGA

In the fourth rung, nonlocal treatment of the exchange part is included. In parts, these functionals make use of the exact exchange energy known from an HF calcu-

² Recently, it was shown that the empirically determined parameter in B88 can be derived analytically [86].

lation. The earliest hyper-GGAs reported [92, 93] were global hybrid functionals, i.e. ones in which the amount of exact exchange energy E_X^{exact} is globally fixed and not depending on local features, with the general form (Eq. 1.7):

$$E_{XC} = aE_X^{\text{exact}} + (1 - a)E_X^{\text{semilocal}} + E_C^{\text{semilocal}} \quad (1.7)$$

At the cost of an additional HF-calculation these functionals often improve upon semilocal functionals and have gained wide popularity as exemplified by the widespread use of B3LYP [79, 88, 94, 95], PBE0 [96], TPSSh [90, 97], TPSS0 [98] and BHLYP [85, 88]. The balance between exact and semilocal exchange however has to be determined empirically and thus all hyper-GGAs are empirical to some extent. While typical values for a around 0.2 have been found to give accurate atomization energies, values as high as 0.5 are required for reaction barrier heights [99].

A more flexible ansatz is provided by local-hybrid methods. They can be formulated to include a variable admixture of exact exchange depending on a local mixing function, which can for example depend on the kinetic energy density τ [100].

1.3.5. Fifth Rung

The fifth rung on the ladder of accuracy considers also unoccupied (Kohn-Scham) orbitals. This is done by either global double-hybrid functionals, where in a post-SCF procedure a part of the semilocal correlation energy is replaced by “exact” correlation E_C^{PT2} , which is computed in a second order perturbation upon DFT orbitals (Eq. 1.8):

$$E_{XC} = aE_X^{\text{exact}} + (1 - a)E_X^{\text{semilocal}} + bE_C^{\text{semilocal}} + (1 - b)E_C^{\text{PT2}}. \quad (1.8)$$

The double hybrid functionals are empirically fitted and possess advantages in the field of weak interactions. Examples include B2PLYP [101], mPW2PLYP [102] or PBE0-dh [103].³

An alternative fifth rung functional can be based on the random phase approximation (RPA) and can thus be parameter-free. This method has only recently attracted renewed attention and is under development. Promising results have just been published [104, 105].

³ PBE0-dh is explicitly not fitted.

1.3.6. Remarks

The computational effort for the DFT methods increases from rung 1 to 3 modestly and thereafter steeply. For main group chemistry and especially for non-bonding interactions the improvements stepping up the Jacob's ladder are significant as evidenced by benchmark calculations [106, 107]. The picture is different for transition metal systems with strong static correlation contributions, for which third or second rung functionals repeatedly outperform fourth rung functionals in the prediction of thermodynamic properties [60, 99, and references therein]. Even the field of weak interactions is not perfectly covered by current double hybrid functionals and they get augmented by empirical van-der-Waals corrections.

2. Probabilistic Optimization Algorithms

2.1. Introduction

Probabilistic optimization algorithms (POAs) constitute a class of optimization algorithms which can be applied when the dimensionality of a search space is very high or the relation between a solution candidate and its “fitness” (function value) is not obvious or too complicated. This is in contrast to deterministic algorithms. POAs apply heuristics to decide which solution candidate should be tested next or how the next candidate could be produced. Although the classification is not straightforward, POAs can be termed Monte Carlo algorithms [108]. They can be grouped into i) evolutionary algorithms, ii) swarm intelligence algorithms and iii) algorithms mimicing physical processes. Examples for i) include genetic algorithms, evolutionary programming and genetic programming, for ii) ant colony optimization and particle swarm optimization, and for iii) simulated annealing and the raindrop method. Algorithms like hill climbing and random optimization are unique and can not be fitted into this scheme. For an overview of POAs see [108]. All of these methods have in common that there is no guarantee to find the global optimum, but they are designed to have shorter runtimes in finding an (eventually local) optimum compared to brute-force optimizations.

2.2. Genetic Algorithms

Genetic algorithms belong to a class of search techniques which try to mimic nature’s methods in evolution, i.e. the evolutionary algorithms. In genetic algorithms operators are applied in analogy to mating and mutation as well as the Darwinistic survival of the fittest. They were developed in the 1970s by Holland [109] and have since been applied with success in a wide field of problems [110].

2.2.1. Terminology

In principle genetic algorithms can be applied to any problem where the property or properties to be optimized depend on one or more variables. The values of the variables are known as “alleles”; the variables themselves are called “genes” and are encoded to form a string called “chromosome” [111]. Therefore, a chromosome encodes an “individual” (or “candidate”) which is a trial solution of the problem. A graphical representation of chromosome, genes and alleles is shown in Figure 2.1.

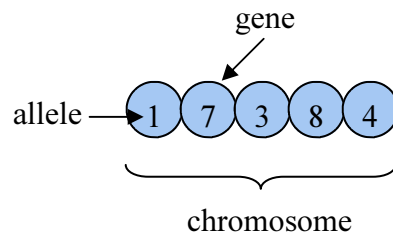


Figure 2.1.. Representation of an individual by its “chromosome” partitioned into “genes”. The value of the genes are “alleles”.

A typical genetic algorithm starts with the setup of an initial population P of N candidates J_i : $P = \{J_1, J_2, \dots, J_N\}$. The candidates are usually generated randomly within the search space, which is the space of all possible individuals \mathbf{J} .

A function f called “fitness function” connects the candidate J_i with the quantity to be optimized, the individual’s “fitness” f_i , $f : \mathbf{J} \mapsto \mathbf{R}$, where \mathbf{R} is the space of all possible fitness values. f is applied to every individual to be evaluated, in the beginning it will be applied to all members of the initial population.

During “selection” a set of rules ω is used to decide whether an individual of the actual population is allowed to reproduce or not $\omega : \mathbf{J}^N \mapsto \mathbf{J}^N$.

After selection, “recombination” is performed $\Xi : \mathbf{J}^N \mapsto \mathbf{J}^N$. This changes the genetic material by usually two methods with an overall probability of p_c , which has to be defined by the user.

The first method is “crossover” and is also called “mating”, in which the chromosomes of two (or more) parents are joined to form “offspring”. An often applied variant is single-point crossover. Here, the parent strings are cut into two parts at the same point and the fragments are recombined as shown in Figure 2.2.

The second method, “mutation”, is a technique to introduce new genetic material. Whereas crossover only leads to the interchange of genetic material, stagnation in

the global optimization process might be observed if the genetic material present in the population is not sufficient to favor optimal solutions. During mutation, which is again applied with a certain probability, one or more genes of an offspring are randomly modified. Two variants can be distinguished: static mutation and dynamic mutation. In static mutation, the mutated gene is assigned a completely random value, while in dynamic mutation a small modification of its original value is performed.

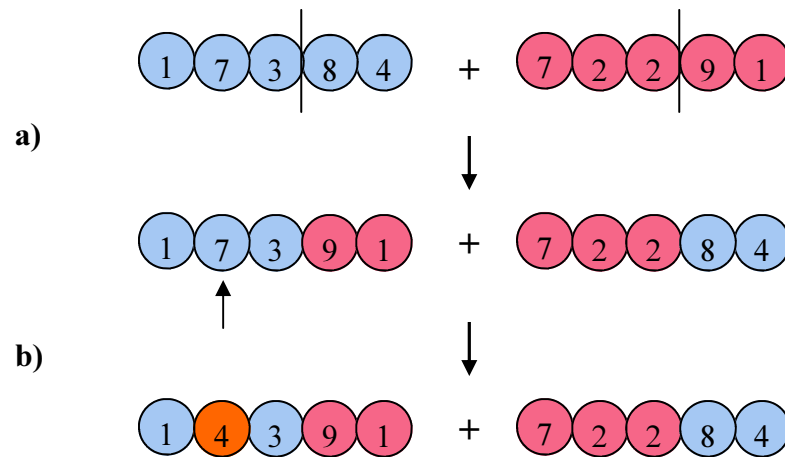


Figure 2.2.. Crossover (step a) and mutation (step b) during an evolution step.

The overall working scheme of a general genetic algorithm is shown in Figure 2.3. Starting with a randomly initialized population, selection is performed. The selected individuals are subjected to recombination with the probability p_c and the offspring (the actual population) is evaluated. In case the problem is solved, f.e. if an individual possesses the desired fitness or the population's mean fitness has reached a threshold value, the algorithm is stopped. If this is not the case, the next iteration cycle is initiated.

At the end of an optimization the genetic code of the population can be inspected for one or more common schemas as shown in Figure 2.4. The identification of such patterns that are frequent for good solutions can point to areas on the chromosome which are most relevant for the desired property.

A key point in every genetic algorithm is the selection method since it focuses the search on promising regions in the search space and thus controls the convergence speed to some extent. The development of the best individual's fitness [112, 113] and of the mean fitness [114] as well as the change in the fitness distribution [115] over the course of the evolutionary process can be analyzed to compare different selection algorithms. The mathematical description of the selection methods is well

established [115, and references therein] and important aspects will be highlighted in the following.

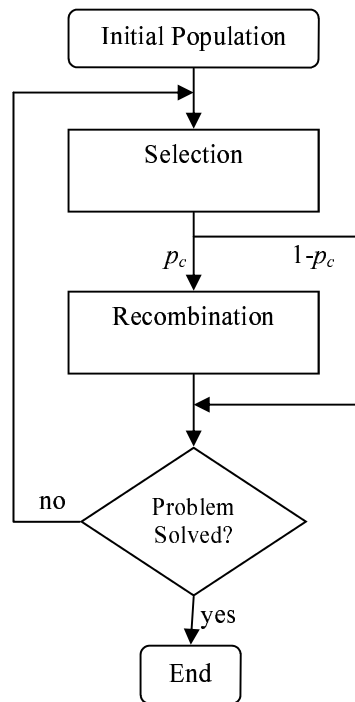


Figure 2.3.. General flowchart of a genetic algorithm.

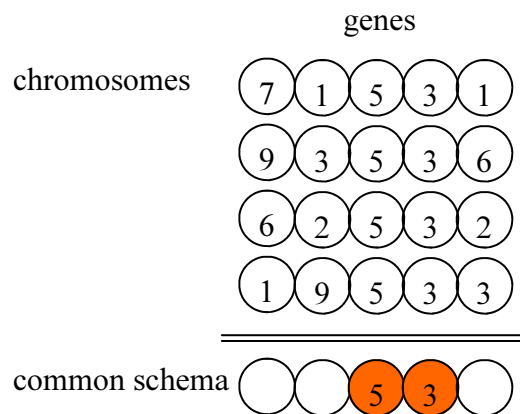


Figure 2.4.. The illustration of a common schema in the genetic representation.

To describe the state of a population P after a given number of iteration cycles τ , the knowledge of the fitness values of all individuals is sufficient [115]. The number of fitness values is limited to a maximum of the number of candidates in the population N : $f_1, \dots, f_n (n \leq N)$. The state can as well be described by the fitness distribution $s(f_i)$, which is a function of the fitness value and assigns to each value $f \in \mathbf{R}$ the number of individuals possessing this value. A selection

method Ω can be mathematically defined as a transformation which changes a fitness distribution s to another fitness distribution s' : $s' = \Omega(s)$. Since we deal with probabilistic methods, usually expected fitness distributions s^* are calculated: $s^* = \Omega^*(s)$.

To derive equations for certain properties of the presented methods, sometimes a continuous fitness distribution has to be assumed. The functions in the continuous case are denoted with a bar and e.g. $\bar{s}(f)$ is written instead of $s(f)$.

An important function for the further argumentation is the cumulative fitness distribution $S(f)$. It returns the number of individuals with fitness values f_i and worse (Eq. 2.1):

$$S(f_i) = \begin{cases} 0 & : i < 1 \\ \sum_{j=1}^{j=i} s(f_j) & : 1 \leq i \leq n \\ N & : i > n \end{cases} \quad (2.1)$$

The reproduction rate $\bar{R}(f)$ can be computed as follows. It is a measure for the ratio of individuals with a certain fitness value after and before a selection (Eq. 2.2):

$$\bar{R}(f) = \begin{cases} \frac{\bar{s}^*(f)\bar{s}(f)}{0} & : \bar{s}(f) < 0 \\ 0 & : \bar{s}(f) = 0 \end{cases} \quad (2.2)$$

For a selection method to be effective, reproduction rates for good individuals should be large $\bar{R}(f) > 1$ and for bad individuals small $\bar{R}(f) < 1$.

A problem that is associated with selection is the loss of diversity p_d . It is the fraction of individuals not selected during a selection process (Eq. 2.3):

$$p_d = \frac{1}{N} (\bar{S}(f_z) - \bar{S}^*(f_z)) \quad (2.3)$$

Since the genetic material of the individuals not selected is lost, high values of p_d tend to lead to premature convergences. As a measure of the selective pressure, the selection intensity I as used by Bulmer can be defined as a dimensionless property (Eq. 2.4) [116]:

$$I = \frac{\bar{M}^* - \bar{M}}{\bar{\sigma}} \quad (2.4)$$

where $\bar{\sigma}$ is the standard deviation. As \bar{M} denotes the average fitness of the population, the selection intensity I quantifies the progress in average fitness during

selection. It is dependent on the initial fitness distribution. To compare it, a distribution has to be assumed. Here, the normalized Gaussian distribution $G(0,1)$ is assumed and the standardized selection intensity I_Ω can be derived (Eq. 2.5):

$$I_\Omega = \int_{-\infty}^{\infty} f \bar{\Omega}^*(G(0,1))(f) df \quad (2.5)$$

with the normalized Gaussian distribution $G(0,1)(f) = \frac{1}{\sqrt{2\pi}} e^{-\frac{f^2}{2}}$.

2.2.2. Selection

In the following, frequently employed selection methods will be presented.

Proportional Selection This method is used in the simple genetic algorithm [112] and is the selection method for genetic algorithms originally introduced by Holland [109]. The probability p_i of an individual i to be selected (Eq. 2.6) is given by

$$p_i = \frac{f_i}{NM} \quad (2.6)$$

with N being the population size and M the mean fitness. This method can only work if all fitness values are larger than zero, and probabilities depend strongly on the fitness function itself. The expected fitness distribution $s^*(f)$ (Eq. 2.7) is given by

$$s^*(f) = s(f) \frac{f}{M} \quad (2.7)$$

and the reproduction rate $R_P(f)$ (Eq. 2.8) becomes

$$R_P(f) = \frac{f}{\bar{M}} \quad (2.8)$$

where \bar{M} denotes the average fitness of the population. It is experimentally observed that the selection intensity is often too low, even at the beginning of optimizations when the variance in fitness values is high [115]. For very similar fitness values, the reproduction rate becomes approximately equal for all individuals and therefore selection pressure vanishes. Because of the invariance to translation, i.e. when the fitness function is shifted by a constant value, the usual standardized selection intensity cannot be derived. Often very low intensities were measured, however [115].

A modification is the rank based selection, which solves the aforementioned problems by ordering the individuals by their fitness, i.e. assigning a rank to each and selecting with a probability calculated from the rank. Variations include the linear and the exponential scaling of the rank.

Truncation Selection A special case of a rank based selection is the truncation selection as used by Crow [117]. Here, only the fitter fraction $(1 - T)$ of the population is allowed to be selected for reproduction but within this group all with the same probability. The expected fitness distribution (Eq. 2.9 and 2.10) is

$$s^*(f_i) = \begin{cases} 0 & : S(f_i) \leq (1 - T)N \\ \frac{S(f_i) - (1 - T)N}{s(f_i)T} & : S(f_{i-1}) \leq (1 - T)N < S(f_i) \\ \frac{1}{T} & : \text{else} \end{cases} \quad (2.9)$$

$$\bar{s}^*(f) = \begin{cases} \frac{\bar{s}(f)}{T} & : \bar{S}(f) > (1 - T)N \\ 0 & : \text{else} \end{cases} \quad (2.10)$$

The reproduction rate $\bar{R}_\Gamma(f)$ is given by Eq. 2.11:

$$\bar{R}_\Gamma(f) = \begin{cases} \frac{1}{T} & : \bar{S}(f) > (1 - T)N \\ 0 & : \text{else} \end{cases} \quad (2.11)$$

The loss of diversity $p_{d,T}$ for this method is (Eq. 2.12)

$$p_{d,T}(T) = 1 - T \quad (2.12)$$

and the selection intensity can be derived as (Eq. 2.13)

$$I_\Gamma(T) = \frac{1}{T} \frac{1}{\sqrt{2\pi}} e^{-\frac{T^2}{2}} \quad (2.13)$$

with T being the truncation threshold (Eq. 2.14):

$$T = \int_{f_c}^{\infty} \frac{1}{\sqrt{2\pi}} e^{-\frac{f^2}{2}} df \quad (2.14)$$

to derive the median fitness f_c .

Tournament Selection Within tournament selection a random number t of candidates is selected from the actual offspring to form a tournament pool. From this pool the individual of highest fitness is chosen as parent for the next generation. This selection is repeated until N parents are found. Using this method, selective pressure can be adjusted by choosing the size of the pool. For large sizes the selective pressure will be high, for small ones also less fit candidates get a chance to reproduce.

After selection, the expected fitness distributions s^* and \bar{s}^* (Eq. 2.15 and 2.16) are:

$$s^*(f_i) = N \left(\left(\frac{S(f_i)}{N} \right)^t - \left(\frac{S(f_{i-1})}{N} \right)^t \right) \quad (2.15)$$

$$\bar{s}^*(f) = t\bar{s}(f) \left(\frac{\bar{S}(f)}{N} \right)^{t-1} \quad (2.16)$$

The importance of the tournament pool-size t becomes clear at a first glance. For $t = 1$ an unchanged initial distribution would be obtained.

The loss of diversity $p_{d,T}$ can be calculated by (Eq. 2.17)

$$p_{d,T}(t) = t^{-\frac{1}{t-1}} - t^{-\frac{t}{t-1}} \quad (2.17)$$

whereas the reproduction rate R_T is given as (Eq. 2.18)

$$\bar{R}_T(f) = \frac{\bar{s}^*(f)}{\bar{s}(f)} = t \left(\frac{\bar{S}(f)}{N} \right)^{t-1} \quad (2.18)$$

Low fitness values lead to reproduction rates of almost zero; the individuals with the highest fitness value have a reproduction rate of t . For a typical tournament pool-size of 5, roughly half of the individuals will not be selected. For a pool-size of 10, already 67% will not reproduce.

The selection intensity I_T for the normalized Gaussian distribution $G(0, 1)$ is given by Eq. 2.19:

$$I_T(t) = \int_{-\infty}^{\infty} tx \frac{1}{\sqrt{2\pi}} e^{-\frac{x^2}{2}} \left(\int_{-\infty}^x \frac{1}{\sqrt{2\pi}} e^{-\frac{y^2}{2}} dy \right)^{t-1} dx \quad (2.19)$$

with t being the tournament size and can be solved analytically for $t = 1, \dots, 5$ [118–120] or approximated by Eq. 2.20:

$$I_T(t) \approx \sqrt{2(\ln(t) - \ln(\sqrt{4.13 \ln(t)}))} \quad (2.20)$$

The intensity for a pool-size of 5 is thus 1.15 and for a size of 10 1.53.

Roulette Wheel and SUS If we take the individuals as selected by the methods described above, the process might be visualized as a simple roulette wheel as shown in Figure 2.5. The individuals, in this example 7, occupy a space on the wheel proportional to their reproduction rate \bar{R}_i . The wheel is then turned N times, selecting each time the individual the pointer directs, to build the population. A problem is that the distribution may be bad – in an extreme case one individual can be selected N times – leading to a high variance in the fitness distribution. A work around is the “stochastic universal sampling” (SUS) approach developed by Baker [121]. Again a roulette wheel might be imagined but instead of one pointer, N equidistant pointers are present at the same time (see Figure 2.6) and the wheel is turned only once.

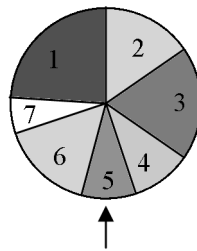


Figure 2.5.. A simple roulette wheel.

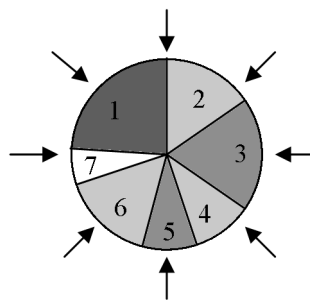


Figure 2.6.. The roulette wheel in stochastic universal sampling. Arrows point at the candidates to be selected.

This method leads to a minimization of variance and the result will be as close as possible to the expected.

In conclusion, it is the objective to select a method with the highest selection intensity at the lowest loss of diversity. Finding the optimal method surely depends on the optimization problem. If the impact of loss of diversity and intensity for a

given problem is known, the choice can be guided by the equations given above. It has to be noted that the equations to compute the selection intensity depend on the assumption of an initial Gaussian distribution of fitness values. For a given problem the distribution can be very different. It is stated by Mühlenbein and Voigt that “if two selection methods have the same selection intensity, the method giving the higher standard deviation of the selected parents is to be preferred” [122]. This gives an additional hint for selecting the “right” method.

2.2.3. Representation Scheme

To make genetic algorithms usable in chemistry, a chemical structure has to be mapped to a chromosome. In chemical nomenclature a common approach is to name a scaffold and define a substitution pattern. For example in 2,3-dichloro aniline the scaffold is substituted in 2- and 3-position by chlorine atoms and the substitution sites 4, 5 and 6 are unoccupied.

A more general approach is the simplified molecular input line entry system (SMILES) [123] notation. The latter describes the substitution pattern for each atom making certain default assumptions on bonding and valancy, which are tuned towards organic chemistry. Nonetheless, the description of complex molecules is feasible with this notation and even chiralities can be distinguished. Tools to convert the SMILES representation to a three dimensional molecular structure exist (for example see [124, 125]). Building blocks can be defined quite easily and hence a bridge can be build between the chromosome’s language of backbone and substituent and a chemical structure. This was first used by Douguet, Thoreau and Grassy for the automated design of small organic molecules [126].

3. Neural Networks

Artificial neural networks are mathematical models, initially developed to model the function of the mammalian brain. They consist of elements (the neurons) which are connected to form a network. Each neuron has inputs from other neurons and one output. The inputs it receives are scaled by the weights w associated with each connection. This is the way synapses are modeled and it leads to the alteration of a signal's intensity x_i to s_i by applying $s_i = w_i x_i$. The neuron itself can be decomposed into a summation unit, summing up all scaled inputs s_i yielding a combined input signal Net , and a transfer unit. In the latter the summed input is transformed into an output signal. To achieve this, many different functions have been proposed. Most frequently used is a sigmoid function, also known as logistic or Fermi function (Eq. 3.1):

$$x_{i,out} = \frac{1}{1 + e^{-(\alpha Net + \theta)}} \quad (3.1)$$

This function has many advantages. Most importantly, its nonlinearity allows a network to treat nonlinear problems. However, by adjustment of the parameter α or the weights w the input signal can also be scaled such that the function behaves nearly linear or that it acts as a step function. The function can be shifted by θ . Its output lies within the range $[0 \dots 1]$.

3.1. Feed Forward Networks

Networks can be distinguished by essentially three parameters: i) the way neurons are connected, ii) the transfer function used in the neurons and iii) the learning process. They all influence the applicability of networks to different problems. The learning process is usually linked to the connection mode. The fields networks are used for are:

Classification During classification an object which can be characterized by various properties is assigned to a category. For this usually an output neuron for

each class is defined and the one showing the largest signal strength indicates the categorization.

Modeling Since neural networks can process data in a non-linear fashion, they are able to express relationships between a set of variables and a dependent, which are too complex to derive an explicit mathematical formula for and hence could not be treated by statistical methods.

Association Comparison of data is possible, since networks can store information of similar kinds. They are for example able to recognize that two IR-spectra belong to the same compound even when there is noise in them (auto-association) [127].

Mapping The transformation of complex information into a simpler one (e.g., projection of a three-dimensional space onto a plane).

Many network types were developed and suit better for the one or the other of the tasks above. One very common type and most frequently used in chemistry related applications [128] is the feed-forward network (FFN) as depicted in Figure 3.1. It is constructed of layers of neurons. The outputs of the neurons of each layer are passed to the neurons of the next layer. The nomenclature is as follows: Each layer is represented by a number equal to the number of neurons in the layer. The first number always refers to the input neurons while the last number refers to the output neurons. For example, 2:1 describes a network consisting of two layers with one input layer of 2 neurons and one output layer of 1 neuron. 2:5:1 describes a network consisting additionally of one "hidden" layer with 5 neurons. A variant of this network architecture is the fully connected FFN, where each neuron is connected with the neurons of all following layers. The first layer contains the input neurons. They usually do not perform any computations but their output is just the data supplied to the net. The last layer contains neurons which present their output to the user.

During learning of an FFN using sigmoid transfer functions, the steepness factor α in Eq. 3.1 is chosen by the user and fixed. For the shift parameter θ a trick is performed. Since a training algorithm which optimizes weights and shift parameters at the same time would be more difficult to be implemented, FFNs are augmented with so called "bias neurons" as shown in Figure 3.2. Their output is always "1", allowing every constant shift value to be added by a suitable weight for this signal. Overall, only weights have to be adjusted during learning. Another trick is to shift the sigmoid function. Since "0" is a particularly bad output value as the value

of the weights won't matter any more, the function is replaced by a *tanh* function to produce output in the range $[-1 \dots 1]$, which accelerates learning. The output signal's intensity $x_{i,out}$ (Eq. 3.2) is calculated as :

$$x_{i,out} = \tanh(\alpha Net) = \frac{2}{1 + e^{-2\alpha Net}} - 1 \quad (3.2)$$

with *Net* being the combined input signals and α a scaling factor.

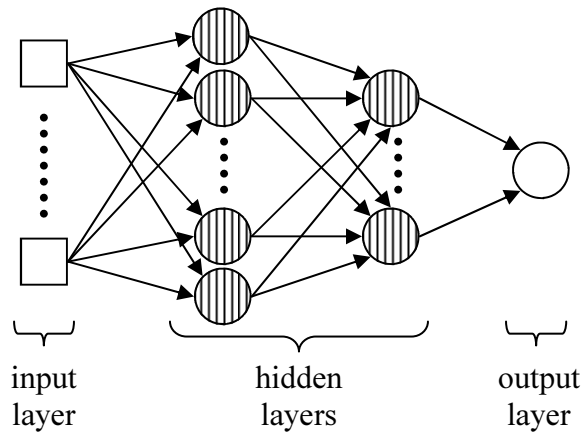


Figure 3.1.. Architecture of a standard feed-forward network.

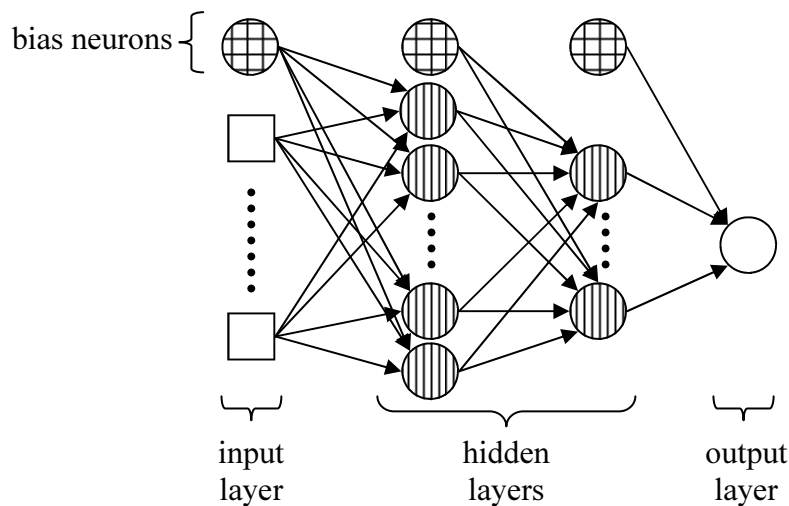


Figure 3.2.. Architecture of a standard feed-forward network with additional bias-nodes.

The actual training of the network supervised, meaning that input and previously known reference output are presented to the network simultaneously. From an input pattern the network computes an output pattern which is compared to the reference and an error is calculated (often the mean squared error (MSE)). The error is of course only known for the output layer. Here, the weights w_{ij} (Eq. 3.3) are

adjusted by a small amount proportional to the derivative of the error function on an output neuron j with respect to the weight of interest:

$$\Delta w_{ij} = -\epsilon(dE/dw_{ij}) \quad (3.3)$$

ϵ is the learning rate which is adjusted by the user. Knowing the derivative of the error function with respect to each weight, the error can be propagated backward to the preceding layer until the input layer is reached. This process is called "back-propagation". For a more detailed description of the mathematical background, the reader is referred to [129, 130]. Many advanced alternatives exist, from which only the quickpropagation algorithm [131] is mentioned here. It assumes that the error-surface formed by the network weights approximates a quadratic function and uses this information during the weight updating process.

On the practical side, it is often not wise to fully train a network. This would usually lead to an over-fitting of the data, since the network learns to reproduce individual patterns. Therefore, the data is usually split into two subsets: the training and the test data. While the network learns only on the training set, its ability to generalize is checked by measuring its error for the test set. When over-fitting occurs, the error in the test set will increase while the error in the training set decreases.

3.2. Applications

Within chemistry FFNs have gained much attention over the past two decades. The fields in which neural networks are applied range from engineering, i.e. process control, over spectra prediction or structure prediction from spectra, secondary or tertiary structure predictions in proteins, to quantitative structure activity relationship (QSAR) predicting for example chemical reactivity. A good introduction and broad overview can be found in [132].

Part III.

Method and Model Evaluation

4. Introduction

For the optimization of catalysts a thorough understanding of the underlying mechanisms is of greatest value. If they are known, thermodynamics and kinetics of the connected reactions might be altered by well-directed modifications of the catalyst's molecular structure. This is even more true when computational chemistry is used as a tool to interpret and predict reactivity. While in experimental chemistry the observable could be the catalytic activity, there is no such quantum mechanical analog. Hence, either the activity has to be connected with quantum mechanical observables of the known reactants and products. Alternatively, the rate determining steps can be identified and relative energies of the associated intermediates and transition state structures have to be calculated explicitly, so that they serve as input for a rate-law, in order to determine the catalytic activity.

In this thesis diimido chromium(VI) complexes are investigated toward their properties as olefin polymerization catalysts. They are potentially more active and tolerant to a broader range of substrates than traditional Group 4 based metallocene catalysts [41]. Only very limited experimental data is available for diimido chromium catalyzed ethene [133–136] and methyl methacrylate, acrylonitrile and vinyl acetate [57, 59] polymerization, whereas homogeneously catalyzed fluoroolefin polymerization is yet completely unknown. Therefore, the predictions of activities in the challenging fluoroolefin polymerization are based in this work on the explicit calculation of intermediates and transition structures.

For the optimization of polymerization catalysts computational high-throughput techniques are a new and promising approach. The application of density functional methods can provide the required accuracies within acceptable computation times. Even in transition metal chemistry these methods show often good agreement with experimental data, but outliers are more frequent than in organic chemistry [137]. The methods have to be calibrated, though. Many benchmarks for density functionals have been performed in the past [60, and references therein]. A search on Thomson Reuters' Web of Knowledge [138] revealed 680 entries for "benchmark functionals OR benchmark DFT". Most of them deal with very specific problems or organic compound libraries, while general benchmarks explicitly for transition metals are much more seldom.

DFT functionals for chromium in oxidation state VI have not been benchmarked yet. Mechanisms which will be derived for the chromium(VI) based polymerization of fluoroolefins and of ethene within this part will be evaluated for the functionals' influence on their probabilities. Because the experimental data is limited, energetics are to be compared with higher-level wave function methods.

5. Imido Chromium Complexes as Fluoroolefin Polymerization Catalysts

5.1. Introduction

A major issue in today's α -olefin polymerization research is the development of catalysts suitable for the homo- and copolymerization of functionalized monomers. Much progress has been made in the last decades in the class of Group 4 metallocene catalysts [43], many new classes of "post metallocene" catalysts were developed [41] to gain access to new monomer combinations and greater control of polymer properties.

Especially fluoro olefins which are used to produce highly resistant polymers, e.g. polyvinylfluoride or polytetrafluoroethene impose serious problems to classical Group 4 based catalysts. The high stability of Group 4 metal fluorine bonds, which can be understood in terms of a hard-hard interaction, leads to rapid catalyst deactivation. Indeed, Group 4 metallocenes were proved to be active defluorination reagents for fluorinated olefins [52, 53]. Coordinative polymerization remains challenging. Consequently, polyfluoroolefins produced in direct polymerization are synthesized under radical conditions in industrial processes today [139]. One outstanding example by Jordan *et al.* – published in the course of this work – proved that metal catalyzed fluoroolefin polymerization is in fact possible [140]. They observed very low levels ($< 0.5\%$) of vinyl fluoride incorporation while copolymerizing ethene and vinyl fluoride with a (phosphine-sulfonato)Pd(Me)(pyridine) catalyst. The soft character of the late transition metal center palladium is considered as a key aspect, which makes its complexes active catalysts in the copolymerization of ethene with many polar olefins [56].

Palladium and other Group 10 based catalysts are not broadly applied in polymerization catalysis, since facile β -H transfer often promotes oligomerization instead of polymerization [141, 142]. Although much progress has been achieved in middle to late transition metal polymerization catalysis [41], Group 4 based catalysts are still used at a large scale in industrial production of poly- α -olefins. A promising route to the somewhat softer metals of Group 6 was highlighted and explored by Gibson *et al.* [133, 134, 143]. By using the isolobal relationship as shown in Figure 5.1, they rationalized the exchange of the monoanionic cyclopentadienyl ligands of the Group 4 metallocenes for dianionic di(organoimido) ligands and synthesized chromium alkyl catalysts. These complexes showed moderate ethene polymerization activity in the presence of standard activators (e.g. MAO) or as well defined alkyl cations. The chemistry of diorganoimido chromium compounds, first accessed by Harlow [144], has evolved during the 1990s and was recently reviewed [145].

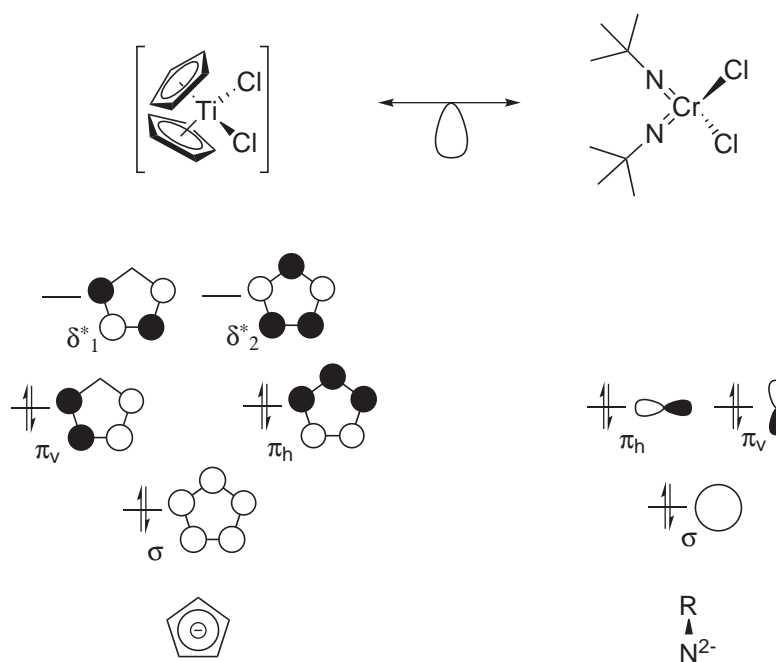


Figure 5.1.. Isolobal relationship between Group 4 metallocene and diimido chromium complexes.

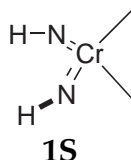
Owing to their lower Lewis acidity compared to cationic Group 6 metal systems, they show remarkably high tolerance for polar, functionalized olefins. Diorganoimido dichloro chromium complexes ($[(RN)_2CrCl_2]$) were shown to tolerate ester groups in the cyclopropanation of olefins [146]. Siemeling was able to polymerize methyl methacrylate, acrylonitrile and vinyl acetate with these complexes, employing the *tert*-butyl imido ($[(t\text{-BuN})_2Cr(CH_2Ph)_2]$) and the chelating 2,5-diimido-2,5-dimethylhexyl ligand based catalysts ($[(NCMe_2CH_2CH_2CMe_2N)Cr(CH_2Ph)_2]$) without addition of an activator. The latter complex exhibited considerably higher activity [57, 59].

These findings led to the question whether neutral, highly tolerant di(organoimido)chromium(VI) complexes can be optimized to accept and polymerize even fluoroolefins. To better understand the tuning possibilities, mechanisms have to be unraveled, which lead to either chain propagation or termination and/or catalyst deactivation. As no experimental evidence is yet known for the desired fluoroolefin polymerization, a purely computational approach is believed to be most efficient in contrast to a random search in the laboratory. The treatment of realistically sized systems is possible by density functional theory and is desired, but the calculation method has to be calibrated first. Therefore, a model system is to be established, which allows for detailed mechanistic investigations and reference calculations with accurate high-level wave function theory methods.

5.2. Results and Discussion

5.2.1. The Model Complex $[\text{Cr}(\text{NH})_2(\text{Me})_2]$

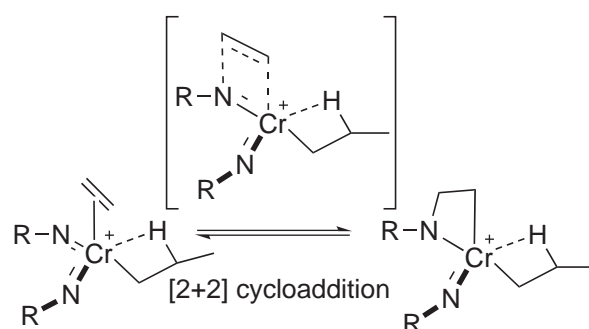
As no experimental data was available, high-level reference calculations had to be performed to underlay the proposed mechanisms with profound theoretical evidence. Thus, a model had to be selected which would be treatable by these methods. For the diorganoimido dialkyl chromium(VI) catalysts, the organoimido ligands were reduced to NH imido groups. The residual alkyl ligands were replaced by methyl groups, which also model the growing polymer chain. The resulting small catalyst model **1S** is shown in Scheme 5.1. For the mechanistic investigations, *gem*-difluoroethene was chosen as a substrate because of its symmetry and its high polarity and electron deficiency. The latter two properties make it on purpose a difficult test case for catalytic activity.



Scheme 5.1. The model complex **1S**.

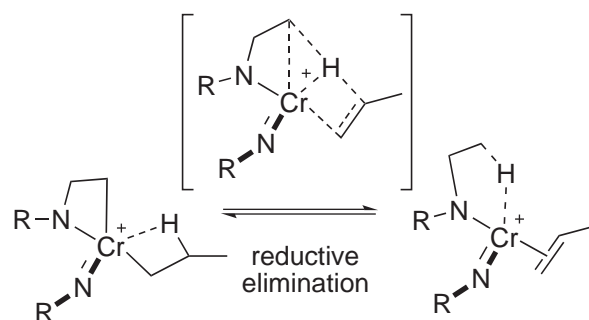
Mechanistic Assumptions Until today the mechanisms of diimido chromium(VI) catalyzed polymerizations of methyl methacrylate and acrylonitrile have not been unraveled. Nonetheless, Siemeling et al. [59] ruled out light induced or spontaneous polymerization, since they did not observe polymerization without the addition of a catalyst. Insertion polymerization proceeding on a cationic metal center was ruled out as well, because activated (cationic) catalysts do not polymerize the polar monomers. Furthermore, they obtained evidence against an anionic polymerization mechanism by the analysis of the polymer microstructure, monomer conversion and molecular weight of the polymers. Finally, (redox-chemical) initiation of a radical polymerization process was considered unlikely since neither chromates nor dichromates lead to polymerization, while the significantly weaker oxidants of the related diimido dialkyl molybdenum(VI) homologues do. Polymerizations were also not affected by the radical scavenger 2,6-di-*tert*-butyl-4-methylphenol (BHT).

Jensen and Børve [147, 148] investigated the polymerization mechanism of ethene with cationic diimido chromium(VI) catalysts at the DFT level. They employed B3LYP as exchange-correlation functional, which will be revisited in section 6.2 in some detail. Besides the direct migratory insertion mechanism, they investigated possible reduction processes to form different catalytically active species. The [2+2] cycloaddition of ethene to the chromium-imido bond to form a cationic four-membered azachromacycle for diimido and di(*tert*-butyl imido) propyl chromium (Scheme 5.2) was calculated to be slightly endothermic.



Scheme 5.2. [2+2]-Cycloaddition of ethene to a cationic imido chromium complex.

The barrier, however, nearly equaled the barrier for the insertion step of polymerization. Subsequent reductive elimination to form a chromium(IV) species *via* a transition state structure possessing a seven membered ring would be kinetically favored for H substituted imido ligands, again compared to the insertion step, and for *tert*-butyl substituted ligands slightly disfavored due to steric repulsion. The reduction is shown in Scheme 5.3.



Scheme 5.3. Transfer of a β -H atom to the azachromacycle and reduction of the chromium center *via* a 7-membered ring.

Nonetheless, following the authors' data this reduction would be essentially irreversible with a calculated Gibbs free energy change of -41.5 kcal/mol for the

imido species at 25 °C. Although these results have to be doubted, as outlined in chapter 6, this reaction path was probed for using the standard calculation approach (*vide infra*), which revealed this pathway to be unlikely; for details see page 57. Therefore, polymerization is deemed to proceed on chromium(VI) centers by an insertion mechanism, which will be discussed in the following.

5.2.2. Model Mechanism

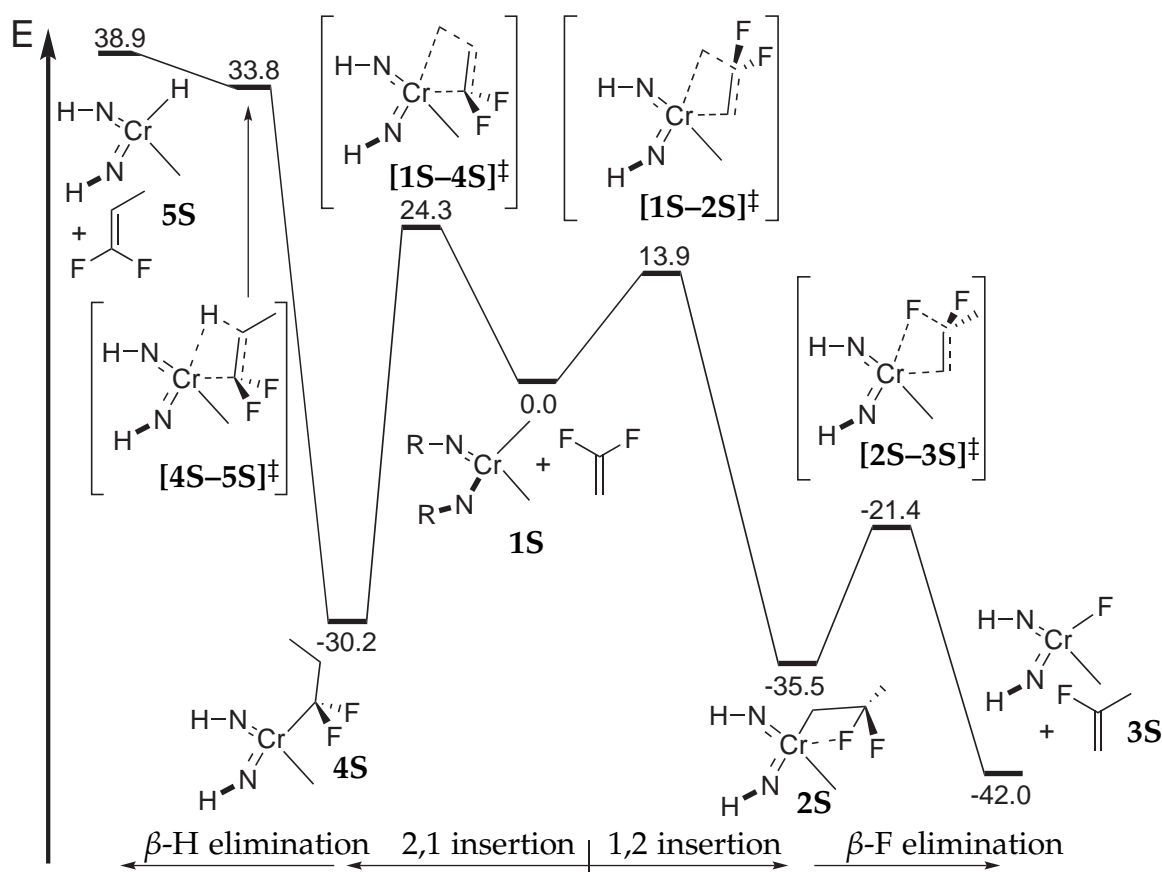
Geometry optimizations were performed at a relatively low level of theory (DFT, BP86/def-SV(P) and def-TZVP for Cr and F) to allow for quick optimizations of larger systems in the high-throughput catalyst search later on. Basis sets of triple- ζ quality for all atoms and different functionals (PBE, PBE-D, B3LYP) were checked, but differences in the structures of the catalysts model **1S** and of the transition state for 1,2 migratory insertion [**1S–2S**][‡] (see Scheme 5.4) were noted to be negligible as can be seen from Table 5.1 and Table 5.2. No symmetry constraints were imposed. The reported energies rely on single-point B2-PLYP-D/def2-TZVPP calculations.

Table 5.1.: Dependence of selected structural parameters on the choice of functional and basis sets for the catalyst model **1S**.

Method	Cr-N / Å	N-Cr-A / °	Cr-C / Å
BP86/def-SV(P),def-TZVP	1.625	112.51	2.004
BP86/def-TZVP	1.631	112.94	2.005
PBE/def-SV(P),def-TZVP	1.625	112.38	2.003
PBE/def-TZVP	1.630	112.79	2.004
PBE-D/def-SV(P),def-TZVP	1.625	112.51	2.004
PBE-D/def-TZVP	1.631	113.06	2.006
B3LYP/def-SV(P),def-TZVP	1.612	112.70	2.002
B3LYP/def-TZVP	1.618	113.21	2.005

An overview of the key reaction steps is given in Scheme 5.4. It deserves a special mention that no stable intermediates with precoordinated fluoro-olefins were found. Hence the insertion mechanism is anticipated to operate through direct insertion of the olefins into the metal methyl bond. This can proceed *via* 2,1-insertion passing through transition state [**1S–4S**][‡] and leading to the β -fluoropropyl substituted product **4S** or *via* 1,2-insertion, passing through transition state [**1S–2S**][‡], leading to the β -fluoropropyl substituted product **2S**. β -Hydrogen elimination from **4S**

via $[4S-5S]^\ddagger$ has a high kinetic barrier of 33.8 kcal/mol and leads to an instable hydrido complex $5S$, which is 38.9 kcal/mol energetically uphill from $4S$; β -hydrogen elimination is therefore unlikely to occur. β -Fluorine elimination from $2S$ would lead to chain termination and catalyst deactivation by the formation of the fluoro complex $3S$, which is 6.5 kcal/mol more stable than $2S$. Chain growth can be expected in two cases: 1) if for a given catalyst 2,1 insertion is significantly faster than 1,2 insertion since β -fluorine elimination would be impossible due to missing fluorine atoms in β position; 2) if β -fluorine elimination is much slower than the 1,2 insertion step and/or the elimination is reversible. Overall chain propagation must be in favor of chain termination and the rate constant of propagation k_{prop} has to be higher than that of termination: $k_{\text{prop}} > k_{\text{term}}$.



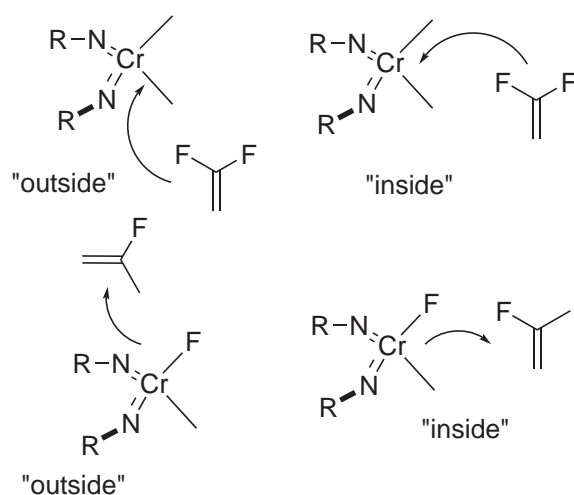
Scheme 5.4. Key reaction steps for *gem*-difluoroethene polymerization and catalyst deactivation. Relative energies in kcal/mol.

Insertions and β -eliminations can proceed *via* two different pathways (see Scheme 5.5), i.e. through an “inside” mechanism where the olefin attacks in between the alkyl groups or leaves in between the fluoro and alkyl ligand respectively, or an “outside” mechanism where the olefin attacks or leaves between

the imido and one alkyl ligand (fluoro ligand respectively). This was examined previously by Watson et al. [53] for the reaction of Schwarz's reagent (Cp_2ZrHCl) with vinyl fluoride. They calculated that the insertion of vinyl fluoride into the Zr – H bond would proceed through an "inside" pathway. This is in line with the behavior of the model system investigated here, for which all insertions and the β -elimination steps for mechanisms proceeding by "outside" pathways have barriers of 3.0 – 13.4 kcal/mol higher in energy than the respective reactions with the "inside" approach. Therefore, only "inside" pathways will be considered for the further discussions.

Table 5.2.: Dependence of selected structural parameters on the choice of functional and basis sets for the transition state structure **[1S–2S]**[‡].

Method	C–Cr–C / °	C–C / Å	Cr–C / Å	C–Cr / Å
BP86/def-SV(P),def-TZVP	54.46	2.177	2.270	2.184
BP86/def-TZVP	53.92	2.166	2.279	2.178
PBE/def-SV(P),def-TZVP	54.55	2.173	2.261	2.181
PBE/def-TZVP	54.06	2.164	2.270	2.176
PBE-D/def-SV(P),def-TZVP	54.65	2.165	2.256	2.166
PBE-D/def-TZVP	54.17	2.156	2.267	2.162
B3LYP/SV(P),def-TZVP	54.51	2.188	2.279	2.187
B3LYP/def-TZVP	54.06	2.179	2.290	2.180



Scheme 5.5. Possible approach directions: "inside" and "outside".

While **1S** adopts a tetrahedral coordination geometry, it becomes distorted trigonal bipyramidal in the transition states for insertion and elimination. In the transition

states the olefin approaches in the trigonal plane which is aligned almost perpendicular to it. The $\text{Cr-C}_{\text{olefin}}\text{-C}_{\text{olefin}}$ plane intersects the yz plane, which is spanned by Cr, N and N at an angle of 99° for transition state $[\mathbf{1S-2S}]^\ddagger$, 95° for $[\mathbf{1S-4S}]^\ddagger$ and 95° for $[\mathbf{2S-3S}]^\ddagger$. The approaching is visualized in Figure 5.2.

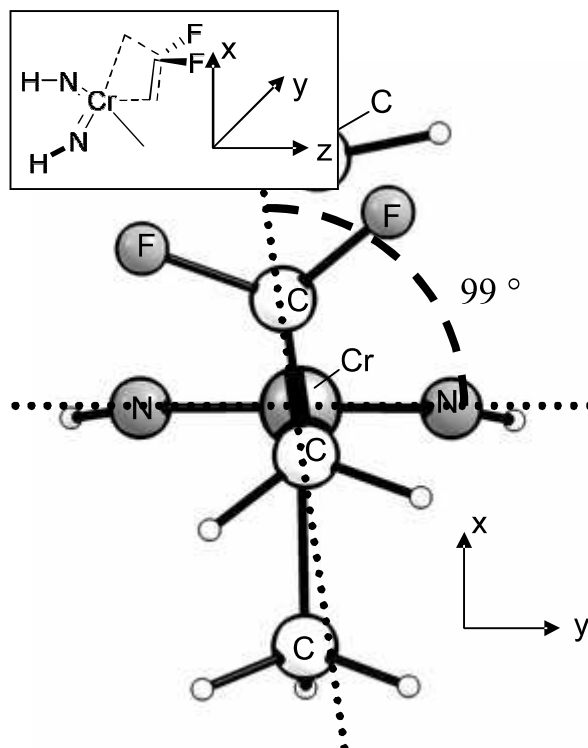


Figure 5.2.. Structure of the transition state $[\mathbf{1S-2S}]^\ddagger$. The olefin approaches almost perpendicular to the yz plane in which the chromium and nitrogen atoms are located.

5.2.3. Reference Calculations

To guide the choice of an appropriate DFT functional and to gain insight into the electronic structure of the model system, MP2 and coupled-cluster calculations (CCSD, CCSD(T)) employing the cc-pVTZ-DK basis sets were performed. These basis sets can be seen as a minimal choice for accurate energy calculations. The calculated reaction energies and barriers can be found in Table 5.3 and Table 5.4 where also the results from the restricted Hartree-Fock calculation are compiled.

As a best estimate for the 1,2 insertion barrier CCSD(T) calculations with aug-cc-pVTZ basis sets were performed and the basis set superposition errors (BSSEs) were estimated in terms of a counterpoise correction. Due to the computational

demands, these extended basis sets were only used exemplarily for the calculation of the barrier for 1,2 insertion. It has to be noted that the use of the counterpoise method is questionable in this case, since non-bonded fragments are not well defined. Nonetheless, each of the reactants was chosen as one fragment. Since bonds are evolving, the BSSE, calculated to be 3.4 kcal/mol, is presumably overestimated in this case. Recently, Jensen proposed an atomic counterpoise method [149], making the estimate of the BSSEs for bonded species possible. This approach was taken for the transition state of the β -F elimination step and the BSSE was estimated to 1.3 kcal/mol¹. Overall the BSSEs at the CCSD(T) level for the investigated reactions seem to be small. For the 1,2-insertion step, the BSSE and the observed decrease in the reaction barrier with the aug-cc-pVTZ basis sets approximately cancel each other. Therefore, the cc-pVTZ basis sets are anticipated to be a good choice for the CCSD(T) calculations.

Table 5.3.: Reaction energies and barriers obtained by various wave function methods. All values in kcal/mol.

Step	HF	MP2	SCS-MP2	CCSD	CCSD(T) cc-pVTZ
1S →[1S-2S] [‡]	52.0	19.1	26.5	26.5	17.9
1S → 2S	-27.8	-38.2	-35.5	-34.3	-34.8
2S →[2S-3S] [‡]	24.0	37.3	35.5	17.3	14.6
2S → 3S	-13.7	-2.2	-6.0	-7.5	-6.8
1S →[1S-4S] [‡]	59.6	38.7	44.4	36.2	27.0
1S → 4S	-19.1	-31.5	-29.2	-27.8	-28.8

It becomes evident that dynamical correlation plays an important role in the description of these reactions, if the huge difference in the predicted reaction barriers are considered between the methods taking electron correlation into account and the HF method. Taking CCSD(T) as a reference, MP2 seems inappropriate since perturbations become too large. This also applies to the CCSD calculations which differ considerably from the CCSD(T) results with a maximum difference in pre-

¹ The ACP(1) scheme as detailed in Jensen's original paper was used for the product of 1,2 insertion **2S** and the transition state of β -F-elimination [**2S-3S**][‡]. For the structure of [**2S-3S**][‡] the bond between chromium and the former α -carbon of the leaving group as well as the carbon fluorine bond was assumed to be intact, but no bond between chromium and the transferred fluorine atom was assumed. For the calculations for **2S** all covalent bonds were considered. $\Delta\text{ACP}(1)=\text{ACP}(1)[\text{[2S-3S]}^{\ddagger}] - \text{ACP}(1)[\text{2S}]$ served as an estimate for the BSSE.

dicted reaction barriers of $\Delta\Delta E_{\max}^{\ddagger} = 9.2$ kcal/mol but only $\Delta\Delta E_{\max} = 1.0$ kcal/mol for the reaction energies.

Table 5.4.: CCSD(T)/aug-cc-pVTZ, CAS and CASPT2 barriers of the 1,2 insertion. All values in kcal/mol. The CCSD(T) calculation includes an estimated BSSE of +3.4 kcal/mol.

Step	CAS			MS-CASPT2
	CCSD(T) aug-cc-pVTZ	[14,14]	[14,13] ANO-RCC-VQZP	
1S →[1S-2S] [‡]	18.8	43.6	44.2	12.7

For Møller-Plesset perturbation theory of the second order (MP2) and coupled-cluster with singles and doubles (CCSD), a number of diagnostics were defined to judge on the quality of the single reference wave function.² Taking into account the \mathcal{T}_1 and the D_1 diagnostic [150, 151], the triples correction energy contribution to the total atomization energy during the CCSD(T) calculations [152] and the values of the largest T_2 amplitudes, it has to be concluded that the electronic structures of the investigated diimido chromium systems are influenced by static correlation. The delicacy of the chromium imido bond had also been noted by Cundari, who performed multiconfigurational SCF calculations on a $[\text{Cr}(\text{H})_2(\text{NH})(\text{CH}_2)]$ model [153].

Although it can be argued that errors imposed to the CCSD(T) calculations by this static correlation might cancel out since equally strong indications of non-dynamic correlation were found in all structures, multi-reference calculations are in need to find proof for this.

The well established MS-CASPT2 method [70, 154, 155] was chosen together with the extensive ANO-RCC-VQZP basis sets for these energy calculations. Let us first

² Two diagnostics are in broad use: the \mathcal{T}_1 [150] and the D_1 diagnostic [151]. \mathcal{T}_1 has a traditional cutoff-value of 0.020 — values above indicate a poor quality of the single-reference based correlation procedure. However \mathcal{T}_1 is not size-intensive and was developed for very small systems. The more modern size-intensive D_1 should be below 0.050 to legitimate the single-reference approach. For the chromium systems in the model reaction scheme average values of 0.040 (+/- 0.004) and 0.187 (+/- 0.022) for \mathcal{T}_1 and D_1 in the CCSD calculations were found, respectively. More recently Karton, Rabinovich, Martin and Ruscic [152] proposed the percentage of the triples correction from a CCSD(T) calculation to the total atomization energy (%TAE([T]) and the percentage of the SCF energy (%TAE(SCF)) of the reference wave function as a measure for non-dynamical correlation. For the intermediates and transition state structures %TAE([T]) = 5.4 (+/- 1.1) and %TAE(SCF) = 55.3 (+/- 6.5) were calculated, indicating at least moderate non-dynamical correlation. An other indicator are the values of the largest T_2 amplitudes which were 0.077 (+/- 0.017).

consider the 1,2 migratory insertion $1\mathbf{S} \rightarrow 2\mathbf{S}$, since its barrier will determine the rate of chain growth. During the course of this reaction the olefin π -bond and one of the chromium methyl bonds will be lost, and a new metal alkyl as well as a carbon carbon bond is formed. Orbitals describing these transforming bonds should be included in the active space. Since both methyl chromium bonds are equivalent for the reactants, both had to be included, leading to 6 electrons in 6 orbitals. Each of the imido ligands has one filled orbital of σ -symmetry and two filled orbitals of π -symmetry available to interact with the metal center. These account for another six bonding and 6 antibonding orbitals leading to a total of 18 electrons in 18 orbitals ([18,18]). The active space could be reduced to [14,13] for which the MS-CASSCF wave function served as the reference for the perturbative MS-CASPT2 treatment.³ The resulting natural orbitals for the lowest root of the MS-CASSCF calculation for the transition state structure are depicted in Figure 5.3 and Figure 5.4.

It can be seen that a large extent of the multi-reference character derives from chromium imido π -interactions. This explains why the weights of the main electronic configurations for the transition state and the reactants was comparable with 63% and 70%, respectively, and is consistent with the expectations drawn from the CCSD and CCSD(T) diagnostics. The barrier of the 1,2 insertion step was estimated to be $\Delta E^\ddagger([1\mathbf{S}-2\mathbf{S}]^\ddagger) = 12.7$ kcal/mol.

Unfortunately, β -fluorine elimination could not be studied at this level of theory, since the active space would grow to an untreatable size by inclusion of the filled fluorine p orbitals.

Compared to the CASPT2 calculations, results obtained with the less sophisticated electron correlation methods MP2, SCS-MP2 and CCSD differ considerably. Only CCSD(T) is in reasonable agreement with the multi-reference approach. This discrepancy between CCSD(T) and the other methods is also observed for the other calculated barriers. Contrasting these findings, the agreement of the different methods for reaction energies is good.

³ The MS-CASSCF calculations were started using 18 electrons in 16 orbitals. From the total of 9 bonding and 9 antibonding orbitals (3 plus 3 for the description of the chromium, methyl and ethene π interactions, 2 plus 2 for the chromium imido interactions with σ symmetry and 4 plus 4 with π symmetry) two antibonding were omitted making computations feasible. During the optimization of the wave function, orbitals with occupation numbers higher than 1.98 or lower than 0.02 were removed from the active space. These were all the orbitals involved in chromium imido σ -type interactions and one antibonding involved in π -type interactions.

Although the weights of the main electronic configurations for the transition state and the reactants were quite low with 63% and 70%, respectively, no leading configurations with weights higher than 0.05 were observed for the lowest lying root.

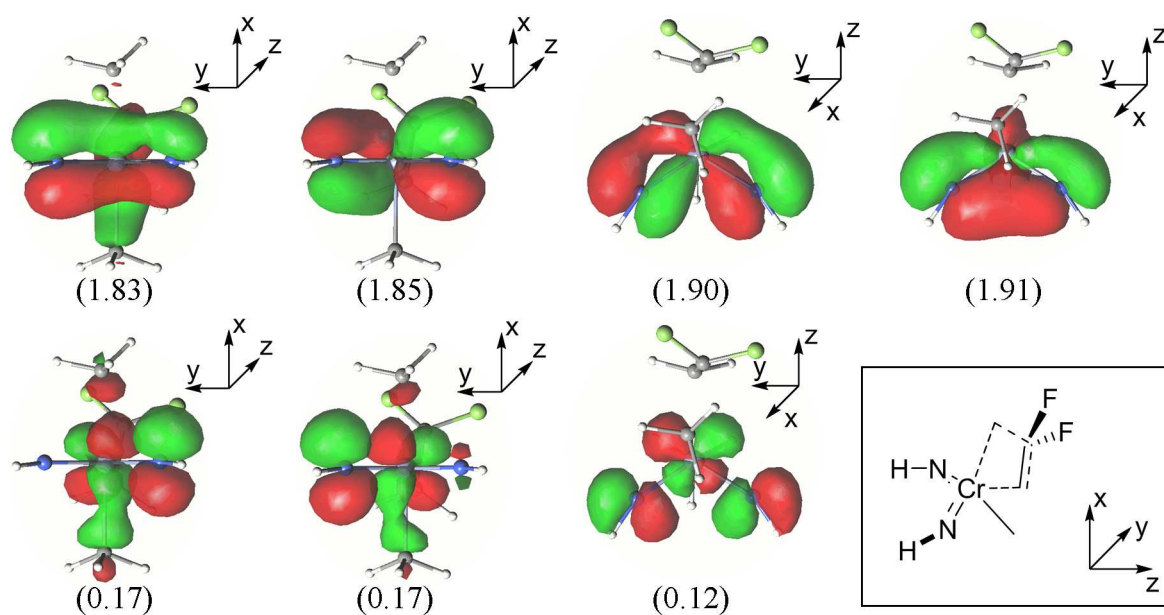


Figure 5.3.. Natural orbitals of the [14,13]-CASSCF calculation involved mainly in interactions between chromium and the imido ligands for the 1,2 insertion transition state structure $[1\mathbf{S}-2\mathbf{S}]^\ddagger$. Occupation numbers are in parentheses. For the definition of the coordinate system see inset, for atom labeling see Figure 5.4.

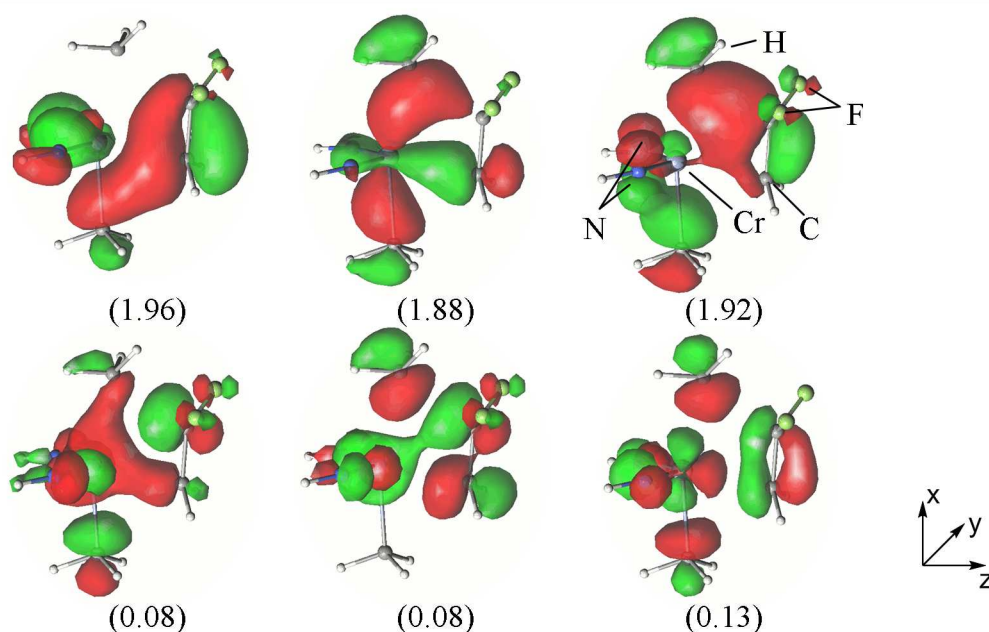


Figure 5.4.. Natural orbitals involving predominantly interactions between the chromium center, the methyl ligands and the olefin's π -system of the [14,13]-CASSCF calculation for the 1,2 insertion transition state structure $[1\mathbf{S}-2\mathbf{S}]^\ddagger$. Occupation numbers are given in parantheses. For a schematic drawing within the same coordinate system see Figure 5.3. Atom colors: light blue = Cr, gray = C, white = H, blue = N and green = F.

5.2.4. Dependence on the Density Functional

Having obtained a set of reference values for reaction barriers and energies at the CCSD(T) and MS-CASPT2 levels, the investigation of the functional dependence at the DFT level followed. To minimize basis set influences, large triple- ζ quality basis sets with extra polarization functions (usually def2-TZVPP) were chosen. Again, single point energy calculations were performed for the model's structures. Functionals of at least gradient corrected quality were tested, including the second-rung GGA functionals BLYP, BP86 and PBE, the third-rung meta-GGA TPSS, the fourth-rung hybrid functionals BHLYP, B3LYP and PBE0, the fourth-rung meta hybrid functionals M06, TPSSh and TPSS0 as well as the fifth-rung double hybrid functionals B2PLYP, B2KPLYP and mPW2PLYP. Grimme's dispersion correction (new parameter set) was applied where parameters were available (denoted as -D) [156, 157]. For TPSSh, BHLYP and M06 parameters have only recently been published for a new improved dispersion scheme (denoted as -D3) [158]. The obtained data is compiled in Table 5.5 and root mean squared deviations from the CCSD(T) results are depicted in Figure 5.5. For both reaction barriers and reaction energies the double hybrid functionals were found to give closest agreement with the CCSD(T) results. For all cases, except for PBE0 and M06 reaction energies and B2PLYP barrier heights, the mean deviation is strongly reduced by employing Grimme's dispersion correction.

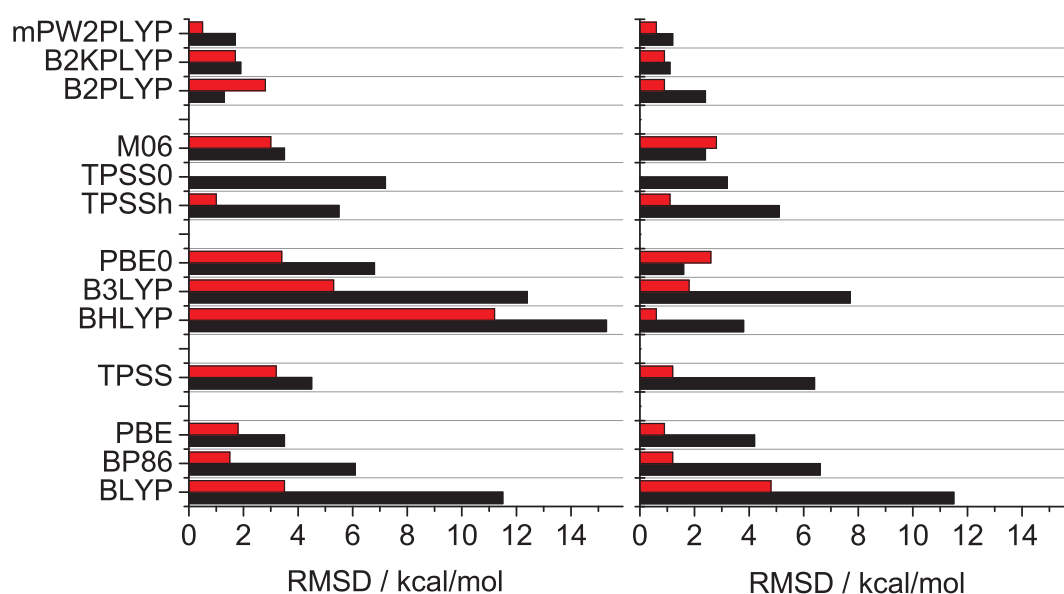


Figure 5.5. Root mean squared deviations for GGA, meta, hybrid, hybrid-meta and double hybrid functionals with (red) and without (black) dispersion correction from CCSD(T) results. Left: reaction barriers. Right: reaction energies.

In general, there are three main sources of error in DFT. The first is the so called self-interaction error, which arises from the mean field Coulomb treatment and its only approximate cancellation in the exchange functional. It is less pronounced in more delocalized systems and therefore leads to an underestimation of barrier heights. The second point is the single determinant approach, which leads to errors in static correlation energy. Static correlation in DFT is accounted for only in an uncontrollable way within the correlation functional. Since for transition states static correlation often increases while the self interaction error decreases, a cancellation of errors can be observed. The third point is the inability to describe dispersion, i.e. energies for molecules having atoms in typical van der Waals distances are overestimated. In hybrid functionals a fraction of exact HF exchange is mixed in. Therefore the self interaction error is reduced. But at the same time the cancellation with the functional's static correlation error is reduced. It has been argued [159] that hybrid functionals are often less well suited for transition metal containing systems because of the higher static correlation contribution. This could explain what is observed in this case, i.e. hybrid functionals, especially BHLYP and B3LYP, overestimate barrier heights and show the poorest agreement with the CCSD(T) results. Barrier heights are reduced for all functionals by the inclusion of the empirical van der Waals correction as would be expected for the more extended transition state structures.

As noted at the CCSD(T) level, the barrier for 2,1-insertion passing through transition state [1S-4S][‡] is considerably higher than the other investigated barriers for all functionals considered. This leaves us with 1,2-migratory insertion and β -fluoro elimination as the two competing reaction pathways. Their relative rates determine whether chain growth or termination will be dominant. As an estimate, neglecting entropic effects and the orders of the rate laws, $k_{\text{prop}}/k_{\text{elim}} = \exp(\Delta\Delta E^\ddagger/RT)$ is considered with $\Delta\Delta E^\ddagger = \Delta E^\ddagger(\beta\text{-F elimination}) - \Delta E^\ddagger(1,2\text{ insertion})$. The term $k_{\text{prop}}/k_{\text{elim}}$ expresses the selectivity of the catalyst, for which values $\gg 1$ are desirable. The predicted selectivities for the different functionals and coupled cluster calculations are depicted in Figure 5.6.

With the two extremes in reactivity predicted by BHLYP and B2PLYP-D a rate constant for 1,2 insertion would be expected in the order of $1.5 \cdot 10^{-14} \text{ M}^{-1}\text{s}^{-1}$ (BHLYP) or $4.0 \cdot 10^2 \text{ M}^{-1}\text{s}^{-1}$ (B2PLYP-D) at unitary concentrations, a difference of 16 orders of magnitude! Selectivity is influenced similarly, where the two extremes are calculated with the DFT functionals BLYP and B2KPLYP-D. While β -F elimination would be predicted to have a 10^3 times higher rate constant than the 1,2 insertion

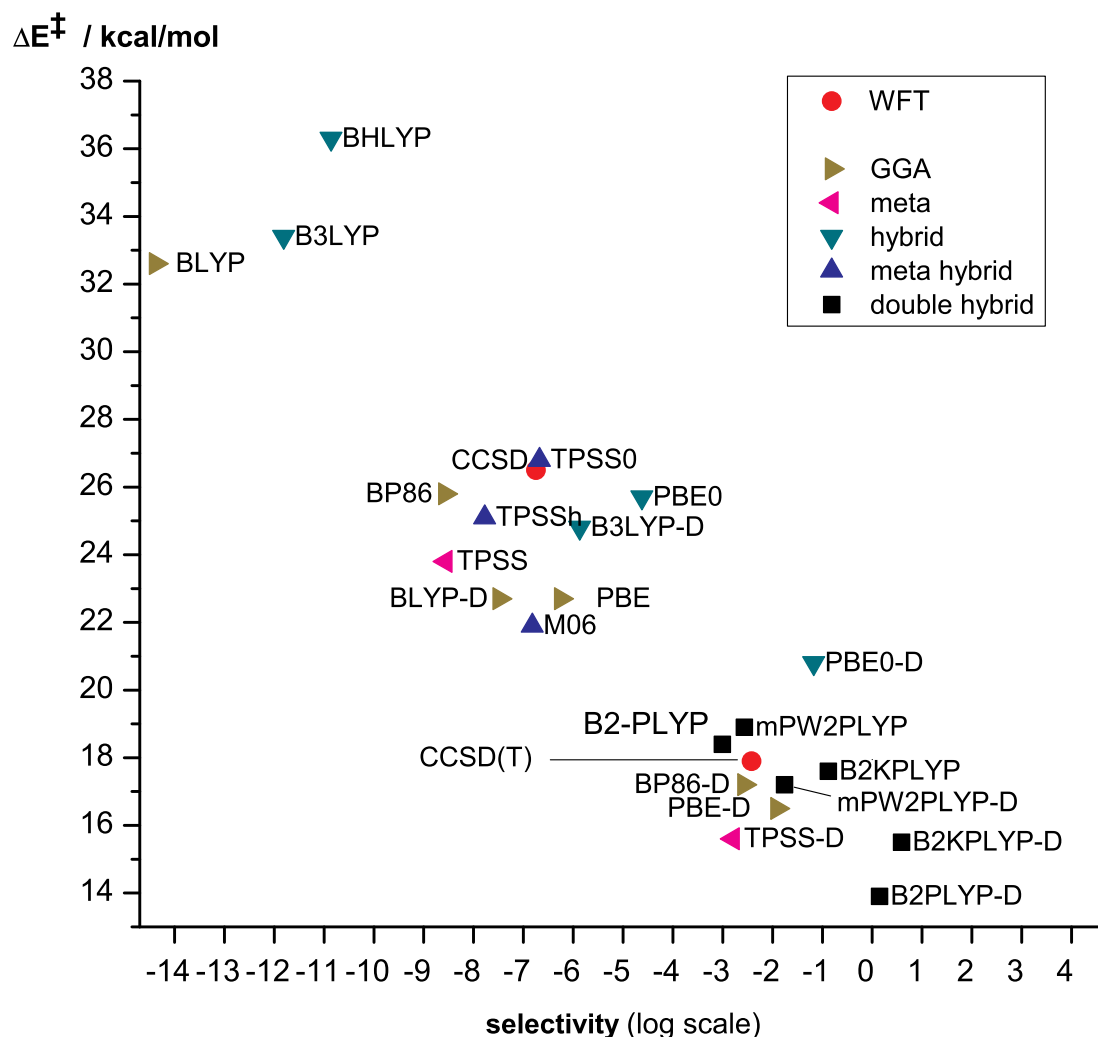


Figure 5.6.. Predicted reactivity in terms of the barrier for 1,2 insertion (ΔE^\ddagger) versus the selectivity of the catalyst (see text) as calculated by different DFT functionals and wave function theory (WFT) methods.

step following the results obtained with the BLYP functional, the use of B2KPLYP-D would reverse our view, with the predicted rate constant for the 1,2-insertion step being 4 times higher. This analysis clearly shows the importance of the choice for a DFT functional to model catalytic processes.

At this point we chose the B2PLYP-D functional to calculate single point energies for all further calculations for two reasons. First, this functional has the closest agreement with the MS-CASPT2 result of 12.9 kcal/mol for the 1,2 insertion barrier. Second, it displays close to excellent agreement with the CCSD(T) results for the β -F elimination barrier and the reaction energies. Since geometrical changes compared to BP86 were minimal, PBE-D was used from now on throughout this work

for geometry optimizations, giving again closest agreement with the MS-CASPT2 results for the barrier of 1,2 insertion and with those of CCSD(T) for reaction energies in the class of the GGA functionals. This makes barrier estimations possible without having to perform costly calculations with the double hybrid functional.

Table 5.5.: Predicted barriers and reaction energies in kcal/mol for the tested DFT functionals. Root mean squared deviation (RMSD) and mean absolute deviation (MAD) values refer to the CCSD(T) results.

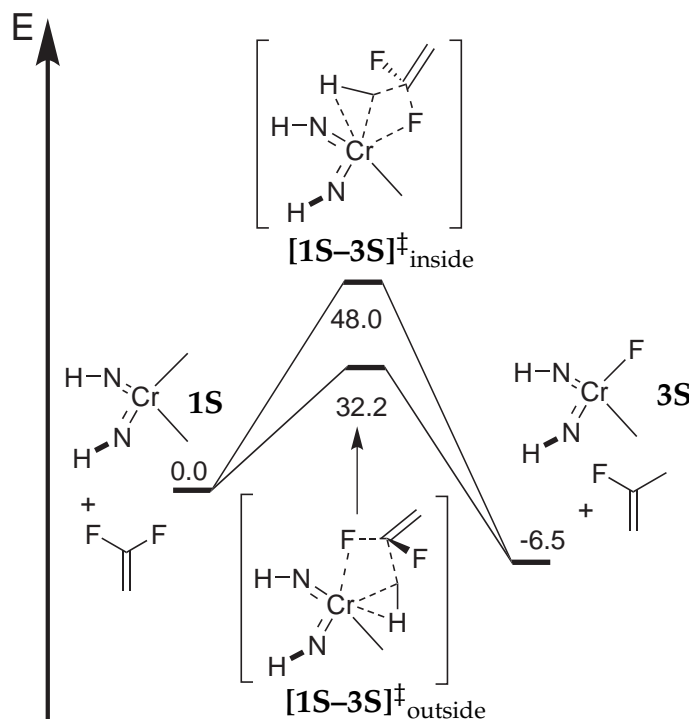
Reaction	$1S \rightarrow [1S-2S]^\ddagger$	$1S \rightarrow 2S$	$2S \rightarrow [2S-3S]^\ddagger$	$2S \rightarrow 3S$	$1S \rightarrow [1S-4S]^\ddagger$	$1S \rightarrow 4S$	RMSD(ΔE)	RMSD(ΔE^\ddagger)	MAD(ΔE)	MAD(ΔE^\ddagger)
Functional										
CCSD(T)	17.9	-34.8	14.6	-6.8	27.0	-28.8				
BLYP	32.6	-22.7	13.0	-19.6	40.4	-19.4	11.5	11.5	11.2	8.8
BLYP-D	22.7	-29.2	12.5	-12.0	29.9	-25.6	4.8	3.5	4.0	3.3
BP86	25.8	-27.1	14.1	-13.2	33.9	-23.2	6.6	6.1	6.0	4.7
BP86-D	17.2	-32.7	13.7	-6.6	24.7	-28.7	1.2	1.5	0.6	1.5
PBE	22.7	-29.6	14.2	-10.8	30.8	-25.8	4.2	3.5	3.5	2.8
PBE-D	16.5	-33.7	13.9	-6.1	24.3	-29.7	0.9	1.8	1.1	1.4
TPSS	23.8	-27.5	12.2	-13.8	31.6	-24.3	6.4	4.5	5.3	4.5
TPSS-D	15.6	-32.9	11.8	-7.5	22.8	-29.5	1.2	3.2	1.5	2.7
BHLYP	36.3	-31.0	21.5	-9.6	44.7	-24.1	3.8	15.3	7.6	9.5
BHLYP-D3	31.2	-34.8	21.3	-6.0	39.3	-28.2	0.6	11.2	4.2	6.5
B3LYP	33.4	-26.6	17.3	-14.5	41.7	-21.7	7.7	12.4	9.1	8.4
B3LYP-D	24.8	-32.3	16.8	-7.9	32.5	-27.2	1.8	5.3	2.7	3.2
PBE0	25.7	-32.7	19.4	-6.5	34.4	-27.0	1.6	6.8	3.0	4.6
PBE0-D	20.8	-35.9	19.2	-2.7	29.2	-30.1	2.6	3.4	2.9	3.1
TPSSh	25.2	-28.8	14.5	-11.9	33.2	-24.8	5.1	5.5	4.9	3.8
TPSSh-D3	19.5	-34.2	14.9	-5.7	26.7	-30.3	1.1	1.0	1.2	0.6
TPSS0	26.8	-30.9	17.7	-9.0	35.2	-25.6	3.2	7.2	4.2	4.8
M06	21.9	-33.5	17.5	-3.0	30.6	-27.5	2.4	3.5	2.9	3.0
M06-D3	21.2	-34.2	17.5	-2.1	29.9	-28.3	2.8	3.0	2.7	2.9
B2PLYP	18.4	-32.6	14.3	-10.0	29.2	-27.3	2.4	1.3	2.0	1.6
B2PLYP-D	13.9	-35.5	14.1	-6.5	24.3	-30.2	0.9	2.8	1.5	1.4
B2KPLYP	17.6	-34.2	16.4	-8.6	29.8	-28.2	1.1	1.9	1.4	1.9
B2KPLYP-D	15.5	-35.8	16.3	-7.0	27.6	-29.9	0.9	1.7	1.0	1.1
mPWPLYP	18.9	-33.8	15.4	-8.4	29.7	-28.1	1.2	1.7	1.3	1.6
mPWPLYP-D	17.2	-35.4	14.8	-6.7	27.6	-29.7	0.6	0.5	0.5	0.5

5.2.5. Alternative Mechanisms

Alternative mechanisms for the deactivation or inhibition of the catalyst could be possible as would be a reductive pathway leading to a different polymerization catalyst or to catalyst breakdown.

5.2.5.1. β -F elimination via σ -bond metathesis

Direct deactivation of the catalyst can be envisaged by σ -bond metathesis since chromium(VI) has vacant d orbitals. Again, fluorine could be transferred via an "inside" or an "outside" mechanism to the metal center, passing the transition state $[1S-3S]^\ddagger_{\text{inside}}$ or $[1S-3S]^\ddagger_{\text{outside}}$ (Scheme 5.6). Transition state structures were optimized for both pathways. For the "outside" mechanism the barrier is calculated to be 32.3 kcal/mol. It features a strong α -H-agostic interaction with the leaving methyl ligand. The Cr-C-H angle is calculated to be 54.0° and the Cr-H distance to be 1.78 Å. The barrier of the "inside" mechanism is calculated to be 48.0 kcal/mol. Here the agostic interaction is less pronounced with a Cr-C-H angle of 60.8° and a Cr-H distance of 2.03 Å. Overall σ -bond metathesis possesses too high barriers to be competitive.

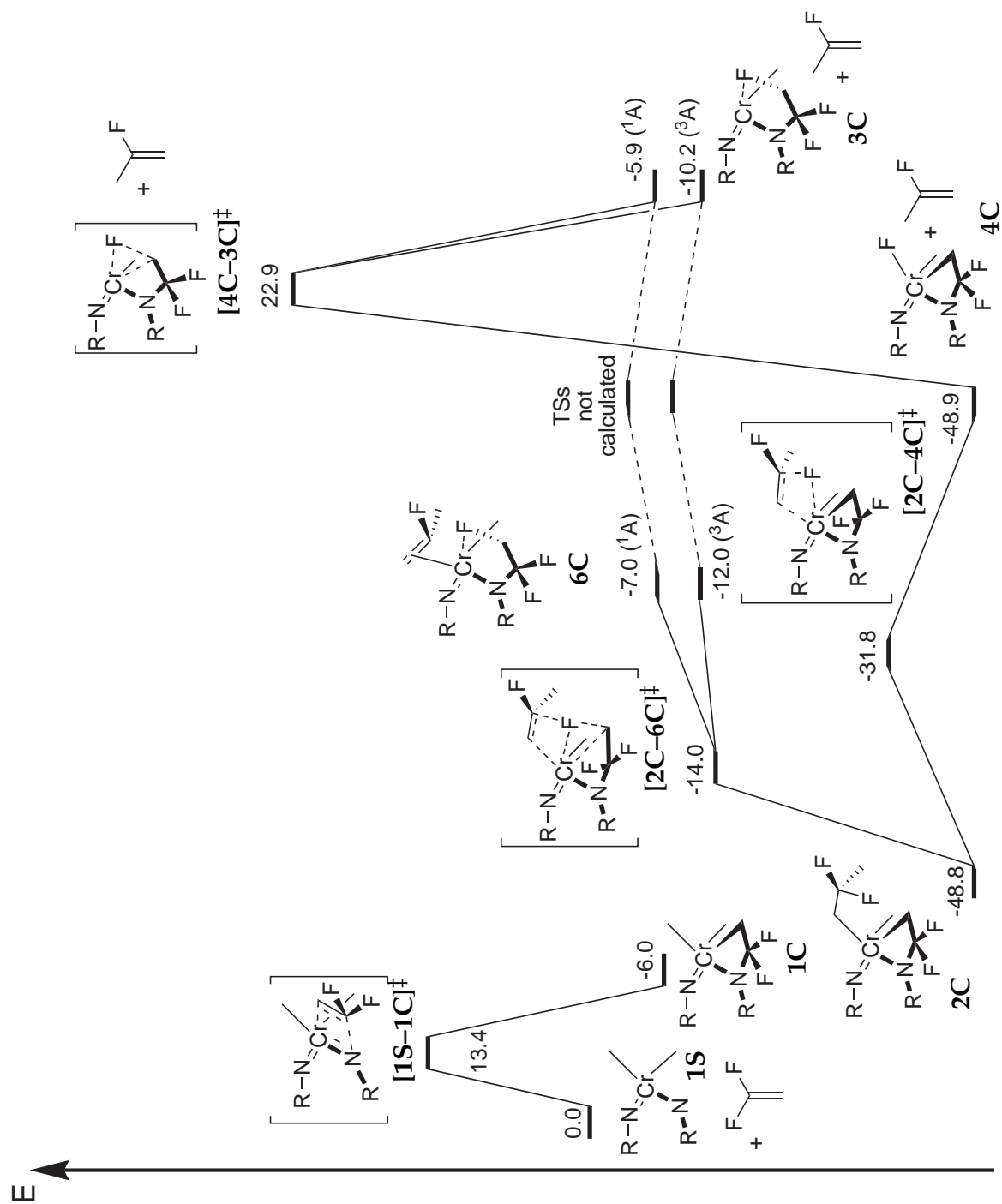


Scheme 5.6. Catalyst deactivation by σ -bond metathesis. Energies relative to reactants in kcal/mol.

5.2.5.2. Cycloaddition of the olefin

Cycloaddition of the olefin to the chromium imido double bond was proposed by Jensen and Børve [148] to be a likely pathway for cationic diimido chromium(VI) complexes. In the calculations performed herein the barrier of 13.4 kcal/mol for the 1,2 cycloaddition of *gem*-difluoroethene passing through [1S-1C][‡] (see Scheme 5.7) to 1S is indeed comparable to the barrier of 1,2 insertion (13.9 kcal/mol), while 2,1 cycloaddition with a barrier of 28.5 kcal/mol for transition state [1S-5C][‡] is not. There seems to be no steric hindering for the former reaction through bulky *tert*-butyl imido ligands since the predicted barrier for di(*tert*-butyl imido) dimethyl chromium is even lower ($\Delta E^\ddagger = 9.8$ kcal/mol).

Since 1,2 insertion is greatly preferred over 2,1 insertion, alkyl chains with fluorine atoms in β position would grow *via* an insertion mechanism during polymerization. Therefore, reductive elimination is only possible *via* fluorine transfer to the azachromacycle and was investigated. Once 2C, an azachromacycle with an alkyl chain bearing β -fluorine atoms, is formed, there are two possibilities to reduce the chromium center, i.e. either via a two-step mechanism or via a concerted one. For the two step mechanism fluorine would first be eliminated passing through transition state [2C-4C][‡] with a barrier of $\Delta E^\ddagger = 17.0$ kcal/mol and would then be transferred to the α -C atom of the azachromacycle to reductively open the ring. This step (passing through [4C-3C][‡] has an estimated barrier of $\Delta E^\ddagger(1A) = 71.7$ kcal/mol. For the concerted mechanism a transition state [2C-6C][‡] with a barrier of $\Delta E^\ddagger(1A) = 34.8$ kcal/mol was found. Considering these high barriers, reductions of the chromium center to Cr(IV) do not seem to be feasible. Therefore the formation of azachromacycles, which proceeds kinetically with a similar probability as insertion steps, is to be viewed as an inhibition reaction. The backward reaction has a barrier of 19.4 kcal/mol since the formation of azachromacycles is not very exergonic.



Scheme 5.7. Cycloaddition of *gem*-difluoroethene to the chromium imido bond and reduction of neutral diimido chromium complexes. Energies relative to reactants in kcal/mol.

5.3. Summary

A small model system has been derived, which allowed the study of fluoroolefin polymerization and chain termination processes with high level wave function theory methods. It could be shown that diimido chromium(VI) compounds cannot be treated reliably with single reference methods. A significant contribution of static correlation was found for all investigated structures. Thus, the DFT calculations were calibrated to a combination of MS-CASPT2 and CCSD(T) results. While geometrical parameters were influenced only to a small extent, the predicted barrier heights and reaction energies depend heavily on the choice of the DFT functional. This makes chemical interpretation difficult, since forecasted catalytic selectivities can even be reversed. It was found, that an empirical dispersion correction is useful for most functionals considered. B2PLYP-D was selected for giving closest agreement with the CASPT2 result and a very close match with the CCSD(T) derived data. PBE-D performed very well in the reproduction of the reference data and was chosen for further geometry optimizations, since it features as a pure functional an excellent accuracy/speed ratio.

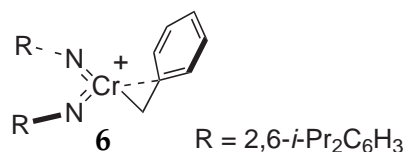
It has to be concluded that DFT methods can not be used as black boxes for these types of reactions.

6. Imido Chromium Complexes as Ethene Polymerization Catalysts

6.1. Introduction

For the polymerization of highly polar substrates non-ionic chromium(VI) compounds have been discussed as promising candidates in chapter 5. Because of their high relevance to industry, α -olefin polymerization catalysts for non-polar substrates have been investigated thoroughly for a long time [19, for a historical overview]. α -Olefin polymers constitute by far the largest amount of plastics produced with polyethene alone having a 65 Mt/a output in 2008 [40]. This highlights the importance of this class of compounds. In recent years much interest has evolved in the field of non-metallocene catalysts to supersede traditional metallocene catalyst by higher activities, different tuning possibilities to influence for example the tacticity, or compatibility with a wider range of co-monomers [41].

Cationic chromium(VI) based diorganoimido complexes have proved to be active polymerization catalysts for ethene [160]. Gibson introduced the benzyl complex **6** (see Scheme 6.1) and its *tert*-butyl imido analog in his original work. Both can be converted to cations by treatment with $[\text{Ph}_3\text{C}][\text{B}(\text{C}_6\text{F}_5)_4]$.

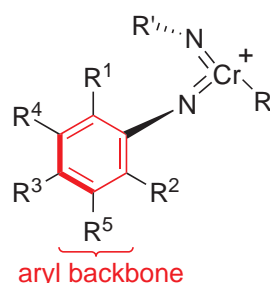


Scheme 6.1. Gibson's catalyst **6**.

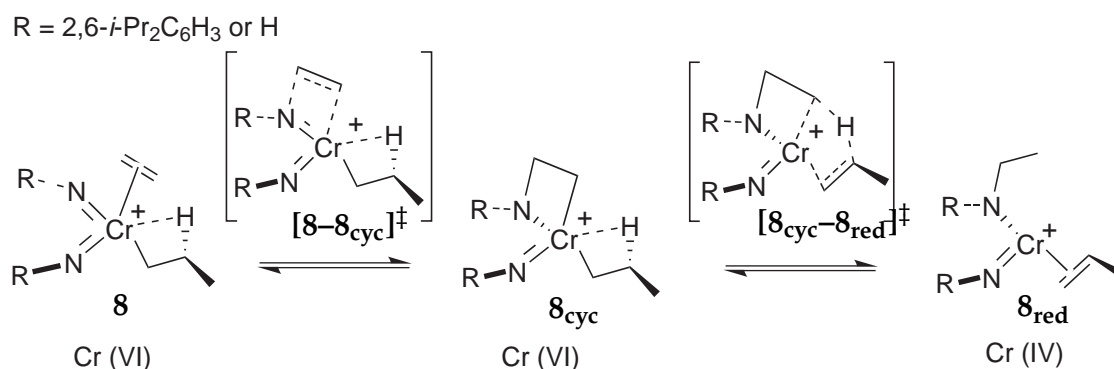
The synthesis of imido complexes has recently been improved by Rufanov, Kipke and Sundermeyer, who were able to utilize a set of substituted arylimido ligands [161]. Thus, the introduction of different arylimido ligands was significantly extended. As the aryl backbone of the arylimido ligands (see Scheme 6.2) leaves much space for different substitution patterns, variation in the ligand delivers many possibilities to advance the catalytic activity and thus improve the overall process of poly- α -olefin production.

The application of computational methods requires their validation in the first place. The experimental data available for the activities of diimido chromium complexes in the catalysis of α -olefin polymerization is very limited. Therefore, high-level techniques have to be used for the calibration work. Omitting this rule of caution, Jensen and Børve conducted DFT investigations on Gibson's *tert*-butyl imido complex and its model for which the *tert*-butyl groups were replaced by hydrogen [147, 148]. The authors discussed different pathways of migratory insertion, which

would either be expected in close analogy to the mechanisms present in Group 4 metallocene catalyzed α -olefin polymerization, or a reductive pathway, as shown in Scheme 6.3. They proposed [2+2] cycloaddition of ethene to one of the chromium imido bonds in the H-imido substituted model educt complex **8-H** to give **8_{cyc}-H**. Consecutive highly exothermic reductive elimination of a hydrogen atom from the alkyl ligand to yield **8_{red}-H** was found to be favorable over migratory insertion steps. They argued that it is likely that a reduced chromium complex serves as catalyst in the experimentally observed ethene polymerization. They had to admit that ranking of barriers with respect to their heights was not possible when the H-imido ligands were replaced by bulky *tert*-butylimido ligands in the model system. The calculated differences in the barriers associated with the reductive pathway or with direct chain growth were minimal.



Scheme 6.2. A cationic arylimido chromium(VI) complex. The aryl backbone is marked in red, R^1 – R^5 define the substitution pattern.



Scheme 6.3. Reduction of the metal center *via* an azachromacycle.

In this work the influence of different DFT functionals on calculated reaction barriers and energies was studied extensively in chapter 5. It was found that the functional B3LYP used by Jensen and Børve is performing poorly in reproducing benchmark level CASPT2 and CCSD(T) results for the closely related non-ionic diimido

chromium complexes. To provide theoretically well founded assumptions of a reaction mechanism, alternative mechanisms are studied in greater detail for cationic chromium(VI) complexes within this chapter. The findings are compared to alternative polymerization pathways to lay a mechanistic basis for further catalyst optimizations.

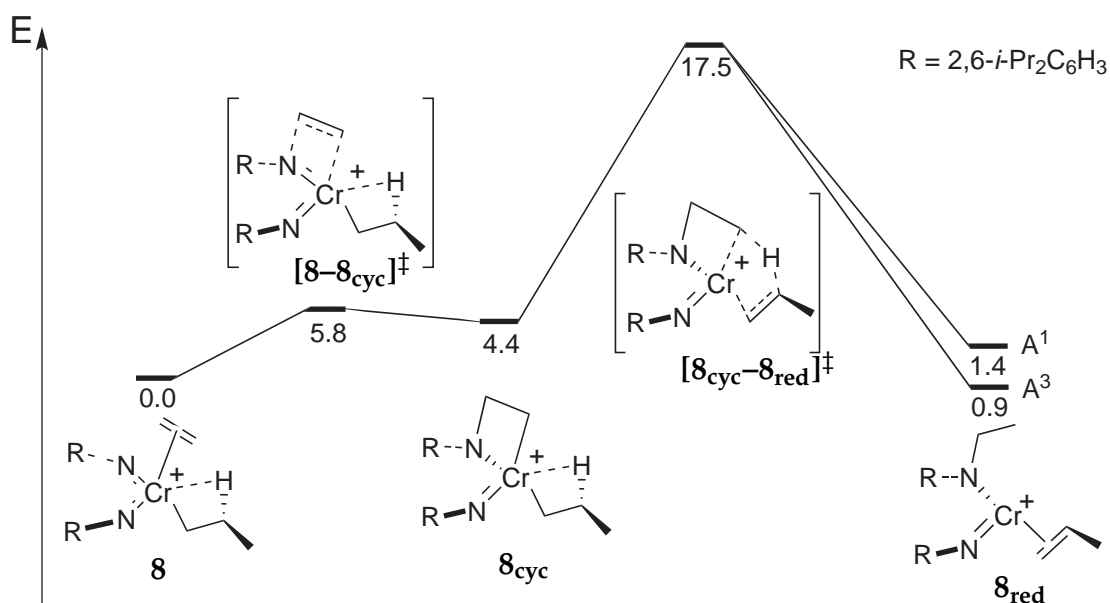
6.2. Results and Discussion

6.2.1. Method Dependence

In this section the investigation of the energetics for both the reductive pathway and for the simple front-side migratory insertion for the propyl substituted di(2,6-diisopropyl phenylimido)chromium(VI)⁺ complex is described (see Scheme 6.3 on page 63 and Scheme 6.5 on page 72, respectively). The method used in the study is PBE-D as it had been derived in the previous chapter. Since cationic species were to be analyzed, solvent effects are anticipated. The continuum solvation methods are computationally very efficient, of which the COSMO model [162] is applied here. To model a typical solvent used for polymerization, in this case toluene, the dielectric constant ϵ was chosen to be 2.4. Since an enormous number of calculations within the optimization of the catalyst was expected, the computational model had to be as efficient as possible. Therefore, the basis sets def-SVP were chosen for the catalyst center and substrate, and def-SV(P) was used for the part of the imido ligands extending beyond the nitrogen atoms. The effect of the reduction of the basis set size will be discussed herein.

Transferred to the full diisopropyl imido substituted complexes, the reductive pathway (see Scheme 6.3) starts at the frontside β -H-agostic ethene complex **8**. It leads over the transition state of [2+2]-cycloaddition [**8**-**8_{cyc}**][‡] to the product, the azachromacycle **8_{cyc}**. The barrier for this step was found to be insignificant with 5.8 kcal/mol, which is visualized in Scheme 6.4. The thermodynamics are slightly unfavorable since the product is energetically uphill by 4.4 kcal/mol. For the cyclic **8_{cyc}**, ring-opening to release the ring strain can be imagined. This could proceed *via* transfer of the β -hydrogen atom from the propyl chain to the ring in analogy to a β -H shift. Passing through transition state [**8_{cyc}**-**8_{red}**][‡] the metal center is reduced at the same time and the chromium(IV) complex **8_{red}** is formed. This step can thus be termed “reductive β -H transfer”. The barrier for this step was found to

be 17.5 kcal/mol. So far, the results are well in line with the ones Jensen and Børve obtained for both imido substituted systems (R=H and *t*-Bu) (see Table 6.1).



Scheme 6.4. Reduction energetics for the di(diisopropylphenyl imido) substituted **8** via an azachromacycle **8_{cyc}**. All values in kcal/mol relative to the educt **8**.

Table 6.1.: Energetics of the reductive elimination and front-side migratory insertion. All values in kcal/mol relative to the side-on complex **8** and its analogs.

Species	R =	H ^a	H	<i>t</i> -Bu	2,6-(<i>i</i> -Pr) ₂ C ₆ H ₃
[8-8_{cyc}] [‡]		4.6	–	–	5.8
8_{cyc}		1.1	-5.6	–	4.4
[8_{cyc}-8_{red}] [‡]		9.5	–	16.7	17.5
8_{red} (A ¹)		-14.9	-20.1	–	1.4
8_{red} (A ³)		-41.5	-16.8	–	0.9
[8-8_{ins}] [‡]		15.6	–	15.5	18.5
8_{ins}		3.6	-3.7	–	-1.1

Calculations performed with the COSMO-PBE-D/def-SVP,def-SV(P) method.

^a Values taken from Jensen and Børve [148].

Only for the next step, the reductive opening of the azachromacycle, a huge energy difference was found. Jensen and Børve obtained energies for the simple reduced H imido species **8_{red}**-H in its triplet state and in its singlet state 41.5 kcal/mol and 14.9 kcal/mol, respectively, lower than for the educt ethene complex **8**-H. The singlet state of the 2,6-diisopropyl phenylimido species **8_{red}** was found to be disfavored by 1.4 kcal/mol and the triplet state by 0.9 kcal/mol in this work.

This discrepancy made the recalculation of Jensen and Børve's values with the same method used here necessary, i.e. with the COSMO-PBE-D/def-SVP,def-SV(P) method. Reaction energies of -20.1 and -16.8 kcal/mol for the reduction to the singlet and triplet state species $\mathbf{8}_{\text{red}}\text{-H}$ were found, respectively. On the one hand, this indicates that the change to the bulky diisopropyl imido ligands leads to a destabilization of the reduced species, especially in the triplet state. On the other hand, the error introduced by the method is large. To clarify the latter issue a small set of test calculations was performed with various methods. The results are compiled in Table 6.2.

Firstly, the influence of basis sets, van-der-Waals (vdW) correction and solvent model was elucidated. The structures were therefore re-optimized with the respective method using the B3LYP functional. Usually a triple- ζ basis set (def2-TZVP) was used for the metal center and double- ζ basis sets (def2-SVP) for all other elements to closely match Jensen's and Børve's approach. The choice of a double- ζ basis set for the metal center as well attributes only a minor change to the computed energy of formation (-0.7 kcal/mol for the singlet and +0.4 kcal/mol for the triplet state). Inclusion of an empirical vdW correction¹ leads to a relative destabilization of the triplet state by 2.3 kcal/mol and of the singlet state by 0.8 kcal/mol while the treatment of solvent effects by a conductor-like screening model (COSMO) did not change the energetics.

Also the combination of vdW corrections and incorporation of solvent effects (COSMO-B3LYP-D2) resembled merely the changes seen for the inclusion of the vdW corrections alone. A change to an even lower basis set level, which was used as a standard within this work (def-SV(P) for the imido-hydrogen atoms and def-SVP for all other atoms) and including vdW correction and solvent effects again, did not affect the energetics significantly.

Using the standard method COSMO-PBE-D2/def-SVP,def-SV(P) Gibbs free energy corrections ΔG_{corr} were computed for standard conditions. They resulted in a minor relative stabilization of 0.1 kcal/mol and 0.4 kcal/mol for singlet and triplet state species respectively.

It is well known that hybrid functionals with large fractions of exact Hartree-Fock exchange mixed in tend to overestimate the stability of higher spin states, whereas pure functionals underestimate it [164, 165]. For transition metal complexes however this can surely not be generalized. Anyways, spin-state splitting

¹ Grimme's empirical vdW correction with revised parameters was chosen [163].

Table 6.2.: Energetics of the reductive β -H-transfer for different computational methods. All values in kcal/mol relative to **8**-H or **8**, respectively.

Method	Compound:		$\mathbf{8}_{\text{red}}$	
	(^1A)	(^3A)	(^1A)	(^3A)
ROHF/def2-TZVP	-58.1	-116.7		
RMP2/def2-TZVP	37.4	38.5		
RCCSD/def2-TZVP	-20.9	-38.4		
RCCSD(T)/def2-TZVP	-13.6	-19.6		
CASSCF(16,15)/ANO-RCC-VTZP	-4.4	-22.3		
CASPT2(16,15)	-8.7	-15.8		
CASSCF(12,12)/ANO-RCC-VTZP	<i>b</i>	-24.0		
CASPT2(12,12)	<i>b</i>	-14.4		
CASSCF(10,10)/ANO-RCC-VTZP	5.4	-24.8		
CASPT(10,10)	-0.6	-12.8		
CASSCF(8,8)/ANO-RCC-VTZP	-18.7	-47.9		
CASPT2(8,8)	-1.9	-19.7		
B3LYP ^a	-14.9	-41.5		
B3LYP/def2-TVZP,def2-SVP	-21.9	-39.4		
B3LYP/def-SVP,def-SV(P)	-23.5	-40.9		
B3LYP-D2/def2-TZVP,def2-SVP	-21.1	-37.1		
COSMO-B3LYP/def2-TZVP,def2-SVP	-22.2	-39.3		
COSMO-B3LYP-D2/dev2-TZVP,def2-SVP	-21.5	-36.7		
COSMO-B3LYP-D2/def-SVP,def-SV(P)	-23.2	-38.4		
COSMO-B3LYP-D2/def2-TZVP,def2-SVP// COSMO-PBE-D2/def-SVP,def-SV(P)	-19.4	-32.9	-1.7	-18.0
COSMO-PBE-D2/def-SVP,def-SV(P)	-20.1	-16.8	1.4	0.9
COSMO TPSSh-D3/def2-TZVP// COSMO-PBE-D2/dev-SVP,def-SV(P)	-17.4	-23.8		
COSMO-OPBE-D3/def2-SVP// COSMO-PBE-D2/def-SVP,def-SV(P)	-22.9	-22.3	-0.9	-4.3

^a Geometries and energies from Jensen's and Børve's work [148].
^b No convergence.

in iron tetracarbonyl was found by Harvey to depend nearly linearly upon the proportion of exact exchange [164]. In line with this, the stability of the triplet state computed with the pure PBE functional is 21.4 kcal/mol lower than computed with the B3LYP functional, including solvent effects and vdW corrections in both cases. At the same time the stability of the singlet state is altered by only 3.1 kcal/mol. It is noteworthy that even the geometry is influenced by the different treatment of the triplet state. This can be seen from the change in the single point energy differences computed with COSMO-B3LYP-D2 on the COSMO-PBE-D2 optimized structures. Here, the change is 3.2 kcal/mol for the triplet state and 2.1 kcal/mol for the singlet state compared to the COSMO-B3LYP-D2 values with the same basis sets.

Overall, the influences of solvent effects and van-der-Waals corrections on the reaction energies are small. The results obtained with the B3LYP functional agree well with the Gibbs free energy of formation calculated by Jensen and Børve for the triplet state reduced species. They do not for the singlet state species². The influence of the density functional on the energy of formation for the triplet state species is large. Coupled cluster and CASPT2 calculations were performed to find reference values.

The basis sets used for the coupled cluster calculations were only def2-TZVP and certainly of the lowest quality permissible for this level of theory. As reference a restricted open-shell Hartree-Fock wave function was chosen since the unrestricted approach led to severe spin contamination. The very large energy deviation of the Hartree-Fock method from the final CCSD(T) and CASPT2 results was not corrected by a perturbative MP2 approach as seen in Table 6.2. The high values obtained for the simple diagnostics $\mathcal{T}_1 = 0.043$ and $D_1 = 0.196$ for **8**-H indicate a level of multireference character similar to that observed in the related uncharged diimido chromium systems investigated previously (see chapter 5). CCSD calculations therefore become unreliable and the deviation from the final CCSD(T) results is not surprising.

For the CAS calculations basis sets of triple- ζ quality with polarization functions were used. CASPT2 calculations were performed to get a quantitative estimate of the energies. Initially an [8,8] active space was tried. It included only the nitrogen-chromium π interactions for **8**. For compound **8**_{red} one of the π -bonds has changed to a nitrogen-carbon σ -bond and the active space was adapted accordingly. The active space was successively extended, including first also the

² Taking into account the very small values of ΔG_{corr} it might be assumed that Jensen and Børve's Gibbs free energy of formation for the singlet state species is incorrect.

chromium-carbon bond in **8** which transforms to a carbon-carbon π -bond in **8_{red}**, yielding a [10,10] space. Then the ethene π -bond was considered as well, leading to a [12,12] active space for which no convergence could be achieved for the singlet state. Although the small change in the predicted reaction energy from a [10,10] to a [12,12] active space indicated convergence with respect to the active space, the nitrogen-chromium σ -bonding interactions were finally considered additionally to obtain convergence for the singlet state as well. Due to the low occupancy, one nitrogen-chromium σ -antibonding natural orbital could be removed leading to the final [16,15] space. The convergence with respect to the active space for the predicted energy of formation for the singlet state species can not be deduced since the [12,12] CAS and CASPT2 results could not be obtained. As convergence for the triplet state seems achieved, it is anticipated for the singlet state as well. The resulting natural atomic orbitals are depicted in Figure 6.1 to Figure 6.3.

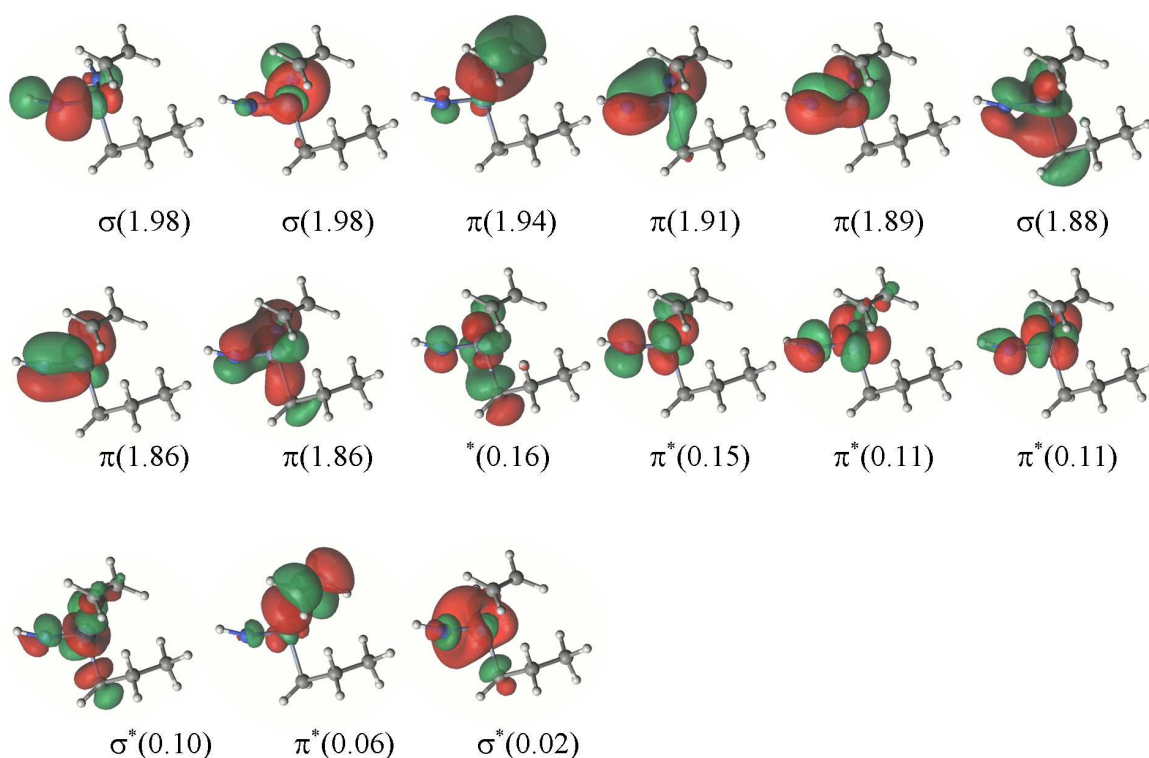


Figure 6.1.. NAOs of the [16,15]-CASSCF calculations for the side-on complex **8-H**.

The energy of formation predicted by CCSD(T) for $\mathbf{8}_{\text{red-H}}$ in its triplet state agrees much better (within 2.8 kcal/mol) with the PBE-D result than with B3LYP. It can be concluded that the energetics of the reduction step can not be evaluated reliably by the DFT methods tested (see Table 6.2). The disagreement of the CCSD(T) and B3LYP results suggests that the reduction and spin-state change is much less exothermic than predicted by B3LYP and that a pure functional is more appropriate in this case. Taking into account the marked destabilization of the reduced species by the introduction of bulky 2,6-*i*-Pr₂C₆H₃ imido ligands, the reductive pathway becomes less favorable compared to migratory insertion. For the direct insertion step passing transition state $[\mathbf{8}-\mathbf{8}_{\text{ins}}]^\ddagger$ to form the β -H agostic pentyl complex $\mathbf{8}_{\text{ins}}$, a barrier of 18.5 kcal/mol was found, which nearly equals the one for the reduction step in case of the 2,6-*i*-Pr₂C₆H₃ imido ligand. The low exergonicity of -1.1 kcal/mol for the insertion step (see Table 6.1) will be significantly risen by the consecutive complexation of a new ethene molecule.

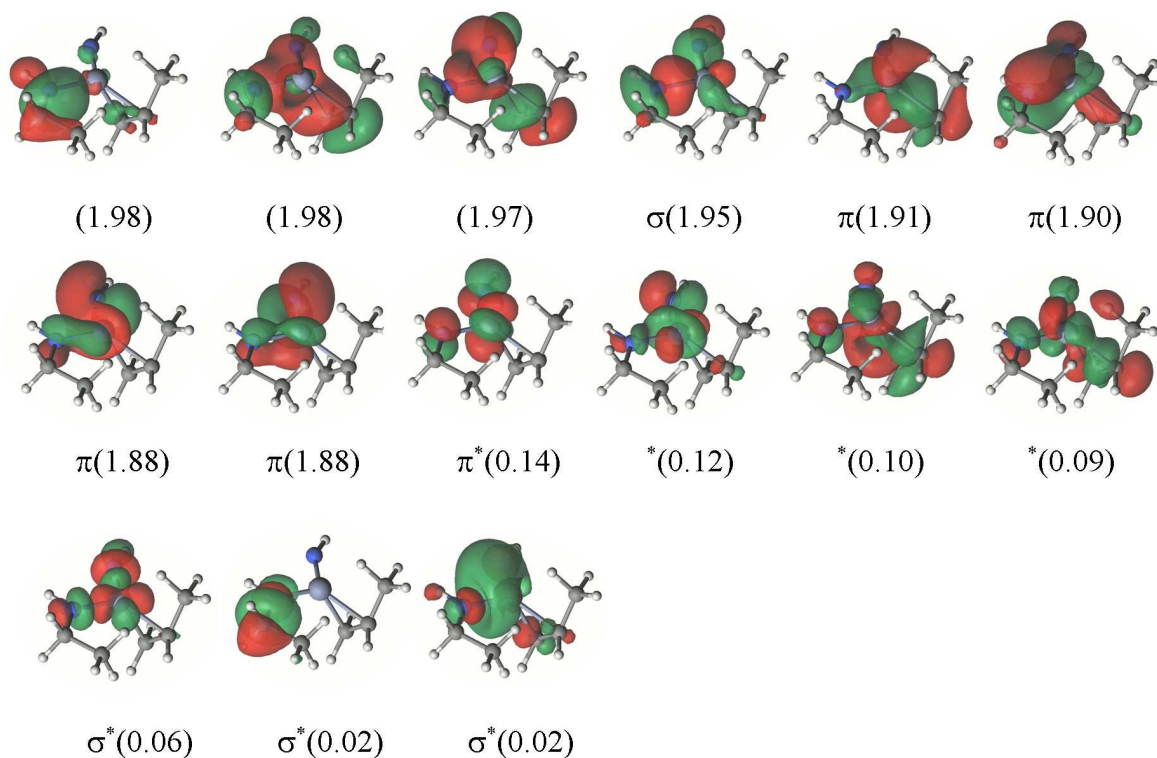


Figure 6.2. NAOs of the [16,15]-CASSCF calculations for the reduced complex $\mathbf{8}_{\text{red-H}}$ in singlet state.

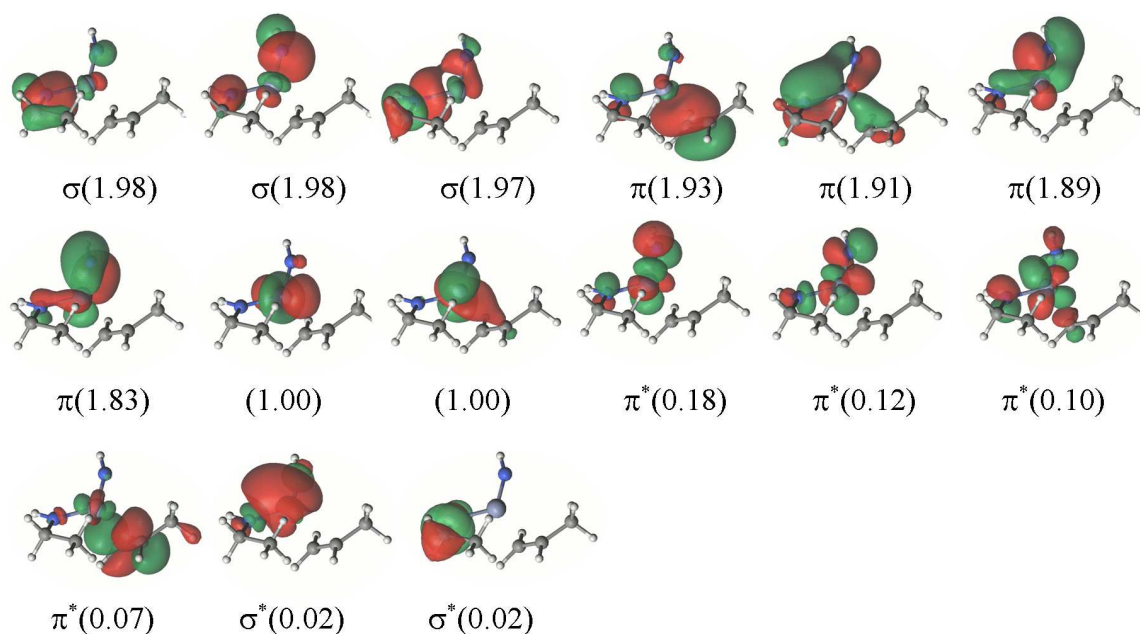


Figure 6.3. NAOs of the [16,15]-CASSCF calculations for the reduced complex $\mathbf{8}_{\text{red-H}}$ in triplet state.

6.2.2. Insertion Mechanism

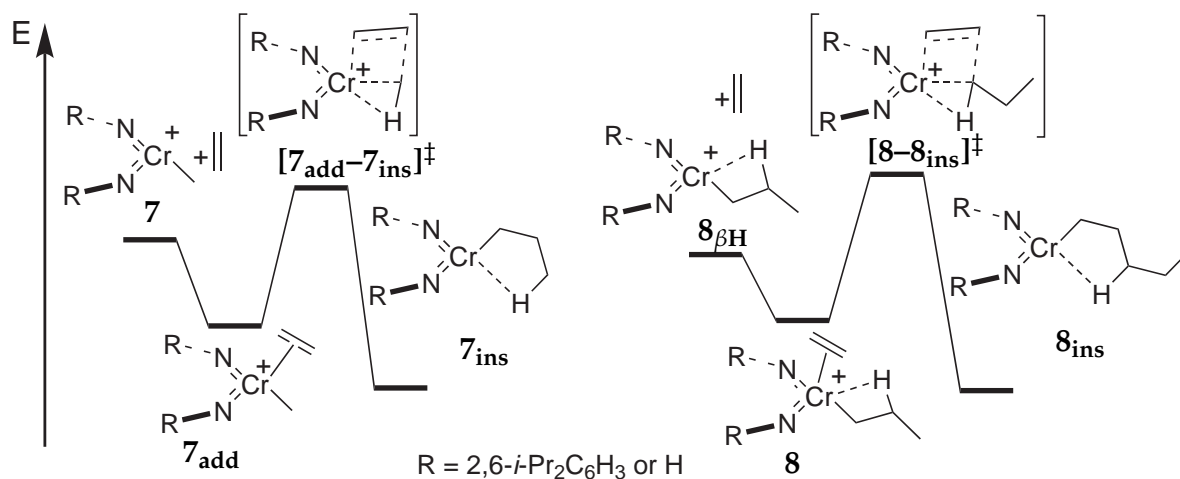
Although the polymerization mechanism is not fully elucidated and a reduction of the metal center could still be doubted, a Cossee–Arlman [25, 26, 166] like mechanism involving a migratory insertion of coordinated ethene into a chromium carbon bond seems most likely and is assumed for this work, as backed by the reference calculations.

As the reduction of computational demand is required to perform the catalyst optimizations later on, a simplification of the model complex $\mathbf{8}$ was conducted and the model complex $\mathbf{7}$, shown in Scheme 6.5, was chosen for the active catalyst in which the growing polymer chain is replaced by a methyl group. Only α -H agostic interactions are included with the methyl ligand. Since only relative barriers of insertion are of interest this seemed to be a fair choice, considering the analysis of the reaction path starting with a propyl ligand, which is described in the following.

The β -H agostic propyl intermediate $\mathbf{8}_{\beta\text{H}}$ readily adds ethene to yield the side-on complex $\mathbf{8}$. From the latter a reaction path was calculated to the γ -agostic product of insertion $\mathbf{8}_{\text{ins}}$.³ It connects the two intermediates *via* direct front-side insertion. Its

³ The reaction path was calculated using the growing string method by Peters, Heyden, Bell and Chakraborty [167] with 11 nodes each and a convergence criterion of 0.001 as maximum perpendicular gradient for a node. Two strings were grown; one from $\mathbf{8}_{\beta\text{H}}$ to the transition state structure $[\mathbf{8}-\mathbf{8}_{\text{ins}}]^\ddagger$ and one from $[\mathbf{8}-\mathbf{8}_{\text{ins}}]^\ddagger$ to the product $\mathbf{8}_{\text{ins}}$.

energy profile and the change of some important geometrical parameters during the course of the reaction are visualized in Figure 6.4, important structures are shown in Figure 6.5.



Scheme 6.5. Insertion reaction. Left part: Model used to generate initial structures for the high-throughput optimizations. Right part: Model for the mechanistic investigations described in this chapter.

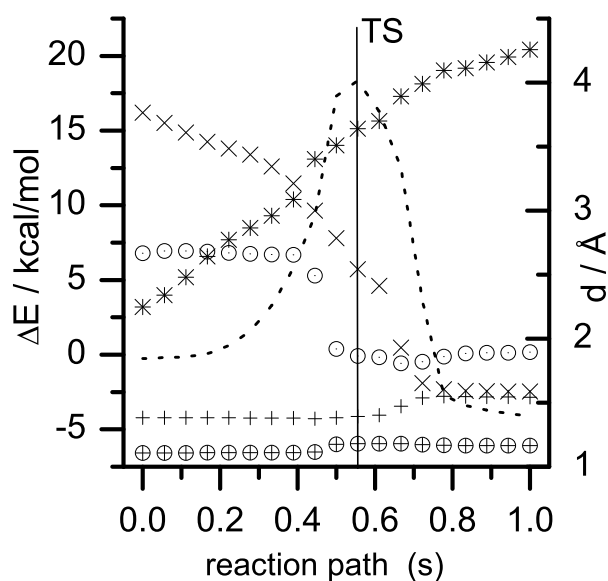


Figure 6.4. Insertion of ethene into the bond connecting chromium and the propyl fragment of $8_{\beta H}$. Energy during the course of the reaction (dashed line) relative to the β -agostic front-side π -complex. Distances d of the forming C-C bond (\times), agostic Cr-H(β) interaction ($*$), agostic Cr-H(α) interaction (\oplus), C-H(α) bond (\odot) and ethene C-C bond ($+$).

The parameter s describes the progress of the reaction in terms of mass weighted coordinates and is normalized to equal 1 at complete product formation. At the

transition state, i.e. the structure with the highest energy in the final string located at $s = 0.56$, the carbon-carbon bond distance of the joining atoms has reached 3.21 Å. This bond shortens continuously on the reaction path to a single bond distance of ≈ 1.6 Å. The carbon-carbon bond of the ethene unit has not stretched compared to the reactant structure. The initial agostic interaction, indicated by a chromium-H(β) distance of 2.07 Å in the reactant, is lost in the transition state, since the bond distance has evolved to 3.64 Å. Most importantly the α -hydrogen atom is interacting strongly with the metal center in the transition state with a Cr-H(α) distance of 1.96 Å and a C-H(α) distance which has stretched by 0.06 Å compared to the reactant and has reached its maximum.

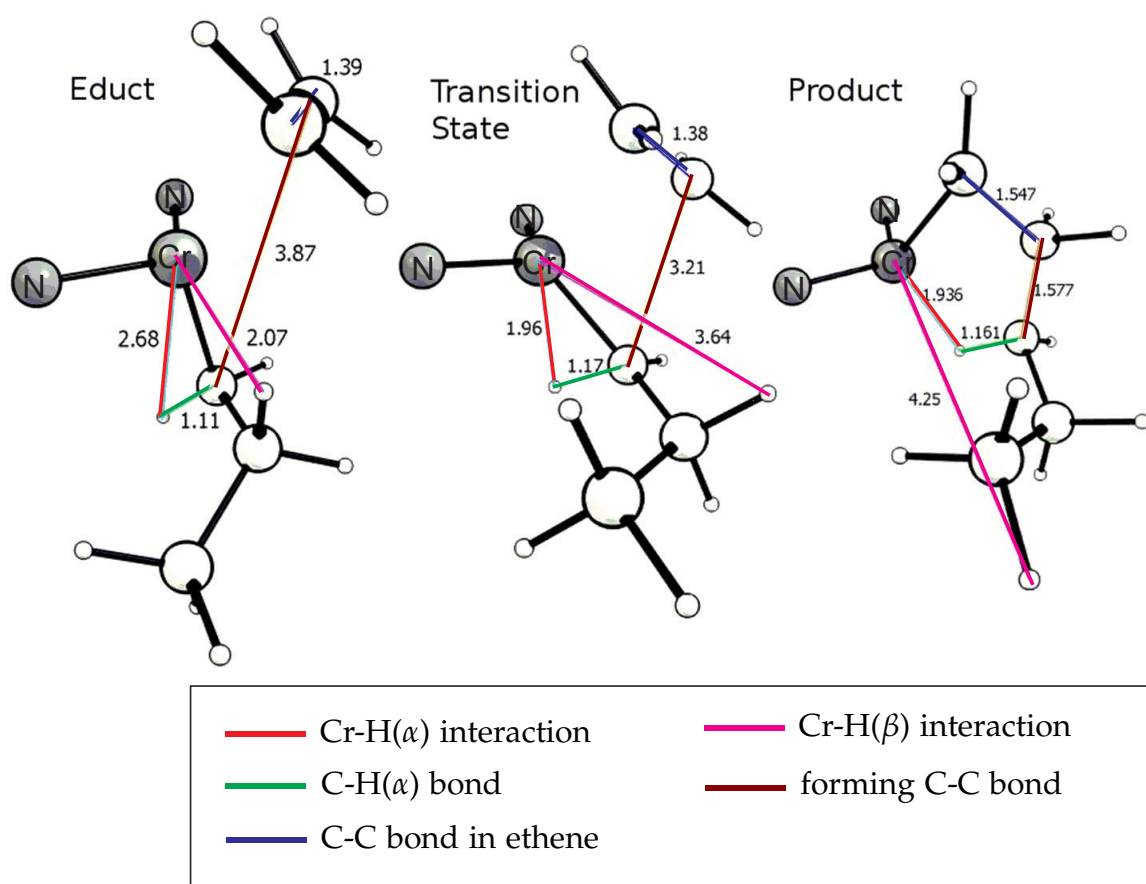


Figure 6.5. Selected distances during the insertion of ethene into the bond connecting chromium and the propyl fragment of **8**. All values in Å. The di(isopropyl)phenyl substituents have been removed for clarity.

With this large distance between the metal center and the β -hydrogen atom, the transition state is not stabilized by a β -agostic interaction. Thus, reducing the propyl unit to a methyl group should not change the transition state's structure significantly. It has to be acknowledged that its energy relative to the reactant

should be lower since the stabilizing β -agostic interaction is missing in the reactant. Nonetheless, during the following catalyst optimization only relative barriers are of interest.

6.3. Summary

Within this chapter the reactivity of cationic diimido chromium(VI) complexes towards olefins has been investigated. Jensen and Børve had suggested that the polymerization might proceed *via* reduced chromium species [148]. This was founded on the B3LYP based calculation of a highly exothermic reduction pathway for an H-imido model complex involving a spin state change from singlet to triplet. Here, it could be shown that the choice of the density functional has a marked influence on the spin state energetics, with B3LYP strongly favoring the triplet state. Reference calculations by CASPT2 and CCSD(T) methods revealed the reduction to be much less exothermic than predicted with the B3LYP functional. The agreement with relative energies obtained by the pure functional PBE were much better. It was further shown that the H-imido model is particularly ill suited to study the reduction since the introduction of the bulky 2,6-*i*-Pr₂C₆H₃ amido ligands lead to a strong destabilization of the reduced species. Overall, the reduction pathway has to be considered less likely compared to an insertion pathway proceeding *via* chromium(VI) centers. As the β -H agostic interaction found in a propyl substituted catalyst model vanishes in the transition state of the insertion step, where only an α -H agostic interaction can be observed, the catalyst model was effectively minimized by exchanging the propyl for a methyl ligand.

Part IV.

Optimizations

7. Introduction

What is optimization? *“Finding an alternative with the ... highest achievable performance under the given constraints, by maximizing desired factors and minimizing undesired ones. In comparison, maximization means trying to attain the highest or maximum result or outcome without regard to cost or expense. Practice of optimization is restricted by the lack of full information, and the lack of time to evaluate what information is available”* (BusinessDictionary.com)

“In mathematics optimization ... refers to the selection of a best element from some set of available alternatives. In the simplest case, this means solving problems in which one seeks to maximize (or to minimize) a real function by systematically choosing the values of real or integer variables from within an allowed set.” (Wikipedia.org)

These two quotations highlight how differently the term “optimization” is used in two research areas. To join the two definitions into one, the “given constraints” could be added to the mathematical function to be maximized by the use of penalty terms. When it comes to the selection of a (mathematical) optimization method, one has to decide between two main classes: deterministic and probabilistic algorithms. A deterministic algorithm is characterized by the fact that in each step there exists at most one way to proceed. The algorithm has finished if there is no way to proceed, e.g. when the gradient equals zero in a gradient based optimization. For a given set of variables the way taken is always identical. Contrasting the deterministic ones, probabilistic algorithms contain a random component. This means that they depend on randomly generated numbers in at least one step. Thus, they are not deterministic [108]. Deterministic algorithms are most often used if a relation between the variables and observables is well known, e.g. geometry optimizations in computational chemistry. If the relation is not too clear or too complex, or the search space has a very high dimensionality, probabilistic algorithms are commonly employed.

In experimental synthetic chemistry, the optimization of a compound with respect to a given property is always ruled by constraints. One very obvious one is that the compound has to be stable or inert to be studied. In computational chemistry this constraint is removed. The beauty is that certain parameters can be explored to their extremes to get better insight into the effect. For example a specific bond in a compound might be stretched or atoms exchanged. This allows substantially more freedom in the design of experiments. The problem of computational chemistry is that after finding an optimal solution, the knowledge has to be transferred back into the laboratory and the corresponding compound has to be synthetically accessible.

Within this work, the optimization of olefin polymerization catalysts for specific substrates is aimed at. Catalytic activity is not a quantum chemical observable but obviously depends on the kinetic barriers associated with the mechanisms leading to polymer formation, which are calculated from quantum chemical observables: energies. This is only one part of the problem. The other is that it also depends on competing steps, e.g. chain termination or catalyst deactivation processes. Furthermore, from a practical point of view, an optimal catalyst has to be thermodynamically accessible. The complexity of the optimization problem is high, because the energies of all relevant intermediates and transition state structures depend in an ill-defined way on the catalysts molecular composition. Therefore, a probabilistic method of optimization was chosen.

Neutral diimido chromium complexes, which show good tolerance towards highly polar olefins as polymerization substrates [57], were investigated with respect to mechanisms leading to the polymerization of *gem*-difluoroethene or deactivation in chapter 5. Their optimization is challenging since no experimental evidence exists. Hence, there is no guideline which parameters of the complex could be altered to improve its properties. It was found that the dependence of the predicted catalytic activity on the computational method, i.e. density functional, is strong. A method was calibrated to the resulting energies from high-level wavefunction theory. During the catalyst optimization the system should not be altered too much because of the danger to invalidate the applied computational method. Hence, the metal chosen, its (formal) oxidation state and the ligand classes have to be kept constant. The substitution pattern on the ligand is left to be altered. This is the object of investigation within this part.

For the ionic diimido chromium(VI) complexes, experimental evidence for their catalytic activity in ethene polymerization exists [133, 160]. Though, the effects of the ligands substitution patterns on the catalytic activities have not been investigated systematically yet and are unclear. Gibson *et al.* synthesized the di(*tert*-butyl)imido benzyl chromium complex and showed that it has a high activity in ethene polymerization [160]. Even higher was the activity reported for the related di(diisopropylphenyl imido) chromium complexes [135]. A variety of routes to access phenylimido chromium complexes exists [136, 161, 168, 169], and the phenyl substituent can be altered in a manifold of ways. Therefore, this class of compound's was chosen for further optimization. Light shall be shed on the influences different ligand substitution patterns have on the catalytic activities.

8. Target Based Random

8.1. Introduction

The potential compatibility of chromium(VI) based polymerization catalysts with highly polar monomers has been outlined in chapter 5. In this chapter the tuning of the diimido ligand toward good fluoroolefin polymerization activities is investigated. In chapter 5 β -fluorine elimination from the growing polymer chain was found to be the major route to catalyst deactivation. The question is, whether it is possible to favor insertion steps leading to polymerization over (fluorine) elimination steps. In other words, can the rate constant of chain propagation (k_{prop}) be increased over that of chain termination (k_{term}): $k_{\text{prop}} > k_{\text{term}}$?

Based on the simple model system **1S** (Figure 8.1), introduced on page 42, geometrical parameters are systematically screened for their influence on the catalytic properties of the metal complex. In case an optimal geometric structure could be derived, the optimization task would be reduced from finding an active catalyst to finding or optimizing a diimido chromium complex resembling the optimal structure. The computational part of the catalyst search is therefore two-stage: firstly, establishing a quantitative structure activity relationship, secondly, performing the optimization towards a good structure.

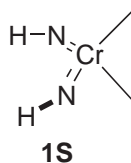


Figure 8.1. The model complex **1S** derived in chapter 5.

8.2. Exploring a Quantitative Structure Activity Relationship: Angle Scanning

Constrained geometry and *ansa*-metallocene catalysts, which allow for the tuning of certain geometric parameters influencing the catalytic properties, play an important role in the field of Group 4 based olefin polymerization [170–172]. It has been found by inspection of the geometries that for the diimido chromium system **1S** two angles alter during the course of insertion and elimination steps (see Table 8.1). The first is the H–N–Cr angle (α) and the second is the N–Cr–N angle (β) (see Figure 8.2). Both can be potentially tuned by a suitable ligand design.

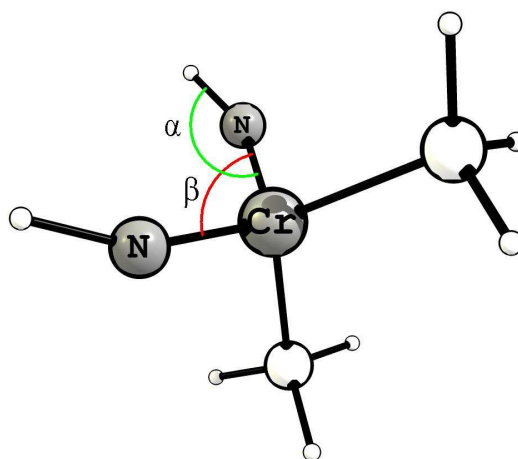


Figure 8.2. Illustration of the definition of α - and β -angle for the model complex **1S**.

Table 8.1.: The angles α and β for important structures.

Compound	β	α
1S	112.5	149.0
[1S-2S][‡]	115.5	156.6
2S	112.9	150.0
[2S-3S][‡]	113.0	153.9
[1S-4S][‡]	119.0	158.6
4S	112.5	148.0

It has to be stressed that compared to the reactant structure of **1S**, the β angle is increased only for the transition state structures of insertion steps and remains approximately constant for the β -F elimination. The α angle increases for all transition states structures.

It is well known [173–175] that the deformation of metal imido angles (α) is facile. Jandciu *et al.* [176] calculated the potential of the R-N-Cr angle deformation by DFT methods and concluded that it is very flat. Here, the potential energy surface is scanned in both the α - and β - space starting from a relaxed geometry with $\alpha = 149.0^\circ$ and $\beta = 112.5^\circ$. With respect to the α angle a very flat surface is found. A change of 20° results in an energy rise of only ca. 6 kcal/mol. The potential for the deformation of the β -angle is much steeper and a change of the β -angle by 20° increases the energy by approximately 12 kcal/mol (see Figure 8.3). Based on these findings small modifications of the β angle seem possible.

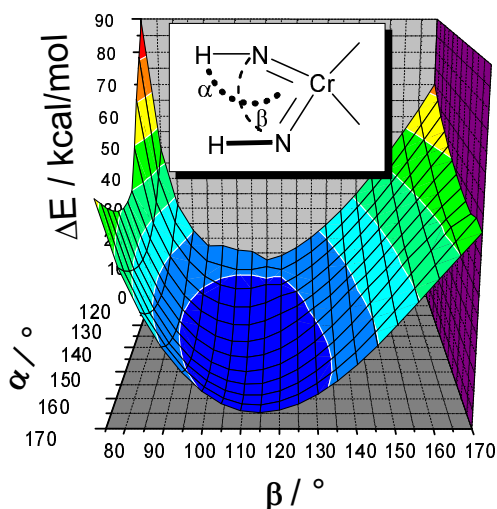


Figure 8.3. Potential energy of **1S** versus the α - and β -angle.

To increase the selectivity of the catalyst, the 1,2 insertion barrier has to be selectively lowered and/or the β -F elimination barrier has to be selectively raised. To investigate the response of the catalyst with respect to these properties, an angle scanning was initiated for the transition state structures as well. For further technical details, see chapter 12. Transition state structures for the 1,2 insertion and β -F elimination steps were optimized under geometrical constraints in the range of $\alpha = 120^\circ - 170^\circ$ and $\beta = 80^\circ - 170^\circ$. The results are visualized in Figure 8.4 and Figure 8.5.¹

Starting from the equilibrium geometry, barriers decrease for both reactions slightly with increasing values of the α angle and strongly with increasing values of the β angle. When changing to high β values for **1S**, we move from an idealized T_d to a $ML_4 C_{2v}$ geometry. The Cr 3d orbital energies in terms of the atomic natural orbital energies are printed for $\beta = 112.5^\circ$ and $\beta = 170^\circ$ in Figure 8.6, where the center of the coordinate system is the metal atom, the z-axis is chosen to intersect the C-Cr-C angle and the carbon atoms are placed in the xz plane. While the d_{yz} orbital is rising in energy, all others decrease. The d_{yz} orbital does not have the proper symmetry to be involved in the bond-breaking bond-forming processes during the 1,2 insertion if the olefin is assumed to be aligned in the xz -plane. Indeed, from the analysis of the natural bonding orbital to natural atomic orbital transformation matrix it can be taken that the d_{z^2} orbital, followed by the $d_{x^2-y^2}$ and d_{xz} orbitals, contributes most strongly to the forming chromium carbon bond in the transition state. Since its energy decreases with increasing β -angle, it can be speculated that the total

¹ Negative values for barrier heights arise from different DFT methods used for geometry optimization (PBE-D/def-SV(P),def-TZVP) and energy evaluation (B2-PLYP-D/def2-TZVPP).

transition state energy is lowered by this effect. Both d_{xz} and $d_{x^2-y^2}$ orbitals have the strongest contribution to the chromium carbon bonds in the educt complex **1S**. Thus the d_{z^2} orbital seems crucial for the relative stabilization of the transition state. The same orbital energy arguments hold for the β -F elimination step except that one of fluorine's filled p orbitals can also interact with the Cr d_{yz} orbital, thus giving rise to a partial increase in energy.

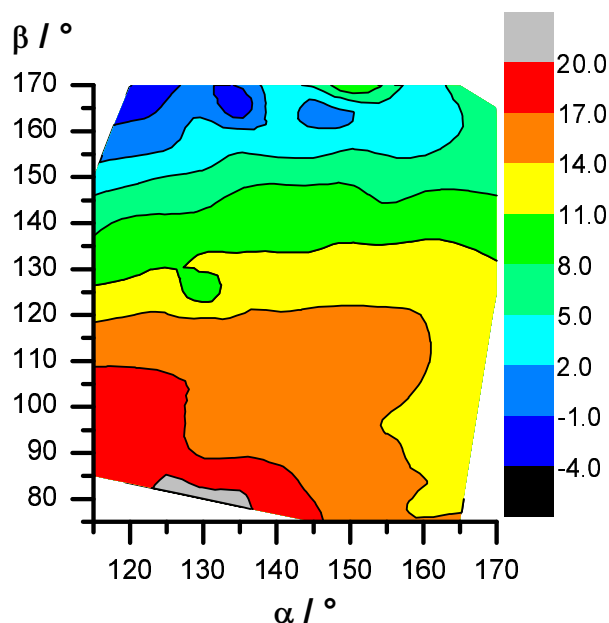


Figure 8.4. Barrier heights (ΔE^\ddagger in kcal/mol) for the transition state of β -F elimination $[2S-3S]^\ddagger$.

The term

$$\Delta\Delta E^\ddagger(\beta\text{-F elimination} - 1,2 \text{ insertion}) = \Delta E^\ddagger(\beta\text{-F elimination}) - \Delta E^\ddagger(1,2 \text{ insertion})$$

determines the selectivity, because these two barriers are associated with the competing processes. The goal is to maximize the selectivity to maximize the probability of insertion steps. A surface plot of $\Delta\Delta E^\ddagger$ values for different α and β angles is given in Figure 8.7. At a parameter set of approximately $\alpha = 140^\circ$ and $\beta = 140^\circ$ a maximum can be identified with the insertion step being favored by 11 kcal/mol over the elimination step. Moreover, 1,2 insertion barriers are predicted to be very low (around 0 kcal/mol) for these geometries. In general a borderline can be drawn at a β angle value of 120° where insertion should dominate over elimination.

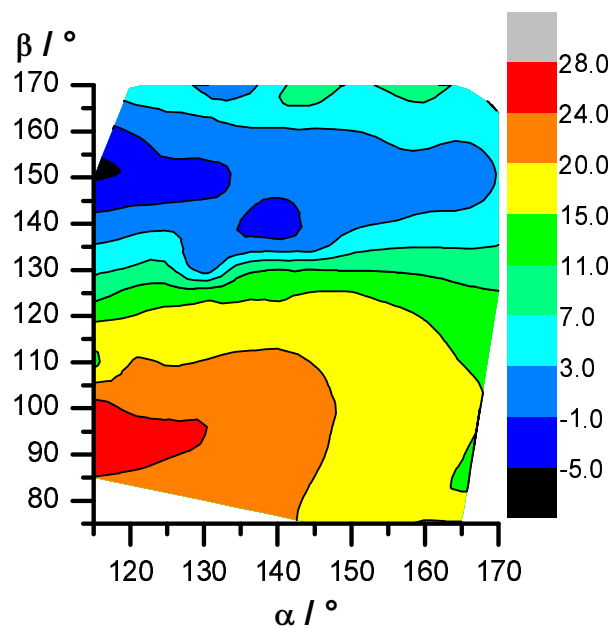


Figure 8.5.. Barrier heights (ΔE^\ddagger in kcal/mol) for the transition state of 1,2 insertion $[1S-2S]^\ddagger$.

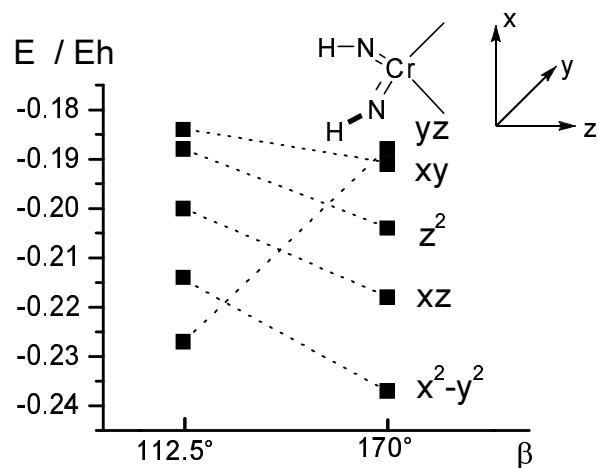


Figure 8.6.. Energies of the Cr 3d atomic natural orbitals in E_h for $\beta = 112.5^\circ$ and $\beta = 170.0^\circ$.

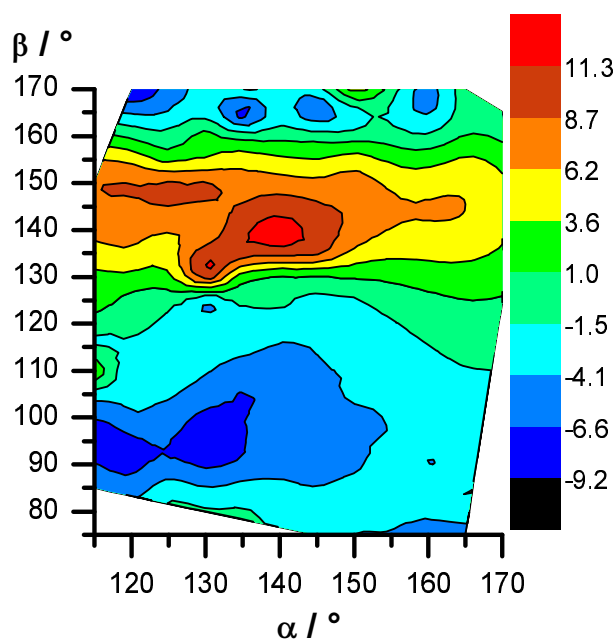


Figure 8.7. $\Delta\Delta E^\ddagger$ (β -F elimination – 1,2 insertion) in kcal/mol.

8.3. Candidate Construction and Evaluation

As the β angle influences both the reactivity and the selectivity to the greatest extent, chromium complexes were searched for, which bear bidentate imido ligands increasing this angle. This search was automated. The flowchart of the candidate construction and evaluation process is shown in Figure 8.8.

A fragments database was created and ligands were assembled statistically from it. It consisted of 13 different fragments as compiled in Table 8.2. Connections to other fragments were possible in all positions marked with "X". A relative probability for being chosen as building block of the ligand was defined and is given in column three. It is for example seven times more likely to find a phenyl unit than an anthracene unit in a ligand. A statistical probability to find a given number of fragments n in a ligand was also defined as tabulated in Table 8.3. The choice of fragments and their probabilities of incorporation was guided by a visual inspection of chelate metalorganic catalysts reported in the literature [177]. During construction, every ligand begins with a terminal imido fragment, is grown with n statistically selected fragments and terminated by a second imido fragment. All remaining linking points were saturated with again statistically chosen termination fragments (see Table 8.4).

In the second step the ligand was attached to a dimethyl chromium unit whose geometry was taken from the model system **1S**. During the following MM2 force-

field optimization the geometry of the dimethyl chromium unit was held constant. The tetrahedral chromium atom was treated as a sp^3 hybridized carbon atom for these calculations.

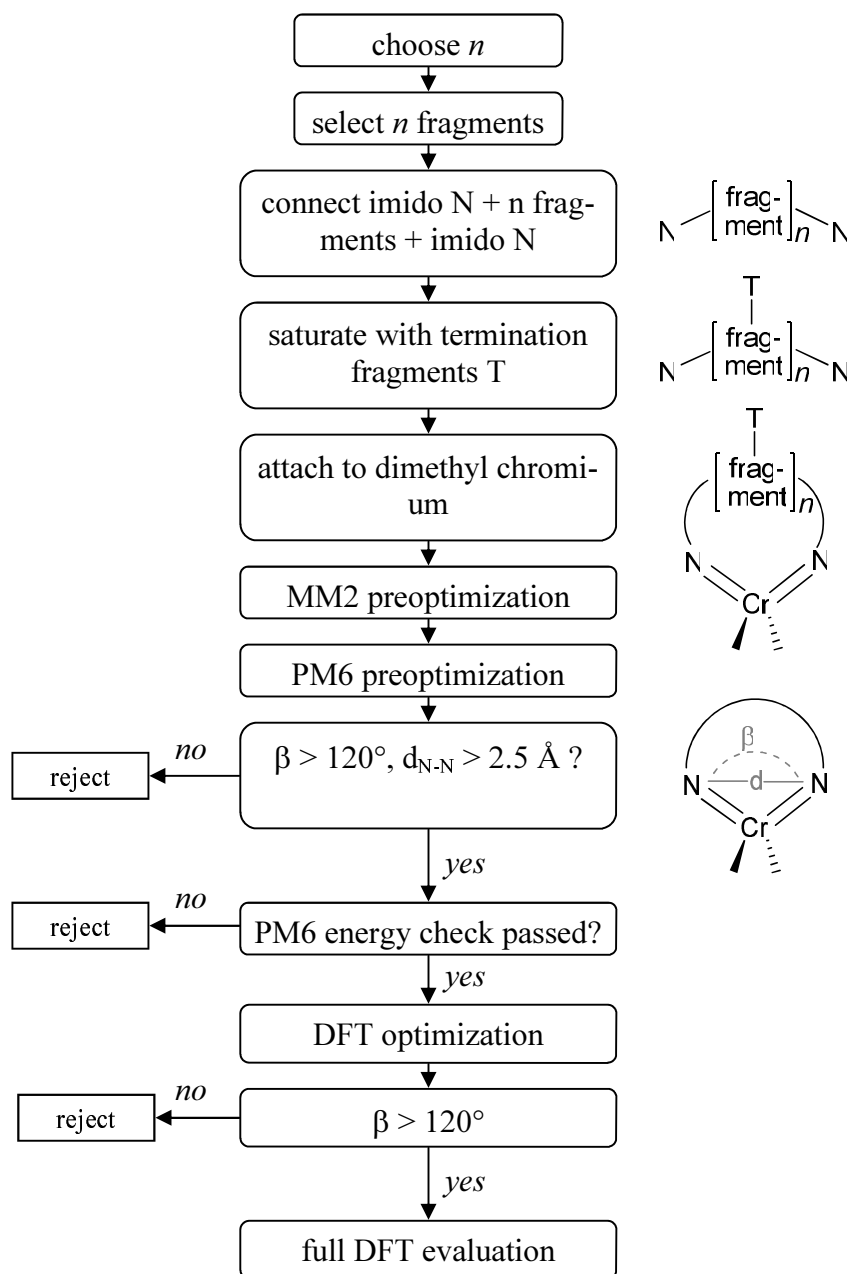
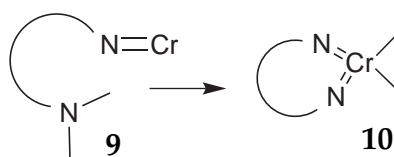


Figure 8.8. Flowchart of the candidate construction and evaluation process.

In the third step the structure was reoptimized employing the PM6 method [178], again keeping the dimethyl chromium unit fixed. This structure was used as starting geometry for subsequent DFT calculations in case the following tests were passed. To reject unsuitable catalyst candidates three tests were employed:

- Is the β angle above a threshold of 120° ?
- Is the distance of the imido nitrogen atoms higher than 2.5 \AA ? (This test is needed to reject structures which collapsed during the PM6 based optimization.)
- Is the structure energetically reasonable?

To judge on that last question an open chain model **9** was assembled, which is preoptimized in the same way as outlined above. Then both catalyst candidate **10** and **9** were freely optimized using PM6 and the computed heats of formation compared (see Scheme 8.1).



Scheme 8.1. Model reaction to estimate ring-strain.

If the formation of **10** was exothermic by more than 100 kcal/mol or less than 0 kcal/mol , the structure was rejected. Typical values of around -40 kcal/mol for the exemplary candidates presented in section 8.4 were found.

After the full DFT optimization of a catalyst candidate the β angle was rechecked to be higher than 120° and otherwise the optimization was canceled. For all further DFT calculations input structures were created in the following way: The model system's structure was taken and the imido ligand removed. The resulting fragment was joined in cartesian coordinates to the candidate's DFT optimized structure having in turn the dimethyl chromium unit removed. Optimizations of intermediates were carried out as outlined above. Optimizations of the transition state structures were performed as described for the angle scanning experiment with the exceptions that a) a full Hessian was computed after the preoptimization step and b) the optimization was stopped if bond distances exceeded or fell below reasonable thresholds. Finally, single point energy calculations were carried out for all computed structures.

Table 8.2.: Fragments used in the construction of imido ligands.

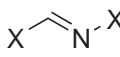
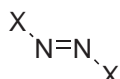
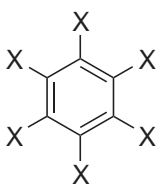
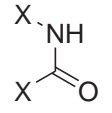
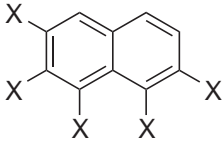
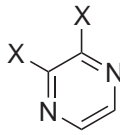
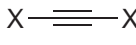
Entry	Fragment	Probability
1		10
2		10
3		25
4		10
5		15
6		70
7		60
8		60
9		23
10		10
11		15
12		12
13		8

Table 8.3.: Probabilities for the assembly of a ligand from the number of n fragments.

n	Probability
2	30
3	34
4	40
5	30
6	15
7	10
8	5
9	1
10	1

Table 8.4.: Termination fragments and their respective probabilities of incorporation.

Entry	Fragment	Probability
1	H-X	100
2	Cl-X	20
3	F-X	15
4	H ₃ C-X	15
5	F ₃ C-X	5

8.4. Exemplary Catalyst Candidates

The examples presented here should serve as structural guidelines for laboratory synthesis. They were selected by visual inspection from the candidates generated by the automatic system since they feature both high β angle values and a simple molecular structure.

The three candidates **K_A**, **K_B** and **K_C** (see Figure 8.9), all exhibit β angles of close to or more than 120° after reoptimization at the DFT level.

These extraordinarily large angles are enforced by highly strained ligand systems, with the terphenyl based candidate **K_C** being an extreme case, for which a value of 27° is found for the out of plane bending of the central to the other to phenyl rings. For the simple reactions of dimethyl chromium with the ligands in their amine form (see Scheme 8.2), energies of formation were calculated and corrected

for zero point vibrational contributions. These values were compared to the ones obtained for a model of Gibson's di(*tert*-butylamido) chromium complex **11** shown in Figure 8.10, for which the benzyl ligands were replaced by methyl ligands. This reference was chosen, since di(*tert*-butylamido)chromium serves as a starting point in the synthesis for many related compounds [145]. This comparison eventually allows to predict problems in laboratory synthesis beforehand.

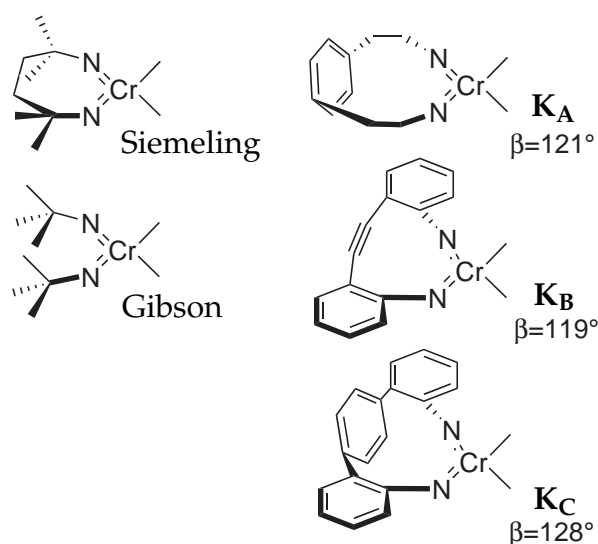
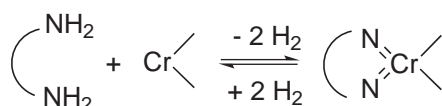


Figure 8.9. Structures of the three exemplary catalyst candidates K_A , K_B and K_C along with the models for Siemeling's and Gibson's catalysts.



Scheme 8.2. Model reaction of dimethyl chromium with ligand precursor.

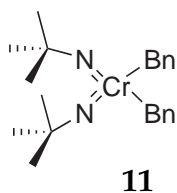


Figure 8.10. Gibson's benzyl substituted di(*tert*-butylamido) chromium complex **11**.

The energies of formation are given in Table 8.5. If an estimate for the entropic contribution of ca. -10 kcal/mol [179] is included for the reaction with bidentate ligands, still K_A , K_B and K_C are found to be thermodynamically less favored by 7.6 to 17.8 kcal/mol. This might give a hint about problems associated with laboratory synthesis.

Table 8.5.: Relative energies of formation (in kcal/mol) for the model reaction and barrier heights for 1,2 insertion and β -F elimination as well as calculated selectivities.

Compound	ΔE	ΔE^\ddagger		selectivity
		(1,2 ins)	β -F	
Gibson	0	10.3	14.3	$8.6 \cdot 10^2$
Siemeling	6.4	15.2	15.8	$2.8 \cdot 10^0$
K_A	17.6	6.9	13.7	$9.7 \cdot 10^4$
K_A^a		11.0	17.7	$8.0 \cdot 10^3$
K_A^b		30.7	17.4	$1.6 \cdot 10^{-6}$
K_B	17.7	8.0	8.4	$1.5 \cdot 10^4$
K_C	27.8	-3.9	13.7	$1.1 \cdot 10^9$

^a values recalculated with the PBE-D/def-TZVP,def-SV(P) method.

^b values recalculated with the B3LYP/def2-TZVPP//PBE-D/def-TZVP,def-SV(P) method.

For the candidates K_A – K_B transition state structures were optimized for 1,2 insertion and β -F elimination and reaction barriers were calculated. They are compiled in Table 8.5 and depicted along with the values for the Gibson type model di(*tert*-butylimido) dimethyl chromium and the model for Siemeling's *ansa*-(2,5-diimido-2,5-dimethylhexyl)dibenzyl chromium in Figure 8.11. As expected from the angle scanning experiment, reactivity and selectivity increase with the β angle.

To reevaluate the method-dependence, for the candidate K_A the barriers were also calculated with the PBE-D and B3LYP functional. In the same way as during the calibrations in chapter 5, B3LYP predicts a reversed selectivity favoring catalyst deactivation while PBE-D is again in good agreement with the B2PLYP-D results (see Table 8.5).

Thus, the diimido motive has been optimized to strained bidentate ligands, which on the one hand increase the reactivity in polymerization and on the other hand renders chain termination processes by β -F elimination less likely.

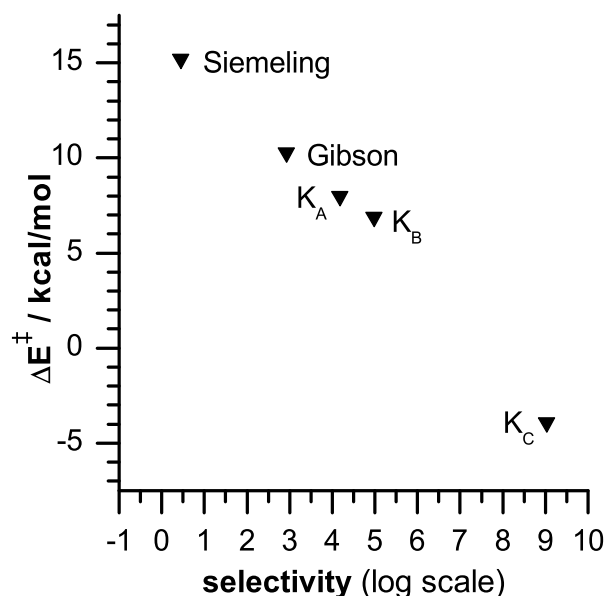


Figure 8.11. Reactivity in terms of the barrier for 1,2 insertion against the selectivity of the catalyst.

8.5. Conclusions

A systematic investigation of two bond angles termed α and β , which can be controlled by ligand design, has been performed. Their influence on the catalytic activity and selectivity of the model diimido dimethyl chromium complex has been computed. It has been found that a β angle of more than 120° increases both reactivity and selectivity in the polymerization process. Under the constraint of a high β angle catalysts were randomly synthesized in silico. It was possible to perform a random search since the effective search space was small. This means from the large search space, defined by the variability in the ligand structure, only a few candidates were actually evaluated for their properties at the time consuming density functional level. The vast majority of candidates was rejected by filters applied already at the early stage of semi-empirical reoptimization. Considering the runtime difference between the property evaluation steps which required time on the order of 1–3 days, and seconds to minutes for the typical preoptimization steps, prescreening of 10^2 – 10^3 candidates per DFT-evaluated candidate was possi-

ble within the available computer setup without requiring any additional computer resources.

The random search led to the proposal of three catalyst candidates, exhibiting high theoretical potential as reactive and selective fluoroolefin polymerization catalysts. Experimental evaluation of one of these candidates, which can be seen as structural guidelines or “leads”, is described in chapter 10.

9. Evolutionary Methods

9.1. Introduction

Genetic algorithms (GAs) play an important role in bioinformatics. They are employed in the field of drug design and for general docking problems as well as in materials science [180, and references herein]. Although the problems to exploit structure-property relationships in order to find a global optimum are existent in many fields of chemistry, only few attempts have been made to combine quantum chemical methods with algorithms suited to solve these problems. Durrant [39] has pioneered in the field of quantum chemical guided catalyst development. He combined genetic algorithms with density functional calculations to identify model complexes which cleave N_2 and form metal nitrides ($2 L_nM + N_2 \longrightarrow 2 L_nM\equiv N$), similar to a system described by Cummins [181–183]. Only very small models were used in this case and problems associated with missing steric contributions were addressed with fixed coordination geometries. The few other works published include i) the optimization of dibenzyl sulfide oligomers to optimally cover a gold nanoparticle by Nagata [184], ii) the development of a DFT-based GA optimization algorithm by Hünnerbein, which was employed for the optimization of the dipole moment and the HOMO-LUMO gap by the variation of substituents of naphthalene, minimization of the activation energy of a Diels-Alder reaction and maximization of the binding energy of dihydrogen on borols [185], and iii) the recent extension of Hartke's and Dieterich's OGOLEM framework [186] to design optimally light-switchable molecules employing semi-empirical methods [187]. All these approaches target on only one parameter to be optimized disregarding for example the important question whether the optimized compounds are stable or not.

Computational resources available to the scientist are steadily increasing. Not seldom can computer clusters of up to 500 CPU cores be found on a working group basis. Powerful enough to treat realistically sized chemical systems, the need to efficiently use this infrastructure was recognized and a suite of programs was to be developed to drive quantum mechanical calculations with genetic algorithms fully automatically. Very high flexibility was to be maintained to adapt the system to a wide range of computationally treatable problems and in particular allow for the multi-factorial definition of a compound's fitness. Details of the technical implementation can be found in chapter 12.

The system was applied to the optimization of cationic diimido chromium(VI) complexes for ethene polymerization. Their relevance has been outlined in chapter 5 (page 40) and overall applicability to olefin polymerization is believed to be by its

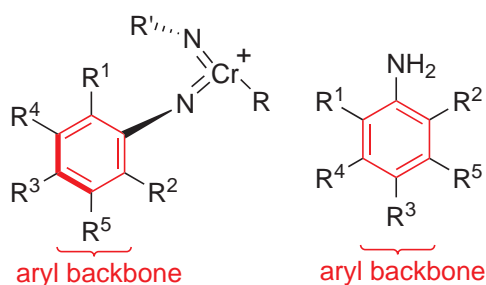
isolobal relationship to the Group 4 metallocenes [58]. However, there were discussions, whether the chromium(VI) species are reduced under the exposure to olefins and the catalytic centers would be chromium(IV) [147, 148]. The reduction has been discussed in chapter 5 and falsified. On the contrary, an insertion mechanism proceeding *via* chromium(VI) centers seems more likely. Nonetheless, trends in catalytic activity have neither experimentally nor theoretically been explored in detail yet. Though, it was noted by Gibson *et al.* that the di(diisopropylphenyl)imido dimethyl chromium complex activated with $B(C_6F_5)_3$ showed qualitatively faster polyethene production than the di(*tert*-butyl)imido dibenzyl chromium activated with $[PhNMe_2H][B(C_6F_5)_4]$. Kipke investigated the effect of imido substitution with a small series of three differently halogen substituted arylimido ligands as well as the *tert*-butylimido and the mesitylimido ligand [136]. She used chloro chromium complexes activated with methyl aluminoxane and concluded that electron withdrawing groups in the imido ligands have an inhibiting effect on the catalytic activity in ethene polymerization. Not in line with this, the activity for the electron poor 2,4,6-trifluorophenyl imido complex was highest amongst the tested catalysts. This invalidates Kipke's conclusion to some extent and underlines the need for further investigations.

Especially the class of arylimido ligands features a manifold of substitution possibilities, in particular considering that a broad range of synthetic routes towards their chromium complexes is known [136, 161, 168, 169]. These are therefore chosen as study subjects. The global optimization system is applied to the substitution pattern in the arylimido ligands in order to identify ligands and typical ligand features which favor low insertion barriers in ethene, thus favoring polymerization.

9.2. Optimization

9.2.1. Optimization Space

For the global probabilistic optimization the space spanned by the substituents on the arylimido ligands was selected, since it can be constructed to contain ligands with a diverse set of both electronic and steric features. The phenyl ring possesses five substitution sites available for derivatization on its carbon backbone as shown in Scheme 9.1.



Scheme 9.1. The aryl backbone marked in red of the arylimido chromium(VI) complexes (left) and its ligand precursors (right). The substituents R^1 – R^5 span the optimization space.

The substituents H, Me, *i*-Pr, Cl, F, OMe, Ph, SO₂Me and CF₃ were allowed to be placed in all positions of the backbone. The alleles together with the substituents they encode are given in Table 9.1. With the five different substitution sites of the phenyl backbone, this optimization space leads to 9⁵ (59049) possible solutions. The encoding on the chromosome is “[R¹]__[R²]__[R³]__[R⁴]__[R⁵]”.

Table 9.1.: Substituents with their genetic codes.

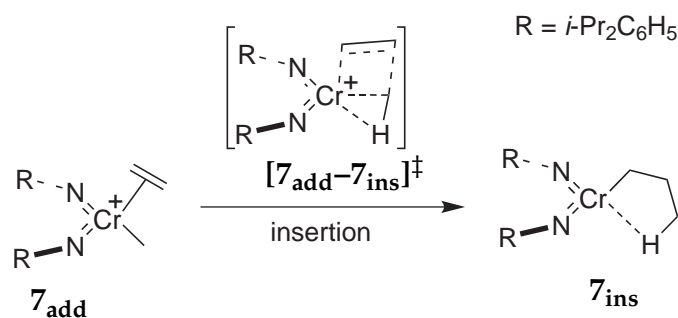
Substituent	allele
-H	0
-Me	1
- <i>i</i> -Pr	2
-Cl	3
-F	4
-OMe	5
-Ph	6
-SO ₂ Me	7
-CF ₃	8

9.2.2. Fitness function

The optimization aimed at the reduction of the barrier for migratory insertion, shown in Scheme 9.2, and thus favor chain propagation. Its rate constant k_{prop} for the rate determining step, which is the actual insertion process starting at the ethene adduct $\mathbf{7}_{\text{add}}$, can be estimated by

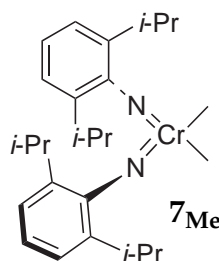
$$k_{\text{prop}}(T) \approx \frac{k_B T}{h} e^{-\Delta E^\ddagger / (RT)}$$

where T is the temperature, k_B Boltzman's constant, h the Planck constant, R the universal gas constant and ΔE^\ddagger the activation energy. Thus, lowering the activation energy will lead to an exponential increase in the reaction rate. As reference the model 7_{Me} (Scheme 9.3) was chosen for the experimentally known di(2,6-diisopropyl phenylimido) complex, as derived in section 6.1.



Scheme 9.2. Insertion of ethene into the chromium-carbon bond.

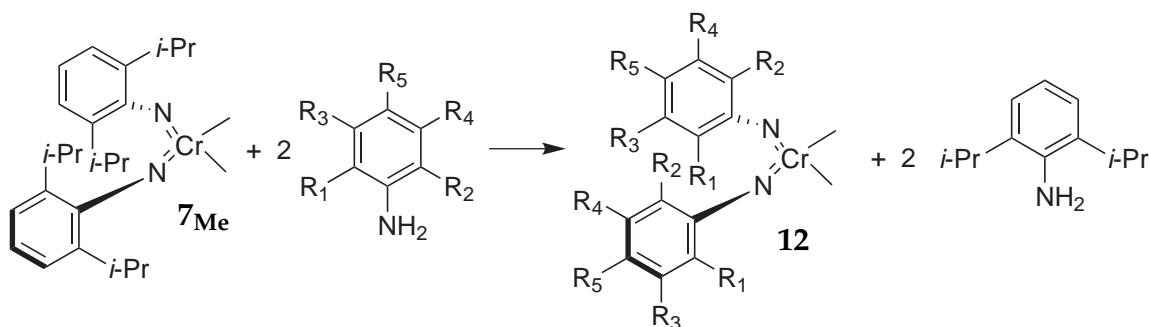
The insertion barrier ΔE^\ddagger for the insertion of ethene into the chromium-carbon bond of this model was calculated to $\Delta E_{\text{ref}}^\ddagger = 15.3$ kcal/mol using the COSMO-PBE-D/def-SVP,def-SV(P) method approved in chapter 6. This computational method was used for all calculations within this chapter.



Scheme 9.3. The reference model complex 7_{Me} .

A decrease of the activation energy can generally be achieved by either stabilizing the transition state or by destabilizing the reactant. If the latter route is taken, the synthesis of these complexes could be potentially complicated, if not impossible. To circumvent this problem, a measure for the ease of synthesis can be incorporated into the fitness function. The reaction energy ΔE_f for a transamination with the reference complex (see Scheme 9.4) to form the candidate **12** was chosen as such a measure. It can be calculated from the absolute energies of educts and products E by

$$\Delta E_f = 2E(2,6\text{-diisopropyl aniline}) + E(\mathbf{12}) - 2E(\text{ligand-precursor}) - E(7_{\text{Me}}).$$



Scheme 9.4. Ligand exchange by transamination.

Within the fitness function the relative importance of ΔE_f and ΔE^\ddagger can be adjusted by offsets. Several runs were performed in which different parameters were tested.

Run 1 High emphasis was laid upon the synthesizability in the first run of the global optimization system. The fitness f_{1a} (Eq. 9.1) was calculated as

$$f_{1a} = \log(e^{\Delta E_f} + e^{\Delta E^\ddagger - 21.3 \text{ kcal/mol}}) \quad (9.1)$$

where ΔE^\ddagger is the candidate's insertion barrier. Initially, 21.3 kcal/mol were subtracted from the ΔE^\ddagger value, hence convergence was favored towards a population which can be synthesized "easily". This value was changed during the run to 6 kcal/mol to favor evolution towards low barriers, yielding the fitness function f_{1b} (Eq. 9.2):

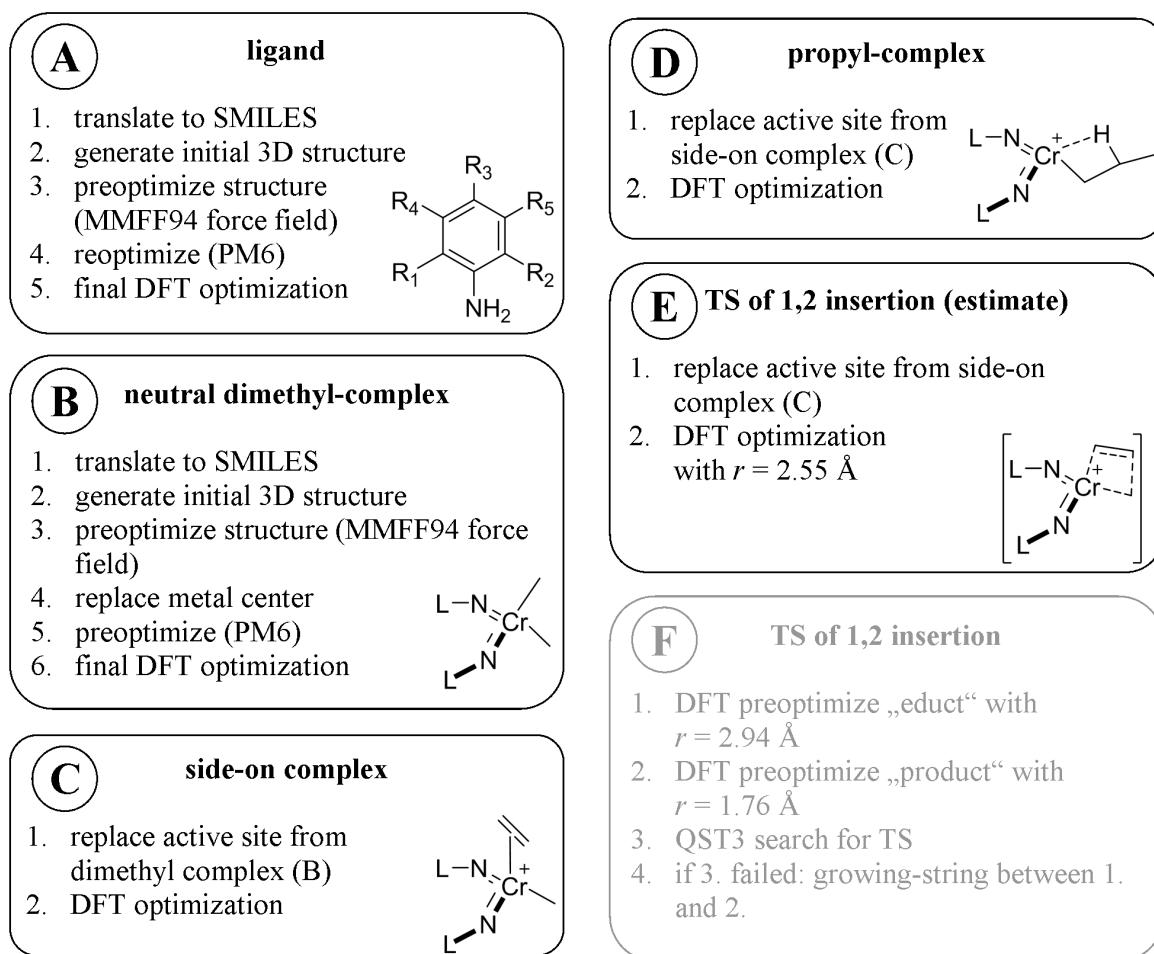
$$f_{1b} = \log(e^{\Delta E_f} + e^{\Delta E^\ddagger - 6 \text{ kcal/mol}}) \quad (9.2)$$

Run 2 and 3 A balanced emphasis was laid upon both synthesizability and activity in the second and third run from the beginning (Eq. 9.3):

$$f_2 = f_3 = \log(e^{\Delta E_f} + e^{\Delta E^\ddagger - 6 \text{ kcal/mol}}) \quad (9.3)$$

9.2.3. Evaluation procedure

During the optimization, the evaluation of the catalyst candidates was split into six individual tasks A–F (see Scheme 9.5).



Scheme 9.5. Individual steps of the full catalyst candidate optimization. Step F is grayed out since it was skipped after correlating QST3 calculated and approximated barrier heights.

In task A the ligand precursor was optimized in a multistep procedure. First the chromosome was translated into a SMILES notation. From this an initial three dimensional structure was generated using the smi23d programs [125], which was then preoptimized using the MMFF94 force field [188]. The structure was reoptimized at the semi-empirical level using the PM6 hamiltonian to create a sensible starting structure for the following final optimization at the DFT level.

In task B the neutral dimethyl complex was constructed in a similar manner as the ligand precursor. In the force field optimization the metal center, for which the coordination sphere is tetrahedral, was treated as a tetrahedral carbon atom since no chromium parameters are available.

Tasks C–F reuse the already cartesian coordinates from a previous step. Only the active site, consisting of the metal center, the methyl- or propyl-ligand and the ethylene molecule, was replaced in *xyz*-coordinates before the structure optimization.

In task E an approximate transition state structure was optimized by fixing the distance of the two joining carbon atoms at a value of $r = 2.55 \text{ \AA}$, which was found after optimization for the transition state structure of the reference catalyst **7** ($[\text{7}_{\text{add}}-\text{7}_{\text{ins}}]^\ddagger$). This distance is considerably shorter than for the isopropyl substituted model **8**.

Task F finally performed the transition state optimization itself. Starting from the estimated transition state structure of task E, two more points were optimized. One was more educt-like with a carbon – carbon bond length r of $r = 2.94 \text{ \AA}$ and one more product-like with $r = 1.76 \text{ \AA}$. Starting from these three structures a synchronous transit-guided quasi-Newton (STQN) search [189, 190] for the transition state structure was initiated. In case it failed (as indicated by a large or small carbon – carbon distance r with $1.7 \text{ \AA} > r > 3.3 \text{ \AA}$, an energy equaling that of the reactant or no convergence), a string was grown between the more product like and the more educt like structure using Peters, Heyden, Bell and Chakraborty's growing-string method [167]. Seven nodes and a loose convergence criterion of 0.01 as maximum perpendicular gradient were utilized and the transition state energy was estimated by the iteratively sought maximum of a spline [191] over the 7 points.

Task F is certainly the most time consuming, especially if the STQN search failed and a string had to be computed. The latter happened in 73% (470 out of the 644 first candidates in run one) of the cases. With the goal to speed up the calculations, the correlation between the approximate transition barrier from task E and the

analytic barrier from the STQN searches was investigated for 174 candidates. A linear correlation described by $\Delta E^\ddagger = (1.044 \cdot \Delta E_{\text{est}}^\ddagger - 0.508)$ was found with $R^2 = 0.952$ (Figure 9.1).

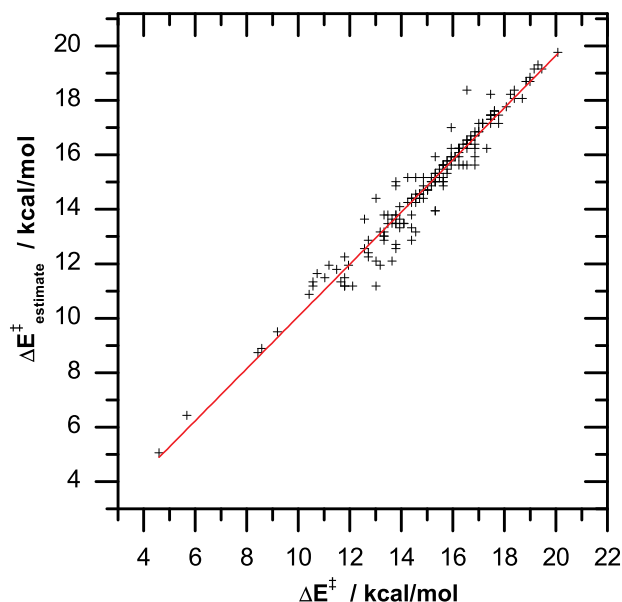


Figure 9.1.. The estimated barrier at the fixed distance of $r = 2.55 \text{ \AA}$ against the STQN optimized barrier of insertion.

The strong correlation between the estimated and the analytically derived barrier justifies the use of estimated barriers in the fitness function. Therefore, starting from individual 645 within the global optimization run one, the fitness values are based on values calculated from the estimated barriers using the linear equation given above and job F was skipped. For runs two and three, this approximation was used from the beginning.

9.2.4. Optimization Runs

Run 1 The global optimization was run with the parameter set given in Table 9.2, which is essentially a scale up from the standard parameter set during the test runs described in chapter 13, employing again a rank based selection algorithm.

The evolution of the fitness during the global optimization run one is visualized in Figure 9.2. After 200 individuals had been evaluated, which were randomly created as a starting population, the average fitness of the parents started to increase. In the beginning, the increase was steep since two effects superimposed: the pool from

which the parents are selected grew larger than the number of selected parents and after that optimization set in. As described above, after 644 calculated individuals, the barrier of insertion was estimated by a linear correlation with the fixed-distance energies. As the correlation is high and the proportion of the barrier's value in f_{1a} (Eq. 9.1) is small, the effect is invisible in the chart.

Table 9.2.: Parameters used during the global optimization runs.

Parameter	run 1	run 2	run 3
$n_{\max\text{run}}$	200	200	200
n_{parent}	200	200	2
n_{pop}	400	400	200
n_{best}	40	40	20
$n_{\max\text{child}}$	20	20	
$n_{\text{pool-size}}$	–	–	5
P_c	0.9	0.9	0.9
P_m	0.2	0.2	0.2

Where $n_{\max\text{run}}$ is the number concurrently running tasks in the optimization system, n_{parent} is the number of potential parents from which 2 are drawn for mating, n_{pop} is the size of the actual population, n_{best} is the number of elitists (fittest ever calculated individuals), $n_{\max\text{child}}$ the maximum number of candidates which are created at once for evaluation, $n_{\text{pool-size}}$ the number of candidates in the pool for tournament selection, P_c the probability of crossover and P_m the probability of mutation. Details of the parameters can be found in chapter 13.

Following the flattening of the mean-fitness curve, which indicates a stagnation in the optimization process, the fitness function was changed to f_{1b} (Eq. 9.2) after 1360 calculated individuals as a test. The fitness of all previously calculated individuals was recalculated. Interestingly, the fitness did not start to rise after introducing the new fitness function, but resumed to decline. Therefore, the experiment was stopped after a further 100 candidate evaluations.

Run 2 As stated above, the only initial difference between run two and one was to calculate the fitness by function f_2 (Eq. 9.3). It can be seen from Figure 9.2 that after the initial population, which consisted of 200 candidates, was evaluated, a steep increase in fitness occurred until twice the population size was reached. From there on a decrease in mean fitness can be observed, ranging approximately from candidate 400 to 800. Hence, after removing the 200 worst candidates from the actual population, no further increase in the fitness was achieved and no additional optimization took place. To increase the diversity, the mutation probability P_m was increased to 0.3 after 755 candidates were calculated, and a constant number of

10 randomly constructed candidates were injected into the group of parents. This means that 10 random candidates were added to the rank based fittest 200 individuals (including the 40 fittest ever calculated). From this pool, every time a new candidate had to be evaluated, two individuals were drawn randomly for mating. After this change and an approximately 200 further individuals which had to pass out of the system, the mean fitness increased again. It formed a maximum at around 1340 calculated candidates and started to decline again thereafter.

Run 3 To probe whether a different selection algorithm could lead to a better optimization performance and a higher maximum mean fitness, a third run was initiated. As selection algorithm the tournament selection was applied as it features a promising loss of diversity / selection intensity profile and was easy to implement. A tournament size of $n_{\text{pool-size}} = 5$ was chosen to achieve a theoretical loss of diversity similar to the one obtained by the truncation selection as in runs one and two. Following Equation 2.17 (page 28) the loss of diversity is

$$p_{d,T}(5) \approx 0.53$$

whereas for the truncation selection with $T = 0.5$, using Equation 2.12, $p_{d,T}(0.5)$ takes a value of 0.5. At the same time a higher selection intensity is achieved with the tournament algorithm of

$$I_T(5) \approx 1.15$$

following Equation 2.20 compared to a value of $I_T(0.5) \approx 0.8$ for the truncation algorithm, which can be calculated from Equations 2.12 and 2.14, given that f_c for the normal Gaussian distribution equals 0.

Again, the mean fitness increased after the first 200 candidates had been calculated as depicted in Figure 9.2. Although after about 830 calculated candidates a phase of stagnation is visible, the mean fitness started to increase again after 1200 calculations to peak at a value of about -8.8 and drop thereafter. After 2225 calculated candidates, it was tried to stop the decline by raising the number of fittest ever calculated candidates kept in the actual population to 60 resulting in a jump in the mean fitness and a consequent increase to -7.5. Thereafter no further improvement in the population's mean fitness was observed.

The fittest individual identified in this run was identified as number 588, compared to number 852 in run 1 and 390 in run 2.

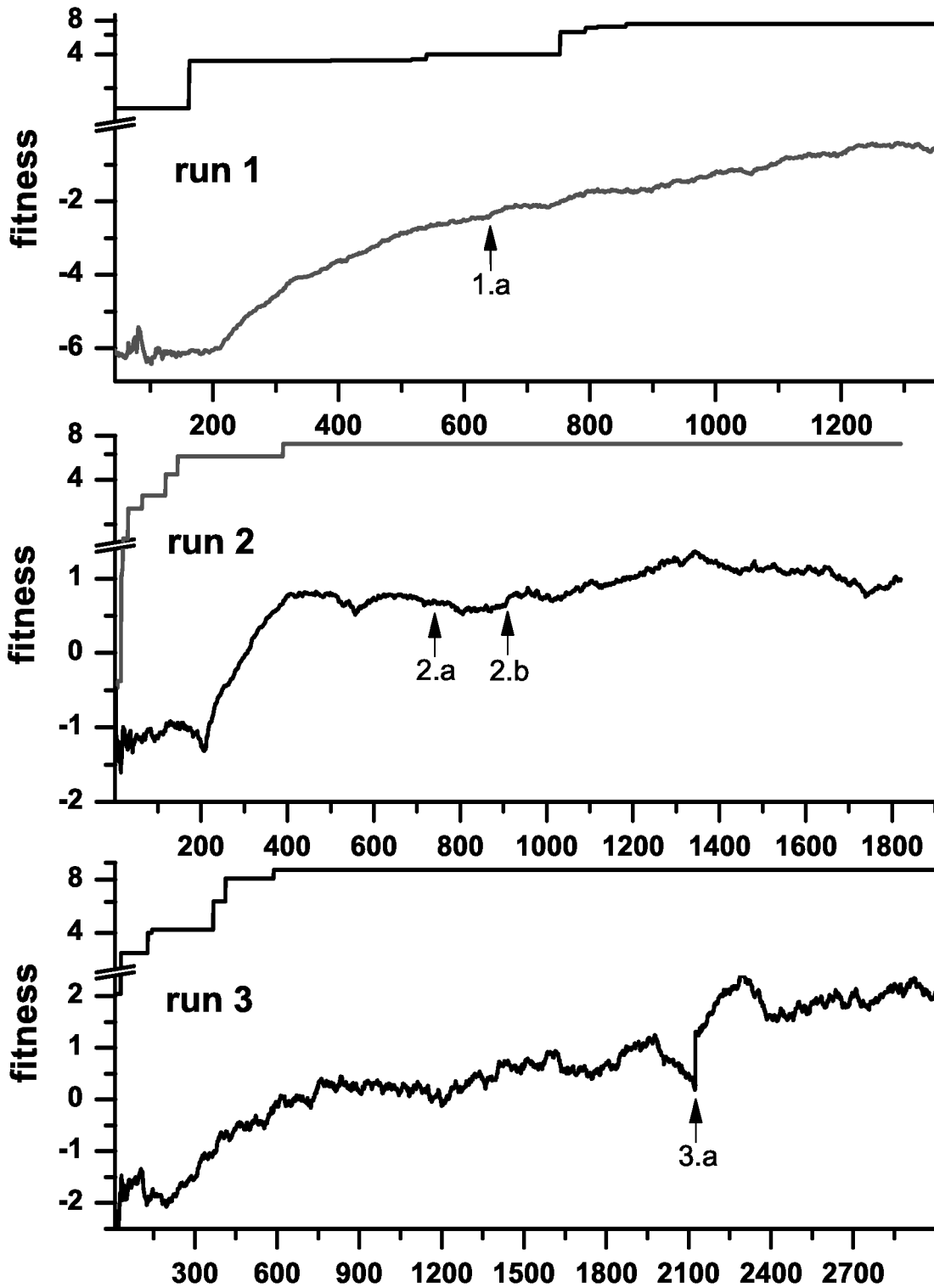


Figure 9.2. Average fitness of the population (lower lines) and maximum fitness (upper lines) during the optimization runs 1–3 versus the number of individuals evaluated (n_{calc}). For runs 2 and 3 the fitness values have been shifted by +10. Please note the logarithmic scale in the upper part of the graphs. 1.a marks the point after which only estimated barriers were used in the calculations of the fitnesses. 2.a marks the parameter change in run 2 and 2.b the following inset of optimization. 3.a marks the change of n_{best} in run 3.

9.2.5. Data Evaluation

During the optimization runs molecular descriptors were calculated and collected:

- after preoptimization with the PM6 method:
 - for the ligand precursors:
 - * the charge at the nitrogen atom $q_{\text{PM6}}(\text{N,ligand})$
 - * the energy of the HOMO $E_{\text{PM6,HOMO}}(\text{ligand})$
 - * the energy of the LUMO $E_{\text{PM6,LUMO}}(\text{ligand})$
 - * the HOMO-LUMO gap $\Delta E_{\text{PM6,gap}}(\text{ligand})$
 - * Schüürmann's MO-shift parameter $\alpha_{\text{PM6}}(\text{ligand})$ and
 - * Pople's and Parr's absolute hardness $\text{Hardness}_{\text{PM6}}(\text{ligand})$
 - for the dimethyl complex
 - * the charge at the Cr atom $q_{\text{PM6}}(\text{Cr})$
 - * Schüürmann's MO-shift parameter α_{PM6}
 - * Pople's and Parr's absolute hardness $\text{Hardness}_{\text{PM6}}$ and
 - * the N–Cr–N angle β_{PM6} .
- after DFT optimizations:
 - for the dimethyl complex
 - * NMR shift parameters, namely the isotropic and anisotropic shielding constants σ_{iso} and σ_{aniso} for the Cr atom, the methyl ligand's carbon atoms and the imido nitrogen atoms
 - * the energies of the HOMO and LUMO as well as their gap E_{HOMO} , E_{LUMO} and ΔE_{gap}
 - * the N–Cr–N angle β
 - * its relative energy of formation $\Delta\Delta E_f$ compared to the energy of formation of the reference complex 7_{Me} .
 - For the cationic side-on complex:

- * the energies of the HOMO and LUMO as well as their gap $E_{\text{HOMO}}(\text{side-on})$, $E_{\text{LUMO}}(\text{side-on})$ and $\Delta E_{\text{gap}}(\text{side-on})$
- * the N–Cr–N angle $\beta(\text{side-on})$
- * its energy of formation $\Delta E_f(\text{side-on})$.
- For the product of insertion, the propyl complex:
 - * the energy of formation from the side-on complex $\Delta E_f(\text{propyl})$.
- For the approximated transition state structure:
 - * the β angle $\beta(\text{TS})$.

The values of the descriptors are plotted against the estimated barriers of insertion $\Delta E_{\text{est}}^\ddagger$ for runs one to three in Figure 9.3 to Figure 9.5.

On a first glance, it becomes evident that there is no clear dependence of the insertion barrier on any of the descriptors. To quantify this, (linear) Pearson's correlation coefficients were calculated and are compiled in Table 9.3. Within all test sets, the strongest correlations were found for $\Delta E_f(\text{propyl})$, the energies of the LUMOs $E_{\text{LUMO}}(\text{side-on})$ and E_{LUMO} , the N–Cr–N angles β and $\beta(\text{side-on})$ as well as the NMR shielding constants $\sigma_{\text{iso}}(\text{Cr})$ and $\sigma_{\text{aniso}}(\text{C})$. Overall, the correlations are very low – the correlation between $\Delta_f(\text{propyl})$ and the barrier being strongest with $R^2 = 0.104$, $R^2 = 0.211$ and $R^2 = 0.213$ for runs one to three, respectively. This correlation is in line with the Bell-Evans-Polanyi principle [192, 193], which states that a linear relationship between activation enthalpy and reaction enthalpy exists for a series of similar reactions. The more exothermic a reaction, the lower the activation enthalpy.

In the quest to find a quantitative structure property relationship (QSPR), which would hopefully allow the calculation of reaction barriers from reactant or product descriptors, a multiple linear regression was performed as reference. The seven aforementioned descriptors with the highest linear correlations from run three, which had the largest number of data points, served as input data. During regression, the angle β turned out to be insignificant (p -value of 0.2308) and was removed from the set of descriptors.

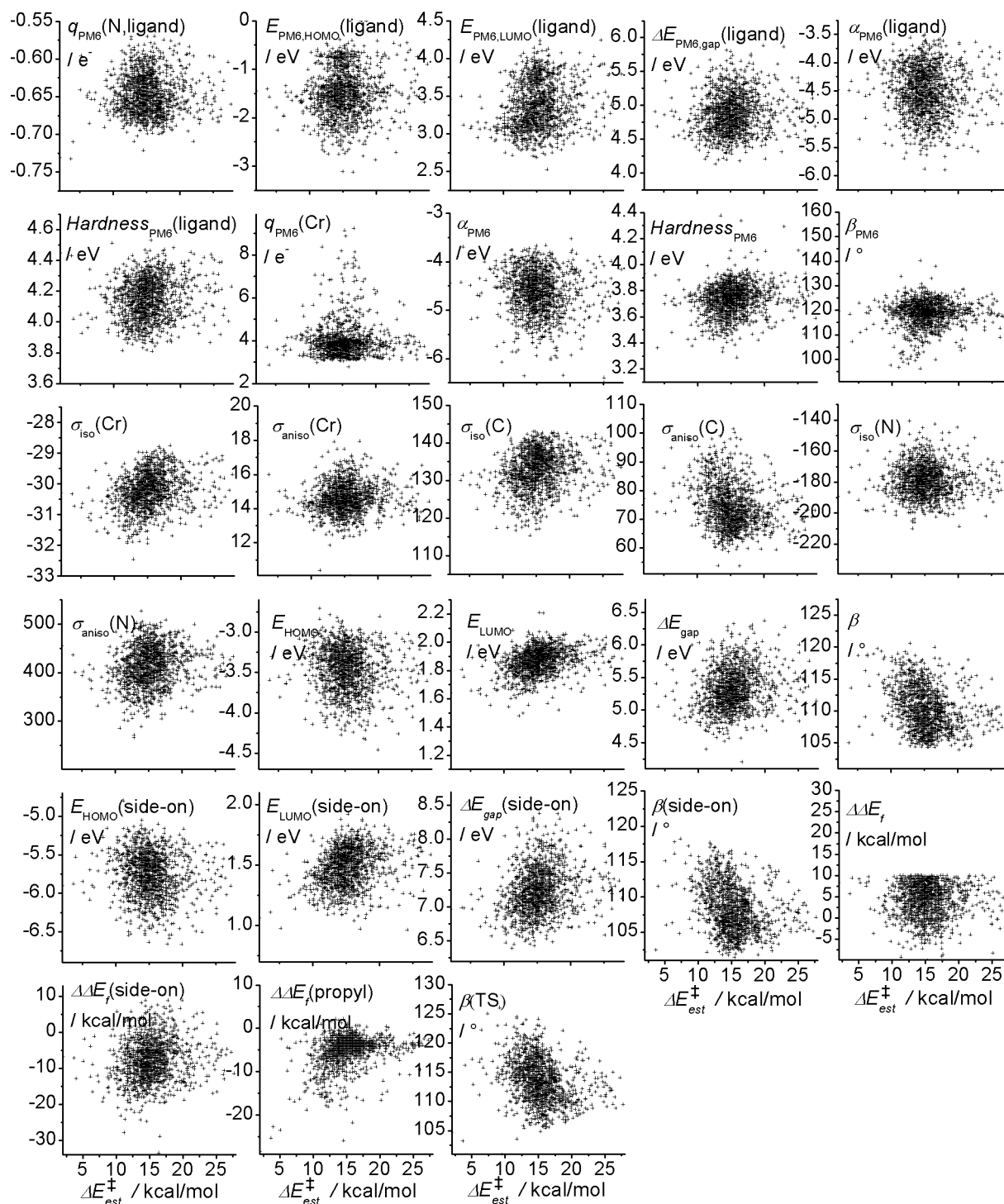


Figure 9.3. Values of the calculated descriptors for run 1 against the estimated barriers of insertion $\Delta E_{est}^{\ddagger}$. The isotropic NMR shielding constants $\sigma_{iso}(Cr)$ and $\sigma_{aniso}(Cr)$ are scaled by 0.01. For definitions of the variables see text.

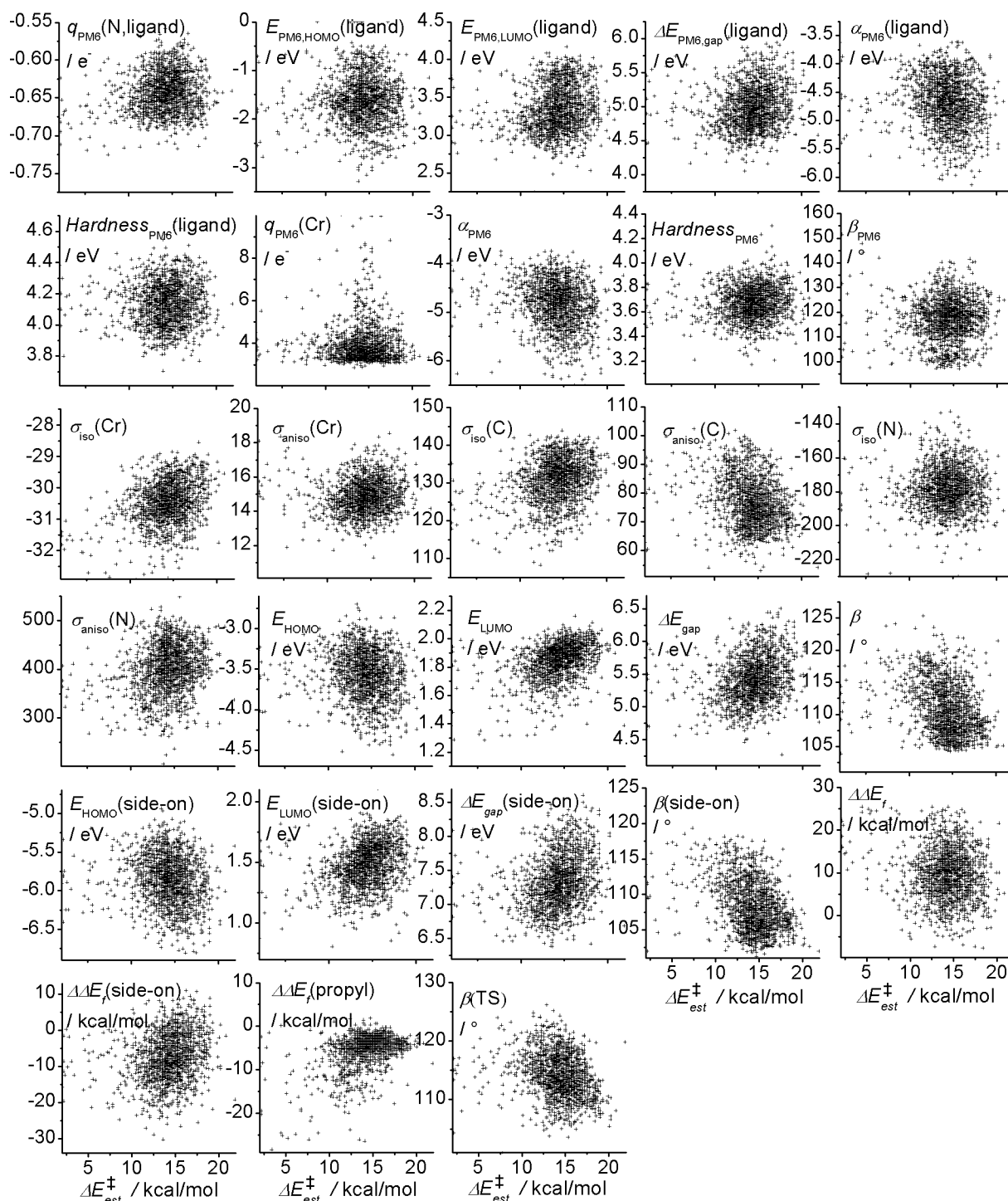


Figure 9.4. Values of the calculated descriptors for run 2 against the estimated barriers of insertion $\Delta E_{est}^{\ddagger}$. The isotropic NMR shielding constants $\sigma_{iso}(Cr)$ and $\sigma_{aniso}(Cr)$ are scaled by 0.01. For definitions of the variables see text.

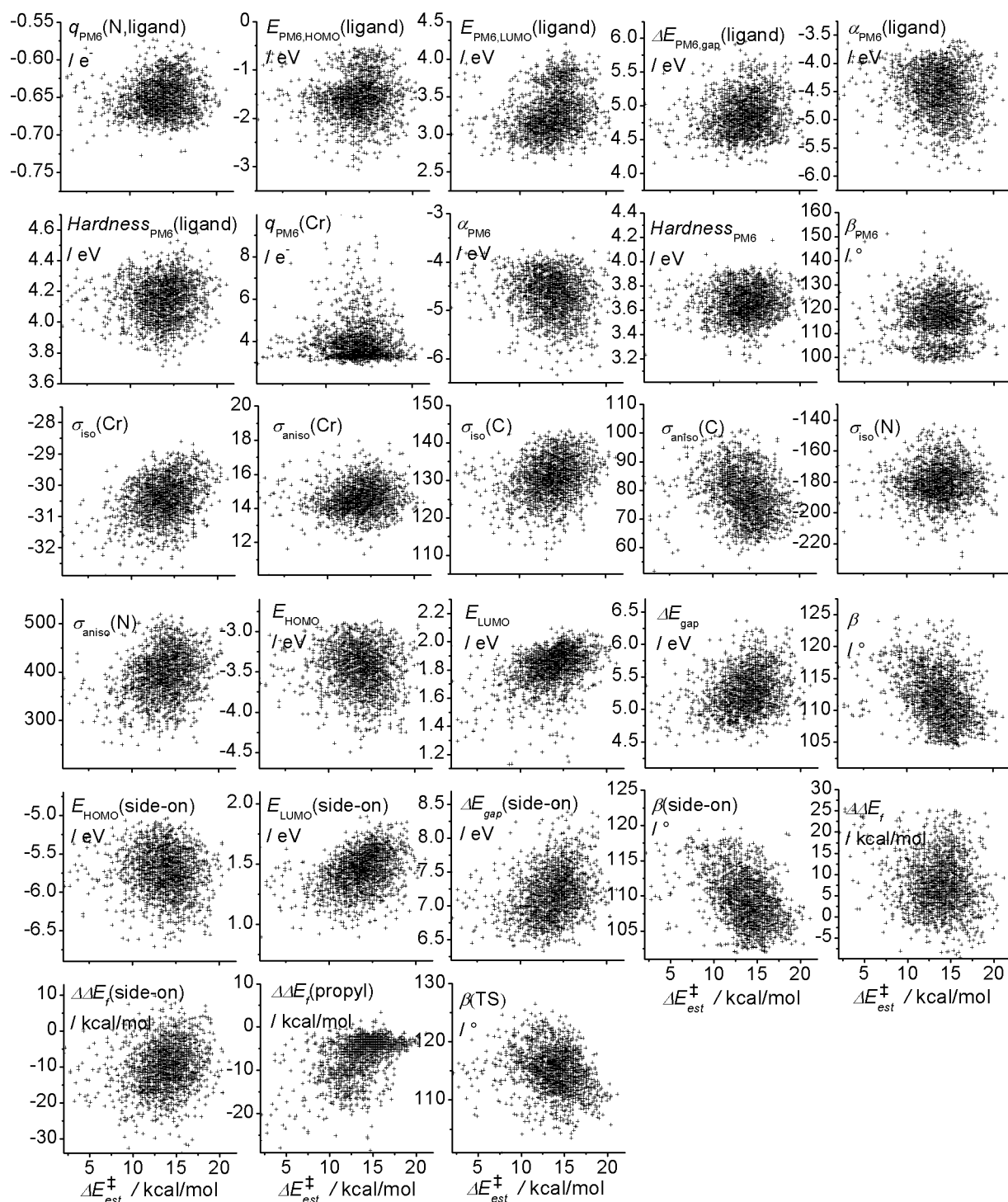


Figure 9.5. Values of the calculated descriptors for run 3 against the estimated barriers of insertion $\Delta E_{est}^{\ddagger}$. The isotropic NMR shielding constants $\sigma_{iso}(Cr)$ and $\sigma_{aniso}(Cr)$ are scaled by 0.01. For definitions of the variables see text.

Table 9.3.: Squared correlation coefficients R^2 for various parameters and calculated estimated barriers of insertion.

Parameter	R^2	R^2	R^2
	run 1	run 2	run 3
$q_{\text{PM6}}(\text{N,ligand})$	0.000	0.015	0.012
$E_{\text{PM6,HOMO}}(\text{ligand})$	0.003	0.000	0.004
$E_{\text{PM6,LUMO}}(\text{ligand})$	0.033	0.028	0.058
$\Delta E_{\text{PM6,gap}}(\text{ligand})$	0.010	0.019	0.025
$\alpha_{\text{PM6}}(\text{ligand})$	0.018	0.015	0.016
$\text{Hardness}_{\text{PM6}}(\text{ligand})$	0.001	0.003	0.005
$q_{\text{PM6}}(\text{Cr})$	0.005	0.000	0.002
α_{PM6}	0.022	0.029	0.026
$\text{Hardness}_{\text{PM6}}$	0.012	0.012	0.006
β_{PM6}	0.004	0.000	0.000
$\sigma_{\text{iso}}(\text{Cr})$	0.045	0.069	0.130
$\sigma_{\text{aniso}}(\text{Cr})$	0.007	0.002	0.010
$\sigma_{\text{iso}}(\text{C})$	0.031	0.058	0.061
$\sigma_{\text{aniso}}(\text{C})$	0.061	0.065	0.072
$\sigma_{\text{iso}}(\text{N})$	0.000	0.152	0.038
$\sigma_{\text{aniso}}(\text{N})$	0.021	0.047	0.003
E_{HOMO}	0.009	0.011	0.009
E_{LUMO}	0.105	0.130	0.171
ΔE_{gap}	0.031	0.050	0.066
β	0.080	0.093	0.119
$E_{\text{HOMO}}(\text{side-on})$	0.010	0.018	0.015
$E_{\text{LUMO}}(\text{side-on})$	0.076	0.056	0.142
$\Delta E_{\text{gap}}(\text{side-on})$	0.046	0.048	0.074
$\beta(\text{side-on})$	0.076	0.123	0.175
$\Delta \Delta E_f$	0.001	0.013	0.011
$\Delta \Delta E_f(\text{side-on})$	0.016	0.035	0.033
$\Delta \Delta E_f(\text{propyl})$	0.104	0.211	0.213
$\beta(\text{TS})$	0.075	0.053	0.055

Using the following Equation (Eq. 9.4)

$$\begin{aligned} \Delta E_{\text{est}}^{\ddagger} = & 35.7298 + 0.004995\sigma_{\text{iso}}(\text{Cr}) + 0.05217\sigma_{\text{aniso}}(\text{C}) \\ & + 2.302E_{\text{LUMO}} + 3.219E_{\text{LUMO}}(\text{side-on}) \\ & - 0.1680\beta(\text{side-on}) + 0.1966\Delta E_f(\text{propyl}) \end{aligned} \quad (9.4)$$

a correlation of $R^2 = 0.390$ could be achieved. A mean absolute error (MAE) of 1.58 kcal/mol is calculated for the prediction of the fitting set whereas the standard error is 2.06 kcal/mol.

The best QSPR can be a complicated formula depending on any of the descriptors. A possible approach is to first select the most important descriptors or construct artificial descriptors which represent a maximum of variance in the variables, as determined by for example a factor analysis or principle component analysis. In a second step a suitable correlation function is searched for, which could be determined, amongst others, by genetic programming. In here, simply the six descriptors, which were most strongly linearly correlated to the estimated insertion barriers, are taken and fed to a neural network. As the performance of neural networks depends on their topology and training, a number of three and four layer feed-forward networks with hyperbolic tangent activation functions was investigated. The values of each descriptor and $\Delta E_{\text{est}}^{\ddagger}$ from run 3 were shifted, such that the mean of the data was 0 and then scaled to map 2.5 standard deviations of the data to -1 and 1 in order to adapt to the input range of the networks. Then the data was split into a training set (1278 points) and a test set (421 points) by randomly selecting approximately 25% of the data-points as test set. The networks were created and trained with the following parameters:

- Network dimensions: 6-2-2-1 to 6-30-12-1 in steps of 2 for the first hidden layer and of 1 for the second hidden layer; 6-2-1 to 6-30-1 in steps of 2; 6-1-1 and 6-1 (a total of 182 different network topologies).
- Activation functions: linear for the input neurons, *tanh* for the hidden and output neurons.
- Bias neurons in each layer.
- Initial weights: (a) $[-0.75 \dots 0.75]$ or (b) $[-0.05 \dots 0.05]$.
- Learning algorithm: quickpropagation (QP) or standard backpropagation (BP).

- Learning rate: (a) 0.07 for QP or 0.007 for BP; (b) 0.7 for QP or 0.07 for BP.
- QP parameters: $\mu = 1.75$; weight decay = -0.0001.
- BP parameters: momentum = 0.
- Maximum epochs: 300000.

As final weight matrix the one producing the lowest mean squared error (MSE) in the test data was taken. The predicted $\Delta E_{\text{est}}^{\ddagger}$ values were correlated against the ones in the test set. Interestingly, the training method and the network topology had only small influences on the predictive performance as can be taken from Table 9.4. The strongest correlation found was $R^2 = 0.444$ for a 6-6-6-1 network. Indeed, R^2 obtained with the 6-1 network is already 0.417. Setting its output neuron's activation function to linear, the same correlation is found, indicating that nearly no improvements are achieved by using a non-linear model.

Table 9.4.: Squared correlation coefficients R^2 for predicted and calculated barriers $\Delta E_{\text{est}}^{\ddagger}$ for the best performing neural networks for each set of training parameters.

A	B	algorithm	parameters	R^2
^a		QP	(a)	0.417
28	8	QP	(a)	0.433
6	6	QP	(b)	0.444
26		BP	(a)	0.419
2	9	BP	(b)	0.434

A: number of neurons in layer 2,

B: number of neurons in layer 3,

^a: output function linear.

It can thus be concluded that feed-forward neural networks are not giving significant improvements over a linear model. The correlation between predicted and calculated barriers remains low with an R^2 of approximately 0.4. It is probable that the non-linear part in the dependence of the barrier on the six selected descriptors is low and a better QSPR can only be build by developing more sophisticated descriptors.

9.2.6. Selected Candidates

As outlined above, it was the goal to optimize imido chromium complexes towards activity and synthesizability. The three optimization sets were filtered for $\Delta E_f <$

10 kcal/mol and the ten best candidates with the lowest barrier of insertion were selected and listed in Table 9.5.

To generalize, a common pattern in the genetic code is sought. It has to be recalled that in run 1 emphasis was put on the synthesizability during optimization. Thus, during optimization different leading patterns should evolve compared to run 2 and 3 and the top performers listed in Table 9.5 are merely accidental findings. For runs 2 and 3 the frequency of occurrence of the "6_2" (run 3) or "2_6" (run 2) pattern in the first part of the chromosomes, which encodes isopropyl and phenyl substituents in ortho position, is marked. And even for run 1 this pattern can be detected in three out of ten samples. A relatively frequent occurrence of the methoxy substituent ("5") in ortho position can also be observed. Unique for run 1 is the occurrence of the methanesulfonyl ("7") group in combination with a small substituent (methyl or hydrogen).

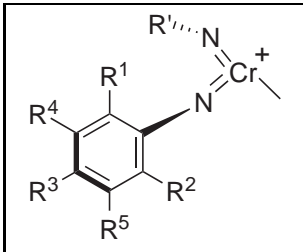
As to the other positions, no clear winning patterns can be identified. For the meta position, a combination of methoxy and trifluoromethyl substituents ("5" and "8") has evolved within run 2, but it can not be found frequently in the other runs. Interestingly, for run 1 the small substituents hydrogen and methyl ("0" and "1") are frequently present in meta position.

Analyzing the transition state structures of the most prominent candidates with ortho isopropyl/phenyl substituents, two stabilizing interactions were noted. The first is an aromatic π -H interaction found in 5 out of 13 transition states, the second an η^1 -chromium-phenyl interaction found in 7 cases.

The aromatic π -H interaction involves on the one hand the phenyl substituent, on the other hand the hydrogen atom. The latter belongs to the methyl ligand and is involved in an α -agostic interaction with the metal center in the transition state. Typical values for the chromium-hydrogen distance within these candidates are found to be around 1.96 Å, whereas the carbon-hydrogen bond is stretched to 1.15 Å as depicted in Figure 9.6. The distance of the agostic hydrogen to the center of the phenyl plane ranges from 2.27 to 2.40 Å. This is a remarkably small distance when compared to other π -hydrogen complexes which have been studied by Tarakeshwar, Choi and Kim.

Table 9.5.: Selected candidates from run one, two and three together with their estimated insertion barriers $\Delta E_{\text{est}}^{\ddagger}$ and energies of formation ΔE_f . The substituents are given as reference.

Code	$\Delta E_{\text{est}}^{\ddagger}$ / kcal/mol	ΔE_f / kcal/mol
run 1		
0_5_4_5_7	1.4	9.7
7_0_6_1_5	2.0	8.3
0_7_5_1_0	3.7	5.7
1_7_5_1_0	4.0	9.3
2_6_4_2_7	5.1	9.2
3_5_6_7_8	5.2	8.3
8_1_5_8_1	6.1	8.3
2_6_3_6_7	6.1	7.5
5_6_4_1_5	6.4	9.7
2_6_8_1_2	6.4	8.6
run 2		
2_5_5_5_8	5.1	6.1
2_6_4_5_8	5.1	8.6
5_6_7_7_7	6.7	5.8
2_6_6_4_8	6.7	6.9
2_6_4_8_8	7.4	5.1
6_2_0_5_8	7.4	8.3
2_1_5_3_8	8.1	3.7
2_6_4_7_2	8.1	3.5
2_3_5_5_8	8.4	5.8
6_8_0_5_1	8.6	5.6
run 3		
2_5_2_3_5	3.7	8.6
6_2_4_5_3	4.1	1.8
6_2_8_7_0	4.3	8.0
6_2_5_5_1	4.4	1.8
6_2_8_2_3	5.5	4.4
2_8_6_2_6	5.8	4.9
6_2_6_7_4	6.1	7.0
6_1_0_2_1	6.9	9.9
0_6_5_0_3	6.9	5.9
5_6_3_7_2	7.0	2.8



R	allele
-H	0
-Me	1
-i-Pr	2
-Cl	3
-F	4
-OMe	5
-Ph	6
-SO ₂ Me	7
-CF ₃	8

The authors have found for example for the HF-benzene complex a distance of 2.28 Å [194].¹ Based on the short distance a strong stabilizing interaction is anticipated.

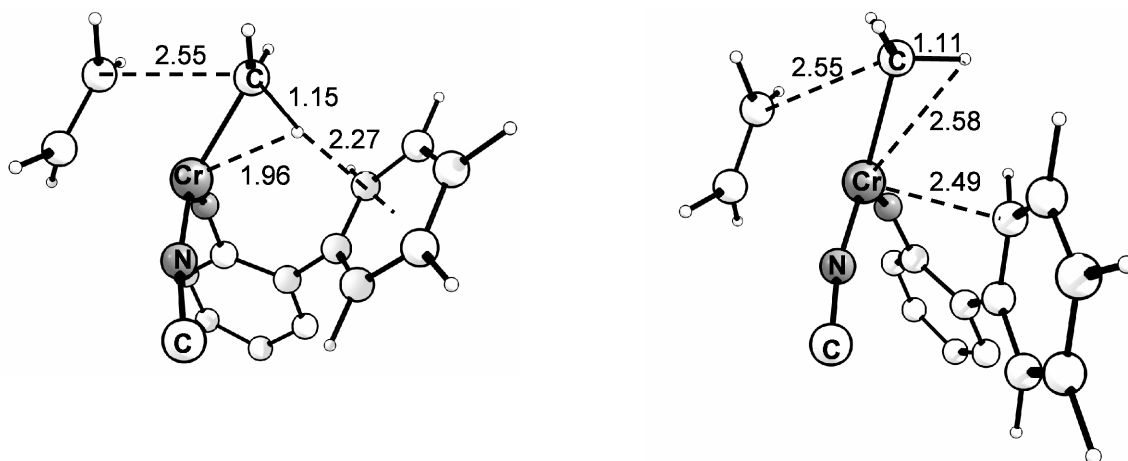


Figure 9.6.. Substructures of the candidates “2_6_4_8_8” (left) and “6_2_4_5_3” (right) transition state structures as examples for H- π and η^1 -stabilization. Selected distances in Å.

The Cr-C_{phenyl} η^1 -bond, as a second stabilizing interaction observed in the transition states, is characterized by a typical chromium-carbon bond distance of 2.49 Å and a sum of angles for the carbon-hydrogen and carbon-carbon bonds of 358.7°. It thereby shows an analogy to Wheland intermediates, found in electrophilic aromatic substitution reactions [195]. The α -agostic interaction has vanished, since the respective coordination site at the metal is blocked by the η^1 -bound ligand. The η^1 -bond can also be termed a δ -agostic interaction and leads to the formation of a six-membered ring.

Another secondary interaction related to the η^1 -type stabilization is observed in the candidates bearing a methylsulfonyl substituent in ortho position of their ligands. Here, the coordination site opened in the transition state is occupied by the binding of one of the methylsulfonyl’s oxygen atoms. An example is given in Figure 9.7.

¹ It is certainly clear that the description of these π -complexes by the use of PBE-D/def-SVP (all atoms involved in the interaction possess polarization functions) is problematic. Tarakeshwar *et al.* have pointed out that electron correlation is crucial to get a good estimate of electrostatic, induction and dispersion energies. They found that already MP2/aug-cc-pVDZ gives good results when compared to experimental and CCSD(T) values. To check, whether the PBE-D calculated values are at least within the same ballpark, the HF-benzene complex was optimized at both the PBE-D/def-SVP and the MP2/aug-cc-pVDZ level enforcing C_{6v} symmetry. The distance of the hydrogen atom to the center of mass of the benzene ring was found to be 2.08 Å for PBE-D and 2.19 Å for MP2. For the (electronic) binding energy -7.7 kcal/mol for PBE-D and -5.9 kcal/mol for MP2 were calculated. This good agreement gives rise to the conjecture that the PBE-D calculated stabilization by the H- π interaction in the transition states is at least reasonable.

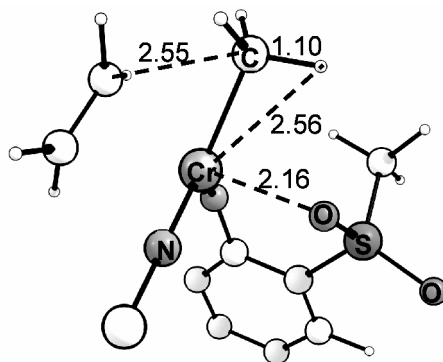


Figure 9.7. Substructure of the candidate “1_7_5_1_0” transition state structure as an example for a stabilization by secondary interaction with the methylsulfonyl substituent. Selected distances in Å.

9.3. Conclusions

Using genetic algorithms, it was possible to optimize substituted di(phenylimido) chromium complexes with respect to their predicted catalytic activities in the polymerization of ethene while retaining a relative ease in synthesis, which was calculated as the reaction energy for a transamination from the experimentally known reference complex' model 7_{Me} .

The optimization process turned out to be more demanding than the simple test optimizations used to derive suitable parameters for the system (see technical part, section 13.3). In run 1, when emphasis was laid nearly exclusively on the synthesis of the complexes, a steady increase in mean fitness was observed. Contrasting this finding, a fitness function offering a balanced incorporation of both synthesizability and catalytic activity presented problems to the optimization system when operated with the truncation selection algorithm and parameters in the standard range. From the Bell-Evans-Polanyi principle it can be foreseen that the latter fitness function should be more difficult to optimize. The more destabilized the side-on complex, the higher the energy difference to the product of insertion. Thus, the barrier for this step is predicted to be lower. But at the same time, it is harder to synthesize the side-on complex. Two trends that point in opposite directions of the fitness. If this relationship is existent, the optimization system has to optimize towards candidates which do not follow this principle and where the barrier is lowered by favorable interactions in the transition state. Although a number of good candidates were generated employing the truncation selection, a change to tournament selection with a higher selective pressure and comparable loss of diversity lead to a more steady increase in the population's mean fitness.

In the statistic evaluation, only weak correlations between calculated descriptors and the barrier could be found. Although the strongest was the one proposed by Bell, Evans and Polanyi, it was still weak with a squared correlation coefficient of only 0.1 to 0.2. A linear QSAR between the six descriptors most strongly correlated with the barrier could be derived, which offers a low correlation of 0.39 between predicted and calculated barriers. Only a slight improvement was achieved by using neural networks to model the QSAR.

Nonetheless, a number of patterns which induce favorable interactions to stabilize the transition state were identified from the analysis of the best candidates from all three runs. On the one hand isopropyl groups in combination with phenyl groups in ortho position of the phenylimido ligands lead to either H- π or η^1 stabilizing interactions. On the other hand methylsulfonyl groups in ortho position can coordinate to the metal center *via* their oxygen atoms and stabilize the transition state in this way.

Complexes bearing these substitution patterns can now serve as lead structures for the laboratory synthesis of potentially highly active catalysts.

Part V.

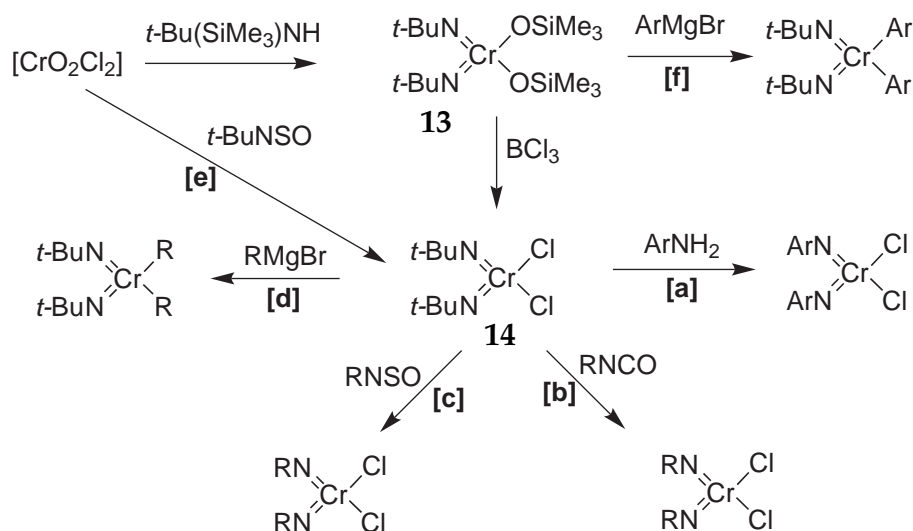
Approaches *in vitro*

10. Lead Syntheses

10.1. Goal and Approach

In chapters 8 and 9 catalysts have been computationally optimized toward activity in olefin polymerization. Experimental proof is desired for both their synthetic accessibility and catalytic activity to demonstrate the transfer of theoretically optimized catalyst to the real world. It was therefore the goal to find synthetic routes to some of the catalyst candidates.

A set of synthetic protocols to access diimido chromium complexes is known in the literature. Most of these routes shown in Scheme 10.1 start from the diimido di(trimethylsilyloxo) chromium complex **13**, which can be obtained by treatment of chromyl chloride with *t*-BuSiMe₃NH [144]. The complex can be transformed into its dichloro analog **14** by reaction with BCl₃.



Scheme 10.1. Possible routes to access diimido chromium complexes.

The further transformations include:

- [a] Imido-ligand exchange by transamination [168].
- [b] Wittig-like [2+2] exchange of imido groups with isocyanates [169].
- [c] Wittig-like [2+2] exchange of imido groups with sulfinylamines [136, 161].
- [d] Alkylation with Grignard reagents [169, 196].
- [e] Direct synthesis of the chloro complexes by reaction of $[\text{CrO}_2\text{Cl}_2]$ with sulfinylamines [136, 161].
- [f] Arylation of the trimethylsilyloxo complex **13** with Grignard reagents [197].

Although the synthetic methods are versatile, none of the routes is universal and the diversity of imido ligands for diimido dichloro complexes is limited. An overview of complexes with the known ligands is given in Figure 10.1.

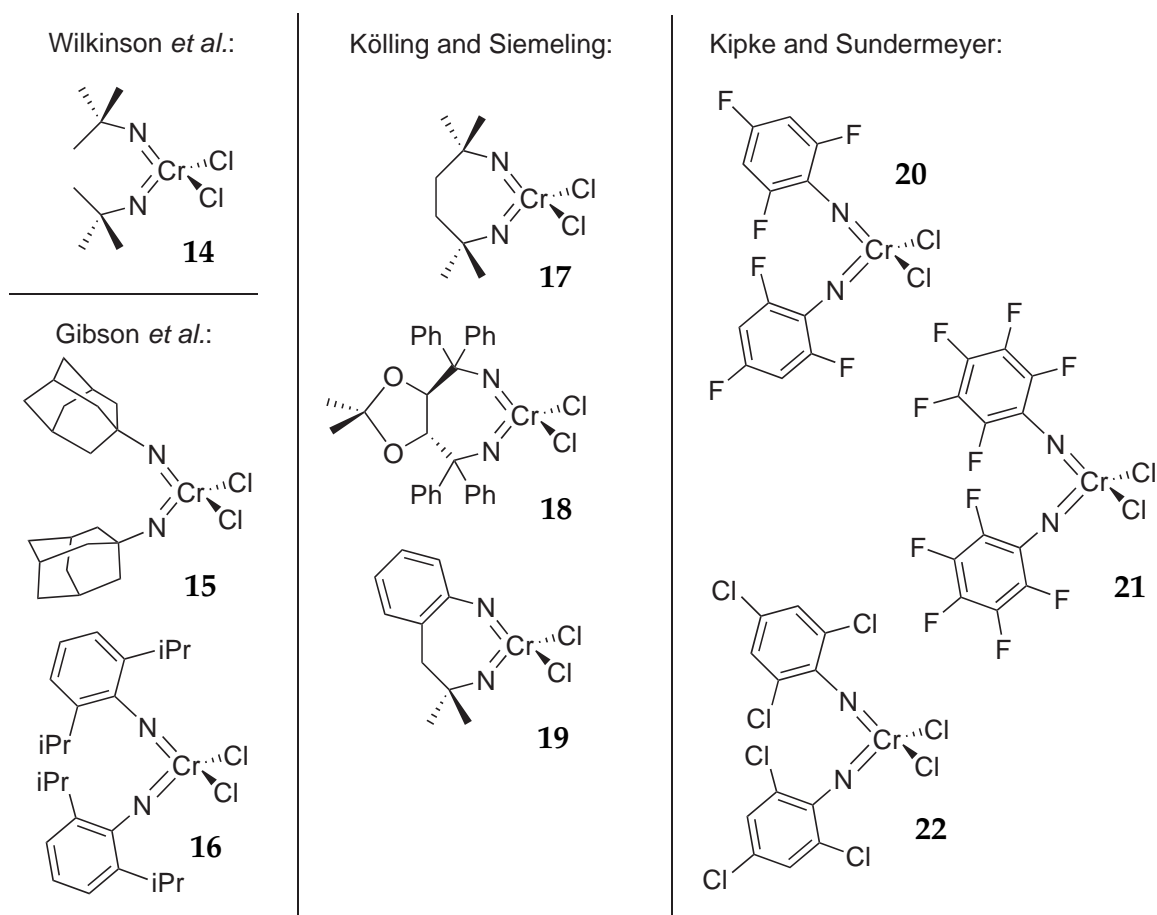


Figure 10.1. Diimido dichloro chromium complexes found in the literature.

The long known *tert*-butyl imido, adamantyl imido and 2,6-diisopropyl imido ligands as in the complexes **14**, **15** and **16** were augmented by Siemeling's and Kölling's series of chelate ligands used to construct **17**, **18** and **19** [57, 59, 198] and Sundermeyer's and Kipke's set of halogenated aryl imido ligands, which can be found in complexes **20**, **21** and **22** [136, 161].

In all known complexes, the α -carbon atoms of the imido ligands are either fully substituted as in **14**, **15**, **17** and **18** or members of a phenyl ring, which is usually itself substituted in α -position, as in **16**, **20**, **21** and **22**. Hence, a high steric demand of the ligands seems to be necessary to stabilize chromium(VI) complexes. Attempts made to introduce isopropylimido, phenylimido and chelate 1,2-bis(2-imidophenyl)ethene to access the complexes **23**, **24** and **25** (see Figure 10.2) all failed [198, and references herein], which was believed to be due to the low steric demand of the ligands. Moreover, the ligation is often unpredictable even for bulky ligands. Although it was possible to obtain the chelate complex **26** featuring a nine-membered ring, the complex **27** was inaccessible (see Figure 10.3) which could not be explained [198].

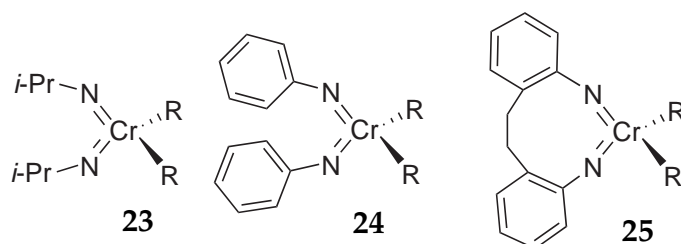


Figure 10.2.. Imido chromium complexes not yet synthetically accessed.

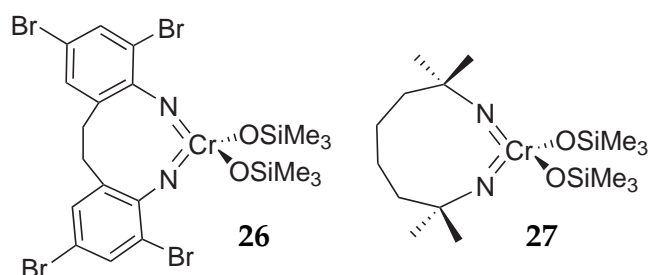


Figure 10.3.. Cyclic silyloxy chromium complexes with nine members in the ring.

In conclusion, high steric demand is anticipated to be important. From the optimizations described in part IV, one candidate from the group of fluoroethene polymerization catalysts and one candidate from the group of ethene polymerization catalysts was selected. As to the first group, the three candidates **K_A**, **K_B** and **K_C** were highlighted. While **K_C** features a very strained ligand system which renders

it thermodynamically the least accessible, the scaffold of \mathbf{K}_A was chosen since the alkyne-bridge in \mathbf{K}_B is susceptible to oxidation by Cr(VI) species [199]. It was anticipated that the introduction of more steric bulk would be necessary. Therefore, the target was not a precursor of the ligand of \mathbf{K}_A but the more demanding analog **1**, see Figure 10.4.

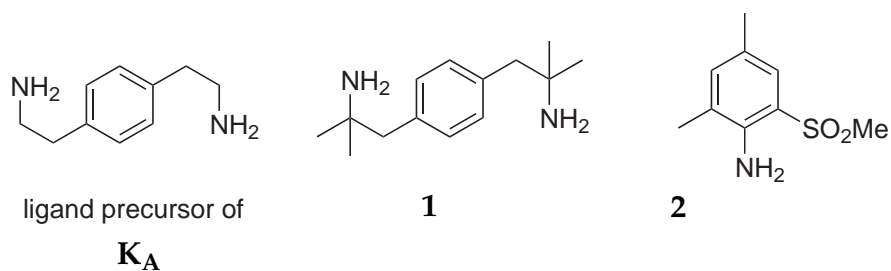


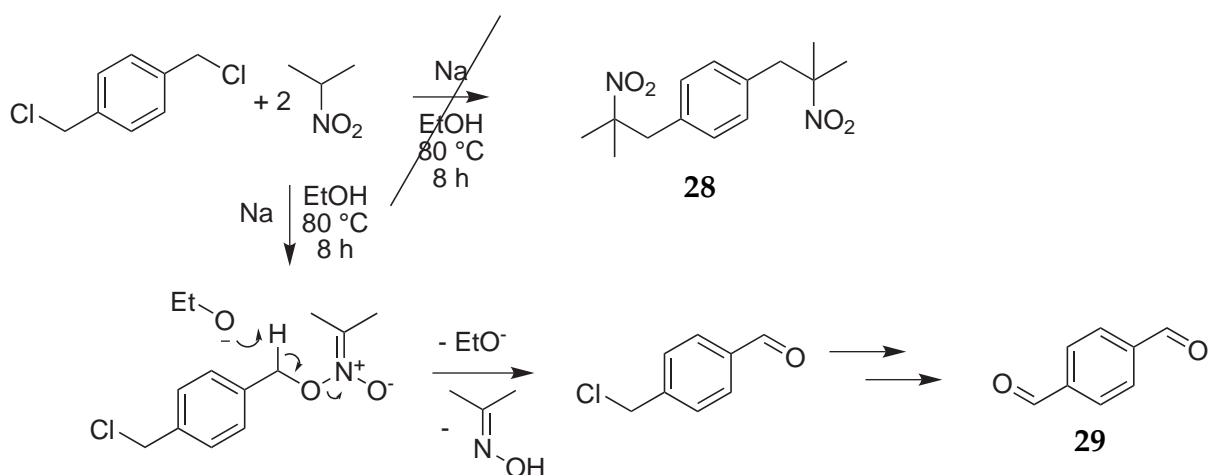
Figure 10.4. Targeted ligand precursors.

As to the second group, the introduction of a methylsulfonyl substituent seemed to be promising. A possible ligand precursor which also exhibits substitution in the second ortho position is the already known 2,4-dimethyl-6-(methylsulfonyl)aniline **2** (Figure 10.4) [200].

10.2. Syntheses of Ligands

10.2.1. 1,1'-(1,4-phenylene)bis(2-methylpropan-2-amine) (1)

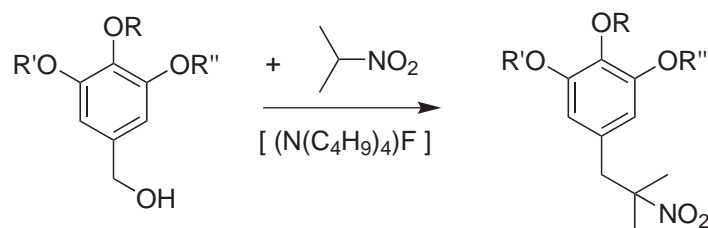
A possible approach to 2-methyl-1-arylpropan-2-amines is *via* their respective nitro precursors and subsequent reduction. Hass and Bender described the treatment of a series of benzyl chlorides with nitropropane under basic conditions [201] shown in Scheme 10.2.



Scheme 10.2. Reaction of 1,4-bis(chloromethyl)benzene with 2-nitropropane in the presence of a base.

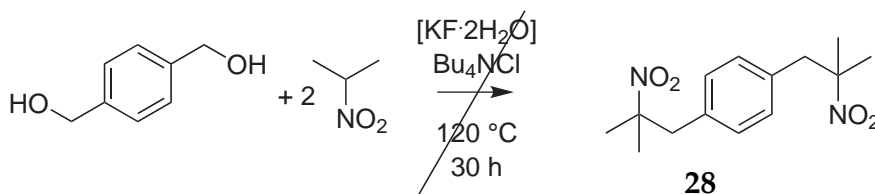
While C-alkylation led to the desired nitro products, O-alkylation afforded aldehydes as final products. Usually, strongly electron withdrawing substituents at the arylrings (i.e. one or more nitro substituents) favor C-alkylation. This route was tried by heating 1,4-bis(chloromethyl)benzene with an excess of nitropropane in a solution of sodium ethanolate in ethanol to access **28**. From this reaction the dialdehyde **29** could be isolated in good yield (83%). The product was identified by comparison of the $^1\text{H-NMR}$ spectrum with literature data [202]. The O-alkylation is assumed to proceed by formation of an instable nitronic ester, which breaks down into an oxime and the carbonyl compound [203].

The conversion of benzyl alcohols with 2-nitropropane into the desired nitro products (see Scheme 10.3) is a second route, first described by Renger [203]. He was able to prepare para hydroxy and para alkoxy substituted 1-(2-methyl-2-nitro)propanebenzenes by applying fluoride ion catalysis.



Scheme 10.3. Synthesis of substituted 1-(2-methyl-2-nitro)propanebenzenes by Renger [203].

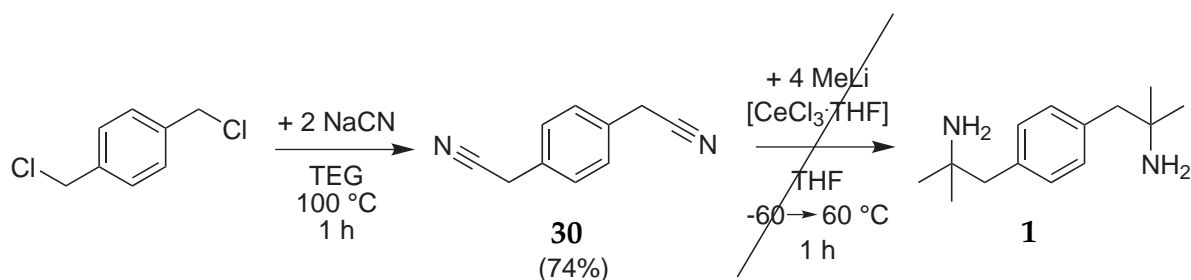
When applied to 1,4-phenylenedimethanol to hopefully obtain **28** (Scheme 10.4), this route led to the formation of a product mixture, which did not contain the desired product. This was indicated by the absence of methyl-proton signals in the raw product's $^1\text{H-NMR}$ spectrum, indicated by the absence of signals in the range from 0 to 2.5 ppm.



Scheme 10.4. Fluoride ion catalyzed reaction of 1,4-benzenedimethanol with 2-nitropropane.

Filtration of the dark brown raw product's solution in dichloromethane over a silica pad yielded a lightly yellow colored filtrate. The residue obtained from this did not show aromatic proton signals in the $^1\text{H-NMR}$ spectrum anymore, which had been present in the raw product's spectrum. Thus, the synthesis by fluoride ion catalysis of **28** was unsuccessful.

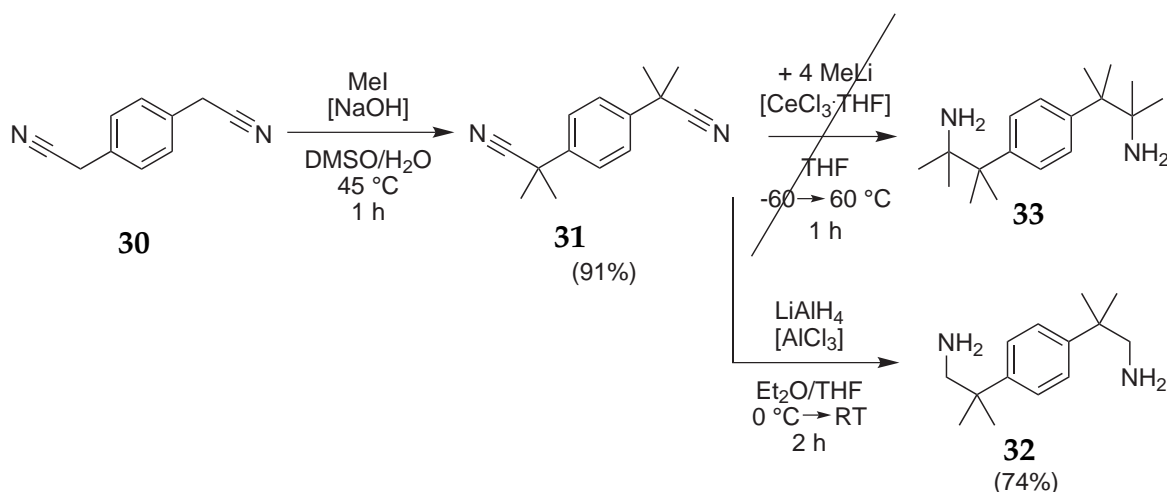
As these simple alkylations failed, an alternative was sought. The double addition of methyl lithium to nitriles to obtain tertiary carbinamines directly was described in the literature, but only for rare cases, for example with α -alkoxy nitriles [204]. By using organolanthanide reagents, especially ones prepared from cerium chloride, a much broader range of substrates could be used. Limanto, Dorner and Devine extended the protocol to substrates bearing relatively acidic α -protons, such as 2-phenylpropanenitrile [205]. These can not be treated for example with methyl lithium due to competing deprotonations [205]. It was attempted to react the dinitrile **30** at low temperatures with MeCeCl_2 prepared *in situ* following Ciganek's protocol [206] (see right hand side of Scheme 10.5).



Scheme 10.5. Reaction steps for the attempted quadruple addition of methyl lithium to the nitrile **30**.

The desired diamine could not be isolated by column chromatography after aqueous workup. The $^1\text{H-NMR}$ spectrum of the obtained residue exhibits a set of peaks ranging from 7.10 – 7.36 ppm. For the symmetrically substituted diamine **1** only a single signal would have been expected. Together with two peaks observed at 1.13 and 1.14 ppm, which could be associated with methyl protons, an asymmetrically substituted product is anticipated, which cannot correspond to the desired diamine.

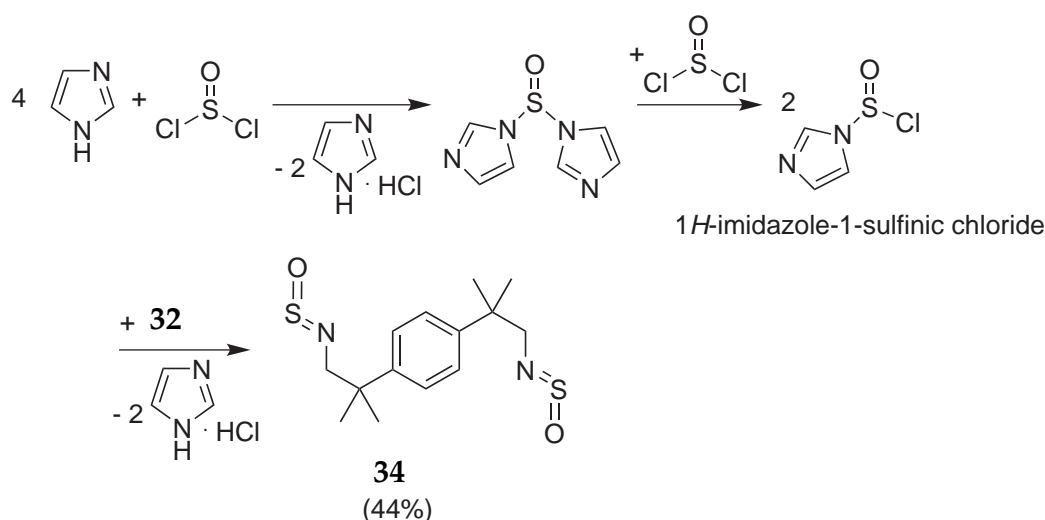
These setbacks led to the idea to block the $\alpha\text{-C}$ atoms of the dinitrile **30** through substitution by methyl groups to form **31** before further methyl addition. The novel dinitrile **31** was obtained in good yields (91%) by treating **30** with methyl iodide under basic conditions (Scheme 10.6). The quadruple addition of methyl cerium was unsuccessful though.



Scheme 10.6. Reaction steps for the (attempted) preparation of the diamines **32** and **33** from the dinitrile **30**.

A mixture of products ¹ was obtained, which was separated by flash column chromatography. In none of the fractions however, evidence for the desired diamine **33** could be obtained by ¹H-NMR spectroscopy. An absence of proton signals for methylene groups, expected in the range 2 – 4 ppm, was found for one of the fractions, but the aromatic signals scattered over a range from 7.0 to 7.5 ppm, which was not in accord with the expected single signal of **33**. Nonetheless, reduction of **31** lead to the diamine **32**. It was reported that arylacetonitriles cannot be reduced with mild reducing agents like H₂/palladium on charcoal [207], but this step was possible with a mixture of LiAlH₄ and AlCl₃. A protocol developed by Nystrom was applied [208]. In the resulting diamine **32**, obtained in 74% yield, the methyl ¹H-NMR proton signals observed at 1.28 ppm are shifted up-field from a value of 1.72 ppm for the educt **31** in CDCl₃, which is readily explained by the less electron withdrawing effect of an amino methylene group compared to a nitrile group. The diamine **32** features less steric demand than the originally intended preligand **1**, but it has the desired rigidity and spacing between the amino-functions and was thus accepted.

As described in section 10.1 (page 126), the introduction of new ligands to chromium(VI) complexes may proceed *via* transamination with the ligand in its amine form, [2+2] exchange as isocyanate or sulfinylamine, or synthesis from chromyl chloride and silylamine or sulfinylamine. Therefore, the conversion of **32** into its sulfinylamine and its silylamine was performed (see Scheme 10.7 and Scheme 10.8, respectively).

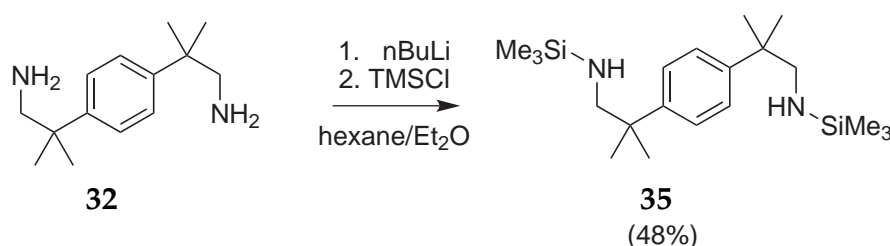


Scheme 10.7. Reaction steps for the preparation of **34** from the diamine **32**.

¹ Thin layer chromatography using triethyl amine/methanol (1:20) as solvent and silica gel as stationary phase revealed 3 UV-active fractions.

For the preparation of the sulfinylamine **34**, a protocol proposed by Kim and Shin was used, involving the generation of 1H-imidazole-1-sulfinic chloride, which converts the amine into the sulfinylamine [209]. By this method, the moisture sensitive sulfinylamine was obtained for the first time. The reaction is given in Scheme 10.7.

The bis(trimethylsilamine) **35** was accessed using a standard protocol involving the deprotonation of the diamine with *n*-butyl lithium and subsequent trimethylsilylation with trimethylsilyl chloride (TMSCl) as shown in Scheme 10.8.

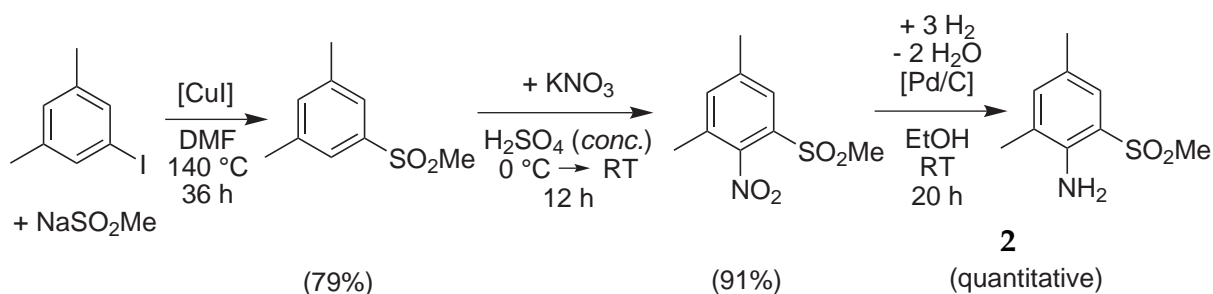


Scheme 10.8. Reaction steps for the preparation of **35** from the diamine **32**.

This reaction was carried out *in situ* for further reactions, but the silylamine was isolated once to verify its formation.

10.2.2. 2,4-Dimethyl-6-(methylsulfonyl)aniline (**2**)

The synthesis of 2,4-dimethyl-6-(methylsulfonyl)aniline (**2**) was described by Wu *et al.* [200] and is outlined in Scheme 10.9.



Scheme 10.9. Reaction steps for the preparation of **2** from 1-iodo-3,5-dimethylbenzene.

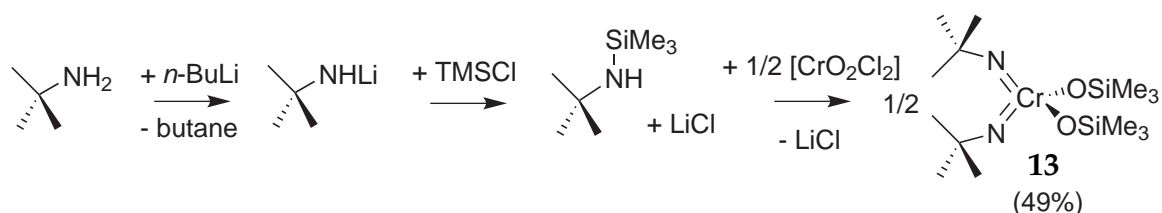
The final step in the original paper is the reduction of the nitro compound to the aniline by Zn/NH₄Cl, which proceeded with only low yields. Contact with air led to a rapid formation of a red colored oxidation product. The oxidation was reversible since the species could be reduced to the colorless aniline **2** with

H₂ employing Pd/C as catalyst. The latter reduction was employed for the further preparations of **2** because of the much easier workup, which involved only filtration and removal of the ethanol solvent *in vacuo*.

The conversion of **2** to a sulfinylamine as described for the diamine **32** was not successful. Only a partial conversion was observed as determined from the ¹H-NMR spectrum, where the characteristic peaks of **2** remained visible. A separation by means of silica-gel column chromatography was impossible because sulfinylamines are known to decompose under these conditions [209].

10.3. Attempted preparations of chelate diimido chromium(VI) complexes (**3** and analogs)

As chromium source either commercially available chromyl chloride [CrO₂Cl₂], or di(*tert*-butylimido)di(chloro)chromium(VI) and di(*tert*-butylimido)di(trimethylsilyloxo)chromium(VI) was used for all attempts described below. For the latter, a shortcut route was developed allowing the one-pot synthesis of the trimethylsilyloxo complex **13** from *tert*-butylamine, chromyl chloride and TMSCl (Scheme 10.10).



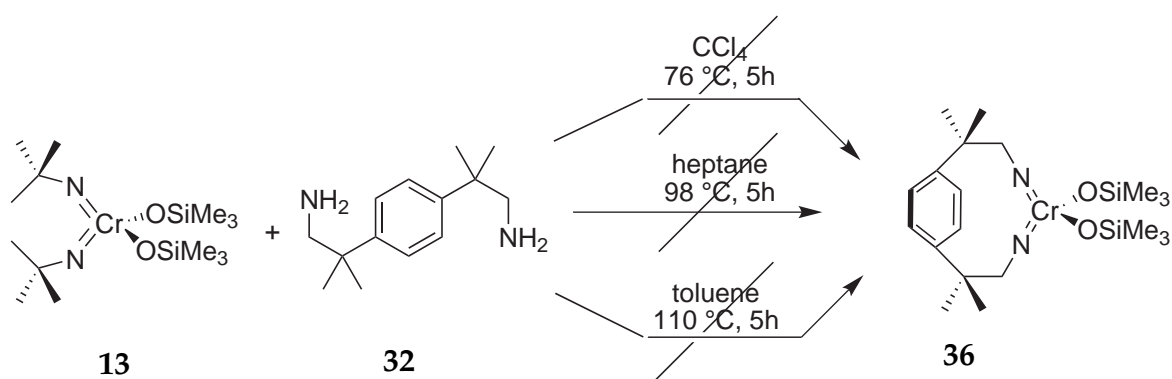
Scheme 10.10. One-pot synthesis of **13**.

It was found that after lithiation of *tert*-butylamine with *n*-butyl lithium and subsequent treatment with TMSCl, the precipitating lithium chloride does not interfere during the reaction with chromyl chloride. Instead it was filtered off after formation of the chromium complex **13**, which was then crystallized from hexamethyldisiloxane to afford the analytically pure compound. The overall yield of 49% compares favorably with the literature value of 54% [144]. The procedure allows the testing of small pro-ligand quantities, when their silylamines can not be purified.

10.3.1. Transaminations

Transaminations were attempted under various conditions employing both the chloro and the trimethylsilyloxo complex in analogy to Scheme 10.1. As *tert*-butyl amine has a boiling point of 46°C, it can readily be removed from the reaction mixture by distillation to shift equilibrium toward the product side. The experiments were usually conducted in resealable Teflon-tapped NMR tubes or small Teflon-tapped Schlenk tubes, so that the refluxing mixtures could repeatedly be subjected to an evacuation to remove the atmosphere. An overview of the applied conditions is given in Scheme 10.11 and Scheme 10.12. Generally, if the reactions were carried out in NMR-solvents the raw reaction mixtures were analyzed by ¹H-NMR spectroscopy. Otherwise, the mixtures were filtered through a plug of glass-fiber, dried *in vacuo* and dissolved in the NMR-solvent for subsequent analysis.

The reactions of the trimethylsilyloxo complex **13** with **32** were carried out by adding the dissolved amine slowly to the deep red solution of the metal complex. As solvents tetrachloromethane, heptane and toluene were tried because of their relatively high boiling points, which would allow for the distillative removal of *tert*-butylamine. No instantaneous color changes were observed upon addition of the amine, however. The mixtures were heated for 2 hours close to the boiling point of the respective solvent and the atmosphere was repeatedly removed every 10 to 15 minutes by evacuation to remove eventually generated *tert*-butylamine. An overview of the attempted reactions is given in Scheme 10.11.



Scheme 10.11. Attempted transaminations from the trimethylsilyloxo complex.

The ¹H-NMR spectra exhibited very broad peaks as shown exemplarily for the product of the reaction in heptane in Figure 10.5. Although peaks are observed which could belong to the educt complex **13** and the amine **32**, the absence of any splitting patterns and the impossibility to define reasonable integrals made a structure determination impossible. Attempts to isolate **37** failed.

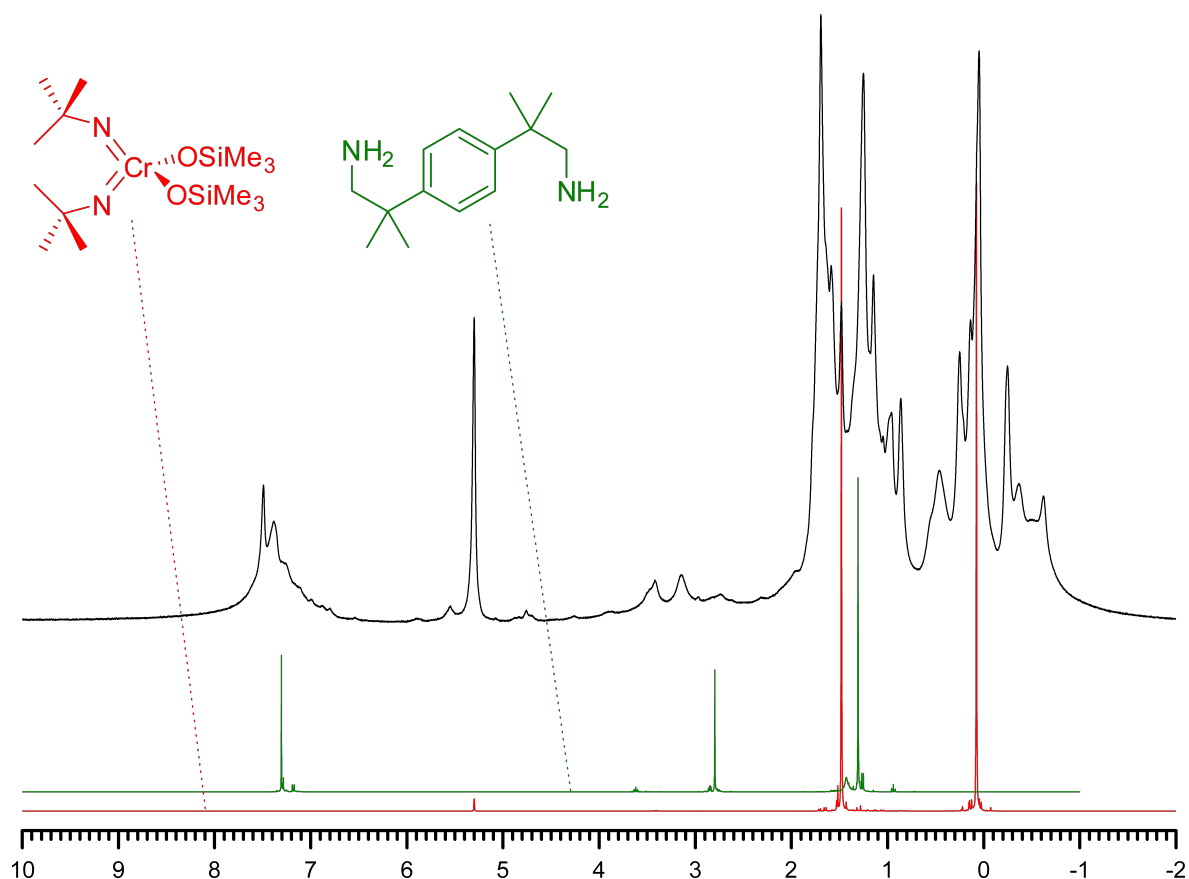
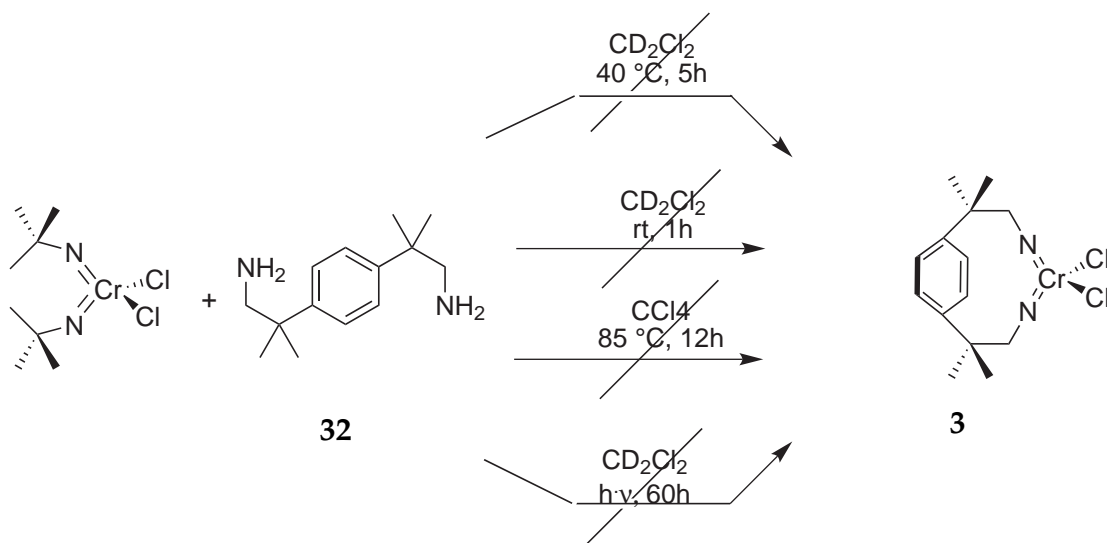
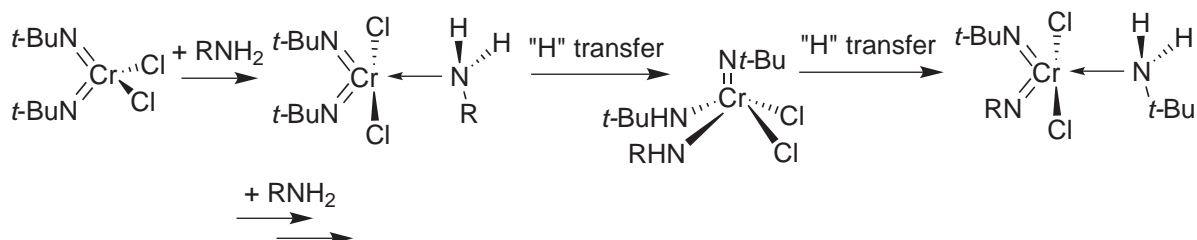


Figure 10.5. Exemplary $^1\text{H-NMR}$ spectra for the attempted synthesis of **38** by reaction of **13** with **32**. Spectrum of the pure educt complex **13** in red, of the diamine **32** in green and of the product in black. All values in ppm.

Notably, when the diamine **32** was slowly added to a stirred, dark red solution of the dichloro complex in dichloromethane, the color changed to yellow as the addition was half finished and turned red-brown after the addition was completed. Within minutes after the start of the addition, precipitation of a brown compound was observed and resolution was not achievable by further heating for extended periods (12h). Nonetheless, prior to heating a broad signal at about 11.7 ppm is observed in the $^1\text{H-NMR}$ spectra. The proposed mechanism of the transamination is shown in Scheme 10.13 [168]. The observed signal at 11.7 ppm is in agreement with the chemical shift for an amido hydrogen of one of the intermediate products, based on a reported shift of 11.84 ppm for the respective hydrogen in the chromium(VI) amido complex **39** (Figure 10.6) [168]. To find proof for the formation of an imido complex, it was tried to isolate the species by crystallization, but no crystalline material could be obtained.



Scheme 10.12. Attempted transaminations from the chloro complex.



Scheme 10.13. Proposed mechanism for the transamination reaction.

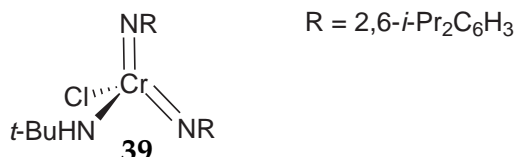
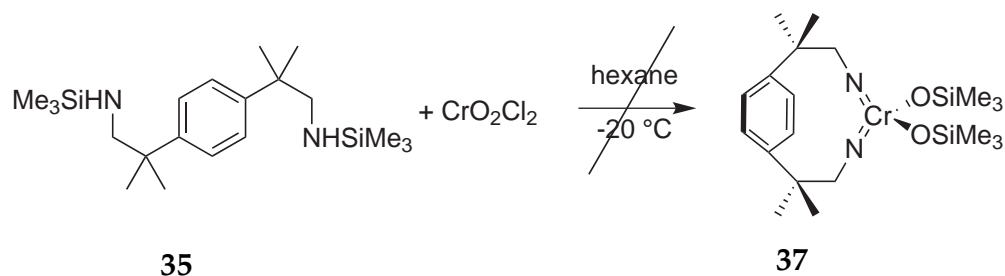


Figure 10.6. The amido chromium(VI) complex **41** synthesized by Coles *et al.*

10.3.2. Synthesis from the trimethylsilylamine **4**

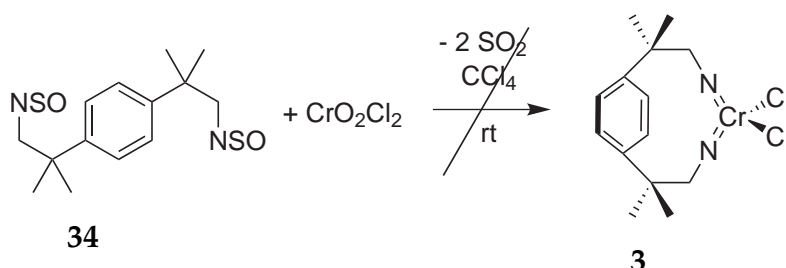
Upon addition of chromyl chloride to a solution of the *in situ* prepared trimethylsilylamine **4** (Scheme 10.14) in hexane at -20°C , a color change was observed from red over brown and to gray and a precipitate formed. The gray precipitate was insoluble even in the more polar solvent dichloromethane and could not be investigated by NMR. If an imido complex had formed, its decomposition occurred so readily that no product **37** could be isolated.



Scheme 10.14. Attempted synthesis of **37** by reaction of the silylamine **4** with chromyl chloride.

10.3.3. Synthesis from sulfinylamine

The reaction of sulfinylamines with chromyl chloride is attractive, since it allows for the direct synthesis of di(imido)di(chloro) complexes as shown in Scheme 10.15 with the release of sulfur dioxide. However, attempts to obtain complex **3** by this route failed. A mixture of chromyl chloride and **34** in CCl_4 turned from red to colorless with concomitant formation of a gray precipitate within 5 minutes at room temperature. Because of its insolubility further analysis was not carried out.

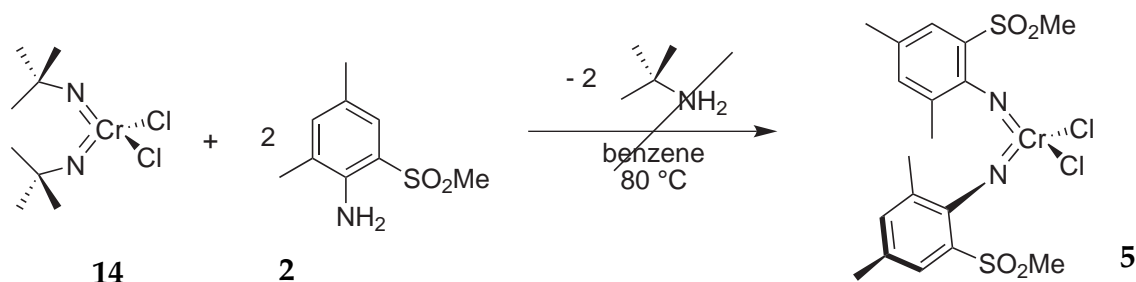


Scheme 10.15. Attempted synthesis of **38** by sulfinylamine metathesis.

10.4. Attempted preparations of the phenylimido complex di((2,4-dimethyl-6-methylsulfonyl-phenyl)imido)di(chloro)chromium(VI) (**5**)

Since the amine **2** was at hand (Scheme 10.16), the transamination was investigated.

Heating the deep red chloro complex **14** with **2** in benzene to 80°C for extended periods yielded in the formation of a brown precipitate. While the integral over



Scheme 10.16. Attempted synthesis of **5** by transamination.

the *tert*-butylimido group's signal at 1.23 ppm was reduced over time compared to the solvent residual signal and to the other signals in the mixture, the $^1\text{H-NMR}$ spectrum provided no evidence for a clean transformation. Notably, small signals at 11.55 ppm and 13.7 ppm were observed after 5 days reaction time, but they vanished during the course of the reaction. These signals could give a hint to the intermediate formation of amido complexes as discussed above for the reaction of **13** with **32**. The overall very broad peaks in the recorded $^1\text{H-NMR}$ spectra allowed no further clear assignment of the peaks to individual protons. Already at room temperature the formation of a precipitate is observed from a solution in benzene after about 30 minutes. As alternative, photolysis at room temperature of a solution of the educts in dichloromethane was tried. In this solvent no precipitation was observed. Typically, 5 mg of the complex **14** were dissolved in 0.5 mL dichloromethane and an equimolar amount of **2**, dissolved in the same solvent, added. The deep red reaction mixture was irradiated using a HPK 125 W mercury lamp. The light was filtered through 3 cm of a 2M sodium nitrite solution to remove light in the UV range. After 7 days, only the starting materials were still present as determined from the absence of any new signals in the $^1\text{H-NMR}$ spectrum.

10.5. Conclusions

The synthesis of new di(imido)chromium(VI) complexes has proved to be a difficult task. The preparation of the chelated complex from **32** was anticipated to be challenging due to the strain which would be introduced. Its complex has been estimated to be ≈ 8 kcal/mol less stable, compared to the di(*tert*-butylimido)di(methyl)chromium(VI) reference, as derived from its analog detailed in chapter 8. Second, its steric demand is less pronounced than any of the known imido ligands. As previously noted [145, 198] sterics play an essential role in the stabilization of diimido chromium(VI) complexes.

Although transamination is an established method for the preparation of di(arylimido) complexes [198], its application to **2** failed. Overall, di(imido)di(chloro)chromium(VI) complexes seem hard to approach, which is reflected by the very limited number of examples known in the literature.

Part VI.
Experimental Part

11. Computational Details

Density Functional Theory Calculations

Fluoroolefin Polymerization Catalysts

Geometry optimizations of all structures in this thesis were performed using gradient-corrected density-functional theory (DFT) in C1 symmetry if not noted otherwise. For the initial investigations of the model system **1S** (see page 42) exchange and correlation was treated by Becke's and Perdew's BP86 functional [85, 87, 210], a self-consistent-field (SCF) convergence criterion of $10^{-6} E_h$ and the standard grid (m3) for numerical quadrature was used [211]. Basis sets of triple- ζ quality with polarization functions (def-TZVP) were used for chromium and fluorine atoms, basis sets of double- ζ quality (def-SV(P)) for all other atoms [212]. All energy and gradient calculations during optimizations were carried out using the TURBOMOLE V5.10 suite of programs [213] within the multipole accelerated RI-J approximation (MARI-J) [214]. The geometry optimizations were driven by Gaussian 03 [215] using the Berny algorithm employing redundant internal coordinates and standard convergence criteria. As interface between Gaussian and Turbomole served a PERL-script by Katrin Wichmann.

Single point energy calculations for BLYP [85, 88], BP86 [85, 87, 210], PBE [83, 84], TPSS [90], BHLYP [85, 88], B3LYP [79, 88, 94, 95], PBE0 [96], TPSSh [90, 97] and B2PLYP [101] were performed using TURBOMOLE V5.10. Basis sets were def2-TZVPP for all atoms. The gridsize was increased to m4, the SCF convergence criterion lowered to $10^{-7} E_h$. For the double hybrid functional the MP2 correlation energy was calculated using the rimp2 program.

For B2KPLYP [216] and mPW2PLYP [102] energy calculations were performed with ORCA V2.6 [217], using the def2-TZVPP basis sets, the RIJCOSX approximation [218] with def2-TZVPP/J auxiliary basis functions and a tight SCF convergence threshold. M06 [91] calculations were performed with JAGUAR V.7.6.110 [219] employing triple- ζ quality basis sets denoted as TZV**.

Structure optimizations for all other than the model system as well as during the angle scanning experiments were performed with the PBE functional and Grimme's revised dispersion correction (PBE-D2) [83, 84, 163].

Ethene Polymerization Catalysts

Structure optimizations and energy evaluations were performed with Perdew's, Becke's and Ernzerhoff's PBE functional [83, 84] used together with Grimme's revised dispersion correction (-D) and the COSMO method. For the latter the dielectric constant $\epsilon = 2.4$ (toluene solvent model) was chosen. Basis sets were def-SV(P) for the part of the ligands extending beyond the amido nitrogen atoms and def-SVP for all other atoms. The quantum mechanical calculations were performed with Turbomole V6.20 using the standard grid (m3) and an SCF convergence criterion of $10^{-6} E_h$. The geometry optimizations were driven by Gaussian 03, employing the Berny algorithm, redundant internal coordinates and standard convergence criteria. As interfaced to Turbomole served a script by Karin Wichmann.

Wavefunction Theory Calculations

Single reference wave function theory calculations (CCSD(T), CCSD, HF) were performed using MOLPRO version 2008.1 [220] employing standard convergence criteria. The cc-pVTZ-DK and aug-cc-pVTZ-DK basis sets [221–223] were received from the EMSL basis set exchange [224, 225]. Multireference calculations were done with the MOLCAS program suite in version 7.2 or 7.6 [226–228] using the built in ANO-RCC [229–231] basis sets and the Douglas-Kroll Hamiltonian. The basis sets were truncated to quadruple- ζ plus polarization quality for the calculations involving *gem*-difluoroethene (**1S**) and to triple- ζ plus polarization quality for the calculations involving the cationic **8** and ethene.

12. Random Construction

12.1. Angle Scanning

During the angle scanning experiment, the N–Cr–N (β) and the Cr–N–C (α) angles were fixed to various values to study their influences on the activity and selectivity of the polymerization catalyst. The transition state structures were optimized in the following way. The transition structures of the fully optimized model system **1S** were taken and α and β angle were altered by the definition of the respective redundant internal coordinates in the Gaussian input. These were the two α angles Cr–N–H and the β angle N–Cr–N; additionally the ligands were forced to stay in plane by a H–N–N–H dihedral angle of 0° to prevent rotation around the Cr–N bonds. No symmetry constraints were imposed, but the two α angles were always kept identical.

In a first step coordinates related to the reaction under consideration were held constant. This were a) the bond distance of the joining carbon atoms for 1,2 insertion, and b) the carbon fluorine bond distance of the bond involved in β -F elimination. Then a preoptimization was performed. In the second step the Hessian matrix of the transition state for the model system **1S** was used to guide the optimization and was not computed for two reasons. First, a force-derivative computation on top of the unoptimized structure might lead to more than one negative Eigenvalue in the Hessian matrix. This would require an algorithm to determine which Eigenmode to follow during optimization, complicating things unnecessarily. Second, computation time would be increased. The Hessian matrices obtained by force-derivative calculations with Turbomole for **1S** (transition states [**1S–2S**] ‡ and [**2S–3S**] ‡) were converted to Gaussian input by the `tf2gf` script. The optimization to the transition state structure was performed without testing for more than one negative Eigenvalue of the Hessian matrix using the Berny algorithm in Gaussian 03 [215].

12.2. Candidate Construction

To screen a large number of potential catalysts a fully automatic screening system was set up. It was implemented in PERL and ran on an Intel Core2 standard PC under Linux 2.6. DFT calculations were passed to the Sun Grid Engine queueing system of the *quantix* computer cluster.¹

¹ For a description of the computational environment see appendix.

The MM2 force field [232] was used as implemented in the TINKER program V 4.2 [233–238]. The tetrahedral chromium atom was treated as a sp^3 -hybridized carbon atom for these calculations.

For the PM6 method [178] MOPAC 2009 [239] was used.

13. Genetic Algorithm: ChemScreen-GA

In this section, the details of the implementation of a genetic algorithm and adaptation to a working group cluster will be described. The coding is performed in the PERL language because it features high flexibility and has extensive text processing capabilities needed to evaluate the quantum chemical programs' output. Due to its script like structure, it is easy to learn and has a large collection of third-party modules available.

In the program system genes are represented by numbers. Within a chromosome each gene, which represents for example a substituent, can be written as integer value in the range [0 . . . 899]. To give a simple example, in a chromosome containing three genes for which 0 = (-H), 1 = (-Me), 2 = (-Ph), the chromosome 1_0_2 would represent (-Me), (-H), (-Ph).

13.1. Selection Method

Traditional genetic algorithms are round based, meaning that a number of candidates are created, their fitnesses are evaluated and parents are selected to breed a new number of candidates for the next round [109, 240]. For the optimization of molecular systems with higher level quantum chemical methods this mode is not feasible. The variation in the time spent to evaluate each individual is large. The size of the candidate can vary which leads to different run times for e.g. geometry optimizations of the candidate and its property calculations. Convergence problems for both the geometry and the electronic wave-function can enhance the problem. These facts would lead to long idle times on the computational resources when the system is waiting for the last candidates of the round to be finished.

A typical usage profile for working group computer clusters shows in our experience peaks during daytime, while a lot of idling is found during the night and in holiday seasons. A constant 100% load would be ideal but it is recognized that the users appreciate close to interactive calculations, i.e. jobs submitted to a queueing system should be executed instantaneously. Therefore, jobs are submitted with a high (UNIX) nice level from the automatic optimization system to an additional queue, which lets them run in the background of all other queues' jobs. This allows to catch close to every free CPU cycle while not interfering with standard jobs. The drawback is that jobs may have vastly different run-times depending on whether their queue slot was occupied or not. This has to be accounted for in the optimization algorithm.

The run-time problems are faced with the following methods. Firstly, a steady state update of the population is used. This means, every time an individual is fully optimized and its fitness calculated, it is added to the population pool where a definable number n_{pop} of individuals are kept. It always contains the youngest children by the time their calculation finished. From this pool parents for the next generation are selected. Secondly, all calculations required to compute an individual's fitness are split in many small jobs. Therefore, every single DFT geometry optimization task is submitted separately to the queueing system to increase the chance of a fair distribution between occupied and empty slots.

Furthermore, run-times are stored in the database. Larger chemical systems will have longer run-times than smaller ones. This generates on purpose an evolutionary force towards smaller systems because the large systems will be added later to the parent's pool than smaller ones thus lowering their chance to be selected as parents. In case two candidates differ from each other in a remote and unimportant site but are equally fit, the smaller of the two will reproduce more rapidly and the optimization will work more efficiently spending less time on unnecessarily large systems. In case a reevaluation of an individual's fitness is requested during the global optimization, its data is read from the database but it is re-added to the pool only after the stored run-time has elapsed.

For the actual selection of parents from the population pool, both a truncation based and a tournament based algorithm were implemented.

Truncation selection For the truncation selection, the actual population is divided into a fitter and a less fit part. The cutoff value effectively equals $T = 0.5$ in all cases below: half of the population is drawn to be potential parents. From these potential parents, each time new candidates have to be created, two individuals are randomly selected for mating. It has to be clarified that within this implementation, T is defined as the ratio of potential parents n_{parents} to the population size n_{pop} : $T = \frac{n_{\text{parents}}}{n_{\text{pop}}}$. At the beginning of the global optimization no potential parents exist since no individuals have been created yet. Then, the genetic code of the candidates is read from a predefined list or created randomly. When the number of evaluated candidates approaches the number n_{parents} , the effective cutoff value approaches 1 ($T \rightarrow 1$) since the best n_{parents} individuals constitute the actual population. As the number of evaluated candidates grows larger, T approaches its final value, which is reached when the number of evaluated candidates becomes larger than the population size (n_{pop}).

Tournament selection In tournament selection a number of t individuals are randomly chosen from the population whenever a parent is needed. To achieve this, a list of the population is created and an index is assigned to each member. Using PERL's `rand()` function t indices are computed and the respective individuals copied to the tournament pool. From this pool of t , the fittest is selected. Again, the problem arises that at the beginning of the optimization less than n_{pop} individuals have been evaluated. Let n_{eval} be the number of already evaluated candidates. The implementation is such that new parents are selected from the population with a probability p of

$$p = \frac{n_{\text{eval}}}{n_{\text{pop}}}$$

At the beginning the probability is zero ($p = 0$); thus all parents are taken from a predefined list or are created randomly.

Although it has been outlined in chapter 2 that a statistic universal sampling (SUS) would provide a close match of the expected to the actual fitness distribution after selection, this algorithm is not implemented. The algorithm requires the creation of whole generations at once, whereas candidates are created continuously in the system described here. This means every time one calculation is finished a new candidate is created.

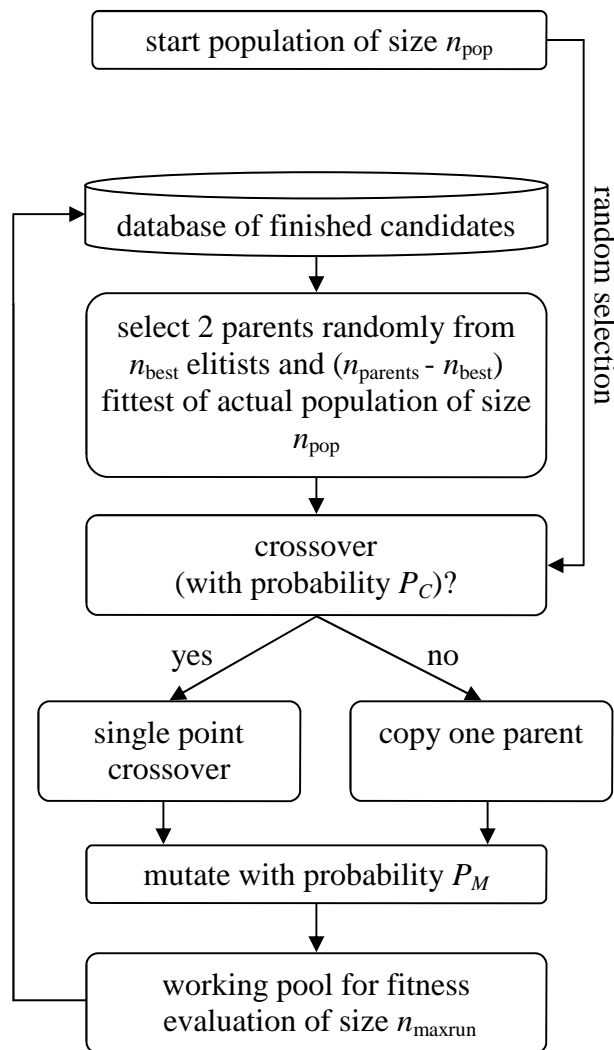
13.2. Logic and Data Handling

An overview of the optimization procedure for the case of truncation selection is given in Scheme 13.1, which is in close analogy to a standard genetic algorithm described in chapter 2.

The program system consists of two main routines split in two PERL programs: `creator.pl` and `runner.pl`; `creator.pl` creates new individuals employing genetic algorithms, whereas `runner.pl` handles the submission of calculation tasks and evaluates fitnesses. Relevant configuration parameters are read in from a file "GA.conf". The flow chart in Scheme 13.2 illustrates the interactions.

Information about individuals is stored in a MySQL database, which is interfaced by a set of routines in the `Chem::DBaccess` module. `Chem::DBaccess` was written to make data handling effective. The actual communication with the database makes use of Bunce's DBI [241] and Galbraith's `DBD::mysql` [242] modules. The program `creator.pl` reads the number n_{run} of individuals currently under investigation

from the database. If this number is smaller than a predefined number of tasks to be treated simultaneously $n_{\max\text{run}}^1$ new individuals are to be created. A list of n_{parent} parents is requested from runner.pl and fed to a modified version of Qum-sieh's Al::Genetic [243] package which creates the child generation of individuals as defined in a configuration file GA.conf. A number of $n_{\max\text{child}}$ randomly selected children are then pushed to the database and thereby passed to runner.pl.

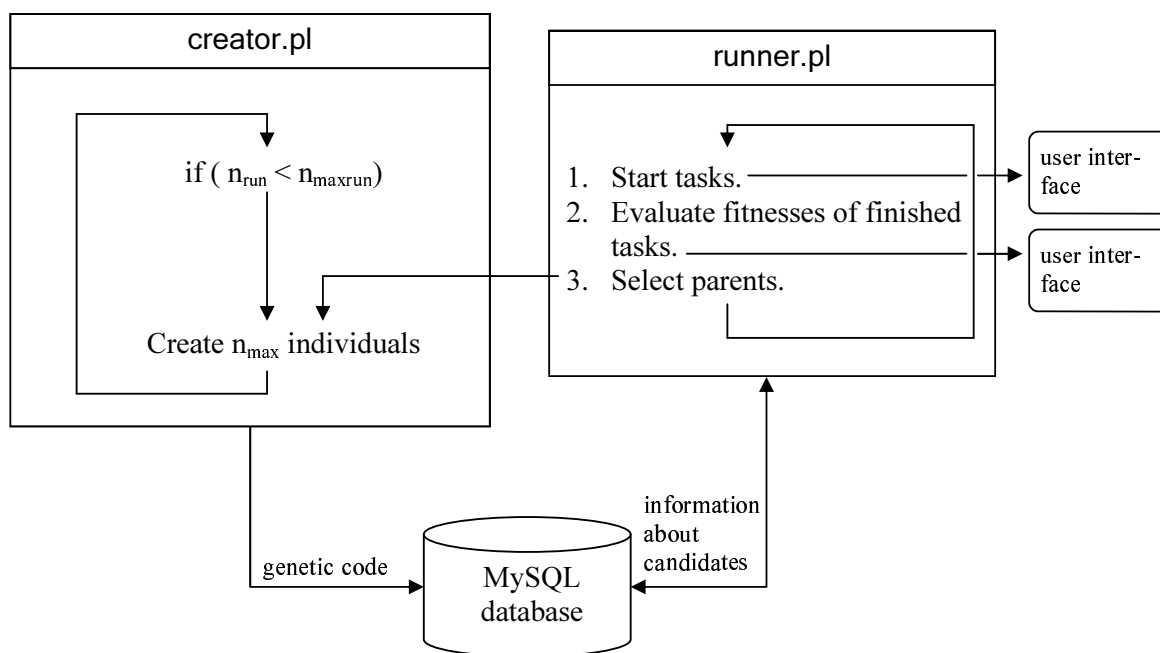


Scheme 13.1. Flow chart of the genetic algorithm. For the definition of the parameters n_{pop} , n_{best} , n_{parents} , $n_{\max\text{run}}$, P_C and P_M see text.

Within its main loop the program runner.pl searches the database for individuals to be examined. Each examination can be split into a number of individual steps to be defined in "GA.conf". A consecutive step will be started when the first is finished

¹ $n_{\max\text{run}}$ should be user-adjusted to match the computational environment. It has to be larger or as large as the number of jobs which shall be executed simultaneously.

and the main loop returns to search the database. The examination is threaded to make use of multi-core computer systems; this means for example that on a quad-core machine four examinations can be started simultaneously. The user is completely free in how the examination will be performed. The only requirements are that the employed program understands the genetic code and can calculate values depending on this code. These values are written to the database either directly or by the use of little helper programs and allow for the evaluation of the individual's fitness later on. The program can for example take the genetic code, derive a chemical structure from it and calculate a molecular property, which it then writes to the MySQL database. The examination program can either run locally on the machine which executes the global optimization system and thus use a threaded parallelization, or detach to a queueing system and make use of a cluster or grid wide parallelization.



Scheme 13.2. Flow chart of the program system.

In a second step the evaluation of the fitness for newly finished tasks is initiated. A program is started, which reads properties from the database and calculates the fitness of the requested individual in a user specified way.

In the third and last step, parents are selected and passed to **creator.pl** when requested by the latter. A list of individuals is created containing the number of n_{best} fittest individuals ever examined and $(n_{\text{parents}} - n_{\text{best}})$ fittest individuals from the actual population. The actual population consists of the last evaluated n_{pop} individuals. For truncation selection, missing individuals are taken from an initial

population and are directly injected into the working pool bypassing the mutation procedure, in case the number of already evaluated individuals is smaller than the required n_{parents} . The details for truncation and tournament selection are given above.

Usually the initial population is randomly constructed, but the user can define its members as well and thus start the optimization within a certain region.

13.2.1. The Fitness Function

A fitness function can be defined in the `fitness.pl` program and returned values are stored in the database. The user has absolute freedom to choose which data is used.

13.2.2. Reproduction Operators

As the system is interfaced to Qumsieh's AI::Genetic package [243], single-point, two-point and uniform crossover exist as predefined operators. Elitist selection (i.e. the probability of passing to the next "generation" for the fittest number of n_{best} individuals equals 1) was added. For the test runs the traditional single point crossover was chosen, but this can be changed in the configuration file. The crossover probability P_c and mutation probability P_m are fixed in the current implementation. It has been shown that an adaptive choice of P_c and P_m can lead to a significant improvement in optimization performance [244]. Here lies a key for improvements in the code. Further developments could involve more problem-specific reproduction operators.

13.3. Aniline Derivatives – Parameter Evaluation

To test the code for robustness and evaluate the influences of the different system parameters, a simple chemical problem was defined. Consider a series of aniline derivatives, which can be substituted in ortho, meta and para position as shown in Figure 13.1. The electronic structure at the nitrogen atom will be influenced by the substituents. Thus, the charge located at the nitrogen atom q_N was defined as the quantity to be maximized.

The choice of substituents was limited to the ones compiled in Table 13.1, allowing for the highest flexibility in ortho position and the least in meta position. Both ortho and both meta positions were only allowed to bear identical substituents, respectively.

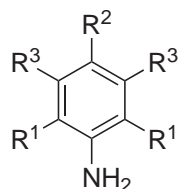


Figure 13.1.. Aniline derivatives.

Table 13.1.: Substituents with their genetic codes for ortho, meta and para position of the aniline derivatives.

Substituent	ortho	meta	para
-H	0	0	0
-Me	1	1	1
- <i>i</i> -Pr	2	2	2
-Cl	3	3	3
-F	4	4	4
-OMe	5		5
-Ph	6		
-SO ₂ Me	7		

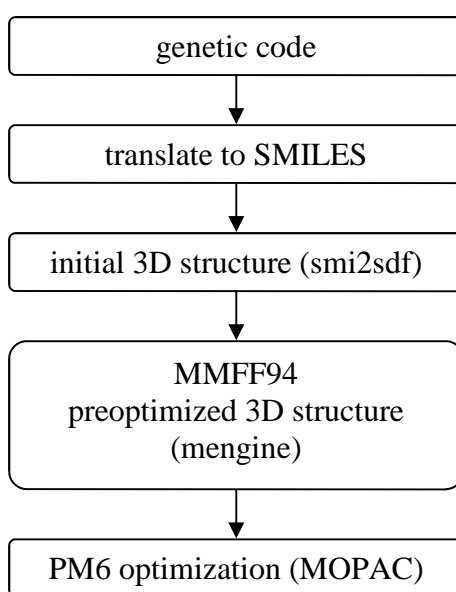
When requested from the global optimization system, a driver program first converts the genetic code to a SMILES [123] notation. This one-dimensional representation is converted to a three-dimensional one using the smi23d programs [125], which employ an MMFF94 force field [188]. The geometries of the preoptimized molecules are then optimized using the semi-empirical PM6 method [178]. The electronic structure was then evaluated with the same method (see Scheme 13.3). Since these calculations required very short runtimes, they were executed locally on the machine which also ran the global optimization system.

The choice of substituents makes up 240 ($8 \cdot 5 \cdot 6$) combinations. This number is certainly too small considering the purpose of the optimization system. Therefore, pairs of two unique individuals are treated as individuals. This approach allows to compute fitnesses for all $240 \cdot 240 = 57600$ individuals from the brute-force optimized fitnesses of all unique individuals. Double counting of combinations of individuals is not removed, because the optimization system is not aware of symmetry (exchange of the two unique individuals). The fitness function f is written as

a simple mean of the charges on nitrogen of the two aniline derivatives $q_{N(1)}$ and $q_{N(2)}$:

$$f = \left(\frac{q_{N(1)} + q_{N(2)}}{2} \right)$$

The brute force optimization revealed two molecules **42** and **43** to feature the extremes in charge located at the nitrogen atom, which are depicted in Figure 13.2. The high negative charge on **43**'s nitrogen atom would eventually not have been expected since the molecule bears two electron withdrawing methylsulfonyl groups. But hydrogen bonds between the sulfonyl's oxygen atoms and the amino-hydrogens overcompensate this effect.



Scheme 13.3. Optimization of the aniline derivatives.

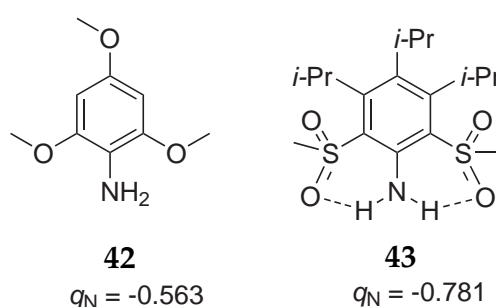


Figure 13.2.. Aniline derivatives with highest and lowest charge located at the nitrogen atom.

For the following test-runs of the optimization system, the substituents were encoded on the unique chromosomes as “[R¹]___[R²]___[R³]”. R¹ denotes the substituents in ortho, R² in para and R³ in meta position as shown in Figure 13.1. The genes of ortho and para substituents are defined as neighbors. Since single point crossover was used during reproduction, a bias towards passing neighbors to the next generation is expected.

The standard parameter set is given in Table 13.2. 100 individuals for the number of running tasks (n_{maxrun}) and 200 as population size (n_{pop}) were selected to closely match settings sensible for a real computer cluster.

Table 13.2.: Standard parameters used in the test runs.

Parameter	Value
n_{maxrun}	100
n_{parent}	100
n_{pop}	200
n_{best}	20
n_{maxchild}	10
P_c	0.9
P_m	0.2

For details of the parameters see text.

All test runs were performed ten times with a fixed parameter set and the results for each set were averaged. To compare the different optimization runs an optimization target was defined. The average fitness of the actual population had to reach the average fitness of the fittest 10% of individuals which can be encoded with the given genetic code.

13.3.1. Mutation Probability

Low probabilities of mutation P_m tend to favor the convergence to a local optimum since solutions are constructed nearly exclusively from the initial populations genetic code. Very high mutation probabilities on the other hand turn a genetic algorithm into a random search machine. Hence, the value of P_m has to be chosen with some care. Mutation probabilities ranging from 0.05 to 0.4 were tried. The results are depicted in Figure 13.3. It can be seen that the search indeed becomes very inefficient if too high probabilities are chosen. Within the lower range [0.05...0.2] no severe influence can be observed. Therefore, the high value of 0.2 was chosen

as default in order to decrease the probability that the system converges to a local optimum.

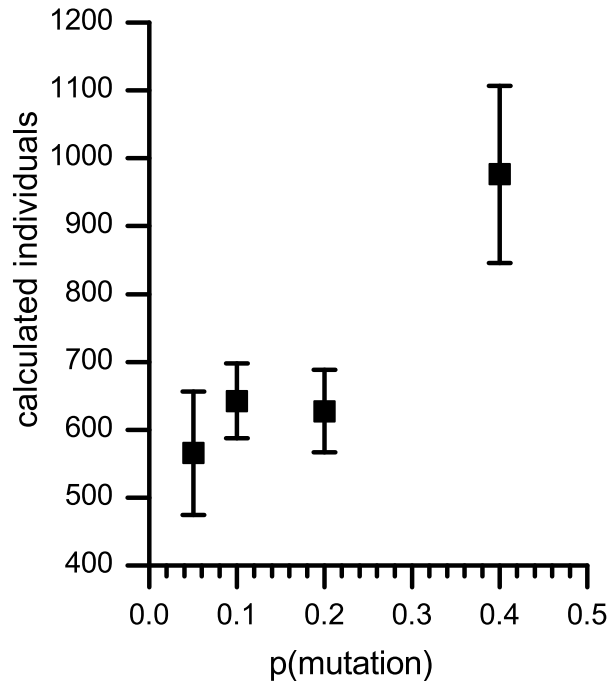


Figure 13.3. Number of individuals that had to be computed until the population's mean fitness reached that of the 10% best performing individuals against the mutation probability.

13.3.2. Number of Elitists

Elitist selection guarantees that a certain number n_{best} of individuals which possess the highest fitness values found so far are kept in the pool of parents. This helps to retain good genetic codes while high mutation probabilities P_m are applied. On the other hand – especially with lower mutation probabilities – convergence to local optima can be favored.

The parameter n_{best} was varied from 0 to 50 (which equaled 0% to 50% of the parents). The optimization target was reached considerably faster with a high number of elitists as can be seen in Figure 13.4. Anyway, since the convergence behavior for more complex optimization tasks can not be predicted, a value as high as 50 appears too aggressive. Also, for the sake of the lower standard deviation at a value of 20, making the performance more reliable, this number was used as default.

In summary, it was possible to show that the optimization performance is not affected dramatically by a variation of parameters in a sensible range supposing robustness of the genetic algorithm. The optimization target was reached in all cases.

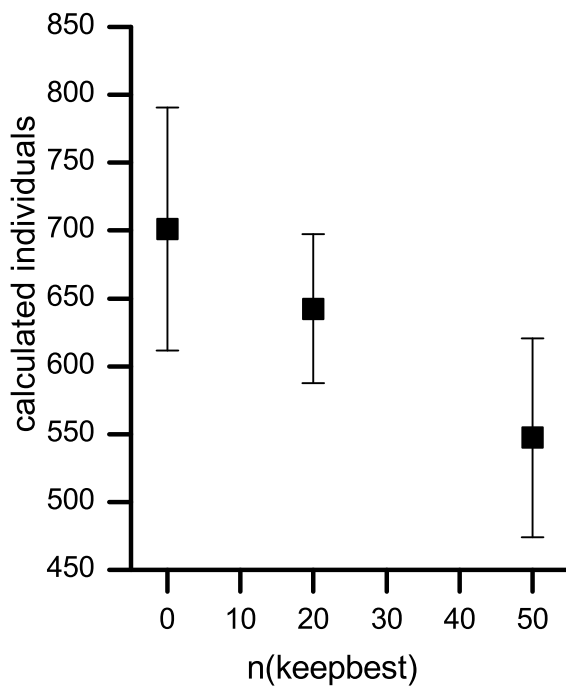


Figure 13.4.. Number of individuals that had to be computed until the population's mean fitness reached that of the 10% best performing individuals against the number of best performing individuals found so far held back in the population.

14. Syntheses of Candidate Catalysts

14.1. Experimental Details

General Techniques

All reactions were conducted under N₂ using Schlenk or glove-box techniques, if not stated otherwise. Solvents were dried using standard techniques (THF, CCl₄, heptane) or were taken from an M.Braun MB SPS-800 solvent purification system (CH₂Cl₂, diethyl ether, *n*-hexane, toluene). Deuterated solvents were dried using standard methods and degassed applying the “freeze-pump-thaw” method.

Characterization

NMR-Spectroscopy

¹H-NMR Bruker Avance 400, 400 MHz
 Varian Gemini 2000 BB, 200 MHz
¹³C{¹H}-NMR Bruker Avance 400, 100 MHz

Chemical shifts are reported in ppm relative to the NMR solvent shifts (CD₂Cl₂, ¹H, $\delta = 5.32$ and ¹³C, $\delta = 53.84$; CDCl₃, ¹H, $\delta = 7.26$ and ¹³C, $\delta = 77.16$; DMSO, ¹H, $\delta = 2.50$).

IR-Spectroscopy

FT-IR Perkin Elmer 1720

Notation for band intensities: vs: very strong, s: strong, m: medium, w: weak.

Elemental analysis

Heraeus CHN Rapid analyzer

Reagents

The following compounds were synthesized as described in the literature:

- 2,2'-(1,4-phenylene)diacetonitrile (**30**) [245]
- 1,5-dimethyl-3-(methylsulfonyl)-2-nitrobenzene [200]
- di(*tert*-butylimido)di(trimethylsilyloxo)chromium(VI) [144]
- di(*tert*-butylimido)di(chloro)chromium(VI) [136, 169]

All other reagents were commercially available from either Fluka, Sigma-Aldrich or Merck and were used as received.

Syntheses

2,2'-(1,4-phenylene)bis(2-methylpropanenitrile) (**31**)

A solution of 3.0 g (19.2 mmol) 2,2'-(1,4-phenylene)diacetonitrile **30** and 5.29 mL (85.0 mmol) methyl iodide in 25 mL of DMSO is heated to 45°C under air. 6.3 mL of 50% NaOH/H₂O are slowly added and the solution is stirred for 1 h. The solution is extracted twice with Et₂O/Pentane (1:1) and the combined organic layers are dried over MgSO₄. After removal of the solvent using a rotary evaporator the residue is recrystallized from 100 mL methyl cyclohexane to afford **31** as pale-orange flakes. Yield: 3.7 g (17.4 mmol, 91%).

¹H-NMR (400 MHz, CDCl₃) δ [ppm] = 7.49 (s, 4H, C_{arom}H), 1.72 (s, 12H, CH₃).

¹³C{¹H}-NMR (100 MHz, CDCl₃) δ [ppm] = 141.3 (C_{arom}(1,4)), 125.9 (C_{arom}(2,3,5,6)), 124.4 (C-C≡N), 37.0 (C_{tert}), 29.2 (CH₃).

Elemental analysis (C ₁₄ H ₁₆ N ₂)	calc.	C 79.21%	H 7.60%	N 13.20%
	found	C 78.84%	H 7.38%	N 13.11%

2,2'-(1,4-phenylene)bis(2-methylpropan-1-amine) (**32**)

12.6 g AlCl₃ (94.5 mmol) dissolved in 100 mL diethyl ether are slowly added to a stirred suspension of LiAlH₄ in 150 mL THF at 0°C. Under vigorous stirring, 4.0 g (18.9 mmol) of 2,2'-(1,4-phenylene)bis(2-methylpropanenitrile) in 50 mL THF is

added drop wise and the mixture is allowed to warm to room temperature for 3 h. It is again cooled to 0°C and 60 mL H₂O, 200 mL diethyl ether and 100 mL 25% NH₄Cl are added subsequently. The organic phase is separated and the aqueous phase is extracted 2 times with diethyl ether. The combined ethereal phases are extracted with 100 mL 5M HCl. Upon addition of 100 mL diethyl ether, the aqueous extract is made alkaline (pH ≈ 14) with 5M NaOH. The organic phase is separated and dried over MgSO₄. Removal of the solvent using a rotary evaporator and drying in vacuum over night reveals the title compound as a colorless wax. Yield: 3.1 g (14.0 mmol, 74%).

¹H-NMR (400 MHz, CDCl₃) δ [ppm] = 7.28 (s, 4H, C_{arom}H), 2.77 (s, 4H, CH₂), 1.28 (s, 12H, CH₃).

¹³C{¹H}-NMR (100 MHz, CDCl₃) δ [ppm] = 144.7 (C_{arom}(1,4)), 126.3 (C_{arom}(2,3,5,6)), 55.0 (CH₂-NH₂), 39.5 (C_{tert}), 26.4 (CH₃).

IR (KBr) $\tilde{\nu}$ [cm⁻¹]: 3368, 3288, 3088 w, 3033 w, 2959 vs, 2923 s, 2869 s, 1904 w, 1587 s, 1511 s, 1475 s, 1361 m, 13009 m, 1276 m, 1169 w, 1018 s, 897 s, 831 s, 593 s.

Elemental analysis (C₁₄H₂₄N₂) calc. C 76.31% H 10.98% N 12.71%
found C 75.72% H 10.63% N 12.35%

***N,N'*-(2,2'-(1,4-phenylene)bis(2-methylpropane-2,1-diyl))bis(1,1,1-trimethylsilylamine) (35)**

100 mg (0.454 mmol) of **32** are suspended in 10 mL *n*-hexane. At -30°C 0.36 mL of a 2.5 M solution of *n*-butyl lithium in hexane is slowly added under stirring. After stirring for 1 h at room temperature, 0.115 mL (0.91 mmol) TMSCl are added at -30°C and the solution is allowed to warm to room temperature. After 2 h the solution is filtered to remove the precipitated LiCl. The filtrate is concentrated under reduced pressure to afford a slightly orange colored oil. Yield: approx. 30 mg (0.21 mmol, 48%).

¹H-NMR (400 MHz, CD₂Cl₂) δ [ppm] = 7.27 (s, 4H, C_{arom}H), 2.79 (d, 4H, ³J=6.9 Hz, CH₂), 1.24 (s, 12H, CH₃), 1.20 (d, 2H, ³J=6.9 Hz, NH), -0.05 (s, 18H, Si(CH₃)₃).

¹³C{¹H}-NMR (100 MHz, CD₂Cl₂) δ [ppm] = 145.7 (C_{arom}(1,4)), 126.4

(C_{arom}(2,3,5,6)), 55.1 (CH₂), 39.8 (C_{tert}), 26.6 (CH₃), 0.2 (Si(CH₃)₃).

2,2'-(1,4-phenylene)bis(2-methylpropanesulfinylamine) (34)

To a solution of 130.2 mg (1.912 mmol) imidazole in 7 mL dichloromethane, 35 μ L thionyl chloride (0.480 mmol) are added at -30°C. The solution is stirred at 20°C for 10 min. The resulting white precipitate is filtered off and washed with 3 mL of the same solvent. The combined filtrates are treated with another quantity of 35 μ L thionyl chloride at -30°C and again stirred at 20°C for 10 min to complete the formation of 1*H*-imidazole-1-sulfinic chloride. A solution of 210 mg (0.956 mmol) **32** in 5 mL dichloromethane is prepared. The sulfinic chloride solution is slowly added to the solution of **44** at -30°C and allowed to warm to room temperature. After stirring for 30 minutes, the precipitated imidazolium chloride is filtered off and washed with 2 mL of dichloromethane. The filtrate is concentrated *in vacuo* and the remainder is heated to 100°C and 1 mbar to be purified by evaporation and recondensation to a water-cooled finger. This affords **34** as pale yellow liquid. Yield: approx. 60 mg (0.0423 mmol, 44%).

¹H-NMR (400 MHz, CD₂Cl₂) δ [ppm] = 7.37 (s, 4H, C_{arom}H), 4.11 (s, 4H, CH₂), 1.40 (s, 12H, CH₃).

¹³C{¹H}-NMR (100 MHz, CD₂Cl₂) δ [ppm] = 144.9 (C_{arom}(1,4)), 126.2 (C_{arom}(2,3,5,6)), 59.9 (CH₂-NSO), 39.2 (C_{tert}), 26.9 (CH₃).

Elemental analysis	calc.	C 53.82%	H 6.45%	N 8.97%	S 20.52%
(C ₁₄ H ₂₀ N ₂ O ₂ S ₂)	found	C 55.04%	H 6.56%	N 9.16%	S 19.51%

Modified Synthesis of 2,4-dimethyl-6-(methylsulfonyl)aniline (2)

500 mg (2.18 mmol) of 1,5-dimethyl-3-(methylsulfonyl)-2-nitrobenzene are dissolved in 80 mL ethanol and approximately 100 mg Pd/C added. The reaction flask is charged with dihydrogen from a 4 L balloon and stirred for 12 h at 30°C. Thereafter, Pd/C is filtered off and the solvent removed in vacuum to afford pure **2** as a colorless wax. Yield: approx. 430 mg (2.16 mmol, 99%).

$^1\text{H-NMR}$ (200 MHz, DMSO) δ [ppm] = 7.25 (m, 1H, $\text{C}_{\text{arom}}\text{H}$), 7.13 (m, 1H, $\text{C}_{\text{arom}}\text{H}$), 3.65 (br, 2H, NH_2), 3.08 (s, 3H, SO_2CH_3), 2.18 (s, 3H, CH_3), 2.13 (s, 3H, CH_3).

Summary

The improvements in both computer hardware and computational chemistry have made the quantum chemical treatment of realistically sized chemical systems possible. Especially density functional theory with its good balance between accuracy and speed has come into the reach of high-throughput computations – the automated calculation of large numbers of structures. The application of high-throughput methods in the quantum-chemical search for homogeneous transition metal based catalysts is lacking and approaches to a high-throughput screening were to be developed in this work.

In olefin polymerization there still is a general need for catalysts which allow the (co)polymerization of polar substrates. In particular polyfluoroolefins are produced in radical processes with an inherent lack of control over the polymer microstructure. Although synthetic alternatives exist, they are either costly or produce non-uniform polymers. It is anticipated that the development of coordinative catalysts for direct insertion polymerization will allow a more efficient and better control of polymer properties. Exemplarily, diimido chromium(VI) complexes have been optimized with respect to their activity in the fluoroolefin and ethene polymerization. Neutral diimido chromium(VI) systems were reported to show catalytic activity in the polymerization of polar olefins; the cationic analogs were known to polymerize ethene.

For the calculation of transition metal compounds by density functional methods, calculated properties often depend strongly on the specific functional employed. A small catalyst model for the neutral diimido complexes has been derived to calibrate the calculation method. Elementary steps for (polymer)chain propagation, chain termination and catalyst deactivation during the reaction with *gem*-difluoroethene have been investigated by density functional methods. It has been found that the 1,2 migratory insertion of the monomer into the metal-polymer bond competes with the β -fluorine elimination from the growing chain. The latter leads to catalyst deactivation by formation of a stable fluoro complex. The geometries of the calculated intermediates and transition state structures are not influenced significantly by the choice of one of the tested density functionals. Energy calculations have been performed as reference employing wave function theory methods, i.e. the CCSD(T) and CASPT2 method. The electronic structures of the formally d^0 configured diimido chromium complexes are influenced by at least moderate static correlation, which renders single-reference calculations unreliable. Thirteen density functionals have been benchmarked against the CCSD(T) and CASPT2 derived data. Generally, double hybrid functionals show the best agreement with the high-level wave function data whereas the tested hybrid functionals perform worst for

barrier heights. A black-box usage of density functional methods for the prediction of catalytic activity is prohibitive. The use of an empirical dispersion correction is beneficial in most cases.

Geometric parameters of the diimido complexes have been investigated in an approach to find a structure activity relationship which guides the catalyst optimization towards fluoroolefin polymerization activity. Optimal catalysts feature an exceptionally large $N_{\text{imido}}\text{-Cr-}N_{\text{imido}}$ bond angle of more than 120° .

An automatic search system has been developed, which assembles and optimizes complexes automatically from predefined fragments by a combination of molecular mechanics, semi-empirical and density functional methods. A set of example complexes has been obtained by variations in the ligand structure. They possess close to optimal geometric structures and high predicted activities.

For the cationic diimido chromium complexes, which polymerize ethene, the nature of the catalytically active species was subject of discussion in literature. Different mechanisms have been probed using density functional methods and CASPT2 reference calculations. Polymerization by an insertion mechanism involving chromium(VI) centers has been found most probable in contrast to a previously reported reduction to a chromium(IV) species. The thermodynamics of the latter reaction had been biased by a too small model system and the choice of an inappropriate density functional.

Under the assumption of an insertion mechanism, phenylimido chromium complexes have been optimized by variation in the substitution pattern at the phenyl groups. Figure of merit has been a combination of density functional derived activity in the polymerization of ethene and thermodynamic accessibility. To guide the optimization, genetic algorithms have been developed and implemented into an automated system, which has been adapted for small to medium sized computer clusters. A strong correlation between the molecular structure and the predicted reactivity in polymerization could not be obtained by either a multi-variate linear model or by the use of neural networks. Nonetheless, substitution patterns have been identified which lead to stabilizing interactions in the transition state of migratory insertion and thus to high polymerization activities.

First attempts to synthesize exemplary catalysts in the laboratory have been made, but no novel structurally authenticated diimido chromium(VI) complex could be obtained.

In summary, density functional based high-throughput methods have been developed and applied to realistically sized transition metal complexes. This led to the discovery of novel potentially highly active polymerization catalysts for fluoroolefins and ethene.

Zusammenfassung

Die Entwicklungen sowohl im Bereich der Computer-Hardware als auch der Computerchemie haben genaue quantenchemische Berechnungen von molekularen Systemen mit realistischer Größe möglich gemacht. Insbesondere Berechnungen, die auf der Dichtefunktionaltheorie beruhen, zeigen ein gutes Verhältnis von Genauigkeit und Geschwindigkeit. Sie eignen sich mittlerweile für High-Throughput-Rechnungen – automatisierte Berechnungen einer großen Anzahl von molekularen Systemen. Für das quantenchemische Screening von Übergangsmetallkomplexen in homogen katalysierten Reaktionen haben High-Throughput-Methoden jedoch bisher kaum Anwendung gefunden. Das Anliegen dieser Arbeit ist es, hierfür Ansätze zu finden.

Für die Co-/Polymerisation polarer Olefine gibt es einen großen Bedarf an neu zu entwickelnden Katalysatoren. Insbesondere Polyfluorolefine werden industriell unter radikalischen Reaktionsbedingungen hergestellt, was eine schlechte Kontrolle über die Polymermikrostruktur mit sich bringt. Bereits bekannte alternative Synthesemethoden sind entweder zu kostenintensiv oder führen zu uneinheitlichen Produkten. Die Entwicklung von Koordinations-Katalysatoren für die direkte insertive Polymerisation würde eine deutlich effizientere und bessere Kontrolle über die Polymereigenschaften ermöglichen. Exemplarisch wurden hier Diimidochrom(VI)-Komplexe hinsichtlich ihrer Aktivität in der Fluorolefin- und Ethenpolymerisation optimiert. Sowohl die katalytische Aktivität neutraler Diimidochrom(VI)-Komplexe in der Polymerisation polarer Olefine als auch die Aktivität der kationischen Derivate in der Ethenpolymerisation ist in der Literatur bekannt.

Bei der Berechnung von Übergangsmetallsystemen mit Hilfe von Dichtefunktionalmethoden zeigen die Ergebnisse oft eine starke Abhängigkeit von dem verwendeten Funktional. Um eine Kalibrierung durchzuführen, wurde zunächst ein kleines Modellsystem für den neutralen Chromkomplex erstellt, woran Elementarschritte der Mechanismen für Kettenwachstum, Kettenabbruch und Katalysatordeaktivierung für die Reaktion mit *gem*-Difluorethen unter Verwendung von Dichtefunktionalmethoden untersucht wurden. Es zeigte sich, dass die 1,2-migratorische Insertion eines Monomers in die Metall-Polymer-Bindung mit der Eliminierung der β -ständigen Fluoratome aus der Polymerkette in Konkurrenz steht. Die letztgenannte Reaktion führt durch die Bildung eines stabilen Fluorokomplexes zur Deaktivierung des Katalysators. Die Wahl eines der getesteten Dichtefunktionale hatte nur einen sehr geringen Einfluss auf die Geometrien der berechneten Intermediate und Übergangsstrukturen. Als Referenz wurden Energieberechnungen mit den Wellenfunktionsmethoden CCSD(T) und CASPT2 durchgeführt. Die elek-

tronischen Strukturen der Diimidochromkomplexe, die eine formale d^0 Konfiguration aufweisen, sind durch statische Korrelation beeinflusst. Die mit dreizehn verschiedenen Dichtefunktionalen berechneten thermodynamischen und kinetischen Daten wurden mit denen der CCSD(T)- und CASPT2-Rechnungen verglichen. Doppelhybridfunktionale zeigten die generell beste Übereinstimmung mit den Daten der Wellenfunktionsmethoden, während die getesteten Hybridfunktionale die schlechteste Übereinstimmung mit den entsprechenden kinetischen Daten lieferten. Es erwies sich, dass Dichtefunktionalmethoden für die Vorhersage katalytischer Aktivität einer genauen Prüfung unterzogen werden müssen und nicht als „Black-Box“-Methoden verwendet werden können. Die Anwendung einer empirischen Dispersionskorrektur hatte in fast allen Fällen eine Verbesserung der Übereinstimmung mit den Referenzdaten zur Folge.

Geometrische Parameter des Diimidochromkomplexes wurden untersucht, um eine Beziehung zwischen katalytischer Aktivität und Struktur herzustellen und so Leitlinien für die Katalysatoroptimierung zu finden. Katalysatoren mit einem besonders großen $N_{\text{imido}}\text{-Cr-N}_{\text{imido}}$ Bindungswinkel von mehr als 120° zeigten dabei optimale Aktivität in der Fluorolefinpolymerisation.

Ein automatisches Screening-System wurde entwickelt, das Komplexe aus vorher definierten Fragmenten konstruiert und anschließend mit einer Kombination aus molekularmechanischen, semiempirischen und Dichtefunktionalmethoden optimiert. Durch die Variation der Imidoliganden konnte so eine Reihe von Beispielkomplexen erhalten werden, die nahezu optimale geometrische Strukturen und hohe potentielle Aktivitäten aufweisen.

In der Literatur ist die Beschaffenheit der katalytisch aktiven Spezies beim Einsatz von kationischen Diimidochromkomplexen in der Ethenpolymerisation diskutiert worden. Es wurden nun verschiedene Mechanismen mit Dichtefunktionalmethoden untersucht und Referenzrechnungen sowohl mit der CCSD(T) als auch mit der CASPT2 Methode durchgeführt. Die direkte insertive Polymerisation an Chrom(VI)-Zentren stellte sich dabei als am wahrscheinlichsten heraus. Dies steht im Widerspruch zu der in der Literatur präferierten Reduktion des Chroms auf die Oxidationsstufe IV, deren prognostizierte Thermodynamik jedoch auf einem zu kleinen Modellsystem und dem Einsatz eines ungeeigneten Dichtefunctionals beruhte.

Darauf aufbauend wurden unter der Annahme eines Insertionsmechanismus Phenylimidochromkomplexe durch Variation im Substitutionsmuster der Phenylgruppen optimiert. Als zu optimierende Größe wurde dabei eine Kombination der

katalytischen Aktivität und der thermodynamischen Zugänglichkeit der Komplexe gewählt. Für den Optimierungsprozess wurden genetische Algorithmen entwickelt und in ein automatisches Optimierungssystem implementiert, das speziell für kleine und mittelgroße Computercluster ausgelegt wurde. Eine starke Korrelation zwischen molekularer Struktur und katalytischer Aktivität wurde weder mit einem multivariaten linearen Modell noch mit Hilfe neuronaler Netze gefunden. Gleichwohl konnten Substitutionsmuster an Liganden identifiziert werden, die über stabilisierende Wechselwirkungen im Übergangszustand die Insertionsbarriere senken und so zu hohen Polymerisationsaktivitäten führen.

Erste Versuche, beispielhafte Katalysatoren im Labor zu synthetisieren, wurden unternommen, doch konnten keine eindeutig zu charakterisierenden neuen Diimidochromkomplexe gewonnen werden.

Insgesamt wurden dichtefunktionalbasierte High-Throughput-Methoden entwickelt und auf Übergangsmetallkomplexe realistischer Größe angewendet. Dies führte zur Entdeckung von Leitstrukturen für neue, potentiell hoch aktive Polymerisationskatalysatoren für Fluorolefine und Ethen.

Appendix

A. Computational Considerations

A.1. Cluster Setup

A.1.1. Introduction

Typical RI-DFT applications for chemistry, as checked here with the Turbomole program suite, perform best if executed serially. Their scaling is moderate up to 4 cores, as shown in section A.2. With modern quad, dual quad, hexa and dual hexa core computers, symmetric multi processing (SMP) and cache-coherent non-uniform memory access (ccNUMA) systems are available, which can perform a calculation in a stand-alone fashion. This means that a parallelization of computing tasks over more than one node is usually not necessary. This renders the performance of interconnections between individual nodes unimportant, which is in contrast to massively parallel setups. An efficient architecture for high-throughput DFT calculations is thus a large number of loosely connected multi-core computers, which can be achieved with e.g. standard gigabit ethernet. Emphasis has to be laid upon proper job scheduling and load balancing for the vast number of individual jobs. Therefore, a distributed-resource management system (D-RMS) is absolutely necessary. For a review of the most common programs, SGE, PBS, LoadLeveler and LSF, see [246].

At the beginning of the project, the computational resources consisted of a small cluster of 16 Intel Core2Duo commodity personal computers running OpenSuSE Linux. These were connected via standard gigabit ethernet; a common directory as well as user access was served from a master node. This cluster, called "**Quantix-cluster**", was augmented by a set of individual workstations with the nickname "**Starfish**" (see Figure A.1). All machines were accessible via SSH and calculations had to be started manually on any free node.

Over time, the equipment grew by the addition of several new workstations to **Starfish** and a new cluster ("**S7Z**") with 7 Intel Core2Quad Siemens workstations. The latter was again set up to possess an additional master node to which user access from the institute's local area network (LAN) was granted and which served the cluster nodes with a common directory as well as yellow-page services. The cluster was equipped with both an Infiniband and a standard gigabit ethernet (GbE) connection. Extensive testing with regard to a D-RMS was performed and finally the Sun Grid Engine (SGE) was chosen as very flexible, easy to maintain and free system. The benefit of an Infiniband interconnection was also evaluated for our working-group's computations.

With the experience gained from these small clusters, it became possible to design and set up the Inorganic Chemistry Computational Cluster (ICCC). This cluster,

which at the time of writing consists of 50 computing nodes, was acquired in three stages. Only the final stage together with its embedding into the existing hardware will be described in the following.

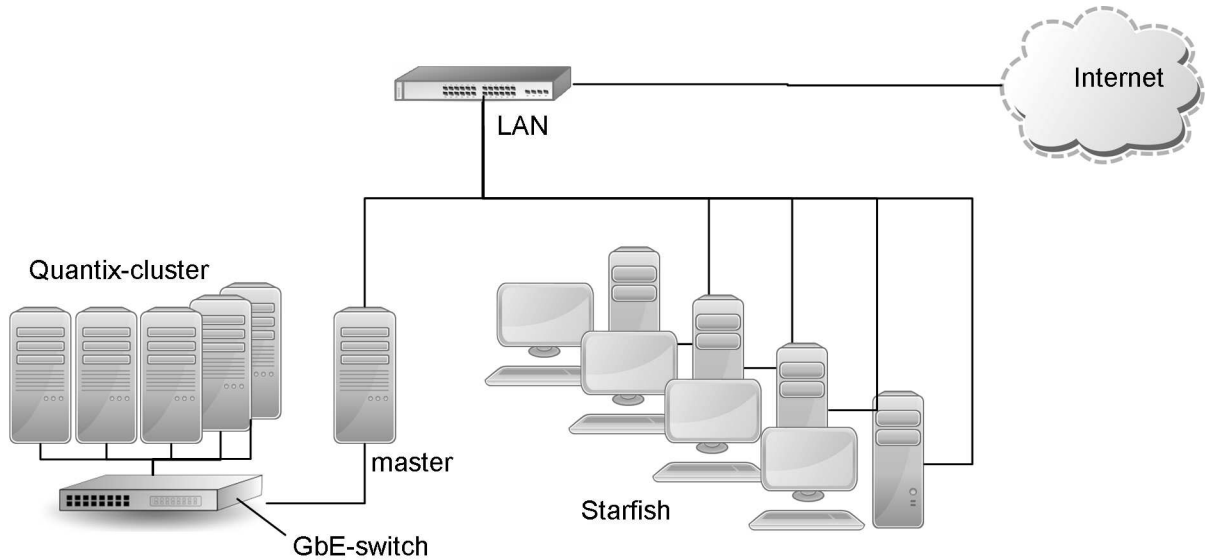


Figure A.1.. Computing hardware resources at the beginning of the project.

A.1.2. Implementation

The actual hardware can be segregated into two blocks. One is the ICCC with its additional service computers and its extension by the former **S7Z** cluster. The other is the **Starfish**. The connections are shown in Figure A.2. An overview of the current cluster hardware is given in the following list.

- Nodes:
 - 24 dual-quadcore Xeon L5410@2.33GHz, 32 GB RAM, 2 · 500 GB HD, 2 · GbE
 - 10 dual-quadcore Xeon X5570@2.93GHz, 48 GB RAM, 6 · 500 GB HD, 4 · GbE
 - 8 dual-hexacore Xeon X5670@2.93GHz, 64 GB RAM, 6 · 500 GB HD, 4 · GbE
 - 8 dual-hexacore Xeon X5680@3.33GHz, 96 GB RAM, 6 · 500 GB HD, 4 · GbE

- 6 dual-quadcore Core2Quad Q6700@2.66GHz, 8 GB RAM, 2 · 500 GB HD, 1 · GbE
- Service computers:
 - Storage: 2 · Xeon E5440@2.83GHz, 32 GB RAM, 8 · 2.0TB + 4 · 1.5TB + 4 · 500GB HD, 1 · Infiniband, 5 · GbE
 - User Access Nodes: (1) quantix (Core2Quad@2.50GHz, 4 GB RAM, 2x 160 GB HD, Infiniband, 3x GbE), (2) quantix2 (dual core Xeon@3.20GHz, 4 GB RAM, 160 GB HD, Infiniband, 3x GbE), (3) acpb20 (dual quad core Xeon X5450@3.16GHz, 16 GB RAM, 4x 750 GB HD, 3x GbE), (4) store2 (Core2Duo 6600@2.40GHz, 2 GB RAM, 500 GB HD, Infiniband, GbE), (5) acpb13 (dual-quadcore Xeon E5345@2.33GHz, 8 GB RAM, 2x 500GB HD, Infiniband, 2x GbE).

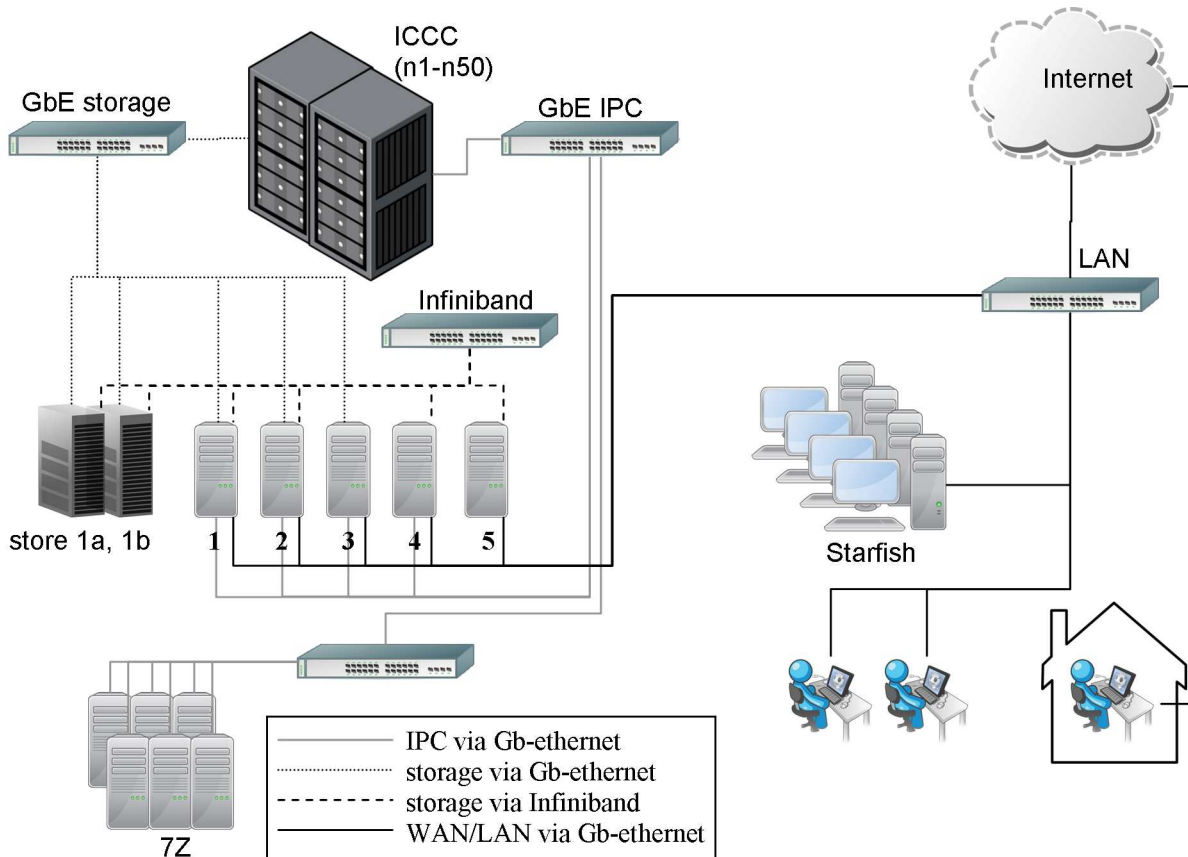


Figure A.2.. Actual computing hardware resources. The service machines are abbreviated as follows: **1** *quantix*, **2** *quantix2*, **3** *acpb20*, **4** *acpb13*, **5** *store2*.

Communication of the ICCC nodes is split into two independent GbE networks. One is dedicated to interprocess communication (IPC), the other to file-access (storage). Each node of the ICCC is connected *via* an individual network card to both

networks. Two storage servers (“store 1a” and “1b”) are connected to the store network with four GbE lines each to allow for high data throughput. Additionally, they are connected to an 10Gb/s SDR-Infiniband network. This network connects the storage intensive service computers *quantix*, *quantix2*, *store2*, and *acpb13* with the storage servers and is only used for file-access. The functions of the service computers will be briefed in the following list.

quantix Main entry point for the users, where jobs are submitted and collected. Web server for documentation (MediaWiki) and reporting (Ganglia). Time server for synchronization. Server for the D-RMS. User authentication. DHCP server.

quantix2 Second entry point for the users. Time server. Fallback-server for the D-RMS. User authentication. DHCP server.

store2 Backup of storage data to the university’s backup server.

acpb13 Export of storage data to the institutes LAN and to the IPC (needed by the 7Z servers which are only connected to the IPC). Special services.

acpb20 Time server. User authentication for *Starfish*. Software export for *Starfish*. DHCP server.

A.1.2.1. Software and Configuration

Storage The most difficult part in the cluster setup was to find a proper configuration for the storage of data. On the one hand, there was a huge amount of data (> 4TB and > 8.5M files at the time of writing). On the other hand, file access should be quick and reliable from the nodes. As to the reliability, the filesystem should be capable of redundantly save files on two different servers in case one of the servers should encounter a hardware failure. The only freely available file system which has this feature is GlusterFS [247]. The two storage servers *1a* and *1b*, each equipped with 8 2TB hard-disks running in an RAID5 array to locally store data, operating under CentOS 5.5 with a custom kernel 2.6.33.7 and OFED 1.5.2, were set up as GlusterFS 3.1.3 servers. Locally, data is stored on ext4 partitions. */cfs* is exported for user data and */opt/qc* for globally available software. On each of the two machines, one GlusterFS-server is running to perform the native GlusterFS export. To these servers, connections are made from GlusterFS-clients on *quantix*, *quantix2*, *store2*, and *acpb13* via the low-latency high-throughput Infiniband. In these cases data replication is performed on the client-side and high-availability is given.

Additionally, on each of the storage servers a second GlusterFS-server is running, connected to the two native servers and re-exporting the filesystem *via* standard NFSv3. These re-exporting servers synchronize data on a server-side basis *via* Infiniband while only one connection from each computing node is required to one of the storage servers. Load distribution is achieved by round-robin DNS when a node makes its NFS-connection to a storage server.¹ This setup has the drawback that in case of a server failure, the nodes writing to that specific server will encounter I/O-errors until a reconnect to the second server takes place. This drawback is eventually overcompensated by write performance, which is theoretically doubled, and the ease of configuration on the nodes, where only a standard NFS-mount has to be performed.

All exported data is backed up incrementally every night to the backup server of the university's computing center using IBM's Tivoli Storage Manager 6.2 *rev.* 2.2. The backup is performed on a dedicated server *store2*, since it was found that CPU-loads during checking of existing data and compression of new data are considerable. Since the Tivoli Storage Manager can not access data from native GlusterFS-mounts and NFS-mounting repeatedly lead to NFS-server failures, a native GlusterFS-mount was piped through a FUSE layer by means of an additional UnionFS mount, which then is accessed by Tivoli.

External access to the filesystem is possible in three ways. *acpb13* performs a re-export as NFS and CIFS to serve both Linux and Windows PCs in the LAN. A filesystem import from any of the servers is possible *via* SSHFS, including *quantix* and *quantix2*, which are externally accessible even from the Internet.

Resource Management and Monitoring For the D-RMS the publicly available and easy to configure SGE 6.2u5 was chosen. Its integration into OpenMPI simplifies software installations to a large extent. The primary server is running on *quantix*. In case a failure should occur, *quantix2* holds a shadow server which will then start a new server.

The hardware resources are divided into four queues, to make assignment of jobs to specific nodes more user-friendly: *acc.q* (the L5410 nodes), *nehalem.q* (the X5570, X5670 and X5680 nodes), *starfish.q* (the Q6700 nodes) and *background.q* (all nodes but jobs are run with nice-level 19). Jobs can be submitted from any authorized

¹ The only exception is the 7Z nodes which only possess one GbE connection. These are connected to the IPC. They mount the filesystems per NFS from *acpb13*, which runs an NFS-reexport server as *store 1a* and *1b*.

submission host, i.e. from all service computers, but additionally any user's desktop PC can be configured to directly submit jobs, given it has mounted the cluster's filesystem.

Monitoring of the cluster is possible either through the integrated tools in the SGE or through Ganglia. The latter was set up to have a uniform and detailed graphical view of both actual and historical cluster state and usage for both **ICCC** and **Starfish**. Served by the Apache web server, Ganglia 3.0.3 runs on *quantix*.

Nodes 1-50 The computing nodes 1–50 are DELL PowerEdge 1950 (Xeon L5410) or DELL PowerEdge R610 (all other) with a 19" form factor. They are mounted in a water-cooled rack. As operating system, OpenSuSE version 11.0 for the PowerEdge 1950 and version 11.2 for all other machines was installed as was a custom kernel version 2.6.38.2. For temporary data, scratch space is provided under */scratch*. A local copy of frequently used quantum chemical software is installed under */opt/qc-local*.

Nodes 7Z The nodes of the former **S7Z** cluster, all Siemens workstations, run OpenSuSE 10.3 with the default 2.6.24 kernel.

Special Services The service computer *acpb13* not only serves as a data relay as described for the storage handling. Well connected to the cluster infrastructure, it is otherwise kept available for special user programs. For the needs of this research project's global optimizations, it ran the MySQL database as well as the genetic optimization system and performed PM6 calculations.

Documentation A detailed documentation of the cluster including usage instructions and example scripts for the queueing system was put up as a wiki, which is accessible at <http://quantix.chemie.uni-hamburg.de>. It is intended to grow with the cluster and shall preserve the experience of its users.

A.2. Scaling

The development of the global optimization system required the knowledge of the scaling behavior of the individual calculations in order to optimize the system with regard to the number of concurrently running jobs. Would it be advisable to perform DFT structure optimizations in parallel to speed up the runtime of an individual candidate during global optimizations?

Two sets of test calculations were performed with TurboMole 6.2 using MPI parallelization to measure the run-time for 5 SCF-cycles. The first involved a system of 51 atoms where def2-TZVPP basis sets were used. The calculation accounted 244 electrons and 1271 basis functions. The second system with lower quality def-SV(P) basis sets, was a 102 atom system with 488 electrons and 960 basis functions. The latter would represent a typical system as created by the global optimization system in chapter 9. Two functionals were used: the global hybrid B3LYP and the pure functional PBE. For PBE the MARIJ approximation was applied, whereas for B3LYP calculations were performed with standard parameters.

The results are depicted in Figure A.3. For the B3LYP calculations scaling is close to linear for both the 51 and 102 atom system and the speedup nearly equals the ideal speedup. The situation for the calculations with the pure functional PBE is much different, where a decent speedup can only be observed up to 4-8 cores. But even within this range, the speedup is much worse compared to B3LYP. For example, the speedup using 8 cores is ≈ 3.7 for the 51 and only ≈ 2.6 for the 102 atom system.

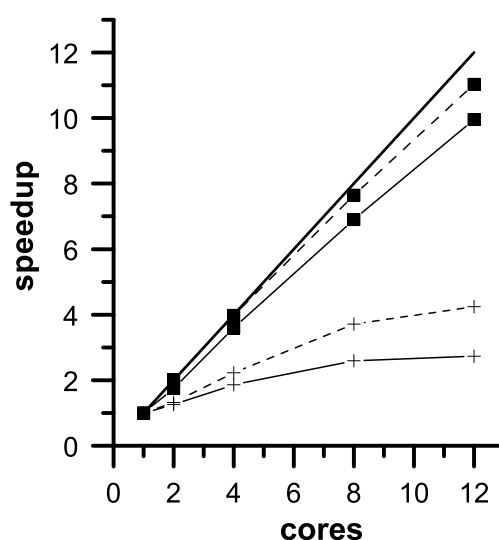


Figure A.3.. Scaling behaviour in TurboMole 6.2 using MPI parallelization. Drawn is the speedup for 5 SCF cycles compared to the serial execution. Results for the B3LYP functional (■) without the MARIJ approximation and the PBE functional (+) with the MARIJ approximation. Two typical calculations are shown: 1271 basis functions and 244 electrons (dashed lines) and 960 basis functions and 488 electrons (solid lines). Ideal speedup is represented by a thick solid line.

Taking into account that the absolute run-time of a B3LYP calculation was approximately thirty times longer than a MARIJ accelerated PBE calculation, the use of a hybrid functional can not be discussed for a high-throughput system. Since the speedup of the MARIJ-PBE calculations is so poor at the current state of implementation, serial execution should be performed whenever possible. For the typical example above, the total throughput would be reduced by a factor of approximately 3 when using 8 cores instead of 1. For the parameterization of the genetic algorithm, this implied a large population size with long run-times for the individuals in contrast to a small population size with shorter individual run-times.

List of Figures

0.1. Structures of polytetrafluoroethene (PTFE) and poly- <i>gem</i> -difluoroethene (PVDF). For PVDF the regular head-tail arrangement of monomer units is printed in black while a head-head arrangement is marked in blue.	6
0.2. General structure of neutral (left) and cationic (right) diimido chromium complexes.	8
1.1. Illustration of a [4,4]-CAS (left) and a RAS (right).	13
1.2. The Jacob's ladder of density functional approximations. Additions are made successively to lead from a "Hartree World" with $E_{XC} = 0$ to the heaven of chemical with sub-1 kcal/mol errors in relative energies. Graphic adapted from [77].	16
2.1. Representation of an individual by its "chromosome" partitioned into "genes". The value of the genes are "alleles".	22
2.2. Crossover (step a) and mutation (step b) during an evolution step.	23
2.3. General flowchart of a genetic algorithm.	24
2.4. The illustration of a common schema in the genetic representation.	24
2.5. A simple roulette wheel.	29
2.6. The roulette wheel in stochastic universal sampling. Arrows point at the candidates to be selected.	29
3.1. Architecture of a standard feed-forward network.	33
3.2. Architecture of a standard feed-forward network with additional bias-nodes.	33
5.1. Isolobal relationship between Group 4 metallocene and diimido chromium complexes.	41
5.2. Structure of the transition state [1S-2S] [‡] . The olefin approaches almost perpendicular to the <i>yz</i> plane in which the chromium and nitrogen atoms are located.	47

5.3. Natural orbitals of the [14,13]-CASSCF calculation involved mainly in interactions between chromium and the imido ligands for the 1,2 insertion transition state structure [1S–2S] [‡] . Occupation numbers are in parentheses. For the definition of the coordinate system see inset, for atom labeling see Figure 5.4.	51
5.4. Natural orbitals involving predominantly interactions between the chromium center, the methyl ligands and the olefin’s π -system of the [14,13]-CASSCF calculation for the 1,2 insertion transition state structure [1S–2S] [‡] . Occupation numbers are given in parantheses. For a schematic drawing within the same coordinate system see Figure 5.3. Atom colors: light blue = Cr, gray = C, white = H, blue = N and green = F.	51
5.5. Root mean squared deviations for GGA, meta, hybrid, hybrid-meta and double hybrid functionals with (red) and without (black) dispersion correction from CCSD(T) results. Left: reaction barriers. Right: reaction energies.	52
5.6. Predicted reactivity in terms of the barrier for 1,2 insertion (ΔE^\ddagger) versus the selectivity of the catalyst (see text) as calculated by different DFT functionals and wave function theory (WFT) methods.	54
6.1. NAOs of the [16,15]-CASSCF calculations for the side-on complex 8-H .	69
6.2. NAOs of the [16,15]-CASSCF calculations for the reduced complex 8_{red}-H in singlet state.	70
6.3. NAOs of the [16,15]-CASSCF calculations for the reduced complex 8_{red}-H in triplet state.	71
6.4. Insertion of ethene into the bond connecting chromium and the propyl fragment of 8_{βH} . Energy during the course of the reaction (dashed line) relative to the β -agostic front-side π -complex. Distances d of the forming C-C bond (\times), agostic Cr-H(β) interaction ($*$), agostic Cr-H(α) interaction (\oplus), C-H(α) bond (\odot) and ethene C-C bond (+).	72
6.5. Selected distances during the insertion of ethene into the bond connecting chromium and the propyl fragment of 8 . All values in Å. The di(isopropyl)phenyl substituents have been removed for clarity.	73
8.1. The model complex 1S derived in chapter 5.	82
8.2. Illustration of the definition of α - and β -angle for the model complex 1S	83

8.3.	Potential energy of 1S versus the α - and β -angle.	84
8.4.	Barrier heights (ΔE^\ddagger in kcal/mol) for the transition state of β -F elimination [2S–3S] ‡	85
8.5.	Barrier heights (ΔE^\ddagger in kcal/mol) for the transition state of 1,2 insertion [1S–2S] ‡	86
8.6.	Energies of the Cr 3d atomic natural orbitals in E_h for $\beta = 112.5^\circ$ and $\beta = 170.0^\circ$	86
8.7.	$\Delta \Delta E^\ddagger$ (β -F elimination – 1,2 insertion) in kcal/mol.	87
8.8.	Flowchart of the candidate construction and evaluation process. . .	88
8.9.	Structures of the three exemplary catalyst candidates K_A , K_B and K_C along with the models for Siemeling’s and Gibson’s catalysts.	92
8.10.	Gibson’s benzyl substituted di(<i>tert</i> -butylamido) chromium complex 11	92
8.11.	Reactivity in terms of the barrier for 1,2 insertion against the selectivity of the catalyst.	94
9.1.	The estimated barrier at the fixed distance of $r = 2.55 \text{ \AA}$ against the STQN optimized barrier of insertion.	105
9.2.	Average fitness of the population (lower lines) and maximum fitness (upper lines) during the optimization runs 1–3 versus the number of individuals evaluated (n_{calc}). For runs 2 and 3 the fitness values have been shifted by +10. Please note the logarithmic scale in the upper part of the graphs. 1.a marks the point after which only estimated barriers were used in the calculations of the fitnesses. 2.a marks the parameter change in run 2 and 2.b the following inset of optimization. 3.a marks the change of n_{best} in run 3.	108
9.3.	Values of the calculated descriptors for run 1 against the estimated barriers of insertion $\Delta E_{\text{est}}^\ddagger$. The isotropic NMR shielding constants $\sigma_{\text{iso}}(\text{Cr})$ and $\sigma_{\text{aniso}}(\text{Cr})$ are scaled by 0.01. For definitions of the variables see text.	111
9.4.	Values of the calculated descriptors for run 2 against the estimated barriers of insertion $\Delta E_{\text{est}}^\ddagger$. The isotropic NMR shielding constants $\sigma_{\text{iso}}(\text{Cr})$ and $\sigma_{\text{aniso}}(\text{Cr})$ are scaled by 0.01. For definitions of the variables see text.	112
9.5.	Values of the calculated descriptors for run 3 against the estimated barriers of insertion $\Delta E_{\text{est}}^\ddagger$. The isotropic NMR shielding constants $\sigma_{\text{iso}}(\text{Cr})$ and $\sigma_{\text{aniso}}(\text{Cr})$ are scaled by 0.01. For definitions of the variables see text.	113

9.6. Substructures of the candidates “2_6_4_8_8” (left) and “6_2_4_5_3” (right) transition state structures as examples for H- π and η^1 -stabilization. Selected distances in Å.	119
9.7. Substructure of the candidate “1_7_5_1_0” transition state structure as an example for a stabilization by secondary interaction with the methylsulfonyl substituent. Selected distances in Å.	120
10.1. Diimido dichloro chromium complexes found in the literature.	126
10.2. Imido chromium complexes not yet synthetically accessed.	127
10.3. Cyclic silyloxy chromium complexes with nine members in the ring.	127
10.4. Targeted ligand precursors.	128
10.5. Exemplary $^1\text{H-NMR}$ spectra for the attempted synthesis of 38 by reaction of 13 with 32 . Spectrum of the pure educt complex 13 in red, of the diamine 32 in green and of the product in black. All values in ppm.	136
10.6. The amido chromium(VI) complex 41 synthesized by Coles <i>et al.</i>	137
13.1. Aniline derivatives.	158
13.2. Aniline derivatives with highest and lowest charge located at the nitrogen atom.	159
13.3. Number of individuals that had to be computed until the population’s mean fitness reached that of the 10% best performing individuals against the mutation probability.	161
13.4. Number of individuals that had to be computed until the population’s mean fitness reached that of the 10% best performing individuals against the number of best performing individuals found so far held back in the population.	162

List of Tables

5.1.	Dependence of selected structural parameters on the choice of functional and basis sets for the catalyst model 1S	44
5.2.	Dependence of selected structural parameters on the choice of functional and basis sets for the transition state structure [1S–2S] [‡]	46
5.3.	Reaction energies and barriers obtained by various wave function methods. All values in kcal/mol.	48
5.4.	CCSD(T)/aug-cc-pVTZ, CAS and CASPT2 barriers of the 1,2 insertion. All values in kcal/mol. The CCSD(T) calculation includes an estimated BSSE of +3.4 kcal/mol.	49
5.5.	Predicted barriers and reaction energies in kcal/mol for the tested DFT functionals. Root mean squared deviation (RMSD) and mean absolute deviation (MAD) values refer to the CCSD(T) results.	55
6.1.	Energetics of the reductive elimination and front-side migratory insertion. All values in kcal/mol relative to the side-on complex 8 and its analogs.	65
6.2.	Energetics of the reductive β -H-transfer for different computational methods. All values in kcal/mol relative to 8-H or 8 , respectively.	67
8.1.	The angles α and β for important structures.	83
8.2.	Fragments used in the construction of imido ligands.	90
8.3.	Probabilities for the assembly of a ligand from the number of n fragments.	91
8.4.	Termination fragments and their respective probabilities of incorporation.	91
8.5.	Relative energies of formation (in kcal/mol) for the model reaction and barrier heights for 1,2 insertion and β -F elimination as well as calculated selectivities.	93
9.1.	Substituents with their genetic codes.	100
9.2.	Parameters used during the global optimization runs.	106

9.3. Squared correlation coefficients R^2 for various parameters and calculated estimated barriers of insertion.	114
9.4. Squared correlation coefficients R^2 for predicted and calculated barriers $\Delta E_{\text{est}}^\ddagger$ for the best performing neural networks for each set of training parameters.	116
9.5. Selected candidates from run one, two and three together with their estimated insertion barriers $\Delta E_{\text{est}}^\ddagger$ and energies of formation ΔE_f . The substituents are given as reference.	118
13.1. Substituents with their genetic codes for ortho, meta and para position of the aniline derivatives.	158
13.2. Standard parameters used in the test runs.	160

Bibliography

- (1) Jewkes, J.; Sawers, D.; Stillerman, R. *The sources of invention*, 2nd ed.; W. W. Norton: New York, 1969, p 98.
- (2) Sax, A. F. *Monatsh. Chem.* **2008**, *139*, 299–308.
- (3) Hoffmann, R. *J. Mol. Struct. (Theochem)* **1998**, *424*, 1–6.
- (4) Irikura, K. K.; Frurip, D. J. In *Computational Thermochemistry: Prediction and Estimation of Molecular Thermodynamics*; Irikura, K. K., Frurip, D. J., Eds.; ACS Symposium Series, Vol. 677; ACS: Washington, DC, 1996; Chapter Computational Thermochemistry, pp 2–18.
- (5) Moore, G. E. *Electronics* **1965**, *38*, 114–117.
- (6) Koomey, J. G.; Berard, S.; Sanchez, M.; Wong, H. *IEEE Ann. Hist. Comput.* **2010**, *33*, 46–54.
- (7) Tsinoopoulos, C.; McCarthy, I. In *Proceedings of the Manufacturing Complexity Network Conference*, University of Cambridge: Cambridge, U.K., 2002, pp 373–385.
- (8) Ondetti, M. A.; Cushman, D. W. Azetidine-2-carboxylic Acid Derivatives., U.S. Patent 4,046,889, 1977.
- (9) Ganellin, C. R.; Roberts, S. M. *Medicinal chemistry. The role of organic chemistry in drug research*, 2nd ed.; Academic Press: London, 1993.
- (10) Kubinyi, H. J. *Recep. Signal Transduction Res.* **1999**, *19*, 15–39.
- (11) Oprea, T. I. *Molecules* **2002**, *7*, 51–62.
- (12) Bone, R.; Salemme, F. R. In *Structure-based drug design*; Veerapandian, P., Ed.; Marcel Dekker: New York, 1997; Chapter The integration of structure-based design and directed combinatorial chemistry for new pharmaceutical discovery, pp 525–539.
- (13) Lewis, R.; Ertl, P.; Jacoby, E.; Tintelnot-Blomley, M.; Gedeck, P.; Wolf, R. M.; Peitsch, M. C. *Chimia* **2005**, *59*, 545–549.
- (14) Ziegler, K.; Holzkamp, E.; Breil, H.; Martin, H. *Angew. Chem.* **1955**, *67*, 426.

- (15) Natta, G. *Angew. Chem.* **1956**, *68*, 869–887.
- (16) Watson, P. J. *Am. Chem. Soc.* **1982**, *104*, 337–339.
- (17) Turner, H. W.; Schrock, R. R. *J. Am. Chem. Soc.* **1982**, *104*, 2331–2333.
- (18) Sinn, H.; Kaminsky, W.; Vollmer, H.-J.; Woldt, R. *Angew. Chem. Int. Ed.* **1980**, *19*, 390–392.
- (19) Mülhaupt, R. *Macromol. Chem. Phys.* **2003**, *204*, 289–327.
- (20) Murphy, V.; Bei, X.; Boussie, T. R.; Brümmer, O.; Diamond, G. M.; Goh, C.; Hall, K. A.; Lapointe, A. M.; Leclerc, M.; Longmire, J. M.; Shoemaker, J. A.; Turner, H.; Weinberg, W. H. *Chem. Record* **2002**, *2*, 278–289.
- (21) Armstrong, D. R.; Perkins, P. G.; Steward, J. J. P. *J. Chem. Soc. Dalton Trans.* **1972**, 1972–1980.
- (22) Cavallo, L. In *Computational Modeling of Homogeneous Catalysis*; Maseras, F., Lledos, A., Eds.; Kluwer: New York, 2002, pp 23–56.
- (23) Breslow, D. S.; Newburg, N. R. *J. Am. Chem. Soc.* **1959**, *81*, 81–86.
- (24) Cossee, P. *Tetrahedron Lett.* **1960**, *1*, 17–21.
- (25) Cossee, P. *J. Catal.* **1964**, *3*, 80–88.
- (26) Arlman, E.; Cossee, P. *J. Catal.* **1964**, *3*, 99–104.
- (27) Brookhart, M.; Green, M. L. H. *J. Organomet. Chem.* **1983**, *250*, 395–408.
- (28) Laverty, D. T.; Rooney, J. J. *J. Chem. Soc., Faraday Trans.* **1983**, *79*, 869–878.
- (29) Froese, R. D. J. In *Computational Modeling for Homogeneous and Enzymatic Catalysis. A Knowledge-Base for Designing Efficient Catalysts*. Morokuma, K., Musaev, D. G., Eds.; Wiley-VCH: Weinheim, 2008; Chapter 7, pp 149–179.
- (30) Schnutenhaus, H.; Brintzinger, H. H. *Angew. Chem.* **1979**, *91*, 837–838.
- (31) Wondimagegn, T.; Wang, D.; Razavi, A.; Ziegler, T. *Organometallics* **2009**, *28*, 1383–1390.
- (32) Davidson, E. R. *Chem. Rev.* **2000**, *100*, 351–352.
- (33) Comba, P.; Hambley, T. W. *Molecular Modeling of Inorganic Compounds*; Wiley-VCH: Weinheim, 2001.
- (34) Fey, N. *J. Chem. Technol. Biotechnol.* **1999**, *74*, 852–862.
- (35) Maseras, F. *Top. Organomet. Chem.* **1999**, *4*, 165–191.
- (36) Vahtras, O.; Almlöf, J.; Feyereisen, M. *Chem. Phys. Lett.* **1993**, *213*, 514–518.

-
- (37) Eichkorn, K.; Treutler, O.; Öhm, H.; Häser, M.; Ahlrichs, R. *Chem. Phys. Lett.* **1995**, *240*, 283–289.
- (38) Greeley, J.; Jaramillo, T. F.; Bonde, J.; Chorkendorff, I.; Nørskov, J. K. *Nat. Mater.* **2006**, *5*, 909–913.
- (39) Durrant, M. C. *Chem. Eur. J.* **2007**, *13*, 3406–3413.
- (40) *Global Polyethylene Market Analysis and Forecasts to 2020*, press release, Global Markets Direct, <http://prlog.org/10196966> (accessed Aug 10, 2010).
- (41) Britovsek, G. J. P.; Gibson, V. C.; Wass, D. F. *Angew. Chem. Int. Ed.* **1999**, *38*, 428–447.
- (42) Gibson, V. C.; Spitzmesser, S. K. *Chem. Rev.* **2003**, *103*, 283–315.
- (43) Frauenrath, H.; Balk, S.; Keul, H.; Höcker, H. *Macromol. Rapid Commun.* **2001**, *22*, 1147–1151.
- (44) Plunkett, R. J. Tetrafluoroethylene Polymers., U.S. Patent 2,230,654, 1961.
- (45) Garrett, J. M. *J. Chem. Educ.* **1962**, *39*, 228.
- (46) Drobny, J. *Fluoroplastics*; Rapra Review Reports, Vol. 16; Rapra Technology: Shawbury, U.K., 2005.
- (47) Ebnesajjad, S. In *Applied Plastics Engineering Handbook*; Kutz, M., Ed.; Elsevier Inc.: Amsterdam, 2011, pp 49–59.
- (48) Chu, B.; K., L. *Macromolecules* **1995**, *28*, 2723–2727.
- (49) Sianesi, D.; Caporiccio, G. *J. Polym. Sci., Part A-1* **1968**, *6*, 335–352.
- (50) Lagow, R. J.; Wei, H.-C. In *Fluoropolymers 1: Synthesis*; Hougham, G., E., C. P., Johns, K., Davidson, T., Eds.; Kluwer Academic Publishers: New York, 2002, pp 209–221.
- (51) Feast, W. J.; Khosravi, E. *J. Fluorine Chem.* **1999**, *100*, 117–125.
- (52) Clot, E.; Magret, C.; Kraft, B. M.; Eisenstein, O.; Jones, W. D. *J. Am. Chem. Soc.* **2004**, *126*, 5647–5653.
- (53) Watson, L. A.; Yandulov, D. V.; Caulton, K. G. *J. Am. Chem. Soc.* **2001**, *123*, 603–611.
- (54) Wondimagegn, T.; Xu, Z.; Vanka, K.; Ziegler, T. *Organometallics* **2005**, *24*, 2076–2085.
- (55) Pearson, R. G. *J. Am. Chem. Soc.* **1963**, *85*, 3533–3539.
- (56) Nozaki, K.; Magro, A. A. N. *Chim. Oggi* **2008**, *26*, 54–58.

- (57) Siemeling, U.; Kölling, L.; Stammler, A.; Stammler, H.-G.; Kaminski, E.; Fink, G. *Chem. Commun. (Cambridge, U.K.)* **2000**, 1177–1178.
- (58) Coles, M. P.; Gibson, V. C. *Polym. Bull.* **1994**, *33*, 529–533.
- (59) Siemeling, U.; Kölling, L.; Kuhnert, O.; Neumann, B.; Stammler, A.; Stammler, H. G.; Fink, G.; Kaminski, E.; Kiefer, A.; Schrock, R. R. *Z. Anorg. Allg. Chem.* **2003**, *629*, 781–792.
- (60) Cramer, C. J.; Truhlar, D. G. *Phys. Chem. Chem. Phys.* **2009**, *11*, 10757–10816.
- (61) Helgaker, T.; Jørgensen, P.; Olsen, J. *Molecular Electronic-Structure Theory*; John Wiley & Sons, LTD: Chichester, U.K., 2000.
- (62) Bartlett, R. J.; Musial, M. *Rev. Mod. Phys.* **2007**, *79*, 291–352.
- (63) Olsen, J.; Roos, B. O.; Jørgensen, P.; Jensen, H. J. A. *J. Chem. Phys.* **1998**, *89*, 2185.
- (64) Banerjee, A.; Simons, J. *J. Chem. Phys.* **1982**, *76*, 4548–4559.
- (65) Laidig, W. D.; Bartlett, R. *Chem. Phys. Lett.* **1984**, *104*, 424–430.
- (66) Piecuch, P.; Kowalski, K. *Int. J. Mol. Sci.* **2002**, *3*, 676–709.
- (67) Gdanitz, R. J.; Ahlrichs, R. *Chem. Phys. Lett.* **1988**, *143*, 413.
- (68) Schrödinger, E. *Ann. d. Phys.* **1926**, *80*, 437–490.
- (69) Møller, C.; Plesset, M. S. *Phys. Rev.* **1934**, *46*, 618–622.
- (70) Andersson, K.; Malmqvist, P. A.; Roos, B. O. *J. Chem. Phys.* **1992**, *96*, 1218–1226.
- (71) Angeli, C.; Cimiraglia, S.; Evangelisti, S.; T., L.; Malrieu, J. P. *J. Chem. Phys.* **2001**, *114*, 10252.
- (72) Nakano, H. *J. Chem. Phys.* **1993**, *99*, 7983–7992.
- (73) Hohenberg, P.; Kohn, W. *Phys. Rev.* **1964**, *136*, B864–B871.
- (74) Dirac, P. A. M. *Proc. Cambridge Phil. Soc.* **1930**, *26*, 376–385.
- (75) Kohn, W.; Sham, L. J. *Phys. Rev.* **1965**, *140*, A1133–A1138.
- (76) Perdew, J. P.; Schmidt, K. In *Density Functional Theory and Its Applications to Materials*; Van Doren, V. E., Alsenoy, K., Geerlings, P., Eds.; American Institute of Physics: New York, 2001, p 1.
- (77) Perdew, J. P.; Ruzsinszky, A.; Constantin, L. A.; Sun, J.; Csonka, G. I. *J. Chem. Theory Comput.* **2009**, *5*, 902–908.
- (78) Slater, J. C.; Phillips, J. C. *Phys. Today* **1974**, *27*, 49–50.

- (79) Vosko, S. H.; Wilk, L.; Nusair, M. *Can. J. Phys.* **1980**, *58*, 1200–1211.
- (80) Perdew, J. P.; Wang, Y. *Phys. Rev. B* **1992**, *45*, 13244–13249.
- (81) Perdew, J. P.; Zunger, A. *Phys. Rev. B* **1981**, *23*, 5048–5079.
- (82) Cole, L. A.; Perdew, J. P. *Phys. Rev. A* **1982**, *25*, 1265–1271.
- (83) Perdew, J. P.; Burke, K.; Ernzerhof, M. *Phys. Rev. Lett.* **1996**, *77*, 3865–3868.
- (84) Perdew, J. P.; Burke, K.; Ernzerhof, M. *Phys. Rev. Lett.* **1997**, *78*, 1396.
- (85) Becke, A. D. *Phys. Rev. A* **1988**, *38*, 3098–3100.
- (86) Elliott, P.; Burke, K. *Can. J. Chem.* **2009**, *87*, 1485–1491.
- (87) Perdew, J. P. *Phys. Rev. B* **1986**, *33*, 8822–8824.
- (88) Lee, C. T.; Yang, W. T.; Parr, R. G. *Phys. Rev. B* **1988**, *37*, 785–789.
- (89) Perdew, J. P.; Chevary, J. A.; Vosko, S. H.; Jackson, K. A.; Pederson, M. R.; Singh, D. J.; Fiolhais, C. *Phys. Rev. B* **1992**, *46*, 6671–6687.
- (90) Tao, J.; Perdew, J. P.; Staroverov, V. N.; Scuseria, G. E. *Phys. Rev. Lett.* **2003**, *91*, 146401.
- (91) Zhao, Y.; Truhlar, D. G. *Theor. Chem. Acc.* **2008**, *120*, 215–241.
- (92) Becke, A. D. *J. Chem. Phys.* **1993**, *98*, 5648–5652.
- (93) Becke, A. D. *J. Chem. Phys.* **1993**, *98*, 1372–1377.
- (94) Becke, A. D. *J. Chem. Phys.* **1993**, *98*, 5648–5652.
- (95) Stephens, P. J.; Devlin, F. J.; Chabalowski, C. F.; Frisch, M. J. *J. Phys. Chem.* **1994**, *98*, 11623–11627.
- (96) Adamo, C.; Barone, V. *J. Chem. Phys.* **1999**, *110*, 6158–6170.
- (97) Perdew, J. P.; Tao, J. M.; Staroverov, V. N.; Scuseria, G. E. *J. Chem. Phys.* **2004**, *120*, 6898–6911.
- (98) Neese, F. *Coord. Chem. Rev.* **2009**, *253*, 526–563.
- (99) Furche, F.; Perdew, J. P. *J. Chem. Phys.* **2006**, *124*, 044103.
- (100) Jaramillo, J.; Scuseria, G. E.; Ernzerhof, M. *J. Chem. Phys.* **2003**, *118*, 1068–1073.
- (101) Grimme, S. *J. Chem. Phys.* **2006**, *124*, 034108.
- (102) Schwabe, T.; Grimme, S. *Phys. Chem. Chem. Phys.* **2006**, *8*, 4398–4401.
- (103) Brémond, E.; Adamo, C. *J. Chem. Phys.* **2011**, *135*, 024106.
- (104) Eshuis, H.; Furche, F. *J. Phys. Chem. Lett.* **2011**, *2*, 983–989.

- (105) Schimka, L.; Harl, J.; Stroppa, A.; Grüneis, A.; Marsman, M.; Mittendorfer, F.; Kresse, G. *Nat. Mater.* **2010**, *9*, 741–744.
- (106) Sousa, S. F.; Fernandes, P. A.; Ramos, M. J. *J. Phys. Chem. A* **2007**, *111*, 10439–10452.
- (107) Goerigk, L.; Grimme, S. *Phys. Chem. Chem. Phys.* **2011**, *13*, 6670–6688.
- (108) Weise, T. *Global Optimization Algorithms – Theory and Application*, 2009, <http://www.it-weise.de/projects/book.pdf> (accessed March 17, 2010).
- (109) Holland, J. H. *Adaptation in Natural and Artificial Systems*; The U. of Michigan Press: Ann Arbor, MI, 1975.
- (110) Goldberg, D. *Genetic Algorithms in Search, Optimization, and Machine Learning*; Addison-Wesley: Reading, MA, 1989.
- (111) Johnston, R. L. *Dalton Trans.* **2003**, 4193–4207.
- (112) Goldberg, D.; Deb, K. *Found. Gen. Algor.* **1991**, *1*, 69–93.
- (113) Back, T. In *Proceedings of the First IEEE Conference on Evolutionary Computation*; Eshelman, L. J., Ed.; Morgan Kaufmann: Pittsburgh, PA, 1994, pp 57–62.
- (114) Mühlenbein, H.; Schlierkamp-Voosen, D. *Evol. Comput.* **1993**, *1*, 25–49.
- (115) Blickle, T.; Thiele, L. *Evol. Comput.* **1996**, *4*, 361–394.
- (116) Bulmer, M. *The mathematical theory of quantitative genetics*. Clarendon Press: Oxford, 1980.
- (117) Crow, J. F. In *Mathematical Topics in Population Genetics*; Kojima, K. I., Ed.; Springer: New York, 1970; Chapter Genetic loads and the cost of natural selection, pp 128–177.
- (118) Blickle, T.; Thiele, L. In *Proceedings of the Sixth International Conference on Genetic Algorithms (ICGA95)*; Eshelman, L., Ed.; Morgan Kaufmann Publishers: San Francisco, CA, 1995, pp 9–16.
- (119) Bäck, T. In *Proceedings of the Sixth International Conference on Genetic Algorithms (ICGA95)*; Eshelman, L., Ed.; Morgan Kaufmann Publishers: San Francisco, CA, 1995.
- (120) Arnold, B. C.; Balakrishnan, N.; Nagaraja, H. N. In *Wiley Series in Probability and Mathematical Statistics*; Wiley: New York, 1992.
- (121) Baker, J. E. In *Proceedings of the Second International Conference on Genetic Algorithms*; Lawrence Erlbaum Associates: Cambridge, MA, 1987, pp 14–21.

- (122) Mühlenbein, H.; Voigt, H.-M. In *Proceedings of the Metaheuristics Inter. Conf.* Osman, I. H., Kelly, J. P., Eds.; Kluwer Academic Press: Norwell, 1995.
- (123) Weininger, D. *J. Chem. Inf. Computer Sci.* **1990**, *30*, 237–243.
- (124) Vainio, M. Balloon. <http://users.abo.fi/mivainio/balloon/index.php>, (accessed Sep 14, 2010).
- (125) Gilbert, K.; Guha, R. smi23d - 3D Coordinate Generation. www.chembiogrid.org/cheminfo/smi23d/ (accessed May 13, 2011).
- (126) Douguet, D.; Thoreau, E.; Grassy, G. *J. Comput. Aided Mol. Des.* **2000**, *14*, 449–466.
- (127) Linker, R. *J. Chemometrics* **2005**, *19*, 492–499.
- (128) Burns, J. A.; Whitesides, G. M. *Chem. Rev.* **1993**, *93*, 2583–2601.
- (129) Hassoun, M. H. *Fundamentals of artificial neural networks*; MIT Press: Cambridge, MA, 1995.
- (130) Hertz, J. A.; Krogh, A. S.; Palmer, R. G. *Introduction To The Theory Of Neural Computation*; Addison-Wesley: Redwood City, CA, 1990.
- (131) Fahlman, S. E. In *Proceedings of the 1988 Connectionist Models Summer School*; Morgan Kaufmann: San Francisco, CA, 1988, pp 38–51.
- (132) *Artificial Neural Networks – Methods and Applications*; Livingstone, D. J., Ed.; *Methods in Molecular Biology*, Vol. 458; Humana Press: New York, 2009.
- (133) Coles, M. P.; Gibson, V. C. *Polym. Bull.* **1994**, *33*, 529–533.
- (134) Coles, M. P.; Dalby, C. I.; Gibson, V. C.; Clegg, W.; Elsegood, M. R. *J. Chem. Soc., Chem. Comm.* **1995**, 1709–1711.
- (135) Coles, M. P.; Dalby, C. I.; Gibson, V. C.; Little, I. R.; Marshall, E. L.; Costa, M. H. R. da; Mastroianni, S. *J. Organomet. Chem.* **1999**, *591*, 78–87.
- (136) Kipke, J. Sulfinylamin-Metathese an Vanadyl- und Chromchlorid: ein neuer Zugang zu Katalysatoren für die Olefinpolymerisation., Dissertation, Philipps-Universität Marburg, 2001.
- (137) Gosh, A. *J. Biol. Inorg. Chem.* **2006**, *11*, 671–673.
- (138) Web of Knowledge. <http://www.webofknowledge.com>, Thomson Reuters: New York (accessed Sep 28, 2011).
- (139) Drobny, J. G. *Technology of fluoropolymers*; CRC Press, LLC: Boca Raton, FL, 2000, p 18.
- (140) Weng, W.; Shen, Z.; Jordan, R. F. *J. Am. Chem. Soc.* **2007**, *129*, 15450–15451.

- (141) Keim, W. *Angew. Chem. Int. Ed.* **1990**, *29*, 235–244.
- (142) Ittel, S. D.; Johnson, L. K.; Brookhart, M. *Chem. Rev.* **2000**, *100*, 1169–1204.
- (143) Coles, M. P.; Dalby, C. I.; Gibson, V. C.; Little, I. R.; Marshall, E. L.; Costa, M. H. R. da; Mastroianni, S. *J. Organomet. Chem.* **1999**, *591*, 78–87.
- (144) Nugent, W. A.; Harlow, R. L. *Inorg. Chem.* **1980**, *19*, 777–779.
- (145) Leung, W. H. *Eur. J. Inorg. Chem* **2003**, 583–593.
- (146) Jan, D.; Simal, F.; Demonceau, A.; Noels, A. F.; Rufanov, K. A.; Ustynyuk, N. A.; Gourevitch, D. N. *Tetrahedron Lett.* **1999**, *40*, 5695–5699.
- (147) Jensen, V. R.; Børve, K. J. *Organometallics* **2001**, *20*, 616–626.
- (148) Jensen, V. R.; Børve, K. J. *Chem. Commun.* **2002**, 542–543.
- (149) Jensen, F. J. *Chem. Theory Comput.* **2010**, *6*, 100–106.
- (150) Lee, T. J.; Taylor, P. R. *Int. J. Quantum Chem.* **1989**, *36*, 199–207.
- (151) Janssen, C. L.; Nielsen, I. M. B. *Chem. Phys. Lett.* **1998**, *290*, 423–430.
- (152) Karton, A.; Rabinovich, E.; Martin, J.; Ruscic, B. *J. Chem. Phys.* **2006**, *125*, 144108.
- (153) Cundari, T. R. *J. Am. Chem. Soc.* **1992**, *114*, 7879–7888.
- (154) Andersson, K.; Malmqvist, P. A.; Roos, B. O.; Sadlej, A. J.; Wolinski, K. *J. Phys. Chem.* **1990**, *94*, 5483–5488.
- (155) Finley, J.; Malmqvist, P. A.; Roos, B. O.; Serrano-Andres, L. *Chem. Phys. Lett.* **1998**, *288*, 299–306.
- (156) Grimme, S. *J. Comput. Chem.* **2004**, *25*, 1463–1473.
- (157) Grimme, S. *J. Comput. Chem.* **2006**, *27*, 1787–1799.
- (158) Grimme, S.; Ehrlich, S.; Goerigk, L. *J. Comput. Chem.* **2011**, *32*, 1456–1465.
- (159) Cohen, A. J.; Mori-Sanchez, P.; Yang, W. T. *Science* **2008**, *321*, 792–794.
- (160) Coles, M.; Dalby, C.; Gibson, V.; Clegg, W.; Elsegood, M. *Chem. Commun.* **1995**, 1709–1711.
- (161) Rufanov, K. A.; Kipke, J.; Sundermeyer, J. *Dalton Trans.* **2011**, *40*, 1990–1997.
- (162) Klamt, A.; Schurmann, G. *J. Chem. Soc., Perkin Trans.* **1993**, *2*, 799–805.
- (163) Grimme, S. *J. Comput. Chem.* **2006**, *27*, 1787–1799.
- (164) Kaltsoyannis, N.; McGrady, J.; Harvey, J. In *Principles and Applications of Density Functional Theory in Inorganic Chemistry I; Structure & Bonding*, Vol. 112; Springer: Heidelberg, 2004, pp 81–102.

- (165) Ye, S.; Neese, F. *Inorg. Chem.* **2010**, *49*, 772–774.
- (166) Arlman, E. J. *J. Catal.* **1964**, *3*, 89–98.
- (167) Peters, B.; Heyden, A.; Bell, A. T.; Chakraborty, A. J. *Chem. Phys.* **2004**, *120*, 7877–7886.
- (168) Coles, M.; Dalby, C.; GibsonWilliam, V.; Elsegood, M. *Polyhedron* **1995**, *14*, 2455–2459.
- (169) Danopoulos, A.; Wilkinson, G.; Sweet, T.; Hursthouse, M. *Dalton Trans.* **1995**, 2111–2123.
- (170) Brintzinger, H. H.; Fischer, D.; Mulhaupt, R.; Rieger, B.; Waymouth, R. M. *Angew. Chem., Int. Ed.* **1995**, *34*, 1143–1170.
- (171) Kaminsky, W. *Adv. Catal.* **2001**, *46*, 89–159.
- (172) McKnight, A. L.; Waymouth, R. M. *Chem. Rev.* **1998**, *98*, 2587–2598.
- (173) Rankin, D. W. H.; Robertson, H. E.; Danopoulos, A. A.; Lyne, P. D.; Mingos, D. M. P.; Wilkinson, G. *Dalton Trans.* **1994**, 1563–1569.
- (174) Jorgensen, K. A. *Inorg. Chem.* **1993**, *32*, 1521–1522.
- (175) Bradley, D. C.; Hodge, S. R.; Runnacles, J. D.; Hughes, M.; Mason, J.; Richards, R. L. *Dalton Trans.* **1992**, 1663–1668.
- (176) Jandciu, E. W.; Legzdins, P.; McNeil, W. S.; Patrick, B. O.; Smith, K. M. *Chem. Commun. (Cambridge, U.K.)* **2000**, 1809–1810.
- (177) *Applied Homogeneous Catalysis with Organometallic Compounds*, 2nd ed.; Cornils, B., Herrmann, W. A., Eds.; Wiley-VCH: Weinheim, 2002; Vol. 1.
- (178) Stewart, J. J. P. *J. Mol. Model.* **2007**, *13*, 1173–1213.
- (179) daPiedade, M. E. M.; Simoes, J. A. M. *J. Organomet. Chem.* **1996**, *518*, 167–180.
- (180) Leardi, R. *J. Chemometrics* **2001**, *15*, 559–569.
- (181) Laplaza, C. E.; Cummins, C. C. *Science* **1995**, *268*, 861–863.
- (182) Laplaza, C. E.; Johnson, M. J. A.; Peters, J. C.; Odom, A. L.; Kim, E.; Cummins, C. C.; George, G. N.; Pickering, I. J. *J. Am. Chem. Soc.* **1996**, *118*, 8623–8638.
- (183) Cummins, C. C. *Chem. Commun. (Cambridge, U.K.)* **1998**, 1777–1786.
- (184) Nagata, T. *J. Organomet. Chem.* **2007**, *692*, 225–233.
- (185) Hünenbein, R. *Moleküldesign mit Hilfe quantenchemischer Methoden.*, Dissertation, Westfälische Wilhelms-Universität Münster, 2001.

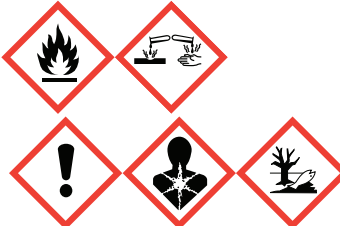
- (186) Dieterich, J. M.; Hartke, B. *Mol. Phys.* **2010**, *108*, 279–291.
- (187) Carstensen, N. O.; Dieterich, J. M.; Hartke, B. *Phys. Chem. Chem. Phys.* **2011**, *13*, 2903–2910.
- (188) Halgren, T. A. *J. Comput. Chem.* **1996**, *17*, 490–519.
- (189) Peng, C.; Schlegel, H. B. *Israel J. Chem.* **1993**, *33*, 449.
- (190) Peng, C.; Ayala, P. Y.; Schlegel, H. B.; Frisch, M. J. *J. Comp. Chem.* **1996**, *17*, 49.
- (191) Williams, J. A. R. Math::Spline - Cubic Spline Interpolation of data. <http://shttp://search.cpan.org/dist/Math-Spline/Spline.pm>, (accessed Okt 26, 2009).
- (192) Bell, R. P. *Proc. R. Soc. Lond.* **1936**, *154*, 414–429.
- (193) Evans, M. G.; Polanyi, M. *Trans. Faraday Soc.* **1938**, *34*, 11–24.
- (194) Tarakeshwar, P.; Choi, H. S.; Kim, K. S. *J. Am. Chem. Soc.* **2001**, *123*, 3323–3331.
- (195) Wheland, G. W. *J. Am. Chem. Soc.* **1942**, *64*, 900–908.
- (196) Coles, M. P.; Gibson, V. C.; Clegg, W.; Elsegood, M. R. J.; Porrelli, P. A. *Chem. Commun. (Cambridge, U.K.)* **1996**, 1963–1964.
- (197) Hursthouse, M.; Motevalli, M.; Sullivan, A.; Wilkinson, G. *Chem. Commun.* **1986**, 1398–1399.
- (198) Kölling, L. Neue Diimidochrom(VI)- und diphosphoraniminatotitan(IV)-Chelatkomplexe – Metallocen-alternative Katalysatoren für die Olefinpolymerisation., Dissertation, Universität Bielefeld, 2001.
- (199) Sheats, W. B.; Olli, L. K.; Stout, R.; Lundeen, J. T.; Justus, R.; Nigh, W. G. *J. Org. Chem.* **1979**, *44*, 4075–4078.
- (200) Wu, C.; Decker, E. R.; Blok, N.; Bui, H.; You, T. J.; Wang, J.; Bourgoyne, A. R.; Knowles, V.; Berens, K. L.; Holland, G. W.; Brock, T. A.; Dixon, R. A. F. *J. Med. Chem.* **2004**, *47*, 1969–1986.
- (201) Hass, H. B.; Bender, M. L. *J. Am. Chem. Soc.* **1949**, *71*, 1767–1769.
- (202) SDBSWeb., National Institute of Advanced Industrial Science and Technology: Japan, <http://riodb01.ibase.aist.go.jp/sdbs/> (accessed Nov 21, 2010).
- (203) Renger, B. *Arch. Pharm.* **1983**, *316*, 193–201.
- (204) Gauthier, R.; Axiotis, G. P.; Chastrette, M. *J. Organomet. Chem.* **1977**, *140*, 245–255.

- (205) Limanto, J.; Dorner, B.; Devine, P. N. *Synthesis* **2006**, *24*, 4143–4150.
- (206) Ciganeck, E. *J. Org. Chem.* **1992**, *57*, 4521–4527.
- (207) Frejd, T.; Klingstedt, T. *Synthesis* **1987**, *1*, 40–42.
- (208) Nystrom, R. F. *J. Am. Chem. Soc.* **1955**, *77*, 2544–2545.
- (209) Kim, Y. H. K.; Shin, J. M. *Tetrahedron Lett.* **1985**, *26*, 3821–3824.
- (210) Perdew, J. P. *Phys. Rev. B* **1986**, *34*, 7406.
- (211) Treutler, O.; Ahlrichs, R. *J. Chem. Phys.* **1995**, *102*, 346–354.
- (212) Weigend, F.; Ahlrichs, R. *Phys. Chem. Chem. Phys.* **2005**, *7*, 3297–3305.
- (213) Turbomole V5.10 2008., TURBOMOLE GmbH: Karlsruhe, Germany, <http://www.turbomole.com>.
- (214) Sierka, M.; Hogekamp, A.; Ahlrichs, R. *J. Chem. Phys.* **2003**, *118*, 9136–9148.
- (215) Frisch, M. J. et al. Gaussian 03, Revision E.01., Gaussian, Inc.: Wallingford, CT, 2004.
- (216) Tarnopolsky, A.; Karton, A.; Sertchook, R.; Vuzman, D.; Martin, J. M. L. *J. Phys. Chem. A* **2008**, *112*, 3–8.
- (217) Neese, F. ORCA, an Ab Initio, Density Functional and Semiempirical Electronic Structure Program Package, Version 2.6, Revision 71., Max-Planck Institut für Bioanorganische Chemie: Mülheim/Ruhr, Germany, 2008.
- (218) Neese, F.; Wennmohs, F.; Hansen, A.; Becker, U. *Chem. Phys.* **2009**, *356*, 98–109.
- (219) Jaguar, V. 7.6., Schrödinger, LLC: New York, 2009.
- (220) Werner, H.-J. et al. MOLPRO, Version 2006.1., University College Cardiff Consultants Ltd.: Cardiff, U.K.
- (221) Dunning, T. H. *J. Chem. Phys.* **1989**, *90*, 1007–1023.
- (222) Jong, W. A. de; Harrison, R. J.; Dixon, D. A. *J. Chem. Phys.* **2001**, *114*, 48–53.
- (223) Balabanov, N. B.; Peterson, K. A. *J. Chem. Phys.* **2005**, *123*, 064107.
- (224) Feller, D. *J. Comput. Chem.* **1996**, *17*, 1571–1586.
- (225) Schuchardt, K. L.; Didier, B. T.; Elsethagen, T.; Sun, L. S.; Gurumoorthi, V.; Chase, J.; Li, J.; Windus, T. L. *J. Chem. Inf. Model.* **2007**, *47*, 1045–1052.
- (226) Aquilante, F.; De Vico, L.; Ferré, N.; Ghigo, G.; Malmqvist, P.-; Neogrády, P.; Pedersen, T. B.; Pitoňák, M.; Reiher, M.; Roos, B. O.; Serrano-Andrés, L.; Urban, M.; Veryazov, V.; Lindh, R. *J. Comput. Chem.* **2010**, *31*, 224–247.

- (227) Veryazov, V.; Widmark, P. O.; Serrano-Andres, L.; Lindh, R.; Roos, B. O. *Int. J. Quantum Chem.* **2004**, *100*, 626–635.
- (228) Karlstrom, G.; Lindh, R.; Malmqvist, P. A.; Roos, B. O.; Ryde, U.; Veryazov, V.; Widmark, P. O.; Cossi, M.; Schimmelpfennig, B.; Neogrady, P.; Seijo, L. *Comput. Mater. Sci.* **2003**, *28*, 222–239.
- (229) Widmark, P. O.; Malmqvist, P. A.; Roos, B. O. *Theor. Chim. Acta* **1990**, *77*, 291–306.
- (230) Roos, B. O.; Lindh, R.; Malmqvist, P. A.; Veryazov, V.; Widmark, P. O. *J. Phys. Chem. A* **2004**, *108*, 2851–2858.
- (231) Roos, B. O.; Lindh, R.; Malmqvist, P. A.; Veryazov, V.; Widmark, P. O. *J. Phys. Chem. A* **2005**, *109*, 6575–6579.
- (232) Allinger, N. L. *J. Am. Chem. Soc.* **1977**, *99*, 8127–8134.
- (233) Kundrot, C. E.; Ponder, J. W.; Richards, F. M. *J. Comput. Chem.* **1991**, *12*, 402–409.
- (234) Ponder, J. W.; Richards, F. M. *J. Comput. Chem.* **1987**, *8*, 1016–1024.
- (235) Pappu, R. V.; Hart, R. K.; Ponder, J. W. *J. Phys. Chem. B* **1998**, *102*, 9725–9742.
- (236) Ren, P. Y.; Ponder, J. W. *J. Comput. Chem.* **2002**, *23*, 1497–1506.
- (237) Ren, P. Y.; Ponder, J. W. *J. Phys. Chem. B* **2003**, *107*, 5933–5947.
- (238) Hodsdon, M. E.; Ponder, J. W.; Cistola, D. P. *J. Mol. Biol.* **1996**, *264*, 585–602.
- (239) Stewart, J. J. P. MOPAC2009., Stewart Computational Chemistry: Colorado Springs, CO, 2008, <http://OpenMOPAC.net>.
- (240) Fraser, A.; Burnell, D. *Computer Models in Genetics*; McGraw-Hill: New York, 1970.
- (241) Bunce, T. DBI - Database independent interface for Perl. <http://search.cpan.org/~timb/DBI-1.616/DBI.pm> (accessed Jan 10, 2009).
- (242) Galbraith, P. DBD::mysql - MySQL driver for the Perl5 Database Interface. <http://search.cpan.org/~capttofu/DBD-mysql-4.020/lib/DBD/mysql.pm>, (accessed Jan 10, 2010).
- (243) Qumsieh, A. AI::Genetic - A pure Perl genetic algorithm implementation. <http://search.cpan.org/~aqumsieh/AI-Genetic-0.05/Genetic.pm>, (accessed Dez 12, 2009).
- (244) Srinivas, M.; Patnaik, L. M. *IEEE Trans. Sys. Man Cybern.* **1994**, *24*, 656–667.
- (245) Radau, G. *Monatsh. Chem.* **2003**, *134*, 1159–1166.

- (246) Yan, Y.; Chapman, B. Comparative Study of Distributed Resource Management Systems—SGE, LSF, PBS Pro, and LoadLeveler.; tech. rep.; Department of Computer Science, University of Houston, TX, 2008.
- (247) GlusterFS 3.2., Gluster, Inc.: Sunnyvale, CA, 2010.

Hazardous Materials

Substance	Symbol	H-, P- and EUH	CMR
Acetone		H: 225-319-336 EUH066 P: 210-233-305+351+338	
Aluminum chloride		H: 314 P: 280-305+351+338-310	
Benzene		H: 225-350-340-372-304-319-315 P: 201-210-308+313-301+310-331-305+351+338-302+352	K 1A, M 1B
Benzophenone		H: 315-319-335-412 P: 261-264-273-280-302+352-304+340-305+351+338-312-321-332+313-337+313-362-403+233-405-501	
1,4-Bis(chloromethyl)benzene		H: 302-315-319-400 P: 273-305+351+338	
Butyllithium in hexanes		H: 225-250-260-304-314-336-361f-373-411 P: 210-222-223-231+232-370+378-422	

Substance	Symbol	H-, P- and EUH	CMR
Calciumhydride		H: 260 P: 231+232-370+378-422	
Carbon tetrachloride		H: 301-311-331-351-372-412 P: 261-273-280-301+310-311-501	K 2
Cerium chloride		H: 315-319-335 P: 261-305+351+338	
Chloroform		H: 351-302-373-315 P: 302+352-314	
Chlorotrimethylsilane		H: 225-312-314-331-335 P: 210-261-280-305+351+338-310	
Chromyl chloride		H: 271-314-317-340-350i-410 P: 201-220-273-280-305+351+338+310	K 1B
Dichloromethane		H: 351 P: 281-308+313	K 2
Diethyl ether		H: 224-302-336 EUH019, EUH066 P: 210-240-403+235	
Ethanol		H: 225 P: 210	

Substance	Symbol	H-, P- and EUH	CMR
Heptane		H: 225-304-315-336-410 P: 210-261-273-301+310-331-501	
<i>n</i> -Hexane		H: 225-304-361-373-315-336-411 P: 210-240-273-301+310-331-302+352-403+235	R _F 2
Lithium aluminum hydride		H: 260-314 P: 223-231+232-280-305+351+338-370+378-422	R _F 2
Methanol		H: 225-331-311-301-370 P: 210-233-280-302+352-309+310	
Sodium		H: 260-314 EUH014 P: 223-231+232-260-264-280-301+330+331-303+361+353-304+340-305+351+338-310-321-335+334-370+378-402+404-405-501	
Sodiumhydroxide		H: 314-290 P: 280-301+330+331-309+310-305+351+338	
Tetrahydrofurane		H: 225-319-335 EUH019 P: 210-233-243-305+351+338	

Substance	Symbol	H-, P- and EUH	CMR
Thionyl chloride		H: 302-314-332 P: 280-305+351+338-310	
Toluene		H: 225-304-315-336-361d-373 P: 210-261-281-301+310-331	R _E 2
Triethylamine		H: 225-331-311-302-314 P: 210-280-303+361+353-305+351+338-310-312	